Università degli Studi di Genova
Facoltà di Scienze Matematiche, Fisiche e Naturali
XVI° ciclo dottorato

Towards the detection of subMeV solar neutrinos in Borexino: data reconstruction and analysis tools

Daniela Manuzio

Internal Advisor:
Dott. Marco Pallavicini

External Advisor:
Prof. GianPaolo Bellini

Index

1 Introduction **1**

2 Solar neutrinos and neutrino oscillations **3**
2.1 The solar model . . . 3
2.2 The solar neutrino experiments and the solar neutrino puzzle before 1998 . 7
2.2.1 The solar neutrino experiments . . . 7
2.2.2 Three solar neutrino problems . . . 10
2.2.3 Astrophysical and non-oscillating neutrinos solutions . . . 12
2.3 Neutrino oscillations and the Super-Kamiokande evidence . . . 13
2.3.1 Oscillations in vacuum . . . 13
2.3.2 Oscillations in matter . . . 14
2.3.3 Atmospheric neutrinos . . . 15
2.3.4 The Super-Kamiokande result: evidence for oscillation of atmospheric neutrinos . . . 17
2.4 The confirmations to the SSM from the nuclear cross sections measurements 20
2.5 A global analysis of the solar neutrino data . . . 22
2.6 The SNO and KamLAND results . . . 24
2.6.1 The SNO neutral and charged current measurement . . . 24
2.6.2 The KamLAND result: evidence for reactor anti-neutrino disappearance . . . 27

3 The experimental layout **31**
3.1 Overview of the BOREXINO Project . . . 31
3.2 The Gran Sasso underground laboratory . . . 32
3.3 The structure of the detector . . . 33
3.3.1 The outer water tank and the water buffer . . . 35
3.3.2 The stainless steel sphere . . . 36
3.3.3 The inactive buffer . . . 38
3.3.4 The inner vessel . . . 38
3.3.5 The scintillator . . . 40
3.3.6 Phototubes and light concentrators . . . 44
3.3.7 The muon detector . . . 49
3.3.7.1 The inner muon veto system . . . 49
3.3.7.2 The outer muon system . . . 50
3.3.8 The flash ADC . . . 50
3.3.9 The calibration system . . . 51
3.3.9.1 The inner PMTs calibration system . . . 52

3.3.9.2 The outer PMTs calibration system . . . 53
3.3.9.3 The optical calibration system . . . 53
3.3.9.4 Calibrations with radioactive sources . . . 53
3.4 Ancillary Plants . . . 54
3.4.1 The fluid handling systems . . . 54
3.4.2 The scintillator purification system . . . 55
3.4.3 The water purification system . . . 57
3.4.4 The nitrogen purification systems . . . 58
3.5 The Counting Test Facility (CTF) . . . 59
3.5.1 The structure of the CTF detector . . . 61
3.5.2 Results from CTF 1 . . . 62
3.5.3 CTF upgrades and the CTF 3 campaign . . . 64

4 The borexino experiment 67
4.1 Background . . . 67
4.1.1 External background . . . 67
4.1.1.1 Sources . . . 68
4.1.1.2 Expected γ rates in the scintillator . . . 70
4.1.2 Internal background . . . 74
4.1.2.1 Sources . . . 74
4.1.2.2 Rejection methods . . . 77
4.1.3 Cosmogenic backgrounds . . . 79
4.1.3.1 Neutron flux from the rock walls . . . 79
4.1.3.2 γ -rays from capture of cosmogenic neutrons . . . 79
4.1.3.3 Radionuclides produced by muons in the scintillator . . . 80
4.1.3.4 Muons and prompt secondaries . . . 81
4.2 Neutrino signal in BOREXINO . . . 82
4.3 The physics potential of BOREXINO . . . 83
4.3.1 Solar neutrino physics from BOREXINO . . . 83
4.3.2 Physics beyond solar neutrinos . . . 84
4.3.3 Supernova neutrino detection in BOREXINO . . . 84

5 Daq and data handling 87
5.1 The electronic chain . . . 87
5.1.1 The expected PMT 's signal . . . 88
5.1.2 The front end electronics . . . 89
5.1.2.1 The inner detector front end electronics . . . 89
5.1.2.2 The outer detector front end electronics . . . 94
5.1.3 The HV power supply . . . 96
5.1.4 The digital read out electronics . . . 97
5.1.4.1 The inner detector digital electronics . . . 97
5.1.4.2 The outer detector digital electronics . . . 100
5.2 The trigger system . . . 101
5.2.1 The trigger alghoritm and the BOREXINO Trigger Board . . . 101
5.2.2 The BTB 's DSP firmware . . . 105
5.2.3 The service-triggers . . . 107
5.2.3.1 VETO signals . . . 108
5.2.3.2 Calibration pulses . . . 109
5.2.3.3 Random triggers . . . 110
5.2.3.4 Calibration laser triggers . . . 111

5.2.3.5 Laser 355 and laser 266 triggers . . . 112
5.2.3.6 Outer muon triggers . . . 112
5.2.4 The clock generator . . . 113
5.2.5 The absolute time clock . . . 113
5.3 The data acquisition system . . . 115
5.3.1 The graphical user interface . . . 115
5.3.2 The slow control . . . 118
5.4 Online Analyzer . . . 119

6 Event simulation code 121
6.1 The Monte Carlo simulation chain . . . 121
6.2 GEneration of NEutrinos and Background . . . 121
6.2.1 Background events . . . 122
6.2.2 Neutrino events . . . 123
6.2.3 The code . . . 124
6.3 Tracking . . . 125
6.3.1 The fortran tracking code . . . 125
6.3.2 The GEANT4 based tracking code . . . 126
6.4 Simulation of the electronics . . . 127

7 Structure of the data analysis 129
7.1 General description of the code structure . . . 129
7.2 Event readout and decoding . . . 130
7.3 The preprocessing algorithm . . . 132
7.4 Data Base interface . . . 135
7.5 Event splitting . . . 137
7.6 Event reconstruction . . . 139
7.6.1 Spatial Reconstruction . . . 139
7.6.2 Energy Reconstruction . . . 139
7.7 Particle identification . . . 140
7.8 Interface to ROOT . . . 141
7.8.1 Output data structure: the BxTree class . . . 141
7.8.2 The ROOT interface routines . . . 144
7.9 The dark noise runs analysis . . . 145
7.10 Time and charge calibration routines . . . 146
7.10.1 The time calibration . . . 146
7.10.2 The charge calibration . . . 147

8 The Air Runs data 149
8.1 The first low level debugging . . . 149
8.2 The time and charge measurement problems . . . 151
8.2.1 The time measurement problems . . . 151
8.2.2 The charge measurement problems . . . 156
8.2.3 The trigger and laser time reference signals . . . 158
8.3 The status of the detector . . . 159
8.4 The calibration laser data . . . 161
8.5 The optical laser data . . . 163
8.6 The dark noise data . . . 170
8.7 Some consistency checks on our electronics . . . 170
8.8 The first radioactive source data . . . 177

8.9 Monte Carlo studies on the splitting algorithm 179
8.10 Air Run V data: the splitting and spatial reconstruction results 183

9 The particle identification methods **187**
9.1 α/β discrimination techniques in BOREXINO 187
9.1.1 The tail to total ratio 190
9.1.2 The Gatti linear discriminant 190
9.1.3 The maximum likelihood functions 191
9.1.4 The Kolmogorov distances 192
9.1.5 The Support Vector Machines 192
9.2 Results on α/β discrimination efficiency with Air Run 8 data 193
9.2.1 The selection of the training set 194
9.2.2 Results with the source on the detector's center 195
9.2.2.1 The basic classifiers efficiencies 196
9.2.2.2 The *primary* svm results 199
9.2.2.3 The *global* svm results 199
9.2.3 Position dependency studies 203
9.2.3.1 The time of flight correction 204
9.2.3.2 The non-correction approach 206
9.3 The source spectrum analysis 208

Acknowledgements **213**

Bibliography **215**

Introduction

The first forty years of solar neutrino research demonstrated that new physics may appear when neutrino experiments are carried out in a new domain of sensitivity or in an unexplored energy range. After the recent exciting developments, that have given a solid experimental evidence of neutrino oscillations in the solar sector, the great challenge is now to make an accurate measurement of the neutrino flux below 1 MeV, a domain in which the solar neutrino flux has been measured using radiochemichal techniques only, without any information about the energy spectrum.

There are three primary reasons for doing low energy solar neutrino experiments. The first reason is to test whether new physics shows up at lower energies: new phenomena may be revealed at energies below 1 MeV, that are not discernible at higher energies (> 5 MeV). According to the currently accepted LMA oscillation solution, for istance, the basic oscillation mechanism switches somewhat below 1 MeV from the MSW matter-dominated oscillations, that prevail at high energies, to the vacuum oscillations that dominate at low energies.
Second, new solar neutrino experiments will provide accurate measurements of the fluxes of the important p-p and ^7Be solar neutrino fluxes, that together amount to more than 98% of the total flux of solar neutrinos predicted by the standard solar model. The rare ^8B neutrino flux is, so far, the only solar neutrino source for which measurements of the energy have been made, but ^8B neutrinos constitute a fraction of less than 10^{-4} of the total solar neutrino flux. These measurements will test the solar model predictions for the main energy-producing reactions, predictions that are more precise than for the higher-energy neutrinos. Moreover, the combination of a ^7Be solar neutrino experiment and a p-p solar neutrino experiment can test experimentally the competition between the two primary ways of terminating the p-p chain: ^3He -^3He or ^3He -^4He [1].
Third, low-energy solar neutrino experiments, ^7Be plus p-p, will make possible a precise measurement of the vacuum mixing angle, θ_{12}, and will yield a slightly improved constraint on θ_{13} and an improved measurement of the sterile mixing parameter $sin^2\eta$ [1].

BOREXINO is a real-time detector for low energy neutrino spectroscopy, nearing completion of construction in the underground laboratories at Gran Sasso. The main experiment's goal is the direct measurement of the flux of the mono-energetic ^7Be solar neutrinos of all flavours via elastic neutrino-electron scattering in an ultra-pure scintillation liquid. The physics potential of such detection technique relies on unprecedented low levels of radioactive background.

Unfortunately, the experiment was in its final installation phase at the Gran Sasso laboratories when, in August 2001, an accident in Hall C caused a small PC spill of about 50 liters, which was drained outside the laboratories. This circumstance led to an immediate

[1] The ratio of the rate of ^3He -^3He reactions to the rate of ^3He -^4He reactions averaged over the Sun can be expressed in terms of the p-p and ^7Be neutrino fluxes.

stop of all the PC related operations and to several legal actions, culminated with the judicial sequestration of the Hall C on May 2002 and with the complete stop of any underground task, except for the purely mechanical jobs.
Finally, in January 2004, the permission to manipulate limited amounts of water in Hall C allowed to resume, at least, the preliminary works for the vessels installation. While we are confident to complete the final installation for the end of this month, we are also hoping that in the next few months a clear perspective will develop, allowing to resume in a well defined time frame all BOREXINO activities.

Meanwhile, in this long stop period, the Collaboration focused its efforts towards activities not implying scintillator or water manipulation, thus essentially on the accomplishment of the residual installations yet to be completed and on the global testing of the overall acquisition system already set up, from the PMT 's, to the electronics, the DAQ and the reconstruction software, including some of the calibration instruments. Particularly, of special importance and success were the several trial data taking runs carried out in the last years, aimed at a global test of the whole acquisition chain. The offline software has been as well an area of significant developments, partly triggered also by the outcomes of the acquisition tests.

This thesis reports on the work that I carried out in the past three years within the BOREXINO collaboration. In the absence of data taken from BOREXINO in full operation, my major activities were the setting up and tuning of the main electronics system of the experiment, the development and test of the data acquisition system, the development of several part of the offline reconstruction code and, finally, the design, development and test of a brand new package for pulse shape analysis and α/β discrimination.

This thesis is structured in two main parts: the first is a short history of the solar neutrino physics and an overview of the BOREXINO experiment, meaning and goals.
I present a brief outline of the recent results on solar neutrino physics in chapter 2, an overview of the BOREXINO detector in chapter 3, and finally chapter 4 summarizes the BOREXINO physics goals and the detection principle. The extremely low background requirements of the detector are also emphasized in this chapter.
The second part of this dissertation is devoted to the areas in which my contribution was more significant and direct: the electronics system commissioning, the data acquisition system and the data analysis software. A thorough description of BOREXINO 's electronic chain, trigger and data acquisition systems is given in chapter 5. The following two chapters are dedicated to the description of the Monte Carlo code for event simulation in BOREXINO and of the *offline* data reconstruction software, that has been a large part of my work. Results from the data analysis of the several periods of acquisition tests taken in the last years are shown in chapter 8 and chapter 9. This last chapter describes the main results obtained in this thesis. Using the reconstruction code described in 7, I have analyzed the data collected with a small calibration source inserted into the BOREXINO detector. The results show that a very good α/β discrimination is possible, if clever techniques are used.

Solar neutrinos and neutrino oscillations

For more than 30 years the solar neutrino anomaly, a deficit of neutrinos emanating from the Sun, has puzzled both physicists and astrophysicists. During these years enormous efforts have been done, both on theoretical and experimental understanding.
Recently, neutrino oscillations of ν_μ and flavour transitions of solar neutrinos became evident, mostly thanks to the results obtained by the SNO and KamLAND collaborations. Yet, oscillation parameters of ν_e to explain the solar neutrino anomaly had not been determined strictly, even if the *"large mixing angle"* (LMA) region is now the only allowed parameter region from the global analysis using all solar neutrino experiments.

A complete understanding of the neutrino oscillation physics and of the solar neutrino spectrum is then still far by being reached. The recent results mostly have come out from the analysis of the ^8B neutrinos, which are a tiny fraction of the total solar flux. Therefore a complete measurement of the solar neutrino spectrum, and particularly in the energy range below 1 MeV, is still extremely interesting, for the understanding of both the solar and the neutrino physics.

This chapter briefly summarizes the history of these 30 years of neutrino research, from the first observation of the solar neutrino deficit to the last results on the physics of neutrino oscillations. A complete description of the recent results and physics implication can be found in [1, 2, 3].

2.1 The solar model

The question of what powers the Sun first raised in the 19th century. Until the late 1800's, it was believed that the energy of the stars was produced in chemical reactions or gravitational contraction. However, the energy that can be produced through these processes is not enough to account for the Sun luminosity integrated over its age, estimated through geological considerations. The solution was provided only in the late 1930's by Hans Bethe [9]. His theory states that the only sources capable of powering the Sun over the billions years required for our solar system by the age of meteorites and terrestrial rocks analysis, are thermonuclear processes occurring in the Sun's core.

It is generally assumed that the original main constituent of the universe was hydrogen. Bethe worked out the basic processes by which in a region of very high temperatures, such as the stellar interiors, four hydrogen nuclei are fused into a helium nucleus. The process:

$$4p \rightarrow \alpha \ + 2\mathrm{e}^+ \ + 2\nu_\mathrm{e} \ + 26.7\,\mathrm{MeV} \tag{2.1}$$

releases two positrons, two electron neutrinos and some excess energy (26.7 MeV).

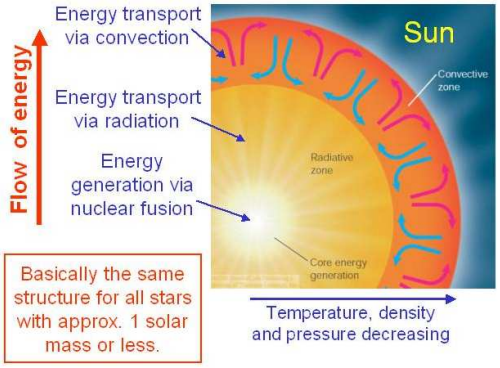

(a) Figure 2.1: Flow energy inside the stellar structure.

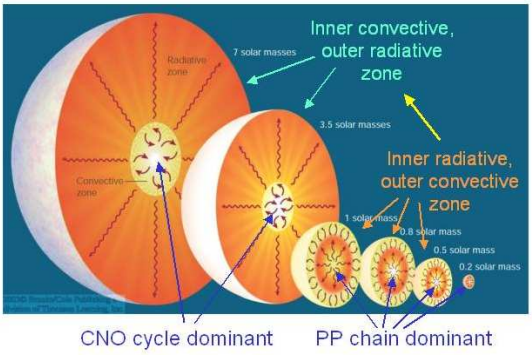

(b) Figure 2.1: Dominant energy sources and transport mechanisms inside the stars.

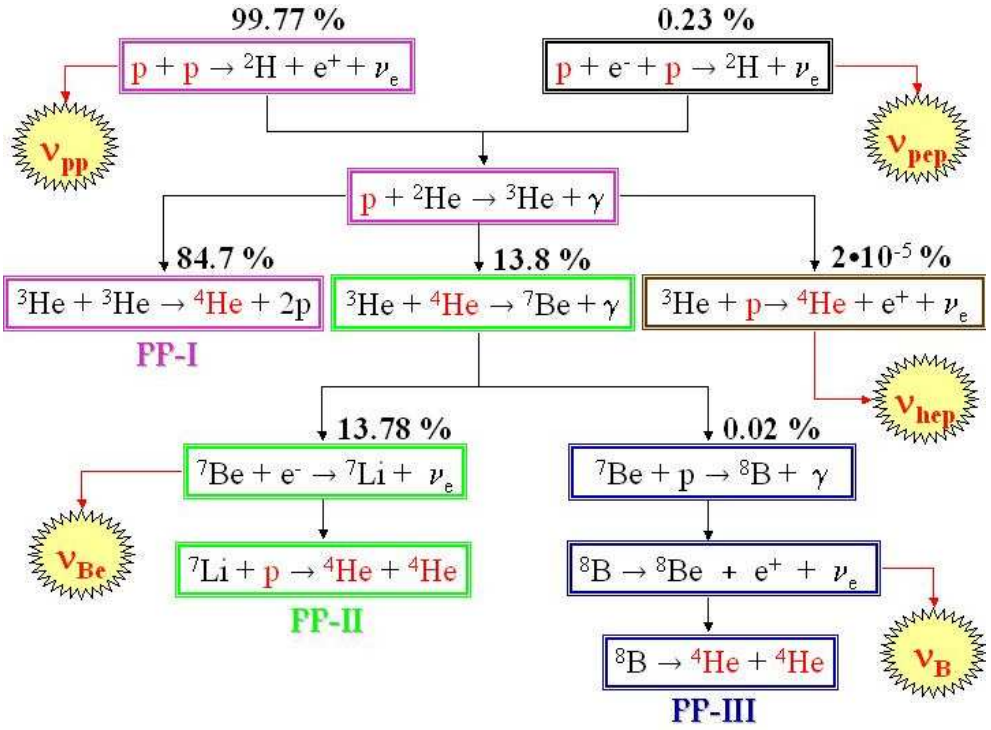

Figure 2.2: The proton-proton (pp) chain of nuclear fusion reactions in the Sun. The % values indicated are the branching ratio of each reaction.

While most of the released energy is carried by photons, that ultimately diffuse to the surface of the Sun and escape in the form of sunlight and other radiation, 3% of it is emanated in the form of low energy neutrinos (E $\leq$ 18.8 MeV).
Bethe discussed two reaction sequences building helium out of hydrogen: the proton-proton (pp) chain and the carbon-nitrogen-oxygen (CNO) cycle. Today the pp process is thought to be the dominant energy source in stars like the Sun and less massive stars, contributing to more than 98% of the sunshine.

Reaction (pp chain and CNO cycle)	***Neutrino source***	***Q [MeV]***	***E_ν [MeV]***	***$<q_\nu>$ [MeV]***
$p + p \rightarrow {}^2H + e^+ \ \nu_e$	pp	0.420	$\leq$ 0.420	0.265
$p + e^- + p \rightarrow {}^2H + \nu_e$	pep	1.442	1.442	1.442
${}^7Be + e^- \rightarrow {}^7Li + \nu_e$	${}^7Be$	0.862 (90%)	0.862	0.862
		0.383 (10%)	0.383	0.383
${}^8B \rightarrow {}^8Be + e^+ + \nu_e$	${}^8B$	17.980	$\leq$ 15	6.71
${}^3He + p \rightarrow {}^4He + e^+ + \nu_e$	hep	19.795	$\leq$ 18.8	9.27
${}^{13}N \rightarrow {}^{13}C + e^+ + \nu_e$	${}^{13}N$	2.221	$\leq$ 1.199	0.7067
${}^{15}O \rightarrow {}^{15}N + e^+ + \nu_e$	${}^{15}O$	2.754	$\leq$ 1.732	0.9965
${}^{17}F \rightarrow {}^{17}O + e^+ + \nu_e$	${}^{17}F$	2.762	$\leq$ 1.740	0.9994

TABLE 2.1: NEUTRINO-EMITTING REACTIONS IN THE SUN, FROM THE pp CHAIN AND THE CNO CYCLE. hep AND ${}^7Be$ NEUTRINO SOURCES EMIT MONOENERGETIC LINES; THE OTHER SOURCES EMIT A CONTINUOUS SPECTRUM. $<q_\nu>$ IS THE AVERAGE NEUTRINO ENERGY.

Since the pp reaction is at the base of the pp chain, the pp neutrino flux is connected directly to the Sun luminosity, but for all the other neutrino sources detailed models describing the conditions inside the Sun are necessary. The Solar Models are, in essence, the solutions of the evolution equation for the stars, based on the fundamental assumption that the Sun is a star of the Main Sequence, spherical and in hydrostatic equilibrium between gravity and the radiative pressure produced by the thermonuclear reactions at its core. The luminosity, the radius, the age and the mass of the Sun are the boundary conditions, while the input data are provided by the energies and cross sections of the nuclear reactions involved. The system of equations is then solved iteratively until there is agreement between the model and the boundary conditions.
The results of several models have been published by different authors, all essentially in agreement. Hereafter, I will consider the model recently published by Bahcall and Pinsonneault [10] (BP00) as the Standard Solar Model (SSM). Table 2.2 lists the solar neutrino spectra and fluxes of each individual source, as predicted by the Standard Solar Model.

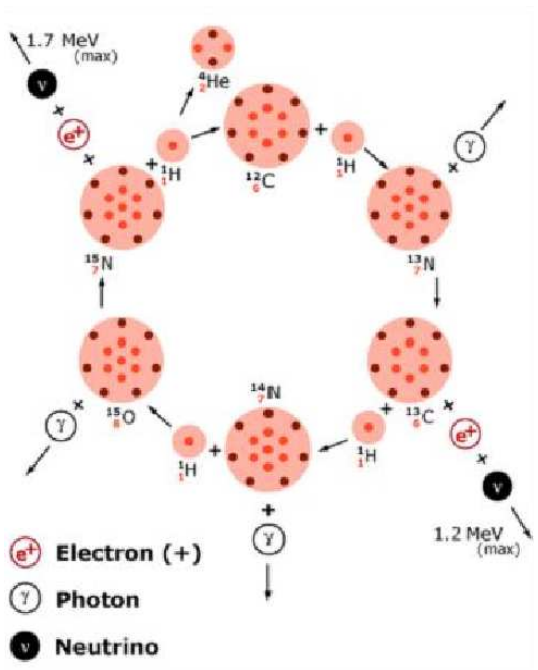

(a) Figure 2.3: The CNO cycle.

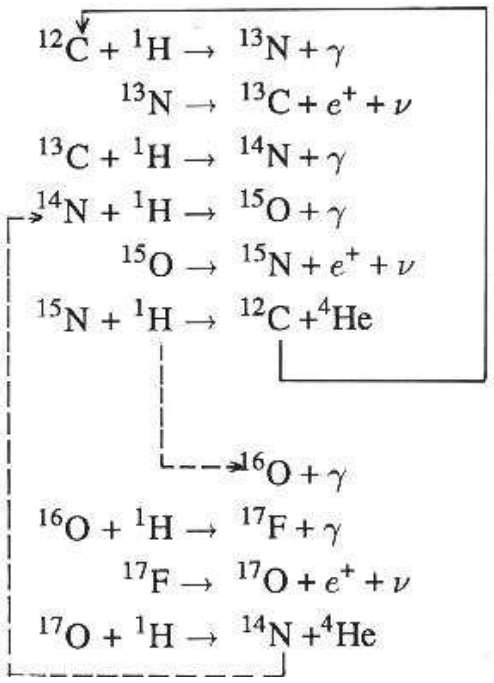

(b) Figure 2.3: The CNO cycle.

Source	***Flux*** $[10^{10}\ \mathrm{cm}^{-2}\mathrm{s}^{-1}]$	***Cl rate*** [SNU]	***Ga rate*** [SNU]
pp	5.96	0.0	69.6
pep	1.4×10^{-2}	0.22	2.8
hep	9.3×10^{-7}	0.04	0.1
^{7}Be	4.77×10^{-1}	1.15	34.2
^{8}B	5.05×10^{-4}	5.76	12.1
^{13}N	5.48×10^{-2}	0.09	3.4
^{15}O	4.80×10^{-2}	0.33	5.5
^{17}F	5.63×10^{-2}	0.0	0.1
Total		$7.6^{+1.3}_{-1.1}$	129^{+8}_{-6}

Table 2.2: Neutrino fluxes predicted by the BP00 solar standard model. The last two columns show the predicted capture rate in the Chlorine and Gallium experiments, measured in Solar Neutrino Units (snu), equivalent to 10^{-36} captures per target atom per second.

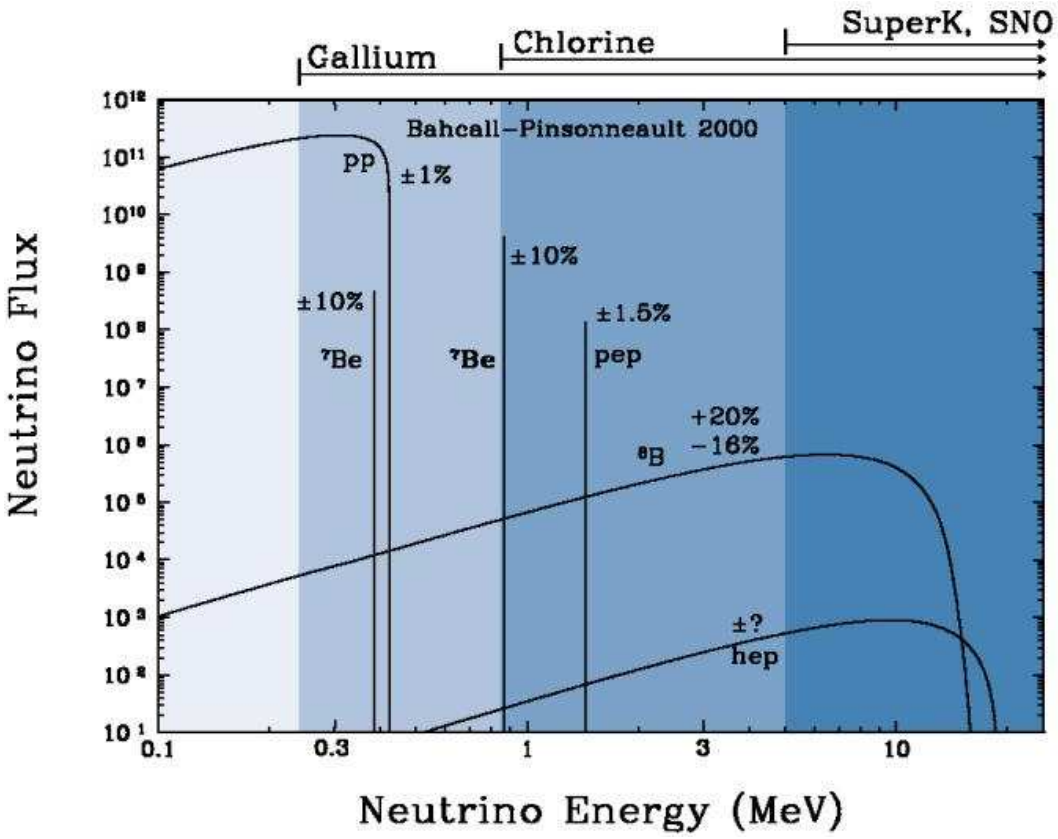

FIGURE 2.4: ENERGY SPECTRUM OF THE PP CHAIN SOLAR NEUTRINOS ACCORDING TO THE BP00 SOLAR MODEL. THE ERRORS FOR THE FLUX PREDICTION OF EACH SOURCE ARE INDICATED.

2.2 THE SOLAR NEUTRINO EXPERIMENTS AND THE SOLAR NEUTRINO PUZZLE BEFORE 1998

2.2.1 THE SOLAR NEUTRINO EXPERIMENTS

The first pioneering experiments that achieved the scientific goal to detect solar neutrinos were radiochemical and water Cerenkov experiments.
Radiochemical experiments were based on neutrino capture reactions by specific isotopes. The reaction products were then chemically separated from the target mass and counted through low background proportional chambers. This radiochemical detection technique is sensitive only to ν_e above some energy threshold and does not convey any information on the time and the energy of the events.

The very first neutrino detector, a 390 m^3 tank full of C_2Cl_4, was operated since 1968 by R. Davis [11] in the Homestake Gold Mine, in South Dakota. The detection reaction was

the inverse β process:

$$\nu_e + {}^{37}Cl \rightarrow e^- + {}^{37}Ar \tag{2.2}$$

and had an energy threshold of 814 KeV. The SSM prediction for the neutrino capture rate in this Chlorine experiment was

$$R_{th} = 7.7^{1.2}_{-1.0}\text{SNU}\ [1], \tag{2.3}$$

while the measured rate, averaged over 25 years of data-taking, were roughly one third of the predicted value:

$$R_{\text{Homestake}} = [2.56 \pm 0.16(\text{stat.}) \pm 0.16(\text{syst.})]\ \text{SNU}. \tag{2.4}$$

(a) FIGURE 2.5: THE TANK CONTAINING THE C_2Cl_4 IN THE HOMESTAKE MINE.

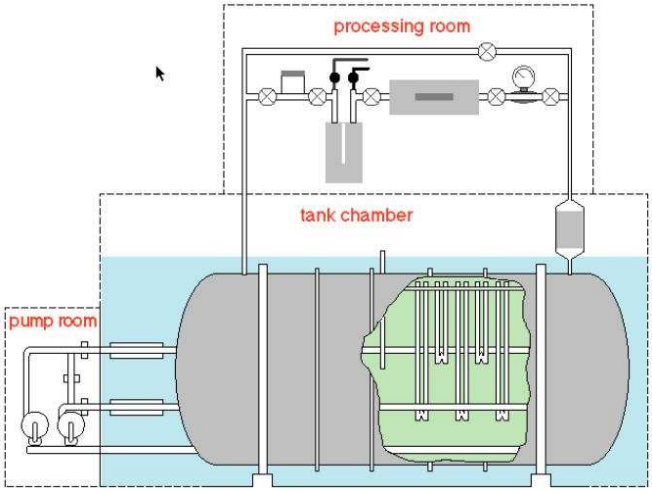

(b) FIGURE 2.5: SCHEMATIC DRAWING OF DAVIS'S CHLORINE EXPERIMENT.

The other three experiments, SAGE [12], GALLEX [13] and GNO [14], used instead the neutrino capture reaction:

$$\nu_e + {}^{71}Ga \rightarrow e^- + {}^{71}Ge \tag{2.5}$$

that has an energy threshold (233 KeV) low enough to allow the detection of *pp* solar neutrinos. The measured neutrino capture rates:

$$R_{\text{SAGE}} = [67.2^{+7.2}_{-7.0}(\text{stat.})^{+3.5}_{-3.0}(\text{syst.})]\ \text{SNU} \tag{2.6}$$

$$R_{\text{GALLEX}} = [77.5 \pm 6.2(\text{stat.})^{+4.3}_{-4.7}(\text{syst.})]\ \text{SNU} \tag{2.7}$$

[1] 1 SNU (Standard Neutrino Unit) is defined as 10^{-36} captures per target atom per second.

$$R_{\mathrm{GNO}} = [65.8^{+10.2}_{-9.6}(\mathrm{stat.})^{+3.4}_{-3.6}(\mathrm{syst.})] \text{ SNU} \tag{2.8}$$

were all about 54% of the predicted rate, confirming the depletion scenario seen by the Chlorine experiment.

In 1983 the first water Cerenkov detector, Kamiokande, was built in a mine in Japan. About 1000 photomultiplier tubes were observing the Cerenkov radiation produced by the neutrino-electron elastic scattering reaction

$$\nu_{\mathrm{x}} + \mathrm{e}^- \rightarrow \nu_{\mathrm{x}} + \mathrm{e}^- \tag{2.9}$$

in the 680 tons fiducial volume of ultra-pure water. In 1994 the detector was shut down and replaced by its large scale upgraded successor: Super-Kamiokande. This 50 kiloton water detector, instrumented with more than 11000 phtomultipliers and facing an inner 22.5 kiloton fiducial volume of ultra-pure water, started data taking in 1996.

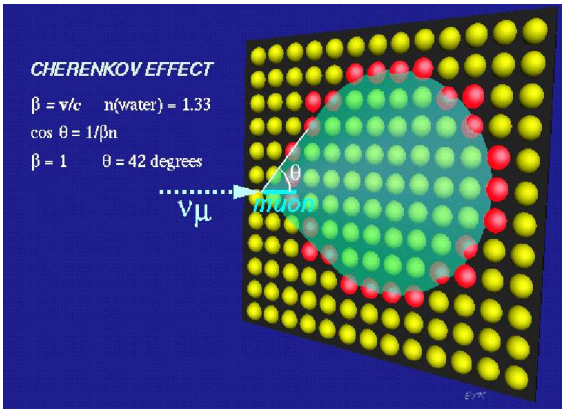

(a) FIGURE 2.6: CERENKOV RADIATION IS PRODUCED WHENEVER THE VELOCITY β C OF THE PARTICLE EXCEEDS C/N, WHERE N IS THE INDEX OF REFRACTION OF THE MEDIUM TRAVERSED AND β IS THE USUAL RELATIVISTIC TERM $(1/\sqrt{1-(v/c)^2})$.

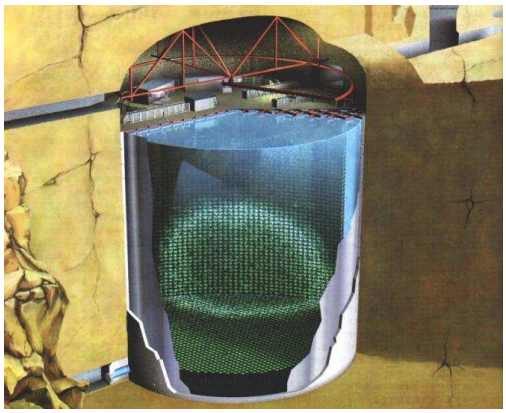

(b) FIGURE 2.6: SCHEMATIC DRAWING OF THE SUPER-KAMIOKANDE DETECTOR.

These experiments had several advantages with respect to their radiochemical predecessors. First, they were real-time detectors: each event was individually recorded and allowed a measurement of the event energy, direction and arrival time. In addition the detection process of equation 2.9 went through both charged and neutral interactions and was sensitive to all neutrino flavours. Nevertheless, their high detection threshold (7.5 MeV in Kamiokande and 5 in Super-Kamiokande) restricted their observable neutrino sources to the ^8B and *hep* neutrinos only. Their results were then presented in terms of measured ^8B flux.
In almost a decade of data taking, the final result of Kamiokande [15]:

$$\Phi_{\mathrm{Kamiokande}} = [2.80 \pm 0.16(\mathrm{stat.}) \pm 0.16(\mathrm{syst.})] \times 10^6 \mathrm{cm}^{-2}\mathrm{s}^{-1} \tag{2.10}$$

was only about one half ($\Phi_{\mathrm{Kamiokande}}/\Phi_{\mathrm{th}} = 0.54 \pm 0.08$) of the predicted SSM flux. Super-Kamiokande greatly increased the precision of this measurement and its latest published

flux [16]:

$$\Phi_{\mathrm{SuperK}} = [2.32 \pm 0.03(\mathrm{stat.})^{+0.08}_{-0.07}(\mathrm{syst.})] \times 10^6 \mathrm{cm}^{-2}\mathrm{s}^{-1} \tag{2.11}$$

was 45% of the BP00 expectation.

2.2.2 Three solar neutrino problems

After more than 25 years of the operation of the Chlorine experiment, the event rate of electron neutrinos[2] above the 814 KeV energy threshold was ~3 times lower than the most detailed theoretical predictions. This discrepancy between the standard model calculations and the observations for the Chlorine experiment was, for more than two decades, the only solar neutrino problem.

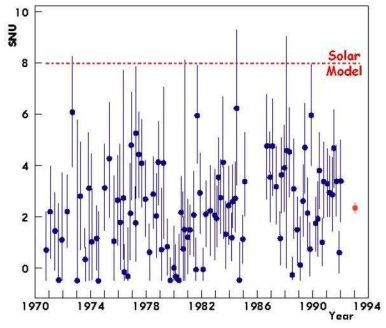

(a) Figure 2.7: The solar neutrino deficit observed by the Chlorine experiment. The red dashed line is the solar model prediction.

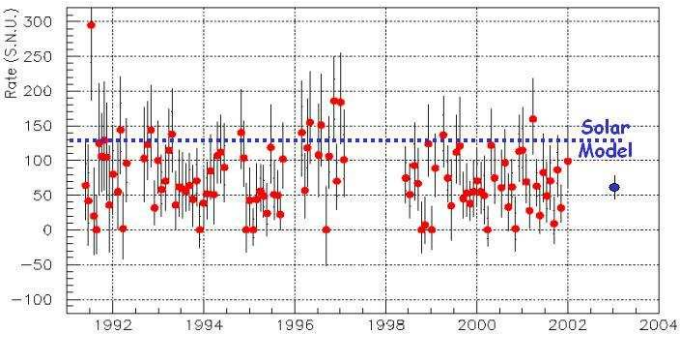

(b) Figure 2.7: The solar neutrino deficit observed by the GALLEX and GNO experiments. The blue dashed line is the solar model prediction.

In 1990 Bahcall and Bethe pointed out a second neutrino problem, resulting from the comparison of the measured event rates in the Chlorine and Kamiokande experiments. Kamiokande detected only neutrinos with energies above 7.5 MeV and, according to the standard solar model, the only important source of these higher-energy neutrinos is the ^8B beta decay. The observed spectrum of electron recoil energies was consistent with that expected from ^8B neutrinos and also the signal directionality left no doubt that they have solar origin: the event rate in Kamiokande was determined by the same high-energy ^8B neutrinos that were expected to dominate the event rate in the Chlorine experiment.
It was then possible to calculate the rate, in the Chlorine experiment, produced by the ^8B neutrinos observed in Kamiokande. The resulting rate, 3.2 ± 0.45 SNU , exceeded the total observed Chlorine rate of 2.55 ± 0.25 SNU . This apparent incompatibility of the Chlorine and the Kamiokande experiments was the second solar neutrino problem.

[2] Most of the predicted rate in this experiment is from the rare, high-energy ^8B neutrinos, although the ^7Be neutrinos are also expected to contribute significantly.

Finally, a third solar neutrino problem emerged from the gallium detectors. In the standard model their measured rate is all accounted for by the pp and pep neutrinos and there is no room for the ^7Be neutrinos, unless something happens to the low energy neutrinos after they are created in the Sun. This problem, often called the problem of the missing ^7Be neutrinos, strongly depends upon the pp neutrinos. Their calculated flux is closely related to the total luminosity of the Sun and therefore approximately independent of solar models: the missing ^7Be neutrinos could not be explained by any change in solar physics.

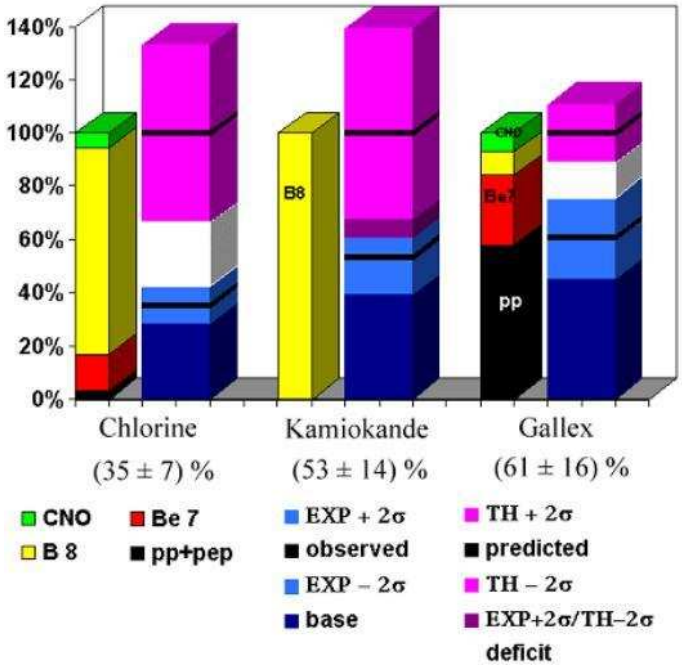

Figure 2.8: Comparison of measured event rates and standard model predictions in the four pioneering neutrino experiments: Homestake, Kamiokande, gallex and sage.

Over the past decades, several variants of standard solar models have been proposed and refined. The predicted neutrino fluxes of 19 models published in the last 10 years are all in reasonable agreement with each other: all falls within the estimated 3σ uncertainties in the model predictions. This agreement demonstrated the robustness of the predictions, since the calculations involved a variety of choices for the nuclear parameters, the equation of state, the stellar radiative opacity, ... that are all included. However, the combined standard model, the standard solar model plus minimal standard electroweak theory, is inconsistent with the observed rates at $\sim 20\sigma$: the standard model predictions do not fit the observed solar neutrino measurements.

2.2.3 Astrophysical and non-oscillating neutrinos solutions

The need for a justification to these solar neutrino problems has driven efforts in two directions: astrophysical solutions and new neutrino physics beyond the minimal standard electroweak model.

One way to solve the solar neutrino problem was to lower the central temperature of the Sun by a few percent. This would mean fewer high-energy nuclear reactions occurring in the solar core and thus, fewer neutrinos being produced and hence detected. There are a number of ways to lower the central solar temperature, invoking mechanisms that the model does not include. Mixing, for istance, would cause fresh fuel to be brought into the core, and thus a lower temperature would be needed to maintain equilibrium. Rotation, convection, or other instabilities such as the ^3He instability could cause mixing in the core. Other more exotic solutions relied on changing the metallicity of the core (that is, changing the relative abundances of the heavy elements), supposing a strong central magnetic field or using hypothetical WIMPs (Weak Interacting Massive Particles), that would replace neutrinos as carriers for part of the Sun's energy.
Yet, the fluxes of high energy neutrinos are especially sensitive to the core temperature, mainly because of the energy dependence of the cross sections. An approximate correlation between the neutrino fluxes from different sources and the core temperature has been derived by Bahcall and Ulrich and used to carry out an analysis to see whether the data could be described by a lower temperature. It resulted clearly impossible [19, 20] to describe the data

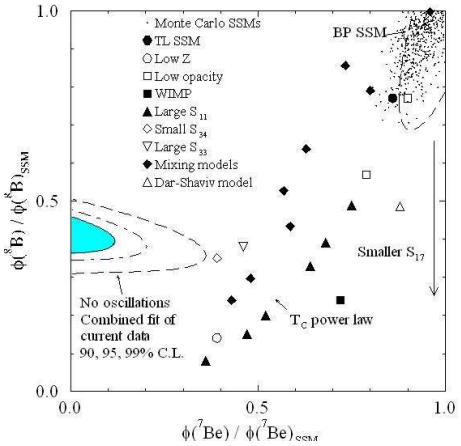

(a) Figure 2.9: On the $\Phi(^7Be)/\Phi(^7Be)_{SSM} - \Phi(^8B)/\Phi(^8B)_{SSM}$ ssm plane one can see the predicted fluxes of ^8B and ^7Be neutrinos for several non-standard solar models compared to the regions allowed by the combined experiments, with confidence levels equal to 90, 95 and 99% . The best fit would occur in the unphysical region of negative ^7Be neutrino flux.

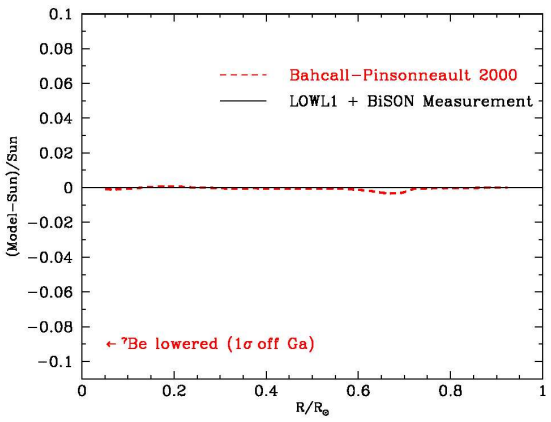

(b) Figure 2.9: The excellent agreement between the calculated (solar model BP00) and the measured sound speeds, shown here as a function of distance from the Sun's core, is one of the most convincing tests of validity of the Standard Solar Model.

with such cool sun models, since the ratio $\Phi(^7Be)/\Phi(^8B)$ would be pushed towards values that are higher than the SSM prediction, while the experimental results go in the opposite direction (figure 2.9(a)).

Other alternative solutions for the solar neutrino deficit, like a spin flavour precession, a neutrino inflight decay or flavour changing neutrino interactions, are also ruled out by the recent results provided by thr SNO and KamLAND experiments.

Finally, also some skepticisms on the unreliability of the solar model predictions started circulating, but they where soon denied by two facts. First of all, the solar neutrino problem was not solved even if the solar models and their flux predictions were not considered. A combined analysis of all the data to undistorted neutrino energy spectra, allowing the *pp* , ^7Be and ^8B fluxes to be arbitrary parameters, failed at the level of 4σ [21, 22] and this result was independent of any astrophysical arguments regarding the basic correctness of solar models. In addition, helioseismology studies demonstrated the robustness of solar models: the agreement between the sound speeds of the Sun predicted by the BP00 model with the values inferred from helioseismological measurements [18] was found at the level of 0.2% (figure 2.9(b)).

The explanation was then likely to lie on an energy-dependent flavor conversion of the neutrinos on their way from the Sun to the Earth.

2.3 Neutrino oscillations and the Super-Kamiokande evidence

2.3.1 Oscillations in vacuum

The first hint to the possibility of an arbitrary mixing between two massive neutrino states came in the 60's, by Maki (1962) and Bruno Pontecorvo [23] (1958,1967). If neutrinos have masses[3]there is no fundamental reason why mass eigenstates should coincide with the weak eigenstates. The three flavour eigenstates $|\nu_\alpha\rangle$ (α =e ,μ ,τ) produced in a weak interaction can be a quantum-mechanical superposition of the mass eigenstates $|\nu_i\rangle$ (i =1,2,3 with mass eigenvalues m_1, m_2 and m_3):

$$|\nu_\alpha\rangle = \sum_{i=1}^{n} U^*_{\alpha i} |\nu_i\rangle \tag{2.12}$$

The 3×3 unitary matrix U is the leptonic mixing matrix, analogous to the Cabibbo-Kobayashi-Maskawa mixing matrix of the quark sector. After traveling a distance R, the neutrino originally produced with a flavour α , will be described by:

$$|\nu_\alpha(t)\rangle = \sum_{i=1}^{n} U^*_{\alpha i} |\nu_i(t)\rangle \tag{2.13}$$

and the probability to detect it as a different flavour (β) neutrino is:

$$P_{\alpha\beta} = |\left\langle\ \nu_\beta\ \right|\ \nu_\alpha(t)\ \left.\right\rangle|^2 = |\sum_{i=1}^{n}\sum_{j=1}^{n} U^*_{\alpha i} U_{\beta j} \left\langle\ \nu_j(0)\ \right|\ \nu_i(t)\ \left.\right\rangle|^2 \tag{2.14}$$

[3]Neutrino oscillations are actually the first sign of physics beyond the Standard Model.

The simplest possible oscillation pattern is when two neutrino mass eigenstates are nearly degenerate and the three-neutrino scenario can be reduced to two lepton flavours mixing. In this scenario we can relate the flavour and mass basis with a single parameter, the mixing angle θ:

$$\begin{cases} |\nu_\alpha\rangle = \cos\theta\,|\nu_1\rangle + \sin\theta\,|\nu_2\rangle \\ |\nu_\beta\rangle = -\sin\theta\,|\nu_1\rangle + \cos\theta\,|\nu_2\rangle \end{cases} \tag{2.15}$$

and write the time evolution equations as:

$$\begin{cases} |\nu_\alpha\rangle = \cos\theta\,|\nu_1\rangle\, e^{-i(E_1 t - \vec{p}\cdot\vec{x})} + \sin\theta\,|\nu_2\rangle\, e^{-i(E_2 t - \vec{p}\cdot\vec{x})} \\ |\nu_\beta\rangle = -\sin\theta\,|\nu_1\rangle\, e^{-i(E_1 t - \vec{p}\cdot\vec{x})} + \cos\theta\,|\nu_2\rangle\, e^{-i(E_2 t - \vec{p}\cdot\vec{x})} \end{cases} \tag{2.16}$$

Under the assumption that neutrino masses are much smaller than the momentum, we can write: $E_i = \sqrt{p_i^2 + m_i^2} \simeq p_i + \frac{m_i^2}{2p_i^2}$. If $p_i \simeq p_j = p \simeq E$ and defining $\Delta m^2 = m_1^2 - m_2^2$, the oscillation probability for a neutrino created at time 0 with flavour α to be detected at time t as a neutrino of flavour α (survival probability) or of different flavour β (conversion probability) can be written as:

$$P_{\alpha\beta} = P(\nu_\alpha \to \nu_\beta; E, t) = \delta_{\alpha\beta} - (2\delta_{\alpha\beta} - 1)\sin^2 2\theta \sin^2\left(\frac{\Delta m^2 t}{4E}\right) \tag{2.17}$$

It is now convenient to introduce the *vacuum oscillation lenght* L_ν:

$$L_\nu = \frac{4\pi E}{\Delta m^2} = \frac{E[\mathrm{GeV}]}{1.27\Delta m^2[\mathrm{eV}^2]}\ [\mathrm{km}] \tag{2.18}$$

and rewrite the oscillation probability 2.17 as:

$$P_{\alpha\beta} = P(\nu_\alpha \to \nu_\beta; E, t) = \delta_{\alpha\beta} - (2\delta_{\alpha\beta} - 1)\sin^2 2\theta \sin^2\left(\frac{\pi R}{L_\nu}\right) \tag{2.19}$$

where R is the source-detector distance. The neutrino transition probability has then an oscillatory behaviour, where the $\sin^2 2\theta$ parameter acts as an amplitude and the mass squared difference Δm^2 is a frequency. If $E/R \gg \Delta m^2 (R \ll L_\nu)$ the oscillation does not have time to give an appreciable effect. In the case of $E/R \ll \Delta m^2 (R \gg L_\nu)$ one must instead take into account that, in general, neutrino beams are not monochromatic. Thus, rather than measuring $P_{\alpha\beta}$, the experiments are sensitive to the average probability $< P_{\alpha\beta} >$. For $R \gg L_\nu$ the oscillating phase goes through many cicles before the detection and is averaged to $< \sin^2\left(\frac{\pi R}{L_\nu}\right) >= 1/2$.

Neutrino oscillation experiments measure $P_{\alpha\beta}$. It is common practice for the experiments to interpret their results in the two-neutrino framework, translating their constraints on $P_{\alpha\beta}$ into allowed or excluded regions in the plane $(\Delta m^2, \sin^2 2\theta)$ by using equation 2.19. An experiment is characterized by the typical neutrino energy E and by the source-detector distance R; to be sensitive to a given value of Δm^2, the experiment should have $E/R \simeq \Delta m^2$. Such experiments cannot achieve any upper bound on Δm^2, since their results can always be accounted for by Δm^2 large enough to be in the region of averaged oscillations $(R \gg L_\nu)$.

2.3.2 Oscillations in matter

When neutrinos propagate in dense matter, the interactions with the medium affect their properties. This fact, originally pointed out by Wolfenstein [24] in 1978 and later reviewed by Mikheyev and Smirnov [25], is due to the different ways neutrinos interact with matter:

while ν_μ and ν_τ are subject only to the neutral current interactions, ν_e interact also via charged current [26] exchanges.

The interaction of neutrinos with the matter fields can be accounted for by the introduction of a refraction index $n_\lambda(\lambda = e, \mu, \tau)$ in the propagating wave function:

$$\begin{cases} |\nu_\lambda\rangle = \sum_j \langle \nu_j \mid \nu_\lambda \rangle |\nu_j\rangle e^{E_j - n_\lambda \vec{p}\cdot\vec{x}} & (j = 1,2,3) \\ n_\lambda = 1 + \frac{2\pi N_e}{p^2} f_\lambda(0) \end{cases} \tag{2.20}$$

The refraction index depends on the electron density N_e and the forward elastic scattering amplitude $f_\lambda(0)$. The difference between forward scattering amplitude for electron neutrinos and the other flavors determines a density-dependent splitting of the diagonal elements in the mass matrix; in other words, the mass eigenstates that propagate in matter are different from the ones propagating in vacuum. The electron neutrino wave function acquires then an additional phase term that does not appear in the wave function for other flavors:

$$\begin{cases} \Delta f(0) = f_e(0) - f_{\mu,\tau}(0) = -\frac{G_F p}{\sqrt{2}\pi} \\ |\nu_e\rangle \propto e^{\Delta\phi} = e^{-i\sqrt{2}N_e G_F x} \end{cases} \tag{2.21}$$

The periodicity of the phase difference $\Delta\phi$ defines the ν -e interaction lenght in matter as:

$$L_m = \frac{2\pi}{\sqrt{2}N_e G_F} \sim \frac{1.7 \times 10^7 [m]}{\rho[g/m^3] < Z/A >} \tag{2.22}$$

This length only depends on the electron density N_e and corresponds to roughly 200 km in the Sun's core and to $\sim 10^4$ km in the Earth.
A mixing angle in matter θ_m can be defined as the angle associated with the rotation matrix that diagonalizes the hamiltonian and is related to the mixing angle in vacuum θ by the following relation:

$$\sin^2 2\theta_m = \frac{\sin^2 2\theta}{(\cos 2\theta - L_v/L_m)^2 + \sin^2 2\theta} \tag{2.23}$$

Equation 2.23 presents a resonant feature: let us assume that, along the path from the Sun's core to the external layers, neutrinos run into a region with such density to have:

$$\frac{L_v}{L_m} = \cos 2\theta \tag{2.24}$$

In this case, $\sin^2 2\theta_m = 1$, and there is local maximal mixing for any non-zero mixing angle in vacuum. In practical terms, even if θ is very small, neutrinos which cross a dense enough region can have a very high probability of converting into other flavours. This phenomenon of matter enhanced oscillations is known as the MSW effect.

2.3.3 Atmospheric neutrinos

Many informations on the neutrino behaviour comes also from the study of atmospheric neutrinos.

Atmospheric neutrinos are produced in cascades initiated by collisions of cosmic rays with the Earth's atmosphere [27]. Some of the mesons produced in these cascades, mostly pions and some kaons, decay into electron and muon neutrinos and anti-neutrinos. The dominant production process is:

$$\pi^\pm \to \mu^\pm + \nu_\mu \ (\overline{\nu}_\mu) \tag{2.25}$$

followed by:

$$\begin{array}{llll} \mu^+ & \rightarrow \mathrm{e}^+ & +\overline{\nu}_\mu & +\nu_\mathrm{e} \\ \mu^- & \rightarrow \mathrm{e}^- & +\nu_\mu & +\overline{\nu}_\mathrm{e} \end{array} \tag{2.26}$$

The ratio of muon neutrinos ($\nu_\mu + \overline{\nu}_\mu$) to electron neutrinos ($\nu_\mathrm{e} + \overline{\nu}_\mathrm{e}$) is then naively expected to be about 2. Actually for neutrino energies above a few GeV the ratio increases, since the probability of a muon's surviving to reach the ground increases with increasing muon energy.

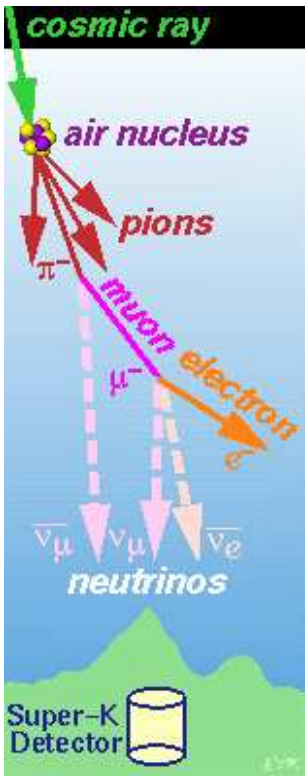

(a) FIGURE 2.10: ATMOSPHERIC NEUTRINOS PRODUCTION IN THE COLLISION OF A COSMIC RAY WITH THE EARTH'S ATMOSPHERE.

(b) FIGURE 2.10: NAIVE PICTURE OF THE HADRONIC SHOWERS RESULTING FROM THE COLLISIONS OF COSMIC RAYS WITH NUCLEI IN THE UPPER ATMOSPHERE. DEEP UNDERGROUND EXPERIMENTS ARE PARTIALLY SHIELDED FROM THIS BACKGROUND.

The predicted absolute neutrino fluxes are uncertain at the 20% level, but the ratios of neutrinos of different flavor are expected to be better than 5% , being essentially independent of the primary cosmic-ray spectrum.

Due to the large cosmic-ray background at the Earth's surface ($\sim 2 \times 10^2$ / m^2/s) atmospheric neutrinos can be detected only by deep underground experiments, observing their charged current interaction

$$\nu\ (\overline{\nu}\ ) + N \rightarrow l^\pm + X \tag{2.27}$$

inside the detector. The flavour of the final state lepton is used to identify the flavour of the incoming neutrino.

Atmospheric neutrinos events are usually categorized into fully contained, partially contained, upward stopping muon and upward through-going muon events. Fully and partially contained events have their vertex positions in the fiducial volume of the detector. Fully contained events have all the visible secondary particles stopping in the detector, while partially contained events have at least one charged track exiting the detector. Upward going muon events are neutrino interactions occurring in the rocks surrounding the detector. Only muon are observed, since electrons, photons and hadrons are absorbed by a few meters of rock. Muons stopping inside the detector are stopping muons, while if the muon track crosses the full detector the events is a through-going muon. Typical neutrino energies of fully contained, partially contained, upward stopping and upward through-going muon events are of the order of 1, 10, 10 and 100 GeV respectively.

Until today two different detection techniques have been employed, both allowing flavour classification of the event. In iron calorimeters (Fréjus [28], NUSEX [29], Soudan2 [30] and MACRO [31]) the detector is composed of a set of alternating layers of iron, as a target, and of some tracking element. In water Cerenkov detectors (IMB and Kamiokande) the target is instead a large volume of water surrounded by photomultipliers which detect the Cerenkov ring produced by the charged leptons.

2.3.4 The Super-Kamiokande result: evidence for oscillation of atmospheric neutrinos

The original formulation of the *atmospheric neutrino anomaly* came in 1992, following the strong suppression of ν_μ -induced events with respect to the ν_e -induced events observed by the two water Cerenkov detectors: IMB [32] and Kamiokande [33]. The measured ratio was smaller than the expected value by a factor of about 0.6. The measurements were reported as:

$$R = \frac{\left[\frac{\Phi(\nu_\mu)+\Phi(\overline{\nu}_\mu)}{\Phi(\nu_e)+\Phi(\overline{\nu}_e)}\right]_{\mathrm{DATA}}}{\left[\frac{\Phi(\nu_\mu)+\Phi(\overline{\nu}_\mu)}{\Phi(\nu_e)+\Phi(\overline{\nu}_e)}\right]_{\mathrm{MC}}} = 0.61 \pm 0.03 \pm 0.05 \tag{2.28}$$

where $\Phi(\nu_\mu)$ and $\Phi(\nu_e)$ are the number of muon-like and electron-like events observed in the detector for both data and Monte Carlo simulation. This ratio largely cancels experimental and theoretical uncertainties and if the physics in the Monte Carlo simulation would accurately models data, R should be 1.

Kamiokande performed separate analyses for both sub-GeV and multi-GeV neutrinos [34] and both showed the same deficit. The collaboration also presented the angular dependence of the deficit for the multiGeV neutrinos with the direction of the reconstructed charged lepton [34] and found that the deficit was mainly due to the neutrinos coming from below the horizon. This was the first real hint suggesting a neutrino oscillation scenario. Since atmospheric neutrinos are produced isotropically at a distance of about 15 km above the surface of the Earth, vertically downward-going neutrinos travel only these 15 km, while vertically upward-going neutrinos travel the full Earth's diameter ($\sim 1.3 \times 10^4$ Km) before interacting in the detector. This long travel inside the Earth could leave the atmpospheric neutrinos free to undergo flavour conversion and to be eventually detected as as neutrinos of a different flavour. Because of the relative small statistic, however, discrimination between $\nu_\mu \leftrightarrow \nu_\tau$ (ν_μ disappearance) and $\nu_\mu \leftrightarrow \nu_e$ (ν_e appearance) oscillations was not possible.

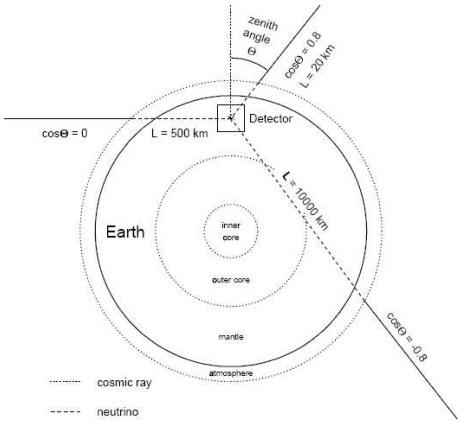

(a) FIGURE 2.11: THE ZENITH ANGLE, PARAMETRIZED IN TERMS OF $\cos\theta$, MEASURES THE DIRECTION OF THE RECONSTRUCTED CHARGED LEPTON WITH RESPECT TO THE VERTICAL OF THE DETECTOR.

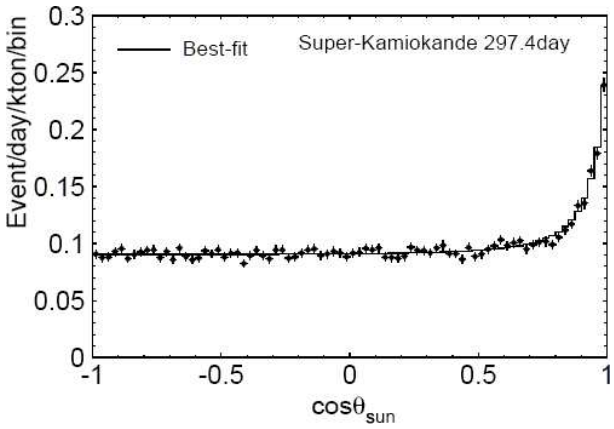

(b) FIGURE 2.11: THE SOLAR NEUTRINO PEAK AS MEASURED BY SUPER-KAMIOKANDE. THE BEST FIT REQUIRES 47% SUPPRESSION OF THE EXPECTED ν_e FLUX.

In the following years the atmospheric neutrino anomaly received important confirmations from the iron calorimeter detectors Soudan2 and MACRO and from the large statistics data of Super-Kamiokande. Finally, in June 1998, the Super-Kamiokande collaboration claimed for the first evidence for atmospheric neutrino oscillations [35], in the two neutrino oscillation scenario: $\nu_\mu \leftrightarrow \nu_x$, where ν_x may be ν_τ or a new, non-interacting, sterile neutrino.

Super-Kamiokande has collected a total of 4353 fully contained (FC) events and 301 partially contained (PC) events in a 33.0 kiloton-year exposure. FC events were separated into those with a single visible Cherenkov ring and those with multiple Cerenkov rings and for their analysis, only single ring events were used. Single ring events were identified as e -like or μ -like based on a likelihood analysis of the light detected around the Cerenkov cone. The FC events were further separated into subGeV ($E_{vis} \leq 1.33$ GeV) and multiGeV ($E_{vis} \geq 1.33$ GeV) samples, where E_{vis} is the energy of an electron that would produce the observed amount of Cerenkov light.

The μ -like data exhibit a strong asimmetry in the zenith-angle, while no significant asimmetry is observed in the e -like data. This asimmetry is defined as: $A = (U - D)/(U + D)$, where U and D are the number of upward-going and downward-going events. The asimmetry is expected to be near zero independent of flux model for $E_\nu > 1$GeV. The measured asimmetry for multiGeV (FC+PC) muons alone deviates from zero by more than 6 standard deviations ($A = -0.296 \pm 0.048 \pm 0.01$).
The following statements can be inferred from the Super-Kamiokande results:

- at present the $\nu_\mu \leftrightarrow \nu_e$ oscillation hypothesy is disfavored with high CL, since SK data show that the ν_e contained events are well described by the SM prediction both in normalization and in their zenith angular dependence. $\nu_\mu \leftrightarrow \nu_e$ oscillations could explain the angular dependence of the ν_μ flux only at the price of introducing an an-

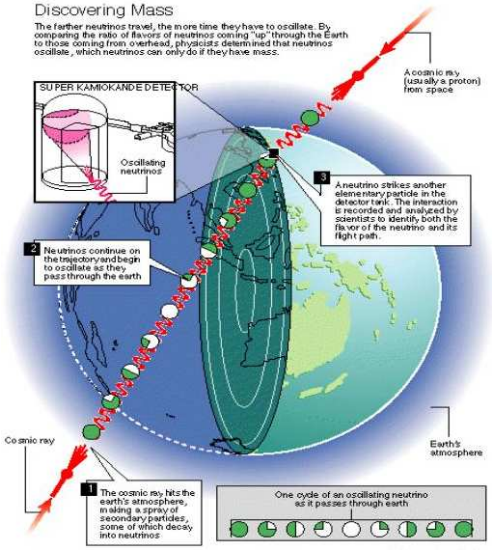

(a) FIGURE 2.12: SKETCH OF THE NEUTRINO OSCILLATION SCENARIO IN THE SUPER-KAMIOKANDE EXPERIMENT.

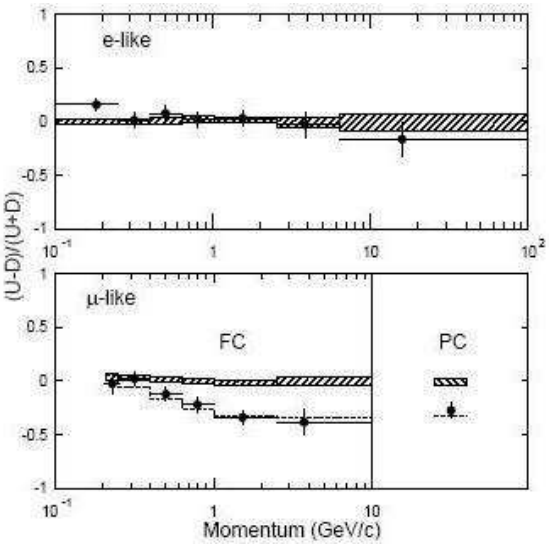

(b) FIGURE 2.12: THE (U-D)/(U+D) ASYMMETRY AS A FUNCTION OF MOMENTUM FOR FC e -LIKE AND μ -LIKE EVENTS AND PC EVENTS. THE MONTE CARLO EXPECTATION WITHOUT NEUTRINO OSCILLATIONS IS SHOWN IN THE HATCHED REGION. THE DASHED LINE FOR μ -LIKE IS THE EXPECTATION FOR $\nu_\mu \leftrightarrow \nu_\tau$ OSCILLATIONS WITH $(\sin^2 2\theta = 1.0, \Delta m^2 = 2.2 \times 10^{-3}\mathrm{eV}^2)$.

gular dependence also of the ν_e flux, in contrast with the data. In addition explaining the atmospheric data with $\nu_\mu \leftrightarrow \nu_e$ transition would have direct implications for the $\overline{\nu}_e \leftrightarrow \overline{\nu}_\mu$ transition. In particular, the $\overline{\nu}_e$ deficit expected in the CHOOZ reactor experiments conflicts with their negative result [36].

- Both the $\nu_\mu \leftrightarrow \nu_\tau$ and $\nu_\mu \leftrightarrow \nu_s$ oscillation hypothesis can consistenly explain the atmospheric neutrino data. To discriminate between the two options one can use the difference in the survival probabilities due to the presence of matter effects for oscillations into sterile neutrinos; all methods strongly favour $\nu_\mu \leftrightarrow \nu_\tau$ oscillations over $\nu_\mu \leftrightarrow \nu_s$. The present data are then in good agreement with two flavour $\nu_\mu \leftrightarrow \nu_\tau$ oscillations, with $\sin^2 2\theta > 0.82$ and $5 \times 10^{-4} < \Delta m^2 < 6 \times 10^{-3}\mathrm{eV}^2$ at 90% confidence level [37].

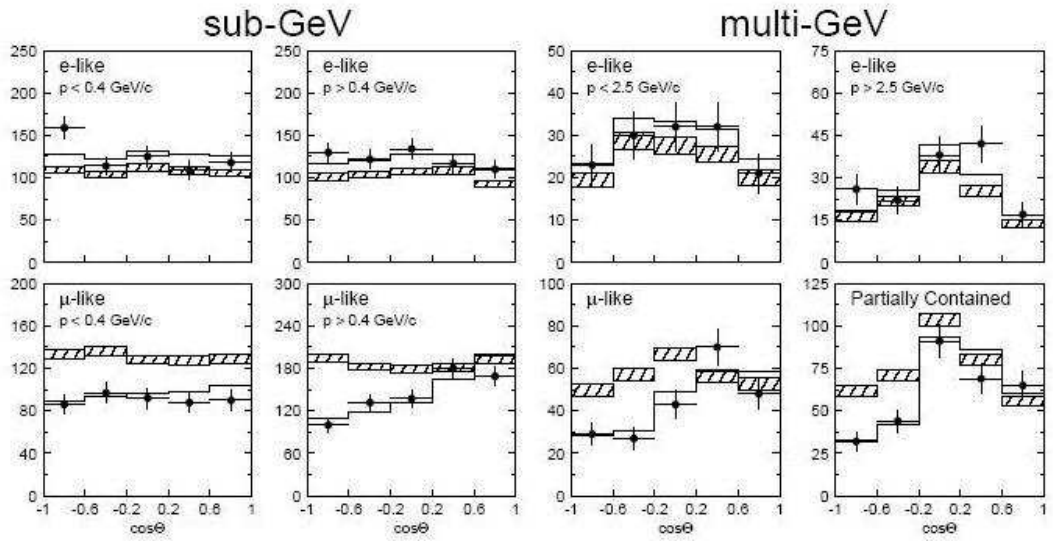

FIGURE 2.13: ZENITH ANGLE DISTRIBUTIONS OF μ -LIKE AND e -LIKE EVENTS FOR SUBGEV AND MULTIGEV DATA SETS. UPWARD-GOING PARTICLES HAVE $\cos\theta < 0$ AND DOWNWARD-GOING PARTICLES HAVE $\cos\theta > 0$. SUBGEV DATA ARE SHOWN SEPARATELY FOR p < 400 MEV/C AND p > 400 MEV/C. MULTIGEV e -LIKE DISTRIBUTIONS ARE SHOWN FOR p < 2.5 GEV/C AND p > 2.5 GEV/C. MULTIGEV μ -LIKE ARE SHOWN SEPARATELY FOR FC AND PC EVENTS. THE HATCHED REGION SHOWS THE MONTE CARLO EXPECTATION FOR NO OSCILLATIONS, NORMALIZED TO THE DATA LIVE-TIME WITH STATISTICAL ERRORS. THE BOLD LINE IS THE BEST-FIT EXPECTATION FOR $\nu_\mu \leftrightarrow \nu_\tau$ OSCILLATIONS WITH THE OVERALL FLUX NORMALIZATION FITTED AS A FREE PARAMETER.

2.4 THE CONFIRMATIONS TO THE SSM FROM THE NUCLEAR CROSS SECTIONS MEASUREMENTS

Helioseismology and the results from the Super-Kamiokande experiment have confirmed the robustness of the standard solar models and strengthened the inference that new physics is required to describe solar neutrino experiments. The uncertainties in the solar model predictions, however, are still a central issue for the solar neutrino research.

Figure 2.4 shows the calculated values for the principal pp solar neutrino fluxes and their estimated uncertainties. The pp and pep neutrino fluxes are predicted with a calculated uncertainty of only $\pm$ 1% and $\pm$ 1.5% ; the ^7Be neutrino flux has an uncertainty of $\pm$ 10% and the ^8B flux is predicted with an error of about $\pm$ 20% . The largest recognized uncertainties that afflict the prediction of solar neutrino fluxes are associated with the laboratory cross sections at low energies for the crucial (^3He (^4He ,γ)^7Be) and the ^7Be $(p,\gamma)^8B$ reactions. The flux of ^8B neutrinos is directly proportional to the rate of the ^7Be $+p$ reaction, while the flux of the ^7Be neutrinos is approximately linearly proportional to the rate of the ^3He $-^4He$ reaction. These low-energy cross sections are measured in laboratories at much higher energies and later extrapolated to the energies of interest for the Sun's fusion reactions. Our ability to interpret the existing solar neutrino experiments is then limited by the imprecision in our knowledge of the relevant nuclear cross sections: a low energy resonance in the (^3He (^3He ,$2p$)^4He) reaction, for istance, would induce a

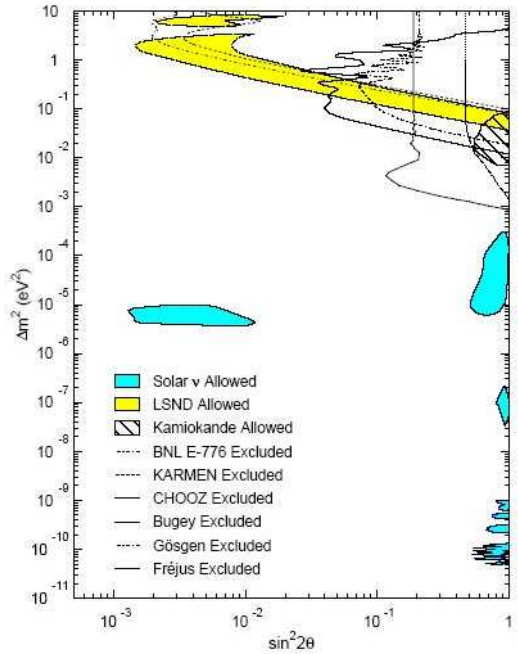

(a) FIGURE 2.14: ALLOWED AND EXCLUDED REGIONS OF PARAMETER SPACE FOR $\nu_\mu \leftrightarrow \nu_e$ NEUTRINO OSCILLATIONS. IN EACH CASE, THE EXCLUDED REGIONS LIE TO THE RIGHT OF THE CURVES.

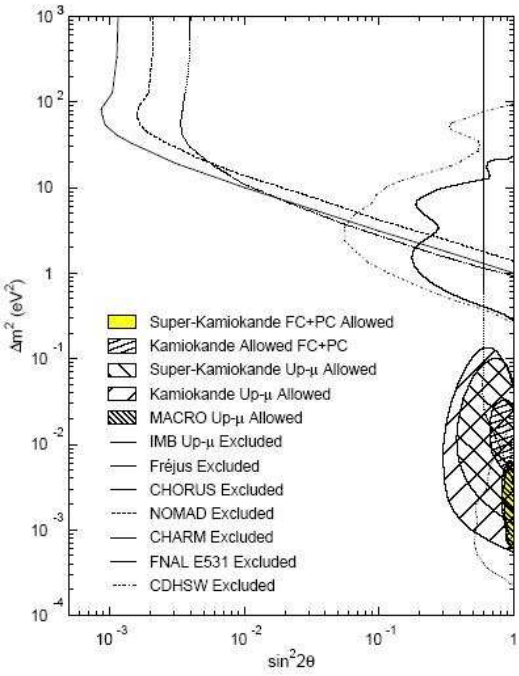

(b) FIGURE 2.14: ALLOWED AND EXCLUDED REGIONS OF PARAMETER SPACE FOR $\nu_\mu \leftrightarrow \nu_\tau$ NEUTRINO OSCILLATIONS. IN EACH CASE, THE EXCLUDED REGIONS LIE TO THE RIGHT OF THE CURVES.

significant suppression of the ^7Be and ^8B neutrinos.

In addition, the knowledge of the nuclear fusion cross sections that determine the branching ratios among the different reactions in the pp chain is needed also to extract the inherent information about the solar interior from the measured neutrino fluxes. To cite the most important example, the predicted rate of neutrino events in the Super-Kamiokande and SNO experiments is directly proportional to the measured laboratory rate of the $^7Be\ (p,\gamma\ )^8B$ reaction (S_{17}) and to the central temperature of the sun: $\Phi(^8B\ ) \sim S_{17}T^{24}$. Therefore, our ability to test solar-model calculations of the central temperature profile of the sun is limited by our knowledge of S_{17} and ,unfortunately, the low-energy cross section factor for the production of ^8B is the least well known of the important cross sections in the pp chain.

The knowledge of these low-energy cross sections has been greatly refined over the past decades. In 1964 estimates of the rate of the ^3He -^3He reaction [38] were 5 times lower than the current best estimate. Since this reaction competes with the ^3He -^4He reaction, which leads to high-energy neutrinos, the calculated fluxes for the higher-energy neutrinos were overestimated in the earliest days of solar neutrino research. The most significant uncertainties, in the rates of the ^3He -^3He , the ^3He -^4He and the ^7Be -p reactions were much reduced after just a few years of intensive experimental research in the middle and late 1960s.

For the solar neutrino research, the most important nuclear physics parameter is the low

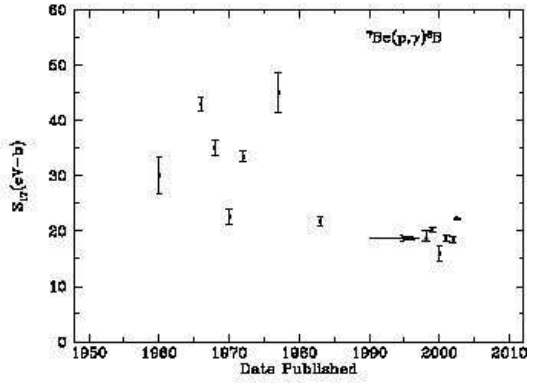

(a) Figure 2.15: The measured values of the low-energy cross section factor for the $^7Be\ (p,\gamma\ )^8B$ reaction as a function of date of publication. The arrow points to the current standard value, used in the BP00 calculations.

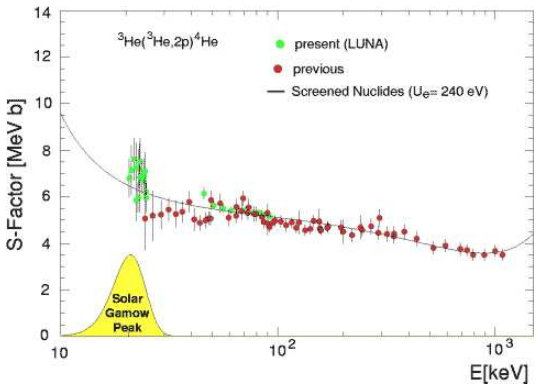

(b) Figure 2.15: The measured cross-section factor S(E) for the $(^3He\ (^3He\ ,2p)^4He\ )$ reaction and a fit with a screening potential U_e. The Gamow peak at the solar central temperature is shown in arbitrary units.

energy cross section factor S_{17} for the $^7Be\ (p,\gamma\ )^8B$ reaction, which gives rise to the critical ^8B neutrinos. Figure 2.15 shows its measured values as a function of the date of publication, and several refined experiments are still in progress to measure it more accurately.
In addition, in 1998 the LUNA collaboration [39] has measured the relevant cross section for the $(^3He\ (^3He\ ,2p)^4He\ )$ reaction at the energies covering the Gamow peak (21.4 KeV), providing no evidence for a hypothetical low-energy resonance over the entire energy range that has been investigated.

2.5 A global analysis of the solar neutrino data

The goal of the analysis of the solar neutrino data in terms of neutrino oscillation is to determine which range of mass-squared difference and mixing angle can be responsible for the observed deficit. In order to answer this question in a statistically meaningful way one must combine all experimental results and compare the predictions in the different oscillation regimes with the observations, including all the sources of uncertainties and their correlations. The main sources of uncertainty are the theoretical errors in the prediction of the solar neutrino fluxes for the different reactions. These errors are due to uncertainties in the nuclear reaction rates, the solar luminosity, the sun age and opacity, ... Another source of theoretical errors arises from the uncertainties in the neutrino interaction cross section for the different detection processes.

The most comprehensive test of solar neutrino oscillations is given by a combined analysis that takes into account the total observed rates and any additional constraint. After the Super-Kamiokande breaking results, a global analysis of the solar neutrino data has been carried out by several authors [40, 41]. The allowed parameters for MSW and vacuum oscillations were inferred using the constraints of the total rates in the Chlorine, GALLEX,

SAGE and Super-Kamiokande experiments, of the Super-Kamiokande energy spectrum and of the Super-Kamiokande zenith-angle dependence.
Figure 2.16 shows the result obtained in [40]. Several oscillation scenarios were compatible with the available data. The LMA (large mixing angle), LOW (low mass) and SMA (small mixing angle) were all equivalently possible solutions, with room for vacuum oscillations (VAC) and sterile neutrinos. The absolute minimum:

$$\begin{aligned} \Delta m^2 &= 5.4 \times 10^{-6} eV^2, \\ \sin^2 2\theta &= 6.0 \times 10^{-3} \end{aligned} \tag{2.29}$$

was reached within the SMA solution ($\chi^2_{\rm min} = 1.7$):

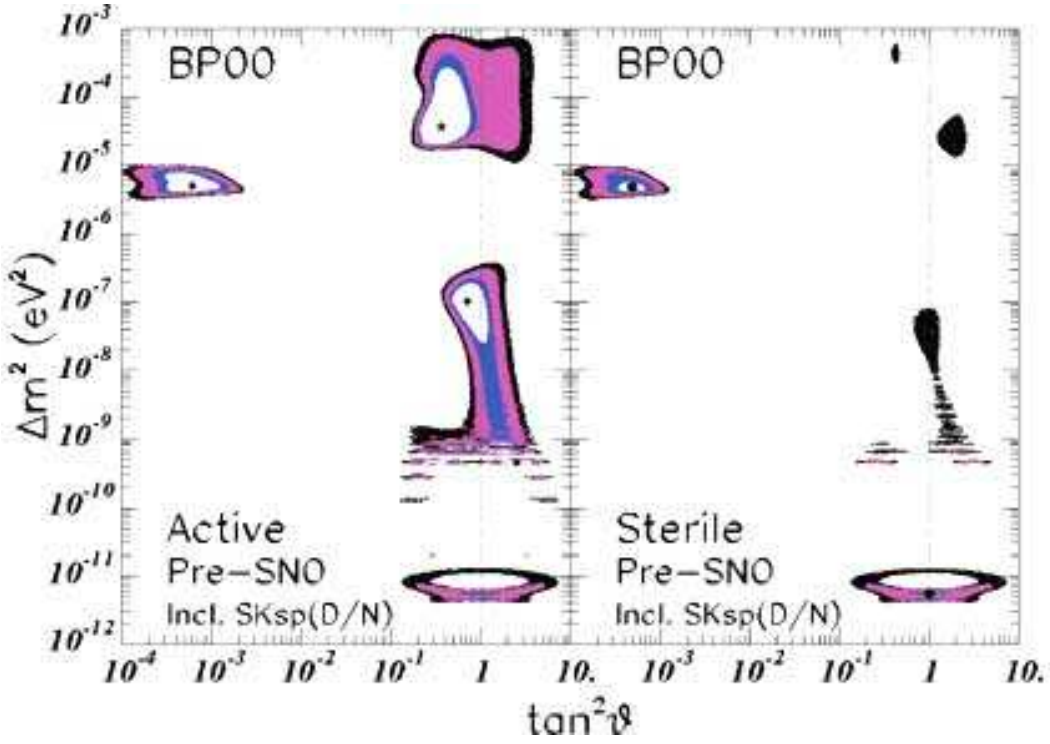

FIGURE 2.16: ALLOWED OSCILLATION PARAMETERS (AT 90% , 95% , 99% AND 99.73% (3σ) CL) FROM A GLOBAL ANALYSIS WITH ALL AVAILABLE DATA AND BP00 CONSTRAINTS.

2.6 The sno and Kamland results

2.6.1 The sno neutral and charged current measurement

The Sudbury Neutrino Observatory (sno) was first proposed in 1987 and it started taking data in November 1999 [42]. The detector is located at the depth of 6010 m of water equivalent in a large cavity excavated in the Creighton mine, near Sudbury in Canada. About 1000 tons of heavy water (D_2O) are contained in a twelve meter diameter acrylic vessel surrounded by a 3 m layer of light water. A geodesic sphere of diameter seventeen meters surrounds the heavy water and supports over 9500 photomultiplier tubes.

(a) Figure 2.17: Schematic drawing of the sno detector.

(b) Figure 2.17: sno detector during construction.

Solution of the solar neutrino problem, and in particular the investigation of neutrino oscillations, required independent measurements of the flux of electron neutrinos and muon and tau neutrinos. sno measures the flux and energy spectrum of electron neutrinos and the flux of all neutrinos via the different ways in which neutrinos interact with the heavy water:

- *Charged Current Reaction:* $\nu_e + d \rightarrow p + p + e^-$
  mediated by the exchange of a W boson. The final electron gets most of the neutrino energy, since it has the smaller mass, and, due to the large energy of the incident neutrinos, it is so energetic to produce Cerenkov light. This absorption reaction is sensitive exclusively to electron neutrinos: a muon neutrino or a tau neutrino interacting in this way must create either a muon or a tau rather than an electron, and solar neutrinos do not have nearly enough energy to do this. The Standard Solar Model predicts about 30 charged current events per day in sno.

- *Neutral Current Reaction:* $\nu_x + d \rightarrow n + p + \nu_x$
  mediated by the exchange of a neutral boson Z^0. The net reaction is to break apart

the deuterium nucleus; the liberated neutron is then thermalized in the heavy water as it scatters around. The reaction can eventually be observed due to gamma rays which are emitted when the neutron is finally captured by another nucleus. The 6.25 MeV gamma rays will scatter electrons which produce detectable light via the Cerenkov process. This reaction is equally sensitive to all three neutrino types above the energy threshold of 2.2 MeV; the detection efficiency depends on the neutron capture efficiency and the resulting gamma cascade. Neutrons can be captured directly on deuterium, but this is not very efficient. For this reason SNO has also developed two additional neutral current systems to enhance the neutral current detection: the load of the heavy water with a chlorine salt (NaCl) and the addition of a grid of ^3He proportional counter tubes. The Standard Solar Model predicts about 30 neutrons per day in SNO.

- *Elastic Scattering:* $\nu_x + e^- \rightarrow \nu_x + e^-$
  This reaction is sensitive to all neutrino flavours, although the electron-neutrino dominates by a factor of six. The Standard Solar Model predicts about 3 electron scattering events per day in SNO.

Basically, the charged current result is a measurement of the ν_e component of the ^8B solar neutrino flux, while the neutral current result is a measurement of the total ^8B solar neutrino flux, independent of leptonic flavour. The ν_e -e result is also sensitive to all flavours, but with reduced sensitivity for ν_μ and ν_τ neutrinos. Demonstrating that neutrinos other than the electron type are arriving from the Sun is thus reduced to a simple comparison: if the number of neutrinos counted using either the deuteron breakup or electron scattering reactions is significantly higher than the number counted with the neutrino absorption reaction, then non-electron flavor neutrinos must be present in the solar flux.

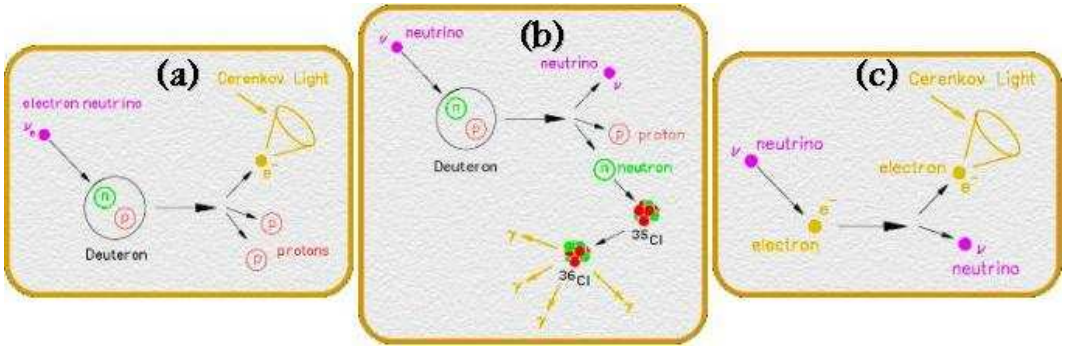

FIGURE 2.18: SCHEMATIC DRAWING OF THE THREE POSSIBLE NEUTRINO INTERACTIONS IN THE SNO HEAVY WATER: CHARGED CURRENT REACTION (A), NEUTRAL CURRENT REACTION (B) AND ELASTIC SCATTERING PROCESS (C).

The first scientific result from SNO came in June 2001, with the conclusion of the so called *first phase*. The charged current (CC) and elastic scattering (ES) fluxes, inferred from the data recorded between November 1999 and January 2001, were compared: if neutrinos from the Sun change into other active flavors, then $\Phi^{CC}(\nu_e) < \Phi^{ES}(\nu_x)$. Using a kinetic

energy threshold of 6.75 MeV, the measured ^8B fluxes assuming no oscillations:

$$\begin{cases} \Phi^{\rm CC}_{\rm SNO}(\nu_{\rm e}) = 1.75 \pm 0.07({\rm stat.})^{+0.12}_{-0.11}({\rm syst.}) \pm 0.05({\rm theor.}) \times 10^6 {\rm cm}^{-2}{\rm s}^{-1} \\ \Phi^{\rm ES}_{\rm SNO}(\nu_{\rm x}) = 2.39 \pm 0.34({\rm stat.})^{+0.16}_{-0.14}({\rm syst.}) \pm 0.05({\rm theor.}) \times 10^6 {\rm cm}^{-2}{\rm s}^{-1} \end{cases} \quad (2.30)$$

excluded the hyphotesis of no flavour conversion at $\sim 3\ \sigma$. CC's ES flux was also compared with the precision measurement by the Super-Kamiokande collaboration of the ^8B flux, using the same ES reaction, and the two rates resulted compatible.
The best fit to the inferred flux of non-electron flavour neutrinos from the Sun was:

$$\Phi(\nu_{\mu\tau}) = 3.69 \pm 1.13 \times 10^6 {\rm cm}^{-2}{\rm s}^{-1} \quad (2.31)$$

Finally, in April 2002, the collaboration reported also the first results using the neutral current reaction measurements. The entire first phase data set was re-analyzed with a lower energy threshold (5 MeV), providing sensitivity to neutrons from the NC reaction. Assuming the standard spectrum shape, the latest results from SNO:

$$\begin{cases} \Phi^{\rm CC}_{\rm SNO}(\nu_{\rm e}) = 1.76^{+0.06}_{-0.05}({\rm stat.})^{+0.09}_{-0.09}({\rm syst.}) \times 10^6 {\rm cm}^{-2}{\rm s}^{-1} \\ \Phi^{\rm ES}_{\rm SNO}(\nu_{\rm x}) = 2.39^{+0.24}_{-0.23}({\rm stat.})^{+0.12}_{-0.12}({\rm syst.}) \times 10^6 {\rm cm}^{-2}{\rm s}^{-1} \\ \Phi^{\rm NC}_{\rm SNO}(\nu_{\rm x}) = 5.09^{+0.44}_{-0.43}({\rm stat.})^{+0.46}_{-0.43}({\rm syst.}) \times 10^6 {\rm cm}^{-2}{\rm s}^{-1} \end{cases} \quad (2.32)$$

clearly proved that only one third of the total neutrino flux above 5 MeV had electronic flavour. Moreover, the total ^8B neutrino flux found by the SNO collaboration from their neutral current measurement, was well in agreement with the standard solar model predictions: in units of the BP00 predicted flux ($5.05^{+1.01}_{-0.81} \times 10^6 {\rm cm}^{-2}{\rm s}^{-1}$) the value obtained was:

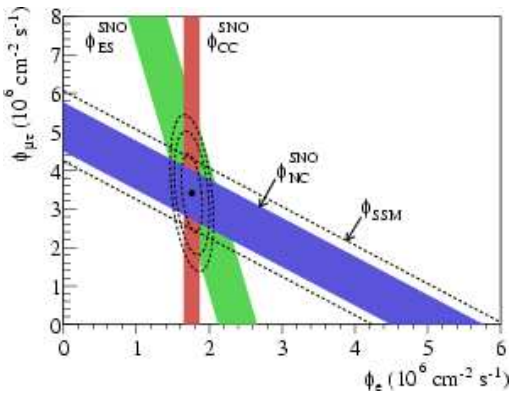

(a) FIGURE 2.19: THE MEASURED $\nu_{\rm e}$ AND ν_μ , ν_τ COMPONENTS OF THE FLUX, ASSUMING THAT THE ^8B NEUTRINO SPECTRUM IS UNDISTORTED COMPARED TO THE SM PREDICTION. THE DIAGONAL BANDS SHOW THE TOTAL ^8B FLUX PREDICTED BY THE SSM (DASHED LINE) AND MEASURED WITH SNO'S NC REACTION (SOLID BAND).

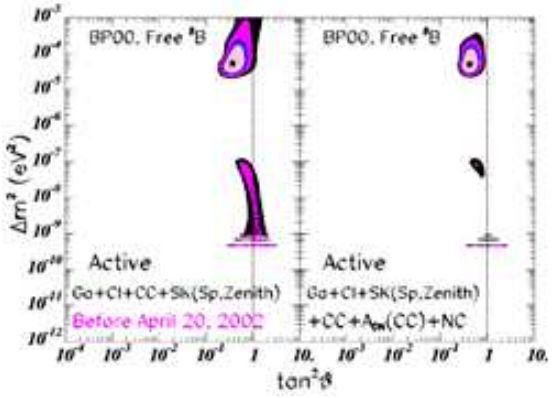

(b) FIGURE 2.19: THE ALLOWED REGIONS IN NEUTRINO OSCILLATION MIXING PARAMETER SPACE BEFORE AND AFTER THE NEUTRAL CURRENT RESULTS FROM SNO, THAT ESSENTIALLY RULED OUT THE SMA SOLUTION.

$$f_B = \frac{\Phi(^8B)}{\Phi_{BP00}(^8B)} = 1.01[1 \pm 0.12](1\sigma) \tag{2.33}$$

The impact of these measurements on the allowed regions of neutrino oscillation parameters was to exclude at ~4 % CL the SMA solution, that was the best fitting solution before April 2002. The LMA became the only allowed MSW oscillation solution at 99% CL; the LOW solution was still allowed, but only at more than 2.5% . The comparison of the allowed regions computed using solar neutrino data prior to April 2002 and after, including the SNO NC and improved CC data and the SNO day-night asymmetry, is shown in figure 2.19(b).

2.6.2 The KamLAND result: evidence for reactor anti-neutrino disappearance

KamLAND is a long baseline neutrino oscillation experiment searching for the oscillation of $\overline{\nu}_e$'s emitted from distance power reactors. The KamLAND detector is located in the Kamioka mine in Japan, at the depth of 2700 m of water equivalent. This underground site is conveniently located at a distance of 150-210 km from several Japanese nuclear power stations. The well characterized $\overline{\nu}_e$ flux from the nuclear power reactors can be determined to ~3% , using the power spectra and burn-up rates, and the comparison of the measured and expected fluxes provides a direct determination of the flavour oscillation parameters.

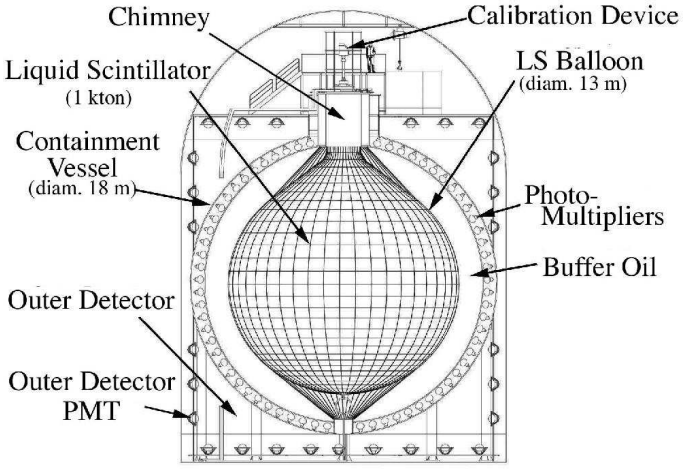

(a) Figure 2.20: Schematic drawing of the KamLAND detector.

(b) Figure 2.20: Map of the nuclear power reactors in Japan.

The KamLAND detector is composed of 1 kton of ultra-pure liquid scintillator contained in a 13 m diameter spherical vessel and monitored by 1900 photomultiplier tubes. A 3.2 kton water Cerenkov detector surrounds the scintillator containment vessel, serving as both a passive neutron shield and as a muon detector.

Nuclear reactors produce $\overline{\nu}_e$ beams with neutrino energies ~MeV. Due to the low energy, electrons are the only charged leptons which can be produced in the neutrino CC interaction.

If the $\overline{\nu}_e$ oscillates to another flavor, the CC interaction can not be observed: oscillation experiments performed at reactors are disappearance experiments. The $\overline{\nu}_e$ with energies above 1.8 MeV gives rise to the inverse β decay reaction:

$$\overline{\nu}_e + p \rightarrow e^+ + n \tag{2.34}$$

and can be identified through the detection of the e^+ and the 2.2 MeV γ -ray from neutron capture on a proton ($n + p \rightarrow d + \gamma$) in delayed coincidence.

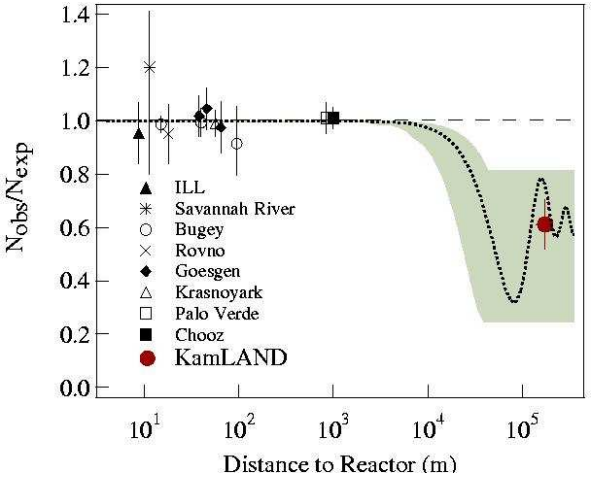

(a) FIGURE 2.21: THE RATIO OF MEASURED TO EXPECTED $\overline{\nu}_e$ FLUX FROM REACTOR EXPERIMENTS. THE SHADED REGION INDICATES THE RANGE OF FLUX PREDICTIONS CORRESPONDING TO THE 95% C.L. LMA REGION FOUND IN A GLOBAL ANALISYS OF THE SOLAR NEUTRINO DATA. THE DOTTED CURVE CORRESPONDS TO $\sin^2 2\theta = 0.833$ AND $\Delta m^2 = 5.5 \times 10^{-5} \mathrm{eV}^2$, REPRESENTATIVE OF RECENT BEST FIT LMA PREDICTIONS.

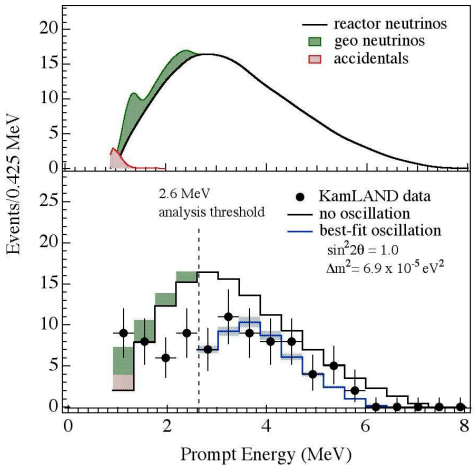

(b) FIGURE 2.21: EXPECTED REACTOR $\overline{\nu}_e$ ENERGY SPECTRUM WITH CONTRIBUTIONS OF GEO-NEUTRINOS AND ACCIDENTAL BACKGROUND (UPPER PANEL) VS THE ENERGY SPECTRUM OF THE OBSERVED PROMPT EVENTS (LOWER PANEL).

The experiment was proposed in 1994 and data acquisition began on January 2002. At the end of 2002, after the first year of data taking, the experiment demonstrated reactor $\overline{\nu}_e$ disappearance at 99.95 % confidence level. The ratio of the number of observed $\overline{\nu}_e$ events to the number of expected events, in absence of neutrino oscillations resulted ($0.611 \pm 0.085(\mathrm{stat.}) \pm 0.041(\mathrm{syst.})$). The probability for this result to be consistent with the no disappearance hypothesis is less than 0.05% .

KamLAND results allowed a big achievement also on solar neutrino physics. Actually, this has been the first experiment to explore with a terrestrial beam the region of neutrino oscillation parameters that is relevant for solar neutrino oscillations. Assuming that CPT is satisfied and that the anti-neutrino measurements by KamLAND apply directly to the neutrino section, the global solution for the neutrino oscillation parameters, determined including the KamLAND results together with the previously known solar neutrino data, populates 6 orders of magnitude less area in neutrino oscillation parameter space ((Δm^2, $\tan^2\theta$)) than the allowed oscillation regions that are determined with just solar neutrino

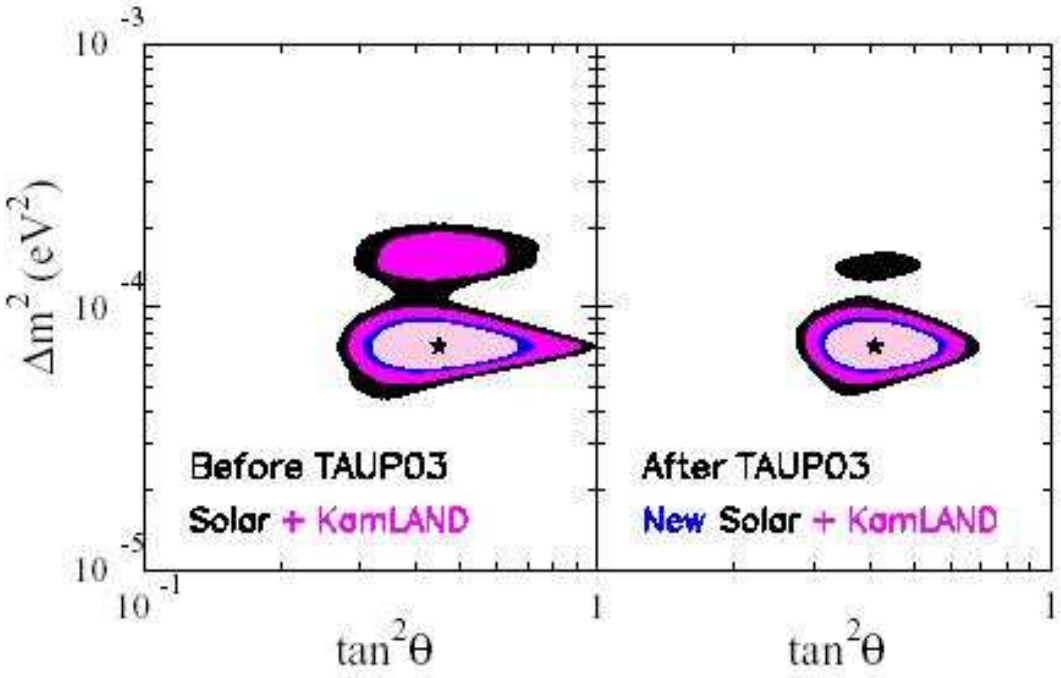

FIGURE 2.22: THE ALLOWED REGIONS IN NEUTRINO OSCILLATION MIXING PARAMETER SPACE, COMPUTED USING ALL SOLAR NEUTRINO AND REACTOR EXPERIMENTAL DATA (KAMLAND RESULT). THE RIGHT PANEL SHOWS THE SITUATION INCLUDING ALSO THE SNO SALT-PHASE DATA AND THE IMPROVED SAGE AND GALLEX-GNO DATA, THAT WERE ANNOUNCED AT THE TAUP03 CONFERENCE, ON SEPTEMBER 2003.

data (see figure 2.22, left panel).
The LMA solution is now the only allowed solution at 3 σ. The LOW, vaccum and SMA solutions are disfavored at, respectively, 4.7σ, 4.8σ and 6.1σ. All alternativea and non standard solar model explanations to the solar neutrino problem that do not include new particle physics (e.g., neutrino oscillations) are also excluded at the 7.9σ CL.

Finally, the latest neutrino oscillation analysis was performed including also the salt-phase SNO data and the refined GNO and SAGE data, announced at the TAUP03 conference, on September 2003. The right panel in figure 2.22 shows the allowed regions for the neutrino oscillation parameters (Δm^2 and $\tan^2\theta$) at 90% , 95% , 99% and 99.73% (3σ) CL. The solar data after the SNO salt phase release disfavors the higher LMA island more than $\Delta\chi^2 = 9$. The SNO salt phase data also improved significantly our knowledge of $\tan^2\theta$, especially the higher values: the 3σ uncertainty in $\tan^2\theta$ is decreased by a factor of order 1.5. The current best fit is:

$$\begin{cases} \Delta m^2 = 7.1^{+0.4\,(+2.6)}_{-0.4\,(-1.6)} \times 10^{-5}\mathrm{eV}^2 \\ \tan^2\theta = 0.42^{+0.05\,(+0.21)}_{-0.04\,(-0.12)} \end{cases} \tag{2.35}$$

The experimental layout

3.1 Overview of the borexino Project

All the existing "*second generation*" solar neutrino detectors have been designed to produce high statistics neutrino signals and to provide precious informations for the understanding of the solar neutrino physics. Among them, BOREXINO is a real time, high-statistics detector specifically designed to measure the ^7Be contribution to the solar neutrinos flux.

Evolving from an original proposal by R. Raghavan [1], the BOREXINO project relies on the efforts of an international collaboration whose principal institutions are from Italy, Germany and the United States. The detector is now almost ready to take data and is housed in the underground facility of the Gran Sasso National Laboratories (LNGS), under the Italian Apennines, at a depth of 3800 mwe. Its main scientific goal is to provide a real time measurement of the ^7Be neutrino flux, insulating it from the other components of the solar neutrino spectrum, and to observe possible periodic variations of the signal.

BOREXINO is an unsegmented detector whose sensitive mass consists of 300 tons of organic liquid scintillator, one third of which will be used as fiducial mass. BOREXINO is sensitive to all leptonic flavours neutrinos, but it is unable to distinguish electron from other flavours. Indeed both charged and neutral currents contribute to the amplitude of the fundamental detection reaction, the elastic electroweak scattering of neutrinos on electrons: $\nu_x + e^- \rightarrow \nu_x + e^-$. The cross section for this reaction is 10^{-44} cm^2 for 0.5 MeV ν_e and it is 4.5 times lower for other flavour neutrinos at the same energy. BOREXINO will measure directly the recoil energy spectrum of the electrons scattered by neutrinos, collecting the scintillation light produced by the scattered electron as it comes to rest in the scintillator, by means of 2200 phototubes.

The liquid scintillator is a mixture of pseudocumene (PC) and fluors (PPO), with relatively high yield: $\sim 10^4$ photons are generated per MeV of deposited energy and $\sim$400 of them are detected. The choice of this high yield organic liquid scintillator allows a low hardware energy threshold of a few tens of KeV. In reality, the contamination of the scintillator with the low energy β^- emitter ^{14}C (Q = 156 KeV) sets the lower detectable neutrino flux at 250 keV.

[1] The original Borex project was initiated in 1987 as a solar neutrino detector for neutral and charged current interactions of ^8B neutrinos on ^{11}B in the target. The design required a 1000-ton fiducial mass of the boron compound trimethylborate as scintillator, from which the project's name originated. BOREXINO was first planned as a prototype for Borex, with only 100-ton fiducial mass. It was soon realized, though, that BOREXINO was large enough to become a unique high rate detector for the more intense ^7Be neutrinos, provided the background at low energy could be reduced. The detection of ^7Be neutrinos became the project's new goal and trimethylborate was replaced by pseudocumene as scintillator, but the name remained.

The predicted counting rate for solar neutrinos in a 100-ton fiducial volume and above the 250 keV energy threshold is 58 events/day, 42 of which are from ^7Be neutrinos, according to the BBP98 SSM. The counting rate per unit mass is 0.5 events/day/ton. BOREXINO does not offer an event-by-event signature or any directional information for the $\nu - e$ scattering events and the signal can be distinguished from the background only statistically. There is, however, a spectral signature for ^7Be solar neutrinos: owing to the monochromatic nature of the ^7Be neutrino radiation, the energy spectrum of the recoil electrons in BOREXINO will feature a sharp *Compton*-like edge at the energy of 665 keV. There is also a temporal signature for the solar neutrino flux: the eccentricity of Earth's orbit provokes a 7 % annual variation of the neutrino rate.
The lack of an event-by-event signature makes it critically important to minimize the rate and understand the spectrum of background events: BOREXINO is the large volume underground experiment with the most challenging background requirements. For a signal/noise ratio of 1, a maximum background rate of 0.5 events/day/ton or 5×10^{-8} Bq/kg in the energy range 250-800 keV (which will be referred to as the Neutrino Window) is required.

3.2 The Gran Sasso underground laboratory

The Gran Sasso Laboratories are located beside the Gran Sasso Tunnel (10.4 km long) on the highway connecting Teramo to Rome. They consist of three experimental halls, conventionally named hall A, B and C, and a series of connecting tunnels and service areas. The three experimental halls, more than 100 m long and about 18 m high, enclose a volume that exceeds 180,000 m^2.

The natural temperature inside the laboratories is 6° C and the relative humidity is near 100 % , but an air conditioning system keeps them on more comfortably values: 18° C for the temperature and 50 % for the relative humidity.

(a) Figure 3.1: the outdoor Gran Sasso laboratories.

(b) Figure 3.1: the underground Gran Sasso laboratories.

The laboratory is located at 963 m over the sea level and the maximum thickness of the rock overburden is 1400 m, corresponding to 3800 m.w.e. Thanks to this shielding the

Underground Laboratories are characterized by a cosmic ray flux that is extremely reduced compared with the external flux: only neutrinos and high energy muons can penetrate through this heavy thickness of rock. Due to their low interaction probability, incoming neutrinos can filter through the rock independently of their energy, but among the 100 muons $/m^2\,s$ that arrive on the Earth surface, only those that have a sufficiently high energy (E > 1.4 TeV) can penetrate the rock shielding. The resulting muon flux inside the laboratories is 1 muon $/m^2\,h$.

In addition, the Gran Sasso rock is also characterized by a low natural radioactivity, resulting in a low radiation noise. The underground laboratories are then the ideal place for delicate experiments that investigates about rare events as solar neutrino interactions or double beta decays.

3.3 The structure of the detector

BOREXINO is composed of several concentrical regions delimited by three different "shells". The detector design arises directly from signal and background requirements and was driven by the following considerations:

- *Neutrino count rate:* given the low cross sections for neutrino interactions, the only way to maximize the neutrino count rate is to increase the target mass as much as possible. To have a SSM neutrino count rate of about 50 ev/day in a pseudocumene scintillator the detector target mass (fiducial mass) must be, at least, 100 tons.

- *Signal/noise ratio:* the strict constraints on the background level in BOREXINO require both the reduction of the naturally occurring radioactive contaminants in the scintillator and the shielding of the active volume (fiducial volume). The first demand is achieved through the implementation of extraordinary purification procedures, both for the active scintillator and for the surrounding shields; the fiducial volume's shielding is realized, instead, by means of a detector structure (see figure 3.2) based on a succession on increasingly pure shells.
  Very stringent requirements are also placed on the construction materials used throughout BOREXINO , from the scintillator containment vessel, to the phototube glasses or to the metallic supports.

- *Detector resolution:* an optimum scintillation-light collection efficiency leads not only to an improved energy resolution, vital for the identification of the ^7Be neutrino edge, but also to a better spatial position reconstruction and α/β discrimination, important for the background discrimination. This has been the major requirement adopted in the selection of the scintillator mixture and of the nylon vessels material and in the design of the light collection apparatus.

- *Solar neutrino signatures in* BOREXINO *:* the two principal ways for BOREXINO to *see* the solar neutrinos are the identification of the ^7Be neutrino edge in the electron recoil energy spectrum and the observation of the $1/R^2$ annual variation in neutrino rate from the Sun (a 7% effect). Our ability to detect either effect will depend critically on the degree of background suppression we are able to achieve.

The following paragraphs give a brief description of the fundamental detector components. The structure of the detector is shown schematically in Figure 3.2. The active liquid scintillator target is contained in a thin nylon vessel and surrounded by a shielding (buffer)

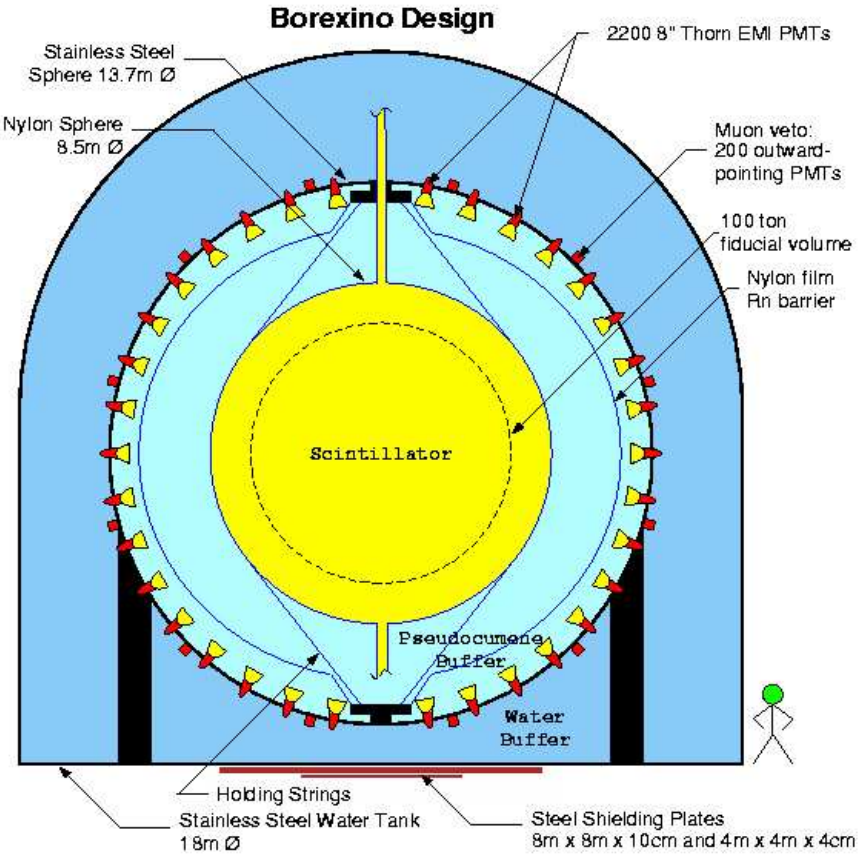

FIGURE 3.2: SCHEMATICS OF THE BOREXINO DETECTOR AT GRAN SASSO. 300 TONS OF LIQUID SCINTILLATOR ARE SHIELDED BY 1040 TONS OF BUFFER FLUID. THE SCINTILLATION LIGHT IS DETECTED BY 2200 PHOTOTUBES. THE OUTWARDS POINTING PHOTOTUBES ON THE STEEL SPHERE SURFACE ACT AS MUON VETO DETECTOR, USING THE CERENKOV LIGHT PRODUCED BY MUONS INTERSECTING THE OUTER WATER BUFFER.

liquid. A stainless steel sphere serves as support structure for the PMTs and contains both the scintillator and the buffer liquid. A water buffer provides the last shielding shell, as well as the active volume for the muon detector.

3.3.1 The outer water tank and the water buffer

The most external shell in BOREXINO is the water tank, a stainless steel domed cylinder, 18 m in diameter and 16.5 m high. The space between the outer water tank and the SSS is filled ultra-purified water. This water is produced on-site from the water coming from the Gran Sasso mountain, through a dedicated Water Purification Plant (WPP, see section 3.4.3). The radiopurity levels of this water are summarized in table 3.1.

	^{238}U , ^{235}Th $[g/g]$	^{nat}K $[g/g]$	^{222}Rn $[Bq/m^3]$
Borexino	10^{-10}	10^{-7}	1
CTF	10^{-13}	10^{-10}	10^{-3}
Raw Gran Sasso Water	10^{-10}	10^{-7}	10^{4}
WPP output	3×10^{-14}	$< 5 \times 10^{-11}$	$< 3 \times 10^{-3}$

TABLE 3.1: RADIOPURITY REQUIREMENTS FOR THE WATER IN BOREXINO AND IN THE COUNTING TEST FACILITY (FIRST TWO ROWS) AND RADIOPURITY PROPERTIES FOR THE RAW WATER AND FOR THE WATER DELIVERED BY OUR WATER PURIFICATION PLANT (LAST TWO ROWS). THE REQUIREMENTS ARE LESS STRINGENT FOR BOREXINO THAN FOR CTF , BECAUSE IN THIS PROTOTYPE THE WATER IS IN DIRECT CONTACT WITH THE INNER VESSEL.

The main function of this water buffer is the reduction of the γ and neutron flux emanated from the rocks of the experimental hall[2].

[2]The composition of the local room γ and neutron fluxes are summarized in tables 3.2 and 3.3. The

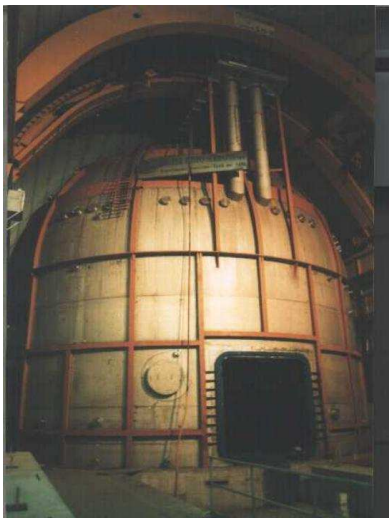

(a) FIGURE 3.3: CLOSE PICTURE OF THE OUTER WATER TANK.

(b) FIGURE 3.3: VIEW OF THE OUTER WATER TANK FROM THE TOP OF THE CTF DETECTOR.

Isotope	***Energy [MeV]***	***Flux*** $[m^{-2} \cdot d^{-1}]$
^{228}Ac	0.911	0.5×10^7
^{214}Bi	1.120	1.4×10^7
^{40}K	1.460	3.8×10^7
^{214}Bi	1.764	1.7×10^7
^{208}Tl	2.614	1.4×10^7

TABLE 3.2: LOCAL γ BACKGROUND IN THE LNGS UNDERGROUND HALLS.

Energy [KeV]	***Flux*** $[10^{-6} \ cm^{-2} \ s^{-1}]$
$0 - 5 \times 10^{-5}$	1.08 ± 0.02
5×10^{-5} -1	1.84 ± 0.20
$1 - 2.5 \times 10^3$	0.54 ± 0.01
$2.5 - 5 \times 10^3$	0.27 ± 0.14
$5 - 10 \times 10^3$	0.05 ± 0.01
$10 - 15 \times 10^3$	$(0.6 \pm 0.2) \times 10^{-3}$
$15 - 25 \times 10^3$	$(0.5 \pm 0.3) \times 10^{-6}$

TABLE 3.3: LOCAL NEUTRON BACKGROUND IN THE LNGS UNDERGROUND HALLS.

A careful analysis of the background has demonstrated that 2 m of water, in addition to the buffer liquid and to the scintillator buffer, are sufficient to absorb almost all the γ and the neutron fluxes originated in the Gran Sasso rocks. Our shielding is then at least 2 m in any direction, except at the very bottom. Here, since the sphere is not vertically centered, it is only 1 m. To compensate this lack, an extra 15 cm steel plate (1 m water equivalent thickness) has been installed under the tank.

Finally, this shield acts also as a Cerenkov detector for cosmic rays, as a part of the muon veto system. To increase the cosmic rays detection efficiency, the internal wall of the water tank is covered by Tyvek sheets, which reflect and diffuse the Cerenkov light radiated by the cosmic rays crossing the water buffer.

3.3.2 THE STAINLESS STEEL SPHERE

The so called BOREXINO outer vessel is a 13.7 m diameter stainless steel sphere (SSS). It is the support structure for the phototubes but it is also the part of the containment system that stands the buoyancy force between the lighter scintillator and buffer liquids and the water.

The 2200 PMTs of the inner detector are mounted directly on its internal surface; on the outer surface there are instead the 200 additional phototubes of the muon veto system.

reduction factor for the 2.6 MeV γ rays from ^{208}Tl is $\sim$100 per meter of water.

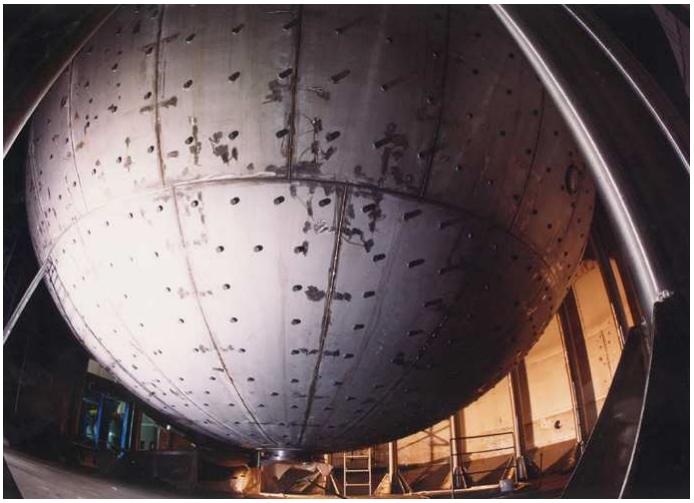

(a) FIGURE 3.4: VIEW OF THE STAINLESS STEEL SPHERE FROM INSIDE THE WATER TANK, BEFORE THE INSTALLATION OF THE PMTS .

(b) FIGURE 3.4: SOME OF THE STEEL LEGS SUPPORTING THE SSS STRUCTURE.

The space between the SSS and the inner vessel is filled with the pseudocumene buffer. The choice of having as buffer liquid the solvent of the scintillator solution allows to match the density of the scintillator, keeping both the nylon film Rn barrier and the inner vessel free from mechanical stresses. The buoyancy force that is produced due to the density difference between the scintillator ($0.87\ g/cm^3$) and water is therefore located on the SSS . This forced the design of the sphere to be based on safety requirements[3].

The sphere is made of 8 mm thick plates in the top hemisphere and 10 mm thick plates in the bottom hemisphere, for a total mass of ~45 tons. It is supported by 20 legs welded to the base plate of the water tank.

In order to assure a high level of cleanliness, especially from particulates, the internal surface of the stainless steel sphere has been pickled and passivated. The percentage of the incident light reflected by the resulting surface is a very important parameter to be known: light reflecting from the sphere back to the phototubes modifies the time distributions of the detected events, resulting in a degradation of α/β discrimination. The direct measurement of the stainless steel sphere reflectivity gave ~40 % . The simulations show that if the reflection is diffuse, rather than specular, most of the reflected light will be trapped behind the light cones and will not significantly disrupt the α/β discrimination.

During the phototube mounting phase, to provide clean-room conditions, the air within the sphere has been filtered. Instead, during the final installation of the nylon vessels, special synthetic Rn-free air will be pumped into the sphere. This will prevent from a build-up of

[3]The SSS must hold the buoyancy force of 1300 m^3 of PC in water (~170 tons), but it must also support its full weight even in the absence of water in the external tank.

the radon daughters on the nylon vessels.

3.3.3 The inactive buffer

The space between the SSS and the inner vessel is filled with 1000 m^3 of buffer liquid. We decided to use the same solvent used for the scintillator solution: pseudocumene. This choice has several advantages:

- its density matches the density of the scintillator within 1 part in 10^3 , minimizing the mechanical stresses on the inner vessel (this is a neutral buoyancy configuration);
- the refraction indexes of the two liquids match within 1 % . The scintillation light is then minimally disturbed during its propagation (since light reflection and refraction at the interface are eliminated) and we have a better position identification;
- the light attenuation length and the scattering mean free path length exceed 5m at the scintillation light wavelength (430 nm);
- its low intrinsic radiopurity (10^{-15} g/g for ^{238}U and ^{232}Th) allows the buffer to have a low impact on the external background rate.

The pure PC is a much less efficient scintillator than the PC +PPO mixture[4]: its light yield is ~20 times lower than the scintillator solution's one. However, even with this small light yield, the background rate of high energy γ -rays coming into the buffer from various detector components (mainly the phototubes) would produce a high background rate. Monte Carlo simulations predict 12 Hz of trigger rate from these events: almost as much as the dominant 20 Hz of ^{14}C background. Most of this background has a low energy, and the residual fraction above the 250 keV threshold would be largely recognizable through the good resolution of the event position reconstruction. Yet, this residual background would be still ~350 ev/day, i.e. a factor 7 larger than the expected ^{7}Be neutrino rate.
To suppress this undesired fluorescence, 5 g/l of dimethylphthalate (DMP) are then added, as a quencher, to the inner buffer. At this concentration the quenching factor for the fluorescence light is about 20. This way, the inner buffer is really a passive shield and the detected events can take place only inside the scintillator. In addition, since the DMP absorption bands are far from the wavelength region of the PMT 's sensitivity, this has no effect on the light mean free path lengths and on the detected Cerenkov light. Finally, the compound has also acceptable radiopurity standards and good compatibility both with PC and nylon.

3.3.4 The inner vessel

The containment system of the liquid scintillator is one of the most challenging components of BOREXINO , due to the various and severe requirements for a successful long-term operation of the experiment:

- in order not to affect the signal detection, it must be optically transparent in the 350-500 nm range, with a haze[5]not larger than a few % ;

[4]Mainly due to the poor match between its emission spectrum and the PMT sensitivity and to its reduced fluorescence quantum efficiency.

[5]Fraction of light scattered above a certain angle.

(a) FIGURE 3.5: PROTOTYPE OF THE INNER AND OUTER VESSELS DURING A GAS FILLING TEST.

(b) FIGURE 3.5: ONE STAGE OF THE INNER VESSEL MANUFACTURE INSIDE THE BOREXINO CLEAN ROOM AT THE PRINCETON UNIVERSITY.

- it must be chemically resistant to aromatic hydrocarbons, like pseudocumene, and have a low permeability for aromatics, water and radon;
- it must preserve its mechanical integrity for several years, in presence of the buoyancy force due to the 0.1 % density difference between the scintillator and the buffer liquid;
- among all materials, excluding the scintillator itself, it must have the lowest radioactive contamination level;
- it must act as a barrier against ^{222}Rn diffusion from the buffer liquid into the scintillator;
- the fabrication and installation must be performed in a clean environment, in order to avoid surface contamination.

The original proposal for BOREXINO was a 2 cm thick acrylic vessel. One of the main drawbacks of this design was that acrylic is not chemically resistant to concentrated aromatics. A protective barrier against the aggressive action of pseudocumene was then necessary. Moreover, when acrylic is immersed in water and if he stress is above a certain level, crazing can occur in the vessel.
When the Counting Test Facility operation started, a different design was then proposed by the Princeton group: a thin membrane nylon bag, 0.5 mm thick (2 m in diameter). Given the success of this vessel during the CTF campaigns, this design was then extended to the larger scale BOREXINO vessel.
The BOREXINO inner vessel is a spherical nylon bag (8.5 m in diameter) made of a nylon-6 film 125 μm thick. Table 3.4 lists the most relevant properties of the this vessel.

The ^{222}Rn barrier factor, the ratio between the ^{222}Rn concentrations inside and outside the vessel, was calculated from the measurements of the diffusivity of radon in the nylon. Actually, the contamination by ^{222}Rn is one of the major concerns in the vessel design.
Being a noble gas, radon is highly volatile and is easily released from any material that

Vessel diameter	8.5 m
Film thickness	125 μm
Nylon type	Nylon-6
^{238}U ***content***	1.7 $\pm$ 0.2 ppt
^{232}Th ***content***	3.6 $\pm$ 0.5 ppt
^{222}Rn ***barrier factor***	$< 10^{-7}$
Transmittance (366 nm)	98.3 $\pm$ 0.6 %
Haze ($< 3.5°$)	0.28 $\pm$ 0.04 %
Maximum load (operating load)	40 Mpa (2Mpa)

TABLE 3.4: THE MOST RELEVANT PROPERTIES OF THE BOREXINO INNER VESSEL.

contains ^{226}Rn , a long-lived isotope of the ^{238}U radioactive chain. Its half-life of 3.8 days is long enough to allow it to diffuse from the inner vessel into the scintillator. The 125 μm thick nylon vessel acts naturally as a barrier[6]against radon diffusion, but since it is so thin, special care was devoted to finding a material with low diffusivity. For a concentration of ^{238}U of 10^{-12} g/g in the inner vessel, the ^{222}Rn emanation gives rise to an equivalent ^{238}U intrinsic contamination of the scintillator of 10^{-17} g/g. Moreover, the deposition of ^{210}Pb , a long-lived radon daughter, on the vessel walls would cause a permanent source of background.
To avoid these problems, the vessel fabrication was done in a controlled clean room environment, where a specially designed radon filter was installed.

The CTF data have shown that γ -rays from the radon contamination in the buffer liquid can be also a major source of external background. A second nylon vessel is then installed outside the inner vessel. This second vessel insulates the inner one from ^{222}Rn and other impurities that might otherwise diffuse into the sensitive volume from the outer regions of the detector, especially the photomultipliers. This vessel is made with the same nylon film used for the inner one, but has a larger (11 m) diameter.

3.3.5 THE SCINTILLATOR

The active target of BOREXINO detector are 300 tons of organic liquid scintillator. A lot of measurements where done to find the best solution for the choice of the scintillator. Finally, after the CTF 1 and CTF 2 campaigns' data analysis, the collaboration decided for a binary mixture of pseudocumene (1,2,4-trimethylbenzene or PC), used as solvent, with PPO (2,5-diphenyloxazole), used as primary fluor in the concentration of 1.5 g/l.
The most relevant physical properties of pseudocumene are listed in table 3.5.

The scintillator optical properties have been widely studied during several laboratory experiments, by using different techniques on small scale samples (few cubic cm^3) and medium scale samples (about 10 liters). However, only the measurements obtained with the Counting Test Facility detector allowed a complete characterization of this scintillator solution. Its main charachteristics are:

[6]The ^{222}Rn barrier factor is the ratio between the concentrations inside and outside the vessel and it is calculated from measurements of the diffusivity of radon in the nylon.

Chemical name	1,2,4-trimethylbenzene
Molecular structure	$C_6H_3(CH_3)_3$
Molecular weight	120.2
Density	0.876
Index of refraction	1.505
Water solubility	57 mg/l at 20° C
Flash point	48° C

TABLE 3.5: THE MOST RELEVANT PHYSICAL PROPERTIES OF PSEUDOCUMENE.

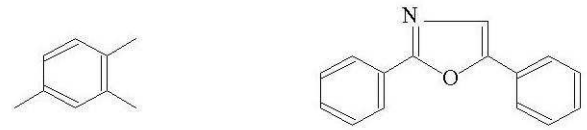

Pseudocumene
(1,2,4-trimethylbenzene)

PPO
(2,5-diphenyloxazole)

FIGURE 3.6: PC AND PPO MOLECULAR STRUCTURES.

- a high primary light yield: about 10^4 photons/MeV;
- an emission wavelength peak at 430 nm (see figure 3.7), i.e. well above the PMT 's sensitivity threshold (about 350 nm);
- a mean free path lenght of the light in the scintillator that excedes 7 m at the peak emission wavelength;
- a short scintillator decay lifetime ($< 4ns$), as required for a good spatial resolution;
- a large difference on the tail of the decay time distributions for α and β excitation modes, that allows an efficient α/β discrimination;
- an α quenching factor greater than 10 in the energy range 5-6 MeV. This constrains the β equivalent energies for most of the α decays in the uranium chain below 0.5 MeV, and hence below the Compton -like ^7Be edge. The energy dependence of the α quenching factor, measured in laboratory, results:

$$Q(E) = 20.3 - E \cdot (1.3\,\mathrm{MeV}^{-1}); \tag{3.1}$$

- a high radiopurity level(10^{-16} g/g of ^{238}U and ^{232}Th), attainable also on a large mass scale (as shown with the CTF detector).

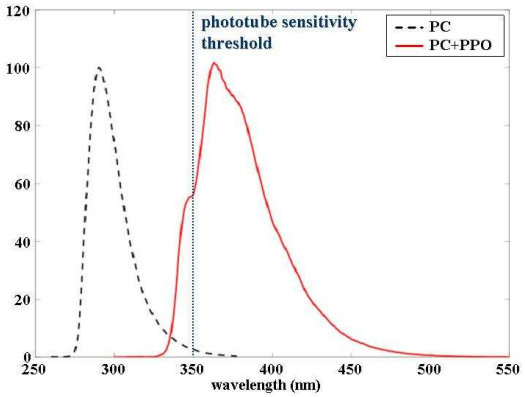

FIGURE 3.7: EMISSION SPECTRA OF PC (PSEUDOCUMENE) AND (PC +PPO) (SCINTILLATOR MIXTURE).

The scintillation properties of organic scintillators are reconduced to the properties of their constituent molecules. Most of the organic scintillator contain molecules with some particular symmetries, leading to structures called "*electronic structure* π ". The electronic levels of an organic molecule with such a π electron system (see figure 3.8) can be divided in spin zero ($S_0 ... S_n$) and spin one ($T_0 ... T_n$) states. Such organic compounds can be really a scintillator only when the energetic gap $S_0 - S_1$ is about 4eV.

Since the thermal energy at 300 K is $\sim$25 meV , at room temperature most molecules are in their fundamental state. When a high energy particle interacts with the organic scintillator, the fast absorption of kinetic energy leads to transitions on the higher molecules' levels. Since the absorption transition from the ground state S_0 to the triplet states T_i is spin- forbidden, the interaction populates only the singlet levels.
These levels decay then, in a few *ps* and non-radiatively, in the S_{1i} states. Since these vibrational levels are not in equilibrium with the nearby molecules, they also loose quickly their energy and populate, in a few tens of *ps*, the S_{10} state. Finally the radiative transitions from this singlet state S_{10} to the ground state S_0 or to one of its vibrational sub-levels gives rise to the fast (typical lifetime of the order of 10^{-9} -10^{-8} s) *fluorescence* light.
In addition, even if the transition from the ground state S_0 to the triplet states T_i is spin-forbidden, the triplet states can be populated by other means, such as the collisional interaction between excited molecules. T_1 is a long-lived state, with a radiative transition lifetime that can range up to few *ms*: the light emission from this state gives rise to the slow scintillator component or *phosphorescence* light.
Finally two molecules in the lowest excited π -triplet state T_1 can collide and result in a molecule in the first excited π -singlet state S_1 and in one in the ground state S_0. The molecule in S_1 subsequently decays to the ground state, with the same spectrum of the main $S_1 - S_0$ radiative transition, but with a delay that is determined by the rate of collisions between T_1 excited molecules. In some scintillators, this slow component (*delayed fluorescence*) can last up to 1 μs .

This briefly summarizes the principle of operation for the unary organic scintillators, i.e. the ones composed by only one type of molecule. Many scintillators, and this is the case of BOREXINO , are instead binary mixtures composed by a solvent and by a salt called

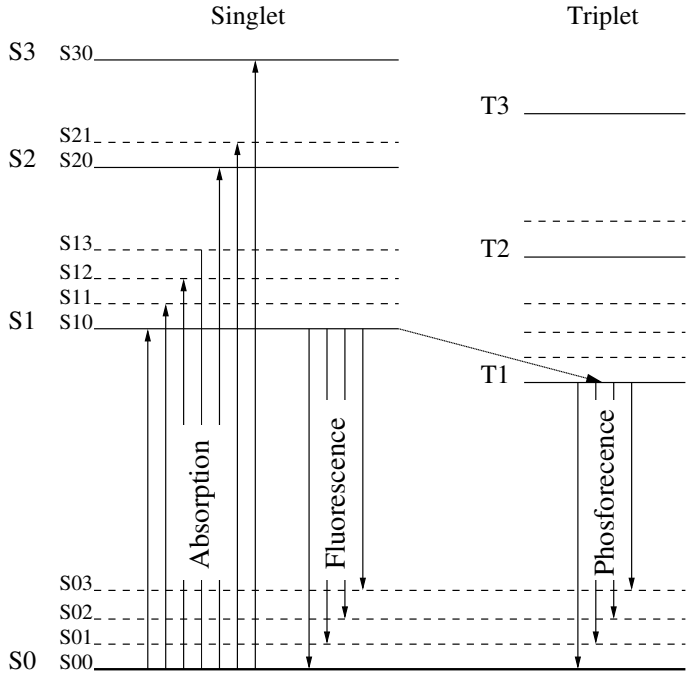

FIGURE 3.8: π -ELECTRONIC ENERGY LEVELS OF AN ORGANIC MOLECULE. S_0 IS THE GROUND STATE. S_1, S_2, S_3 ARE EXCITED SINGLET STATES. T_1, T_2, T_3 ARE EXCITED TRIPLET STATES. THE THIN LINES ARE VIBRATIONAL SUBLEVELS.

fluor. In this mixtures the energy transmission among different molecules is of primary importance: the energy collected by a huge amount of solvent can be transmitted to the fluor and converted in light. Often also a third component, the wave-shifter, is added. This substance absorbs the scintillation light at the primary emission and re-emits it with a different wavelength spectrum. By matching its spectrum with the PMT 's sensitivity window, we can increase the efficiency of the light detection. A more detailed description of these scintillation mechanisms can be found in reference [54, 55].

The relationship between energy deposition and scintillation light emission is the *yield*. The yield depends on the particle type and energy. The energy dependence is, in principle, linear, but several effects can cause a non-linear *quenching* effect.
Scintillation light quenching may result from molecular interactions between the excited π - states and other excited or ionized molecules. This effect depends on the density of excitons and ionized molecules and, owing to their greater energy loss per unit pathlenght, is larger for α particles than for electrons.

Finally, also the relative intensity of the fast and slow scintillation components depends on the particle type[7]. The difference between the pulse shape of the scintillation light induced by α and β particles is the α/β discrimination capability of the scintillator (see

[7]The slow component of the scintillation light is less affected by the quenching effect. The relative intensity of the slow emission is then larger for α particles.

figure 3.9). The scintillation light's pulse shape can be described with the sum of three exponential decay curves. The shortest decay time is the main scintillation component.

$$f(t) = \sum_i \frac{q_i}{\tau_i} e^{-\frac{t}{\tau_i}} \qquad \text{where} \sum_i q_i = 1 \tag{3.2}$$

The three exponential decay times for the α and β -γ radiation for the BOREXINO scintillator are quoted in table 3.6. These are the values measured in laboratory for small scale samples.

Excitation	***First component***		***Second component***		***Third component***	
	τ_1 [ns]	q_1 [%]	τ_2 [ns]	q_2 [%]	τ_3 [ns]	q_3 [%]
α	3.25	63.0	13.5	17.8	60.0	11.9
β -γ	3.57	89.5	17.6	6.3	59.5	4.2

TABLE 3.6: DECAY TIMES AND PROBABILITIES FOR THE DIFFERENT SCINTILLATION COMPONENTS, IN CASE OF EXCITATION BY EITHER α OR β -γ RADIATION. THE VALUES HERE REPORTED HAVE BEEN QUOTED IN A LABORATORY MEASUREMENT.

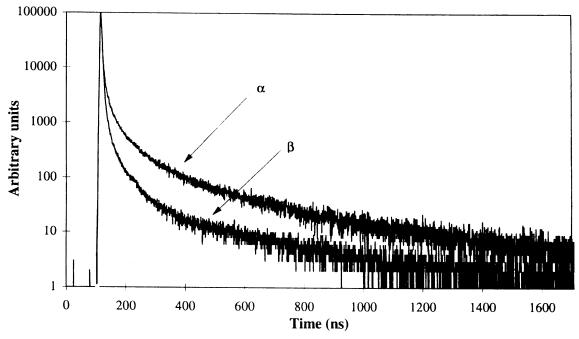

(a) FIGURE 3.9: TIME DECAY DISTRIBUTIONS FOR SCINTILLATION PULSES DUE TO α AND β EXCITATIONS.

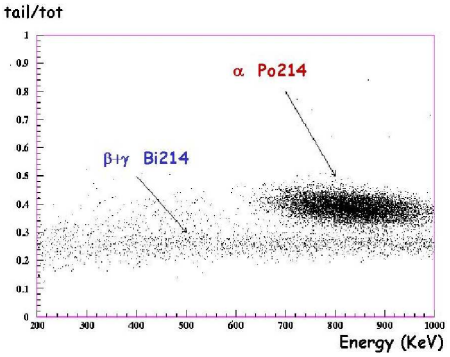

(b) FIGURE 3.9: RESULTS ON THE PULSE SHAPE DISCRIMINATION BETWEEN α AND β EVENTS OBTAINED IN THE CTF DETECTOR.

3.3.6 PHOTOTUBES AND LIGHT CONCENTRATORS

The scintillation light in BOREXINO is detected by an array of 2240 photomultipliers (PMTs) mounted inside the Stainless Steel Sphere. In addition, 200 PMTs mounted outside the

sphere detect the Cerenkov light of the muon tracks, acting as a muon veto system (see section 3.3.7).

The selection of the PMT model has been carried out taking into account PMTs already on the market and prototypes still in developing phase, in strict collaboration with various manufacturers. Extended test measurements have been done on the ETL (formerly known as "EMI") 9351, the Hamamatsu R4558, R1449 and R3600, the Burle C83061E and the Photonis (formerly known as "Philips") XP1082.

The guideline parameters adopted for the tube selection were:

1. a high photocathode quantum efficiency ($> 21\%$) in the wavelenght region around 420 nm, where the scintillation light is sharply peaked. The spatial and time resolutions and a low trigger threshold rely on this parameter;
2. a low transit time spread (< 1.3 ns), necessary for a good time and position reconstruction;
3. a low radioactivity glass. The radioactivity content of the specially commissioned Schott glass bulbs (3×10^{-8} g/g of ^{238}U , 1×10^{-8} g/g of ^{232}Th , and 2×10^{-5} of K_{nat}) is about 10 times better than normal glass. Even with these values, the PMTs are still the largest source of external γ background;
4. a low after-pulse frequency ($< 5\%$). This can affect α/β discrimination;
5. a low dark count rate (< 20 KHz) to avoid instrumental background and keep within reasonable limits the random trigger rate;
6. a good single photoelectron pulse height resolution (single p.e. peak to valley ratio > 1.5). This assures a precise threshold setting and a good stability control of the tube performances during the detector's operation;

(a) FIGURE 3.10: CLOSE VIEW OF ONE OF THE BOREXINO PMTS , DURING THE SEALING PROCESS.

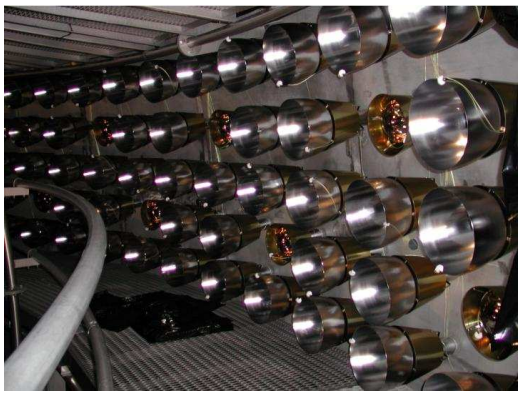

(b) FIGURE 3.10: INSIDE VIEW OF THE SSS , WITH THE PMTS ALREADY ISTALLED.

Finally the 8" ETL 9351 phototube was identified as the best for the operation in our detector. The selection was performed evaluating the impact of the main technical features of the candidates on the overall detector performances.
This tube has an hemispherical photocatode with a radius of curvature of about 11 cm, resulting in a minimum projected area of 366 cm^2 . The cathode is an emissive bialkali type layer (CsKSb); the bulb, a low radioactive Schott 8246 glass, has been carefully analysed in the germanium facility at Gran Sasso.
The ETL 9351 specifications are reported in table 3.7.

Voltage for gain 10^7	1650 V	typ
Maximum voltage	2200 V	max
Maximum voltage between cathode and first anode	900 V	max
Rise time	4 / 6 ns	typ
Fwhm	7 / 10 ns	typ
Fall time	8 / 12 ns	typ
Linearity peak current at $q = 10^6$	8 mA	typ
Linearity peak current at $q = 10^7$	10 mA	typ
Linearity integrated charge at $q = 10^6$	80 / 120 pC	typ
Linearity integrated charge at $q = 10^7$	100 / 150 pC	typ
SER P/V signal	2.5	typ
Photo-cathode sensitivity at 420nm	26.5 %	typ
Transit time spread fwhm	2.8 ns	typ
Pre-pulsing $(2\sigma - 20\sigma)$	3 / 6 %	max
After-pulsing $(0.05 \div 12.4\ \mu s)$	2.5	typ
Dark current at $q = 10^7$	25 nA	typ
Dark counts at $q = 10^7$	3000	typ

TABLE 3.7: BOREXINO PMT 'S SPECIFICATIONS.

The inner detector PMTs are uniformly mounted on the internal surface of the stainless steel sphere. Each device is immersed partially in the buffer and partially in the outer water (the final part of the end-caps and the high-voltage cables and connectors). The muon veto PMTs are instead outside the sphere and therefore completely immersed in water.
A large R&D effort was put into finding the best materials to seal the PMT bulb to the stainless steel can, while guaranteeing the safe and reliable operation of the PMT during several years immersed in water and pseudocumene. A milestone of the PMT sealing campaign was the successful testing of 50 PMTs in the Two-Liquid Test Tank. During this test 49 PMTs were operated for 4 months without any failure in a PC/water environment, realistically mimicking the definitive situation in BOREXINO .

Only 1800 PMTs out of the 2200 of the inner detector are the real neutrino detector; the remainder are part of the muon veto detector. The *neutrino detector* PMTs are coupled to optical concentrators, to increase the light collection efficiency (see figure 3.13).
The shape [44] of the concentrator collects on the PMT 's window only the photons incoming with an incidence angle lower than 44°, reflecting back all the others. This direction corresponds to photons coming from the edge of the inner vessel, plus a 5° tolerance to misalignment: the concentrator receives only the light coming from the solid angle region of

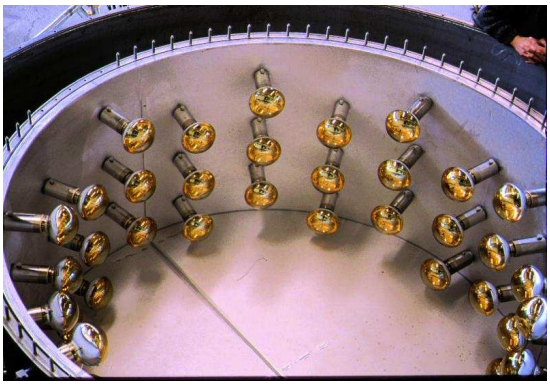

(a) Figure 3.11: CTF2 PMTs installed on the Two-Liquid Test Tank (TLTC).

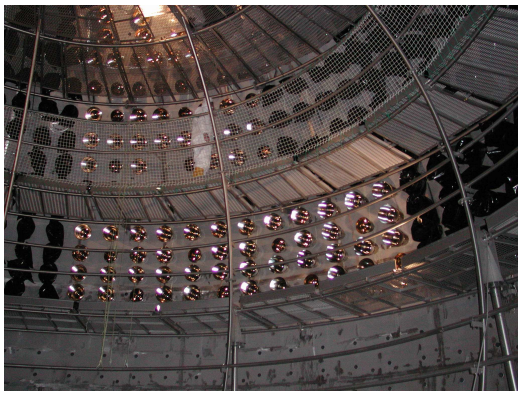

(b) Figure 3.11: inside view of the SSS during the PMTs installation phase.

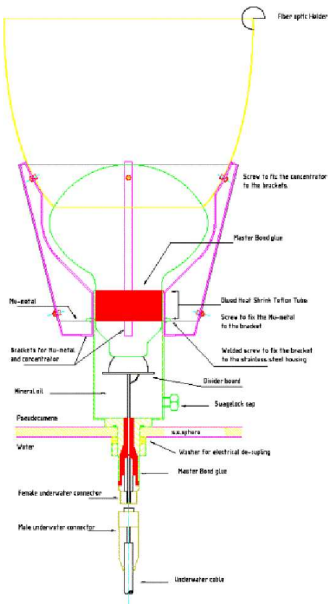

(a) Figure 3.12: Borexino PMT 's mechanical assembly layout.

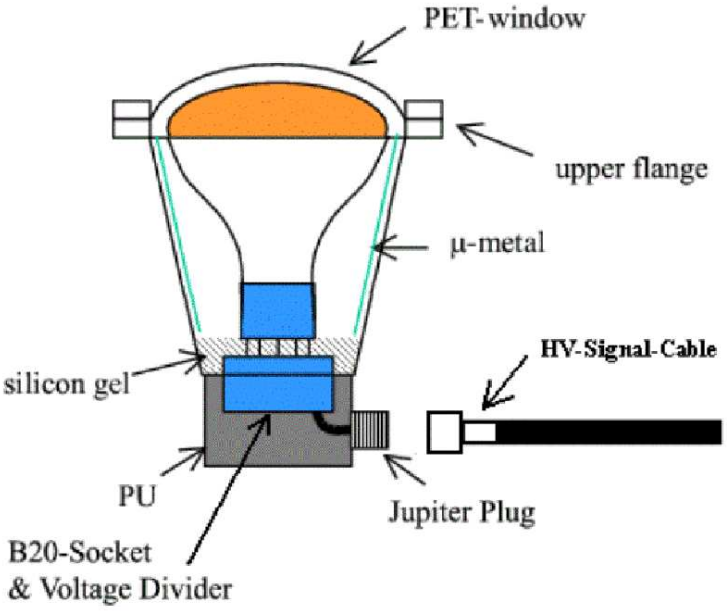

(b) Figure 3.12: Design of the PMT encapsulation insulating the tubes from the ultapure water of the water tank.

the inner vessel. Taking into account an aperture diameter of 20 *cm* and a reflectivity value,

averaged over the scintillator emission spectrum, of ∼90% , the effective light collection area is increased by a factor 2.4. The fraction of solid angle covered by the inner detector PMTs is then 32% .

Finally, to shield the tubes from the Earth magnetic field[8]all PMTs are also equipped with a mu-metal sheet [45, 46].

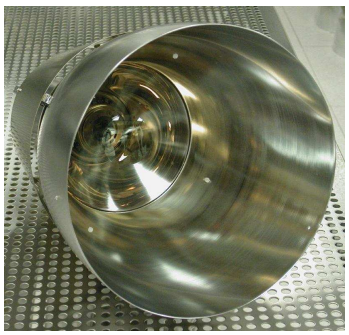

(a) FIGURE 3.13: FRONT (PHOTOCATHODE) VIEW OF A PMT COUPLED TO THE LIGHT CONCENTRATOR.

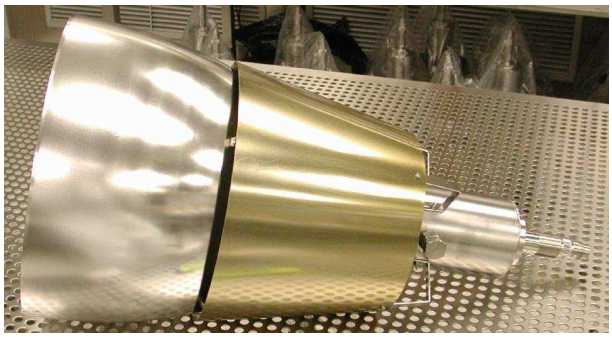

(b) FIGURE 3.13: A LIGHT CONCENTRATOR ALREADY MOUNTED ON ONE OF THE INNER DETECTOR'S PMTS . THE CONCENTRATORS ARE MADE OF ANODIZED ALUMINUM.

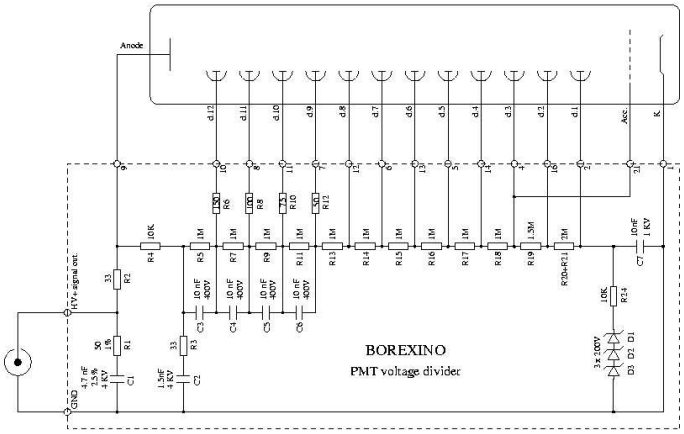

FIGURE 3.14: THE PMT 'S VOLTAGE DIVIDER SCHEMATIC. THE THREE ZENER DIODES BETWEEN THE FIRST DYNODE AND GROUND MAINTAIN THE FIELD BETWEEN THE FIRST DYNODE AND THE PHOTOCATHODE CONSTANT FOR SMALL HV VARIATIONS. THE PMT GAIN CAN BE ADJUSTED BY CHANGING THE HV.

[8]The presence of a magnetic field significantly affects the gain and time resolution of the phototubes.

3.3.7 The muon detector

Even if extremely reduced by a shield of 3800 m.w.e., the residual cosmic ray flux inside the underground laboratories is still a major concern for BOREXINO . The rate of muons intersecting the external water tank or the SSS and producing Cerenkov or scintillation light is still ~10000 events/day. A good set of offline rejection methods can lower this number up to ~25 muons/day (see Section 4.1.3.4), but to identify this residual background events a specific physical hardware system has been designed and constructed. This system is composed of two sets of photomultiplier tubes, one inside and one outside the Stainless Steel Sphere.

3.3.7.1 The inner muon veto system

About 400 photomultipliers out of the 2200 mounted inside the SSS , were specifically installed to detect the Cerenkov radiation produced by muons passing through the buffer and scintillator. These PMTs do not mount the metal light concentrators: the muon tracks grazing the outer buffer have a higher relative yield than the inner neutrino events.
Hence the ratio of the photoelectron yield in the PMTs without and with light cones, is higher for Cerenkov events in the buffer than for neutrino events in the Fiducial Volume.

The efficiency of this *fraction test* has been quoted through Monte Carlo simulations [47]. An aggressive cut can easily exclude 95% of Cerenkov events in the outer buffer, while abandoning only a few percent of neutrino events.

3.3.7.2 The outer muon system

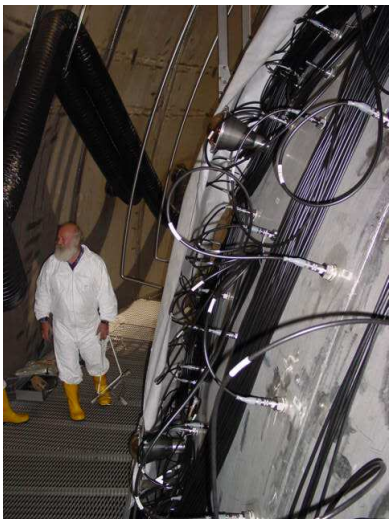

(a) Figure 3.15: top view of the borexino outer muon veto system.

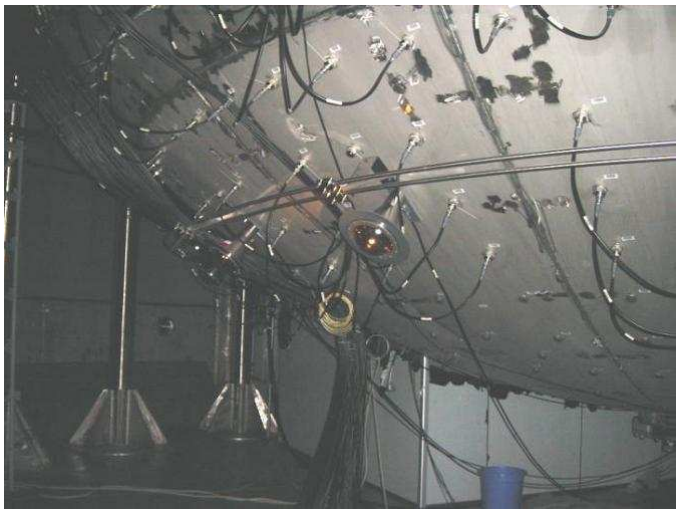

(b) Figure 3.15: bottom view of the muon veto system, with one PMT already installed

The region of the BOREXINO detector between the SSS and the water tank is filled with 2200 tons of ultrapure water. Besides acting as a passive radiation shield, this volume contains also the Cerenkov detection system for muons: the outer muon detector.
The 208 outward-pointing photomultipliers, the same model (EMI 9531) of the inner detector's ones, mounted outside the SSS are equipped with wave shifter plates and connected to an independent electronics system. To increase the photoelectron yield and the number of hit PMTs the outer SSS surface is partially covered by a thin layer (200 μm) of Tyvek[9], that reflects the Cerenkov radiation.

Assuming no light obstruction, each muon track should light $90 div 150$ PMTs , with a maximum yield of about 500 photoelectrons on the PMTs closest to the track. However, even in a worst-case light obstruction scenario the number of hit PMTs is still acceptable.
The expected veto efficiency is well over 90% . The outer muon detector should eliminate well over 4500 out of the 5000 muon tracks crossing the inner detector every day. The inner detector's fraction test and an offline software analysis are then performed on the remainder, yielding to a final muon-induced background lower than the desired 1 event/day.

3.3.8 THE FLASH ADC

The signal from a PMT is AC coupled to a front end card (see section 5.1.2 for more details) that performs noise filtering, pre-amplification, shaping and integration of the input signal. Each front-end board provides also an analog sum of 12 linear output signals that extend the dynamic range of the system to ~30 MeV, by means of a flash ADC system (FADC).

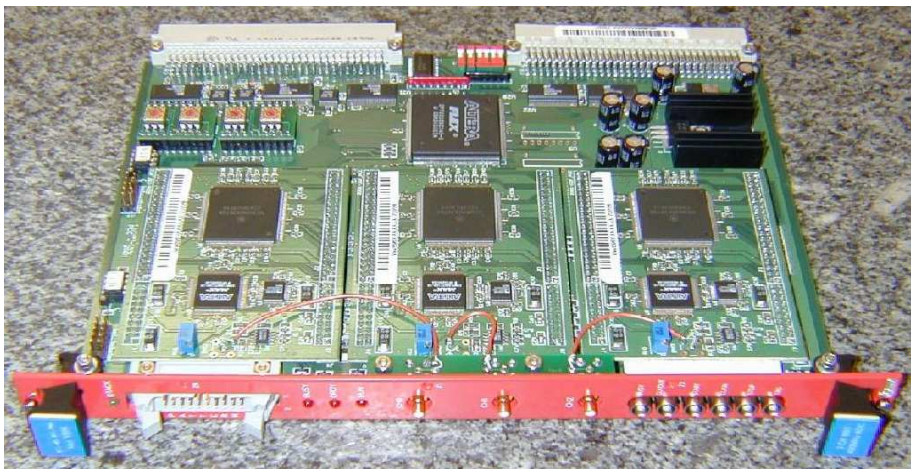

FIGURE 3.16: THE FLASH ADC CARDS USED FOR THE DIGITALIZATION OF THE ANALOG SUM OF THE PMTS ' SIGNALS.

34 C.A.E.N. boards perform the digitalization of the partial sums of 16/24 PMTs and of

[9]Tyvek has a diffuse reflectivity that, in the 300 to 500 nm spectral range, goes from 60 to 90% .

the total sum of all PMTs . The digitalization rate is 400 Mega samples/s, that means a 2.5 *ns* precision. The system runs continuously, but the data are acquired and saved only after a trigger interrupt from the main BOREXINO Trigger Board (BTB). Upon this interrupt, all data in a 10 μs window before the interrupt are saved. A zero suppression algorithm to discard empty data in applied on-line: the number and the size of the stored data windows depends then on the real activity in the event.

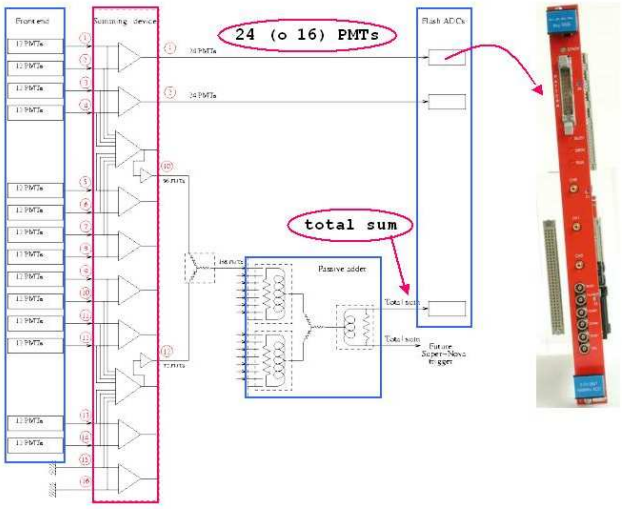

(a) FIGURE 3.17: THE FLASH ADC SUM SYSTEM.

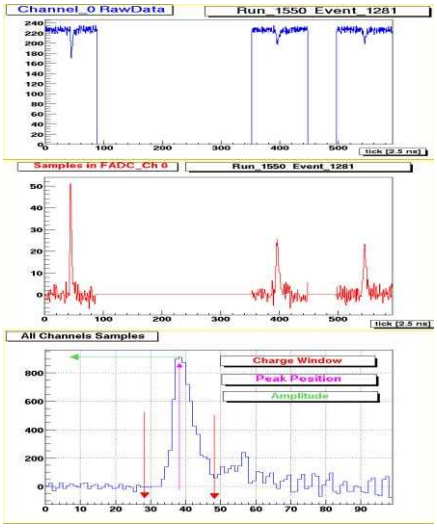

(b) FIGURE 3.17: THE FLASH ADC DATA FLOW: THREE WINDOWS AND THE ONLINE ZERO-SUPPRESSION ALGORITHM; THE OFFLINE PEDESTAL SUBTRACTION AND THE PULSE CHARACTERIZATION.

3.3.9 THE CALIBRATION SYSTEM

The background rejection capability of BOREXINO relies on the good time and charge calibration of the detector.
The most effective analysis cut for the internal background, the α/β discrimination with pulse shape analysis (see chapter 9), depends on a precise position reconstruction's resolution. Also the effectiveness of all the external background rejection methods (see section 4.1) relies on the position and energy reconstructions' precisions to disentangle the true neutrino signal from the unwanted background.

Position resolution is limited by the scintillator fluorescence decay time ($\sim$3.5 *ns*), the PMT transit time jitter ($\sim$1 *ns*) and the inter-PMT time equalization. Given the decay time and jitter constraints, the only possibility to optimize this resolution is to maintain the PMT equalization at a sub-*ns* level. In the same way, energy resolution is limited by the single photoelectron response of the PMTs . The charge calibration consists in finding the conversion factor between the measured ADC channel number and the number of photoelectrons detected.

An dedicated optical calibration system was then built with this purpose. This system allows not only a precise charge calibration and inter-PMTs time equalization of the detector, but also an easy handle to monitor, run-time, the stability of the system. In addition, we plan also to use also complementary methods, such as active tags of trace impurities in the scintillator or the insertion of known radioactive sources, to have the clearest understanding of the efficiency of our detector.

3.3.9.1 The inner PMTs calibration system

BOREXINO has two independent calibration systems, respectively for the time equalization and charge calibration of the photomultipliers of the inner and outer detectors.

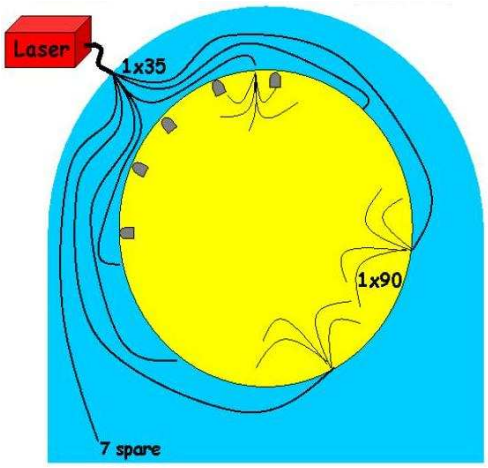

(a) Figure 3.18: A sketch of the inner PMTs calibration system.

(b) Figure 3.18: The optical fiber bundles used for PMT calibration.

The inner system must illuminate all PMTs at the single photoelectron level, in order to measure the single electron response (SER) parameters of each PMT , but must allow also higher illumination levels, to verify the linearity of the PMT response.

The basic concept of this system is the distribution of a fast light pulse to all the PMTs through the consecutive multiplexing of optical fiber bundles [48].
The light source is a PicoQuant diode laser emitting a fast (50 ps time width) light pulse at a wavelength of 394 nm, where the photocatode quantum efficiency reaches 27% . The maximum peak power is 400 mW, corresponding to 1.7×10^7 photons/pulse. The laser can be pulsed both externally and internally, with a maximum repetition rate of 40 MHz. The standard working condition (5.2.3.4) is to pulse it through an external trigger coming from the main trigger system.

The inaccuracy of this system is dominated by the precision of the fiber length differences, which are lower than 1 cm: this means a time inaccuracy lower than 0.05 *ns* . Being this value widely contained within the 1 *ns* PMT 's time jitter, the time spread due to this system does not contribute to the time resolution of the detector.

3.3.9.2 The outer PMTs calibration system

The outer muon veto detector is calibrated by a completely self-standing system. Calibration is performed with a fast LED system coupled to optical fibers. The LEDs are mounted on the inside wall of the external tank. The dynamic range of the system ranges from the Poisson statistics to more than 200 photoelectrons and is independently programmable for each channel. The time spread of the entire system (LED+PMT +electronics) is in the range of 1 *ns* and decreases with increasing intensity.

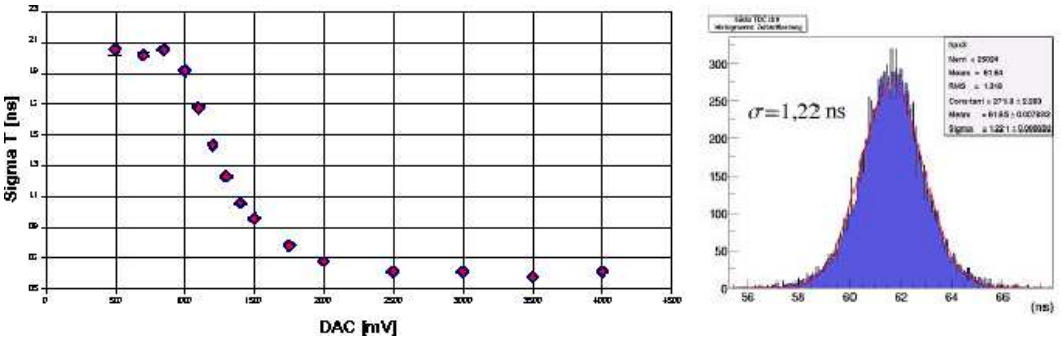

Figure 3.19: Evaluation of the overall time spread of the muon veto system.

3.3.9.3 The optical calibration system

This system was designed to measure and monitor the stability in time of different parameters concerning the production and the propagation of scintillation light in our detector. Together with the detection of light, already addressed with the calibration system, these are the fundamental processes determining the quality of the signal in our experiment.

We can distinguish two subsystems. The internal system, an ultraviolet laser connected to the inner vessel volume through an optical fiber, excites the scintillator and allows a deep understanding of the absorption-reemission effects of the scintillation mechanism. Actually two lasers are used: the first emits at 266 nm, within the absorption bands of PC , the second at 355 nm, within the overlap region between absorption and emission spectra of PPO .
The external system sends instead light beams across the scintillator and buffer liquid, in order to monitor the stability of the optical trasparency of the two materials. The radial beams system produces light beams from the SSS in the direction of the centre of the detector while the oblique system is mounted at some distance from the SSS and points towards PMTs without the light concentrator. The primary light source is the 394 nm diode laser used for the timing calibration system, but also the 355 nm laser can be used.

3.3.9.4 Calibrations with radioactive sources

The use of radioactive sources in BOREXINO is complementary to the optical methods. The goal is to monitor important parameters like the absolute energy calibration, the α/β discrimination efficiency and the radial profile of external γ showers.

This calibration system can be divided in an internal and an external sub-systems. Calibrations with radioactive sources inserted inside the inner vessel are planned to measure the different energy scale between α , β and γ particles, the position resolution and the particle identification efficiency at different energies.

The calibration with a radioactive source inside the active scintillator volume implies, however, a certain risk for the detector. An alternative method is instead to use γ -emitting sources located outside the sensitive detector volume. The goal of this calibration is to study the position reconstruction and the external background rejection efficiencies.

In addition, an unambiguous and straightforward test of the overall detector response can be provided by the calibration with a high intensity neutrino source. A good candidate is a ^{51}Cr source ($^{51}Cr + e^- \rightarrow {}^{51}V + \nu_e$): its half-life is 27.7 days and it produces monoenergetic neutrinos in the energy range of ^{7}Be neutrinos (0.75 MeV at 90% and 0.43 MeV at 10%). A source with an activity of 1.7 megaCurie, comparable to the one used by the GALLEX experiment for its calibration, would produce about 900 counts/month of data taking, that is comparable with the neutrino rate numbers. The source could be inserted in an existing tunnel under the detector.

Finally also the ^{14}C present in the scintillator and the 2.2 MeV γ -ray emitted in the capture of cosmogenic neutrons on protons provide two natural calibration sources to continuously monitor the energy response of the detector.

3.4 Ancillary Plants

3.4.1 The fluid handling systems

Several fluid handling systems are required to perform a variety of tasks:

- prepare and store the scintillator mixture of PC and PPO ;
- purify the scintillator and eventually the buffer liquid;
- produce high-purity water;
- produce high-purity nitrogen to use in scintillator and water purification;
- fill with 1300 tons of pseudocumene the inner vessel, the inner buffer and the outer buffer regions;
- fill the external tank with 2000 tons of pure water;
- fill CTF with 4 tons of scintillator and 1000 tons of pure water.

The main components of these fluid handling systems are the scintillator, water and nitrogen purification plants, the scintillator storage tanks[10], the filling stations and the interconnection tubings. To maintain a high purity level and avoid ^{222}Rn and ^{85}Kr contamination from the air, all the systems were made with electro-polished stainless steel and high quality valves and fittings. The entire fluid handling system has been flushed with nitric acid, rinsed by copiously flowing deionized water, dried with flowing nitrogen and finally leak-checked with helium.

[10] Four storage tanks, with a capacity for 100 tons of pseudocumene each. The extra tank can be used for a faster batch purification of the scintillator prior to the filling.

3.4.2 The scintillator purification system

Pseudocumene for the scintillator is collected on-line at the Enichem production facility (Sarroch, Sardinia) and immediately shipped to Gran Sasso to minimize cosmic ray exposure. Its quality is then improved by on-line purification. The sources of radioactive impurities identified as potentially the most troublesome[11] for a low background scintillator detector are:

- ^{238}U , ^{232}Th and ^{226}Ra from suspended microscopic dust particles;
- ^{222}Rn , ^{85}Kr and ^{39}Ar from air exposure;
- ^{222}Rn emanating from the materials of construction;
- ^{210}Pb build-up on the surface of the scintillator containment vessel;
- ^{40}K from the PPO ;
- ^{7}Be of cosmogenical production on ^{12}C

The scintillator purification system includes five different plants, implementing methods targeted at the reduction of different types of radioactive contaminants. The plants can be used independently or combined, for pre-filling or for online purification.

[11] An important source of radioactive impurity in the scintillator is actually missing: ^{14}C . Carbon is present in the pseudocumene molecule and no purification technique can eliminate this background. The scintillator formulation itself must then minimize this background.

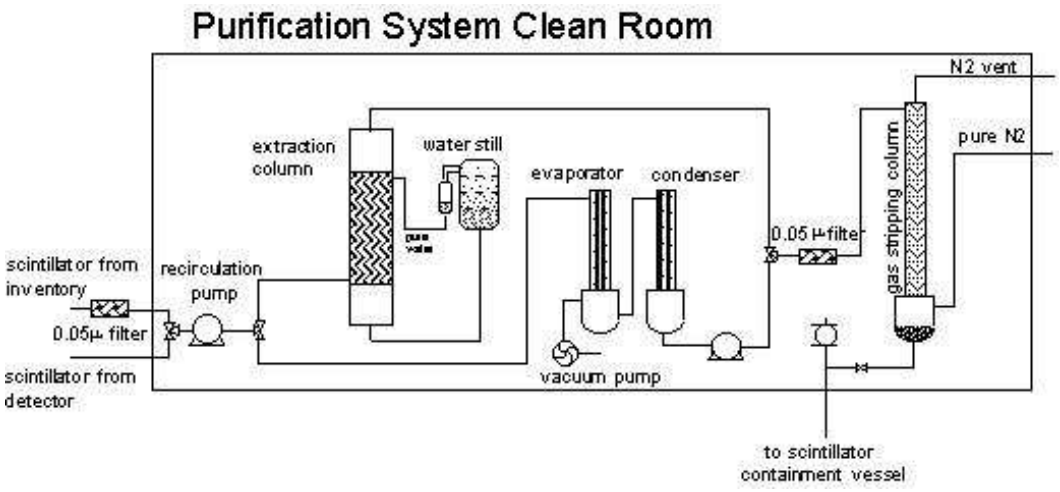

Figure 3.20: Schematic of the scintillator purification system for ctf . The scintillator is either water extracted or vacuum distilled, filtered and stripped with nitrogen before being returned to the scintillator containment vessel.

- a *nitrogen counter-current stripping column:* to remove dissolved gas impurities, such as ^{222}Rn and ^{85}Kr , as well as water dissolved in the scintillator;
- a *vacuum distillation unit:* to remove low volatile and non ionic contaminants (such as metals and dust particles), degraded solvent molecules and ^{7}Be impurities;
- a *water extraction unit:* to remove ionizable species, such as the metals in the ^{238}U and ^{232}Th chains and ^{40}K ;
- a *silicagel column chromatography unit:* with the same purpose;
- a *filtration system:* to remove suspended dust particles larger than 0.05 μm .

A list of the radiopurity requirements for the different isotopes, together with the strategy or purification methods used to achieve them, are summarized in table 3.8. This table was extracted from reference [49], where the reader can find a complete description of the system.

radio isotope	***source***	***typical concentration***	***tolerable level***	***reduction strategy***
^{14}C	cosmogenic bombardment of ^{14}N	$\frac{^{14}C}{^{12}C} \leq 10^{-12}$	$\frac{^{14}C}{^{12}C} \leq 10^{-18}$	petroleum derivate (old carbon)
^{7}Be	cosmogenic bombardment of ^{12}C	3×10^{-2} Bq/ton carbon	$< 10^{-6}$ Bq/ton carbon	distillation or underground storage
^{222}Rn	air and emanation from materials	100 radon atoms/cm^3 air	1 radon atom/ ton scintillator	nitrogen stripping
^{210}Pb	surface contamination			positional discrimination
^{238}U ^{232}Th	suspended dust organometallic	2×10^{-5} g/g dust	$< 10^{-16}$ g/g scintillator	water extraction distillation
^{40}K	dust or contaminant in fluor	2×10^{-6} g/g dust	$< 10^{-13}$ g/g in scintillator $< 10^{-11}$ g/g in fluor	water extraction or fluor solution
^{39}Ar ^{42}Ar	air	1 Bq/m^3 air		nitrogen stripping
^{85}Kr	air	1 Bq/m^3 air		nitrogen stripping

TABLE 3.8: RADIOPURIRY REQUIREMENTS AND PURIFICATION STRATEGIES FOR BOREXINO .

These purification techniques have been successfully tested with laboratory tests and in the CTF .
A schematic diagram of the purification system for the CTF is shown in figure 3.20. In normal operation, the scintillator is removed from the bottom of the scintillator containment

vessel, pumped through the purification system positioned on the top of the water tank, and mixed back in with the scintillator in the active detector. Scintillator is pumped through a countercurrent water extraction column, followed by a 0.05 μm filter. The scintillator, saturated with water, is passed countercurrently through a gas stripping column where water and dissolved gases are stripped by high purity nitrogen. Finally the scintillator passes into a holding vessel which sets the pressure head in the scintillator containment vessel. In the alternate mode of operation the scintillator bypasses the water extraction system and is vacuum distilled in a falling film evaporator/condenser unit.

The three different CTF campaigns revealed the inherent possibility of radon infusion, stressing the necessity of ^{222}Rn removal by nitrogen sparging, and showed the removability of accumulated radon by-products (^{210}Po and the daughter activities ^{210}Pb) through several cycles of water extraction.
The performance of the solid column purification was also evaluated in the CTF 2 campaign. The results showed the achievability of ultimate ultra-purity in an aromatic solvent. The system effectively reduced the internal background in the 5 ton liquid scintillator detector from 470 ± 90 events/day to the detection limit of the detector, ± 45 events/day, in the neutrino energy window.

3.4.3 The water purification system

Both in BOREXINO and CTF ultrapure water is employed for several aims. It is the main shielding of the active volume, it has a fundamental role in the scintillator purification processes (water extraction) and it is used, during the installation phases, to clean all of the detector's components.

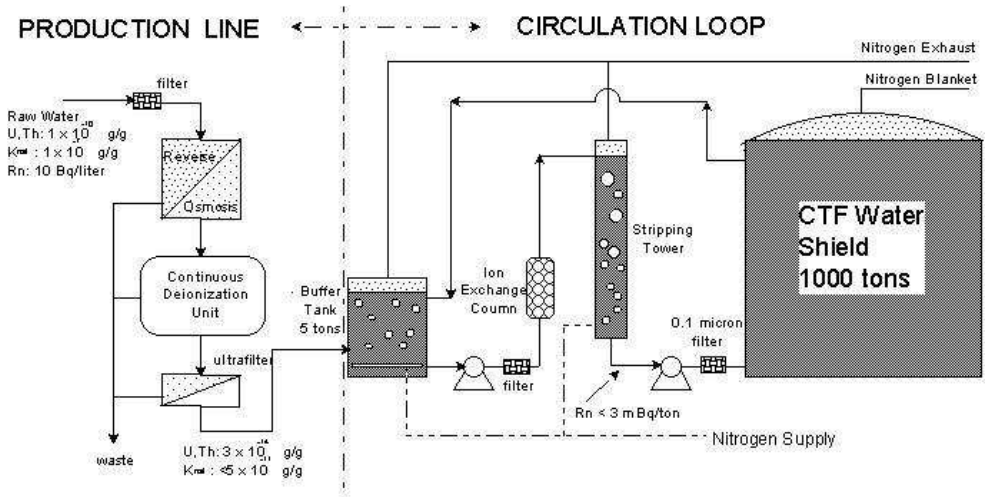

FIGURE 3.21: THE WATER PURIFICATION SYSTEM USED FOR BOREXINO AND CTF .

Our water purification system has been operating in Gran Sasso since the startup of the CTF , in 1994. The system, shown schematically in figure 3.21, is constructed principally of

PVC and teflon coated steel and consists of a filling plant and a re-circulation loop.
During the CTF initial filling the plant was operated in a production mode, purifying the raw water from the LNGS supply. Water is first pre-filtered (0.1 μm filters), passed through a reverse osmosis unit, deionized in a continuous deionization unit (CDI) and eventually stripped in a counter-current nitrogen stripping column, 5 m tall. The nitrogen stripping is critical to remove the high ^{222}Rn content of the raw water (approximately 10^4 Bq/m^3). The measured contamination levels of the purified water achieved with this plant are reported in table 3.1, together with the radiopurity requirements for the filling of both BOREXINO and CTF .

After the initial filling the water was then continuously repurified in a recirculation mode. Water was drawn off the overflow at the top of the water shielding tank, passed through a deionizer and through the nitrogen stripping column and returned to the main water tank.

The plant can purify 2 m^3 /h in either the recirculation or production mode. The continuous deionization unit (CDI) reduces the ionic activity of the raw water from 10^{-10} g U,Th/g-water to 10^{-14} g U,Th/g-water (10^{-13} g U,Th/g-water $\sim 10^{-6}$ Bq/m^3). The radon content in the water after nitrogen stripping[12]is reduced to approximately 10 mBq/m^3 A complete and detailed description of the water plant, of its components and of the techniques can be found in references [50] and [51].

3.4.4 The nitrogen purification systems

Ultra-pure nitrogen gas is used in great quantities in the scintillator and water purification processes, essentially to reduce gaseous contaminations (^{222}Rn and ^{85}Kr). In addition, nitrogen is used also during the detector operation to keep the scintillator saturated under an inert gas blanket. This is needed in order to accommodate small volume changes without increasing the mechanical stresses of the containment vessels and to maintain the scintillator free of oxygen, that quenches the scintillation light.

In order to reach the desired radon purity in the scintillator, ~ 1 μBq /m^3 (1 atom/ton), the nitrogen must contain less than ~ 1 μBq radon/m^3 nitrogen. This requirement is about a factor 100 beyond the standard techniques and a new technology for large scale ultra-purification of N_2 was thus developed.

The BOREXINO nitrogen plant consists of three liquid nitrogen storage tanks, 6 m^3 each, two atmospheric evaporators and a water bath electric heater to produce N_2 gas. Two qualities of gaseous nitrogen can be provided by the plant: regular nitrogen (1 mBq radon/m^3 nitrogen) and high pure nitrogen (10 μBq radon/m^3 nitrogen).
The primary source of nitrogen is the liquid nitrogen commercialy delivered to the LNGS and stored in the three tanks. The regular nitrogen is produced by direct evaporation of the liquid. The high purity nitrogen is produced by charcoal column purification of the liquid N_2 prior to evaporation. Up to 100 m^3 /h of high purity N_2 can be supplied via electro-polished lines equipped with high quality valves. Quality control of these gases is done after ^{222}Rn concentration on charcoal with miniaturized radon proportional counters. The monitoring sensitivity is a record: ~ 0.5 μBq /m^3 for ^{222}Rn . For a detailed description of the system see reference [52].

[12] With a nitrogen to water volumetric flow ratio of 10.

(a) Figure 3.22: The three liquid nitrogen storage tanks housed outside Hall–C .

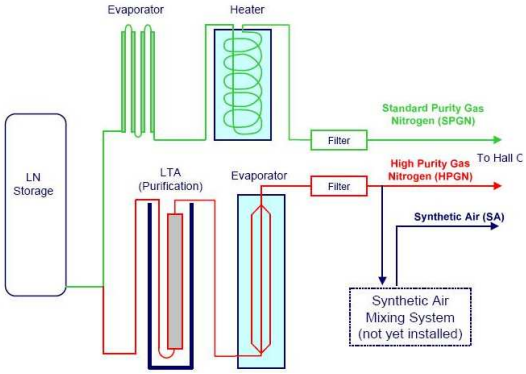

(b) Figure 3.22: Block diagram of the nitrogen plant.

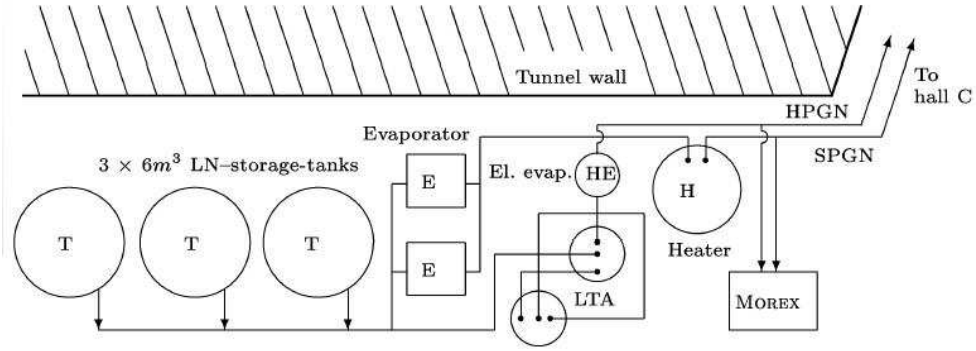

Figure 3.23: A sketch of the nitrogen plant housed outside Hall–C .

3.5 The Counting Test Facility (CTF)

The scientific goals of borexino impose very stringent requirements on the admissible background and the key of the feasibility of this experiment is an extremely low internal background. This can be achieved only by means of scintillator purification. The efforts spent in a long research and development project permitted to identify several solutions for the scintillator and the related purification methods. The identified solutions were promising because they allowed to achieve the design goals of internal radioactive contamination in laboratory test performed on small-scale scintillator samples. However, when borexino was first proposed, direct radiopurity measurements in scintillators were only possible for small samples.

Therefore in 1991 a small-scale prototype of the borexino detector, the so called Counting

Test Facility (CTF) was constructed and installed in Hall C of the Gran Sasso Laboratory.

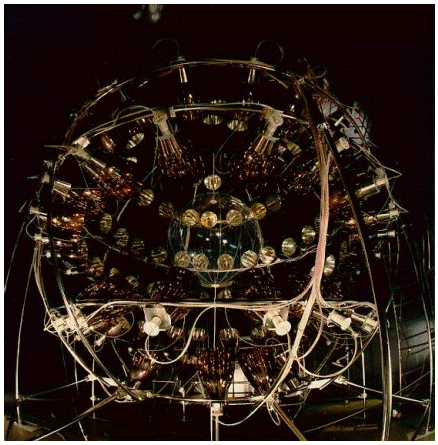

(a) FIGURE 3.24: THE OPEN STRUCTURE SUPPORTING THE CTF PHOTOTUBES.

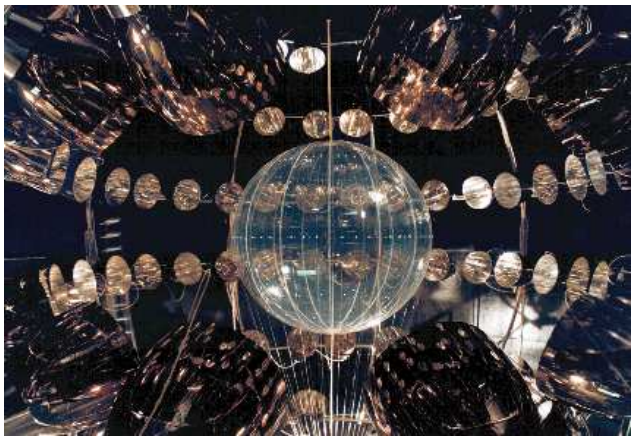

(b) FIGURE 3.24: THE CTF INNER VESSEL SURROUNDED BY THE 100 PMTS BEFORE THE FILLING OF THE DETECTOR.

The goals of the CTF detector were:

- to check the contamination from the natural radioactive chains (^{238}U and ^{232}Th) at the level of 5×10^{-16} g/g;
- to measure the ^{85}Kr contamination in the liquid scintillator with an upper limit of 10^{-13} g/g;
- to measure the ^{14}C /^{12}C relative abundance at the level of 10^{-18} ;
- to perform a radioactivity screening of the construction materials;
- to test and develop different cleaning and purification methods of the scintillator and of the buffer fluids, during the construction and installation of the main detector and of the auxiliary plants.
- to completely characterize the scintillator optical properties;
- to perform spectroscopy at very low energies in a multi-ton detector;

The Counting Test Facility is not designed to detect neutrinos: its limited dimensions do not allow us to define a fiducial volume or to measure the total internal counting rate at the level of the ^{7}Be neutrino interactions (0.5 counts/day/ton). The signal in CTF are the main background sources of BOREXINO .
Nevertheless, during the CTF data taking we developed analysis techniques to study the total background rate, overcoming as much as possible the lack of a fiducial volume definition. Exploiting the spatial reconstruction of the events, these techniques allowed to push the CTF sensitivity to $\sim$15 times the neutrino interaction rate.

3.5.1 The structure of the CTF detector

The conceptual design for the CTF detector is the same as BOREXINO , only with a smaller mass and a smaller number of shielding layers.

The detector sensitive mass is 4 tons of organic liquid scintillator. Two samples of liquid scintillator were tested: the first is the PC +PPO mixture already described in Section 3.3.5 and used for BOREXINO . The second scintillator, tested in a dedicated CTF campaign (CTF 2), is based on PXE solvent (phenyl-o-xylylethane, C_16H_18, density 0.99 g/cm^3).
The scintillator is contained in a 2m diameter transparent nylon vessel (inner vessel) mounted at the center of a stainless steel open structure that supports 100 phototubes which detect the scintillation signals. The PMTs are coupled to optical concentrators and view the inner vessel with ∼20% of optical coverage. The entire detector is built on cleanroom construction standards. The whole system is then placed within a carbon steel cylindrical tank (10m tall, 11m diameter) whose internal walls are coated with Permatex, a black epoxy resin. This tank contains ∼1000 tons of ultra-pure water, which provides a shielding of ∼4m against neutrons originating from the rock and against external γ -rays from the PMTs and other detector materials. Unlike BOREXINO , CTF does not have an inner/outer buffer structure and the inner vessel is directly immersed in water. Given the larger surface-volume ratio, under certain aspects CTF is actually a more delicate experiment than BOREXINO , since the inner vessel surface contamination is a more critical issue and the water purity requirements are higher.

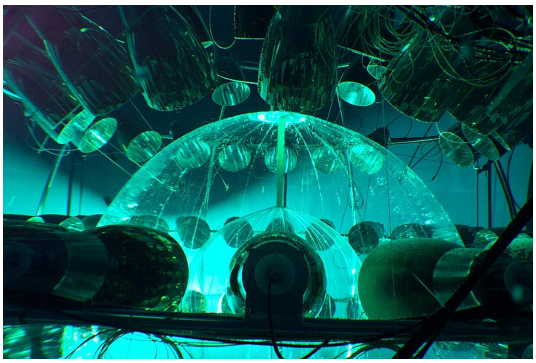

(a) Figure 3.25: view of the CTF detector during the water filling before CTF 3 runs.

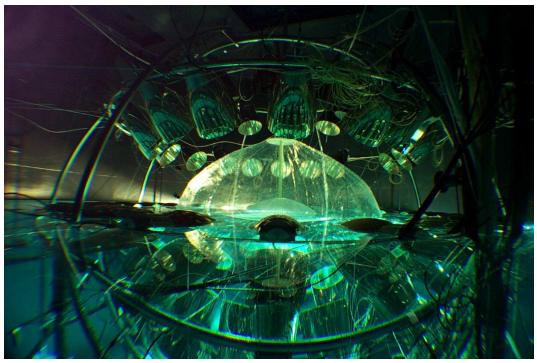

(b) Figure 3.25: view of the CTF detector during a water filling operation.

The readout electronics is designed so that the trigger signal is given by 6 photomultiplier hit within 20 *ns* . There are 64 channels, 28 linked to single phototubes and 36 linked to two coupled phototubes. For each channel, an ADC collects and digitizes the charge signal and a TDC measures the time between the trigger signal and the hit. Additional features are the acquisition and storage of the shape of the overall pulse, obtained through the analog sum of all the outputs, the pulse shape discrimination, used to discriminate between α and β events, and the capability to measure the delay between two subsequent triggers, within 8 ms, using a long range TDC.

The ancillary systems for CTF include the fluid handling systems for water and scintillator purification and for nitrogen sparging. CTF own also an independent PMT calibration system. This system is the prototype of the larger BOREXINO 's calibration system, and is based on the distribution of laser pulses through a bundle of optical fibers.

3.5.2 Results from CTF 1

The first period of operation and data-taking (CTF 1 campaign) was carried out from January 1995 to July 1997. The most relevant tests performed in this phase were the measurement of the coincidence and single events rate, the use of the scintillator purification systems and the test of the performances of several analysis methods.
The main results obtained in this campaign were:

- *Detector resolution:* the scintillation light yield in CTF was 300 photoelectrons/MeV. This leads to an energy resolution of 9% and a position resolution of 12 cm, at the energy of the ^{214}Po line - 751 keV.
- ^{14}C *:* the CTF low energy spectrum, shown in figure 3.26(a), was normalized, between 70 keV and 150 keV, to the expected ^{14}C spectral shape, obtained from Monte Carlo simulations. This gave a ^{14}C concentration in the liquid scintillator of:

$$\frac{^{14}C}{^{12}C} = (1.94 \pm 0.09) \times 10^{-18} g/g$$

- ^{232}Th *:* the concentration of ^{232}Th was inferred from the measurement of the decays of its daughters through the IsotopeBi(β)212$^{212}Po(\alpha$) delayed coincidence tag ($\tau_{1/2}$= 0.30μs). The result was :

$$\left[^{232}Th\right] = \left(4.4^{+1.5}_{-1.2}\right) \cdot 10^{-16} g/g$$

- ^{238}U *:* the delayed coincidence tag used for ^{238}U was the $^{214}Bi(\beta$) $^{214}Po(\alpha$) decay ($\tau_{1/2}$= 164 μs). However, there were strong indications that the $^{214}Bi(\beta$) $^{214}Po(\alpha$) coincidence rate was not due to intrinsic ^{238}U scintillator radioactivity, but rather diffusion of radon from the water into the inner vessel. This phenomenon was demonstrated by raising the Rn leveling the water and observing a positive linear correlation between the number of events arising from Rn in the water (via γ -rays) and the number of events which can only arise from Rn inside the vessel. The measured delayed coincidence counts due to intrinsic ^{238}U and diffused ^{222}Rn corresponds to an equivalent uranium concentration of:

$$\left[^{238}U\right] = (3.5 \pm 1.3) \cdot 10^{-16} g/g$$

- *Purification:* the effect of the purification systems on the scintillator intrinsic contamination was studied by means of an analysis of the radial distributions of the single events. Figure 3.26(b) shows the radial distributions of the events' positions, obtained from the position reconstruction algorithm. The lines represent the expected distributions, from Monte Carlo simulations, for external and internal events, muons and surface background events. A fit of the data resulted in an internal rate of 600 events/day before the purification and in an upper limit of <30 events/day after the purification[13].

[13] In CTF the expected ^{7}Be neutrino signal, in the 250 keV-800 keV energy window, is 2 events/day: the sensitivity of CTF is too strongly limited by the external background to detect neutrinos.

- *α/β discrimination:* in CTF 1 the discrimination between α and β events was done computing the tail to total ratio, i.e. the ratio of the pulse tail, integrated above 48 *ns* , over the total charge. At the energy of the ^{214}Po line (751 keV) the efficiency of α rejection was 97% , with a β misidentification of 2.5% . At lower energies, the α identification was ranging from 90% to 97% , with a β misidentification of 10% .
- *Light propagation:* the main features of light propagation in a large scintillation detector were investigated taking advantage of the three dimensional light collection in CTF . In particular, the investigation of the absorption and re-emission of light by the fluor (inelastic scattering) showed that this process affected 44 % of the detected light, with a corresponding increase of the effective scintillation decay time from 3.5 ns in small-scale laboratory measurements to 5.5 ns in CTF .

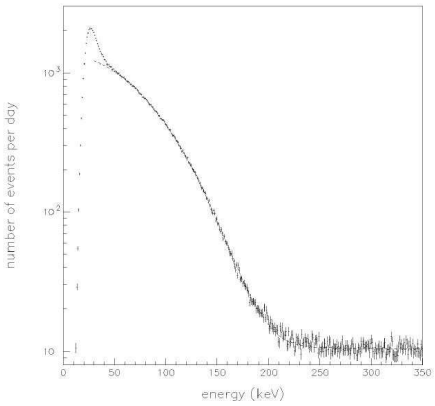

(a) FIGURE 3.26: ^{14}C β -SPECTRUM BETWEEN 20 KEV AND 350 KEV MEASURED IN THE CTF . THE ENDPOINT ENERGY OF ^{14}C IS 156 KEV.

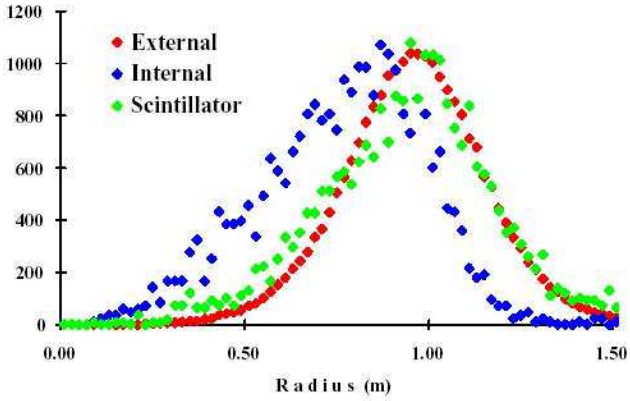

(b) FIGURE 3.26: RADIAL DISTRIBUTION OF SCINTILLATION EVENTS IN CTF , AFTER PURIFICATION, COMPARED TO THE TYPICAL DISTRIBUTION OF INTERNAL EVENTS (OBTAINED WITH ^{222}Rn INSERTION IN THE SCINTILLATOR) AND EXTERNAL EVENTS (OBTAINED WITH ^{222}Rn INSERTION IN THE WATER SHIELD). THE RADIAL DISTRIBUTION OF SCINTILLATOR EVENTS CLEARLY RESEMBLES THE EXTERNAL DISTRIBUTION.

These results demonstrated experimentally a series of important points on which the BOREXINO design is based. Organic liquid scintillators can be obtained with extremely low levels of radioactive impurities. The nylon vessel technique was successfully employed for containing the scintillator and the on-line purification demonstrated its effectiveness. The capabilities of the analysis methods of delayed coincidences, position reconstruction, and pulse-shape discrimination were demonstrated.
Yet, the high level of external background signalled the crucial need to control the activity of radon in the buffer liquid. To reach this purpose, the design of BOREXINO incorporates an additional nylon vessel to serve as a Rn barrier.

3.5.3 CTF UPGRADES AND THE CTF 3 CAMPAIGN

The CTF detector was upgraded in 1999 with the installation of new PMTs and two new nylon vessels, in which the outermost serves as a Rn barrier. After the CTF 2 phase of tests with an alternative scintillator, the CTF 3 phase started in May 2001. The detector was filled with the scintillator batches for BOREXINO in November 2001 and for the following seven monthes tests proceeded steadily. ^{14}C from all the pseudocumene deliveries was measured and several scintillator purification tests using the BOREXINO plants were carried out. Figure 3.27 shows the chronology of the purification tests carried out in the last campaign, together with the radon contamination profile.

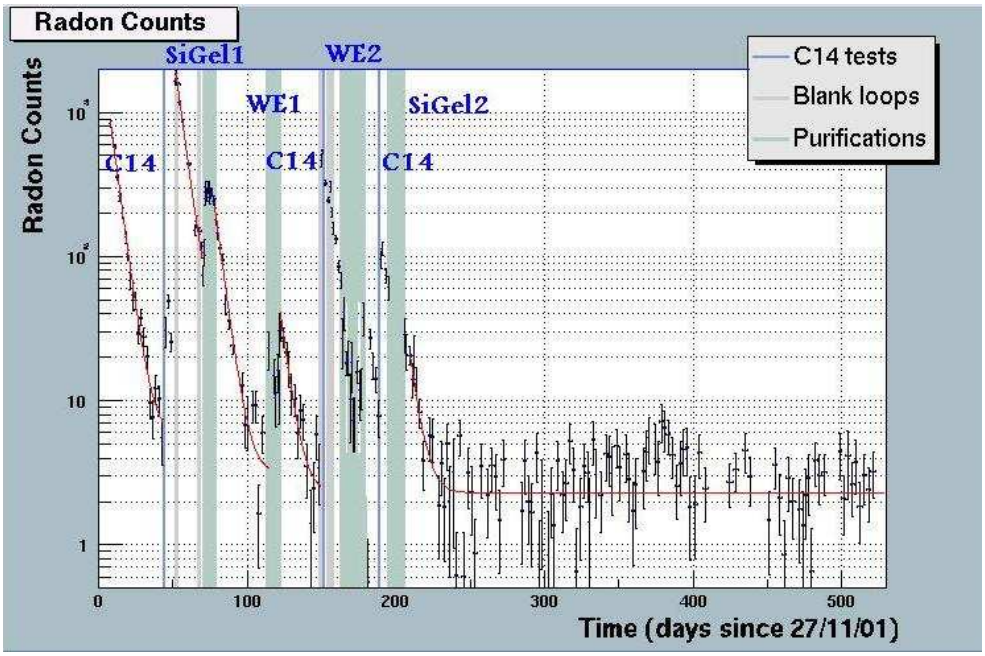

FIGURE 3.27: THE RADON CONTAMINATION PROFILE IN CTF 3, AS A FUNCTION OF THE CHRONOLOGY OF OPERATIONS AND TESTS CARRIED OUT WITH THE DETECTOR. THE DATA ARE SHOWED BETWEEN NOVEMBER 27, 2001 AND APRIL 17, 2003. THE EVENTS ARE IDENTIFIED VIA THE $^{214}Bi(\beta)^{214}Po(\alpha)$ DELAYED COINCIDENCE. THE FITS ARE PERFORMED WITH A DECAYING EXPONENTIAL WITH THE RADON MEAN LIFE (5.5 DAYS) PLUS A CONSTANT.

A sudden and unexpected shutdown of all the activities involving any fluid handling operation in Hall–C came in August 2002 and since then the detector has been unperturbed, although still taking data.

The ^{14}C actvity was measured by fitting the energy spectrum with a simulated one, where the amplitude was used as the fit parameter. From the amounts of PC delivered with each batch, the average ^{14}C content in the scintillator resulted:

$$R(\frac{^{14}C}{^{12}C}) = (5.0 \pm 2.0) \times 10^{-18} \tag{3.3}$$

that is about 2.5 times higher than the value measured during CTF 1 $(1.94 \pm 0.09) \times 10^{-18}$ but is still within our specifications.
An accurate monitoring of the detector using the radon $^{214}Bi(\beta)^{214}Po(\alpha)$ delayed coincidence was also possible. Radon enters the detector through many pathes, included any fluid operation. Figure 3.27 shows the radon profile since the initial loading, correlated to the purification tests made on the detector. The fits were performed with a decaying exponential plus a constant. The exponential decay constant (229 ± 6 μs) resulted well compatible with the ^{214}Po mean life. The constant term, which indicates the number of random coincidences that pass the energy cuts, yields a contamination from random coincidences of $\sim$1 event/day, that is essentially negligible if the radon levels are high enough.
The concentration of ^{238}U can be inferred from the radon data, using the $^{214}Bi(\beta)^{214}Po(\alpha)$ correlation and assuming secular equilibrium. A fit of the $^{214}Bi(\beta)^{214}Po(\alpha)$ count rate decay was done with a decaying exponential with the radon mean life (5.5 days) plus a constant, that is the residual count rate which comes from the radon decaying inside the scintillator at a constant rate [53]. The ultimate plateau of 1.5 $^{214}Bi(\beta)^{214}Po(\alpha)$ events/day in the CTF inner vessel corresponds to an equivalent ^{238}U contamination of $(3.5 \pm 0.7) \times 10^{-16}$ g/g. This would yield $\sim$120 counts/day from every isotope in the chain in the BOREXINO inner vessel.
Finally it was demonstrated that nitrogen stripping with high purity nitrogen has been very effective in eliminating krypton [53].

The borexino experiment

4.1 Background

With a count rate lower than 50 events/day from solar neutrinos, the limiting factor to the BOREXINO sensitivity is the signal-to-background ratio. The background requirements to have a S/B ratio equal 1 are very stringent: the rate must not be higher than 0.5 events/day/ton, or 5×10^{-8} Bq/kg, in the Neutrino Window 250-800 KeV.
It is natural to distinguish the background in an internal and an external background, according to the position of the background source inside or outside the scintillator volume. The next sections illustrate the main background sources and estimate the expected rates, in both cases.

4.1.1 External background

By *external* background we refer to any background due to γ radioactivity in the materials outside the inner vessel, such as the construction materials and the surrounding rocks, as well as the cosmic ray interactions in the underground environment.
An important role in the detector design is played by the need to screen the fiducial volume from this kind of background. This impacts the architectural design and demands extraordinary care in the selection of the materials, by characterization of radiopurities.

The major γ -ray background arises from the naturally occurring radioactivity in the rock environment and in any outer parts of the detector, such as the PMTs , the light concentrators, the ancillary parts for the nylon vessels, the SSS and so on.
The detailed structures of the radioactive decay chains of ^{238}U and ^{232}Th are shown in figure 4.1 and figure 4.2. Each chain contains several γ -emitting daughters. The overall γ spectrum for both families is shown in figure 4.3, where secular equilibrium is assumed within the chain. The most relevant γ peaks are ^{208}Tl (2.6 MeV) and ^{228}Ac (0.9 MeV) in the thorium chain and the two ^{214}Bi lines (1.7 and 1.1 MeV) in the uranium chain.
^{40}K is also a concern for external background, with its 1.46 MeV γ line (10.7% B.R.). Although potassium is a widespread contaminant, due to its chemical affinity with sodium, the radioactive isotope ^{40}K has a relatively low abundance, equal to 0.0117% and can be a problem only in sources close to the inner vessel, such as the nylon endcaps.
Another potential danger comes from ^{60}Co : it can be typically found in stainless steel and produces two γ lines with energies of 1.33 and 1.17 MeV. The decay schemes for ^{40}K and ^{60}Co are shown in figure 4.4.

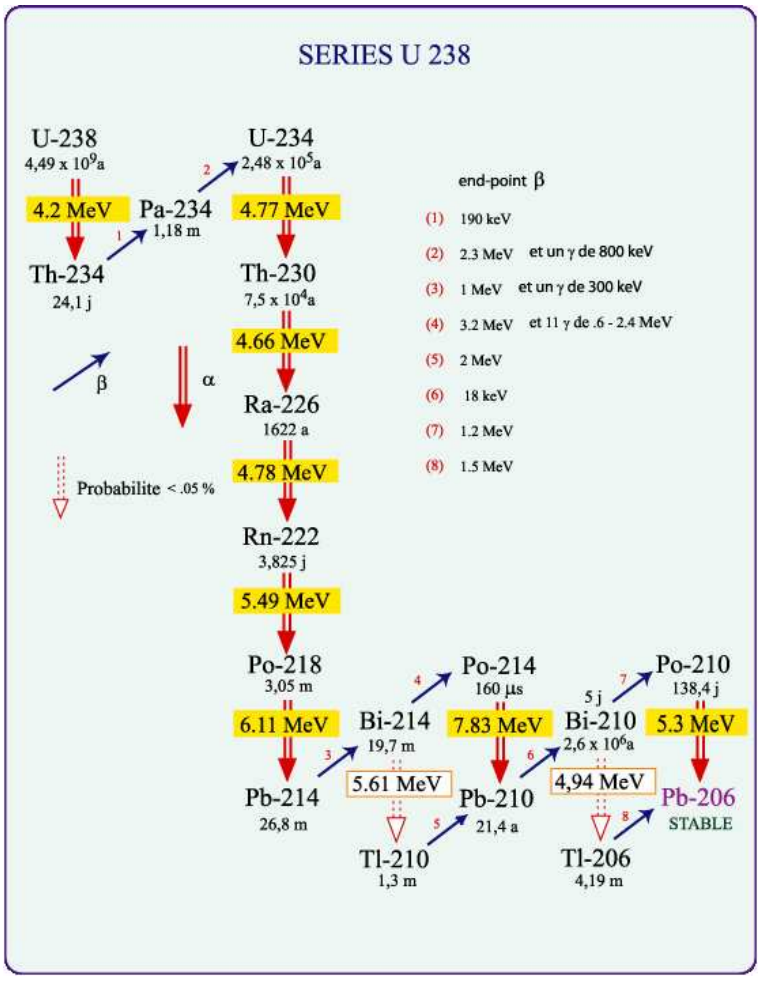

FIGURE 4.1: ^{238}U RADIOACTIVE CHAIN.

4.1.1.1 SOURCES

All detector components, e.g. the phototubes, the vessel material and the buffer fluids, are the major source of external background. Table 4.1 lists, for each material, its radioactive impuriy, the total mass employed, and the resulting activity, considering only the γ -emitting decays.

The nylon vessel is extremely thin and is made with a very low radioactivity material, so is contributes much less than its auxiliary supports. In particular, the steel supports of the outer vessel, cause a localized event distribution, since they are near the north and south poles of the Outer Vessel. For the PC buffer contamination, we assume a value ten times higher than the contamination of the active PC scintillator. Even in this conservative assumption, the radiopurity values are better than for the water produced in the purification

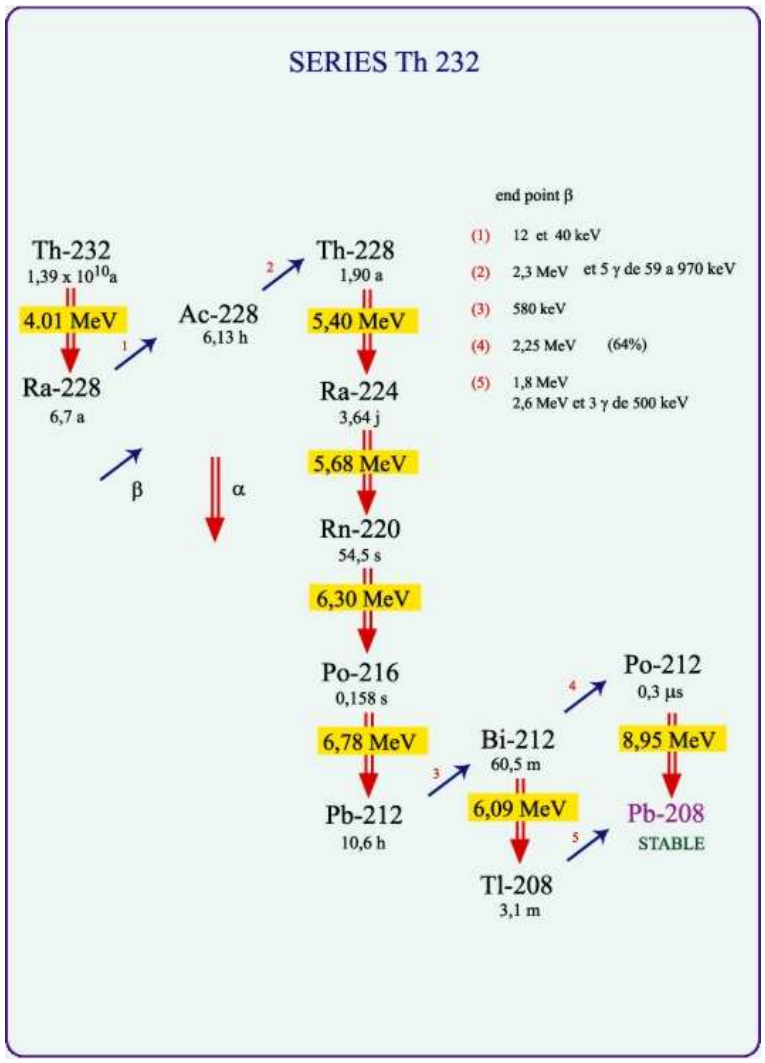

FIGURE 4.2: ^{232}Th RADIOACTIVE CHAIN.

plant[1]. The PMTs contribute the most to the external γ activity, even if the chosen glass bulb has a particularly high radiopurity level (1/10 that of normal glass). The light concentrators are made from aluminium in order to resist the chemical aggression of PC and have a high contamination from ^{232}Th . They have a lower activity than the PMTs , but they are closer to the detector center, so the expected event rates in the scintillator volume are comparable. Finally the SSS is further away from the center so it contributes less than the PMTs .

[1]This was one of the reasons for choosing PC as the buffer material.

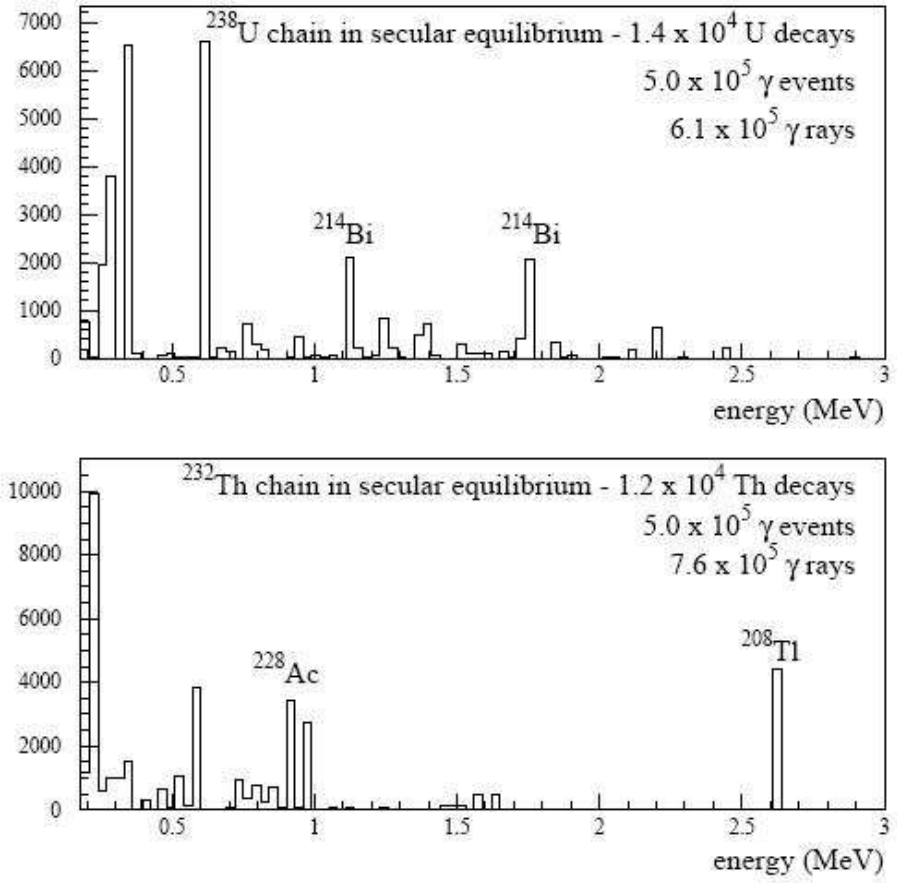

FIGURE 4.3: γ SPECTRA OF THE ^{238}U AND ^{232}Th FAMILIES, IN THE HYPOTHESIS OF SECULAR EQUILIBRIUM WITHIN THE CHAINS. FOR EACH DECAY OF THE PROGENITOR, THERE ARE, ON AVERAGE, 3.62 EVENTS WITH γ EMISSION IN THE ^{238}U CHAIN AND 4.14 IN THE ^{232}Th CHAIN. A GOOD PORTION OF THESE EVENTS EMIT MULTIPLE γ 'S, HENCE THE TOTAL AVERAGE NUMBER OF γ -RAYS PRODUCED PER EACH DECAY OF THE PROGENITOR IS 4.4 IN THE ^{238}U CHAIN AND 6.3 IN THE ^{232}Th CHAIN.

Figure 4.5 shows the distribution of these external γ sources inside the detector.

The γ activity emanated from the rock walls of the laboratory is another source of external background. The total measured flux is 1.5×10^8 γ $/m^2/$d; however among these, the only penetrating components are a few high energy lines, mainly from ^{208}Tl , ^{214}Bi and ^{40}K , that contribute 54% of the total flux (see table 4.2).

4.1.1.2 EXPECTED γ RATES IN THE SCINTILLATOR

The calculation of the expected external background rates inside the BOREXINO detector requires a detailed Monte Carlo propagation of the γ -rays from their origin to the active detector volume. The propagation of this γ background was simulated with the GENEB code

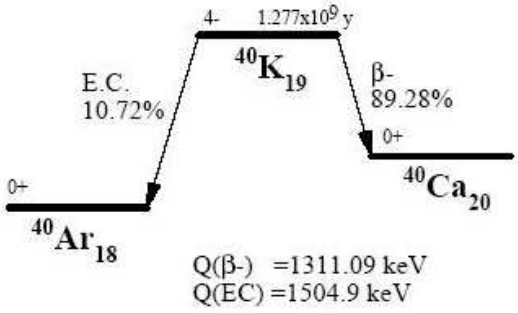

(a) Figure 4.4: Decay scheme for ^{40}K .

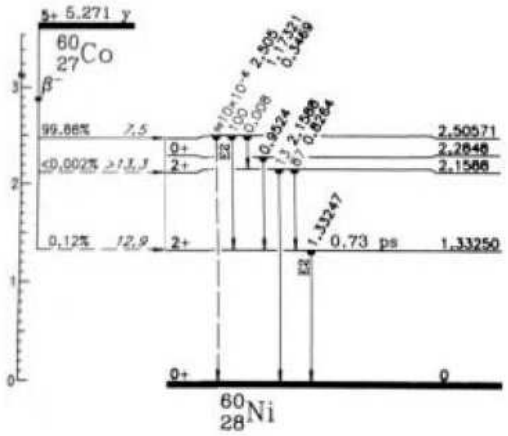

(b) Figure 4.4: Decay scheme for ^{60}Co .

Detector Component	^{238}U ***[g/g]***	^{232}Th ***[g/g]***	K_{nat} ***[g/g]***	***Mass [g]***	***Activity [γ /d]***
Nylon vessel	2×10^{-12}	4×10^{-12}	1×10^{-8}	3.2×10^{4}	0.5×10^{3}
IV nylon endcaps	5×10^{-11}	2×10^{-12}	1×10^{-6}	2.1×10^{4}	1.0×10^{4}
OV steel endcaps	1×10^{-9}	2×10^{-9}	7×10^{-8}	1.5×10^{4}	1.5×10^{5}
PC buffer	1×10^{-15}	1×10^{-15}	1×10^{-12}	$1000\ m^3$	5.0×10^{3}
^{222}Rn in buffer		1 mBq/m^3		$1000\ m^3$	2.2×10^{5}
Light concentrators	1×10^{-8}	1.3×10^{-7}	6×10^{-6}	6×10^{6}	2.6×10^{8}
PMTs	3×10^{-8}	1×10^{-8}	2×10^{-5}	9×10^{6}	1.2×10^{9}
SSS	7×10^{-10}	3×10^{-9}	7×10^{-8}	7×10^{7}	1.1×10^{9}

Table 4.1: Radioactive impurities in the Borexino materials, contributing to the external background. All the quoted radiopurity values are results from measurements, except the values for the PC buffer, that are conservative assumptions.

and the resulting rates are presented in table 4.3, for the 250 keV-800 keV energy window.

The external background depends not only on the materials radiopurity but also on the position resolution of the detector. Each γ ray propagating through the detector generates an electromagnetic shower and deposits its energy in several different interaction points[2]. While a few high energy γ rays can reach the scintillator with their full energy, most of the external background consists of tail of electromagnetic showers that start outside the inner

[2]The typical average value of an electromagnetic shower extension is of the order of ~40 cm.

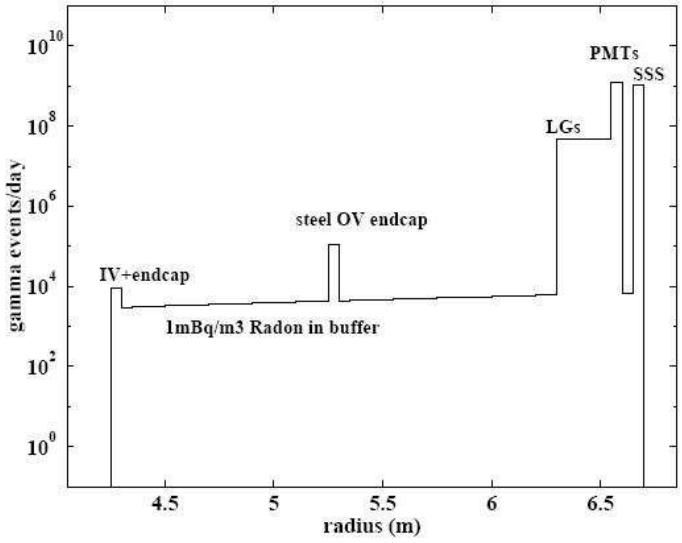

FIGURE 4.5: RADIAL DISTRIBUTION OF EXTERNAL γ SOURCES IN BOREXINO , IN THE REGION BETWEEN THE INNER VESSEL AND THE STAINLESS STEEL SPHERE. IV AND OV ARE THE INNER AND OUTER VESSELS, LGS ARE THE LIGHT CONES, PMTS THE PHOTOTUBES AND SSS THE STAINLESS STEEL SPHERE.

Isotope	***Energy [MeV]***	***Flux*** $[m^{-2} \cdot d^{-1}]$
^{40}K	1.460	3.8×10^7
^{214}Bi	1.120	1.4×10^7
^{214}Bi	1.764	1.7×10^7
^{228}Ac	0.911	0.48×10^7
^{208}Tl	2.614	1.35×10^7
Total		8.7×10^7

TABLE 4.2: γ RAY FLUX FROM THE ROCK SURROUNDING THE LABORATORY TUNNEL.

vessel and contribute only with low energy interactions in the most external regions of the sensitive volume. The position of these external background event is not that of a point-like interaction, as it is for or α or β events, but it can be described as a shower energy-weighted "*center of gravity*", where each interaction point is weighted by the number of detected photoelectrons it originates. The event position provides therefore an important handle to identify and reject these background events with a "*fiducial volume*" cut.
The effects of this volume cut are quoted in table 4.3: the external background rates are quoted in the entire scintillator volume (300 t) and in three *reduced* volumes (200, 160 and 100 t).

The radial distribution of these events (see figure 4.6(b)) and the comparison of the

Detector component	*Scintillator volume 100 ton*	*Scintillator volume 160 ton*	*Scintillator volume 200 ton*	*Scintillator volume 300 ton*
Nylon vessel	0.002	0.03	0.4	56
IV /OV endcaps	0.016	0.91	9.1	955
PC buffer	0.017	2.5	22	1453
Light concentrators	0.054	2.3	18	896
PMTs	0.081	3.6	28	1294
SSS	0.005	1.6	12	496
Total	0.18 ± 0.05	11 ± 0.4	89 ± 1	5163 ± 8

TABLE 4.3: EXPECTED RATES OF EXTERNAL γ BACKGROUND IN THE NEUTRINO ENERGY WINDOW, IN THREE FIDUCIAL VOLUMES AND IN THE WHOLE SCINTILLATOR VOLUME (300 TON). THE REPORTED VALUES ARE QUOTED IN EVENTS/DAY.

expected background rates with the SSM prediction (~0.05 neutrino events/day/ton), shows that the external background has a very steep radial dependence, going from prohibitive in the whole scintillator volume to negligible values in the last 100 ton fiducial volume.

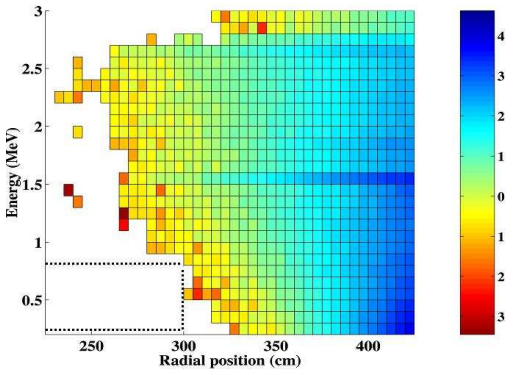

(a) FIGURE 4.6: MONTE CARLO SIMULATION OF THE EXTERNAL BACKGROUND, CORRESPONDING TO 10 DAYS OF DATA ACQUISITION. PLOTTED IS THE ENERGY (MEV) VS. THE DISTANCE FROM THE CENTER OF THE INNER VESSEL (CM). THE DOTTED BOX AT THE LOWER LEFT CORRESPONDS TO THE WINDOW OF INTEREST FOR ^7Be NEUTRINOS IN BOREXINO . THE COLOR CODE ON THE RIGHT IS THE $\log_{10}$ OF THE NUMBER OF EVENTS.

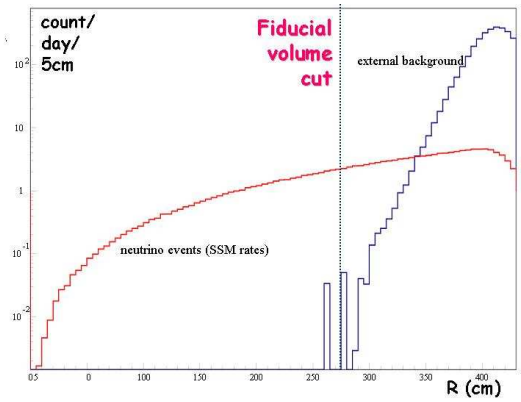

(b) FIGURE 4.6: RADIAL DEPENDENCE OF THE EXTERNAL BACKGROUND COMPARED TO THE NEUTRINO SIGNAL.

The design value of the BOREXINO fiducial mass is therefore indicatively fixed at 100 ton, corresponding to a sphere with 3 m of radius. It can, in principle, be larger, and this

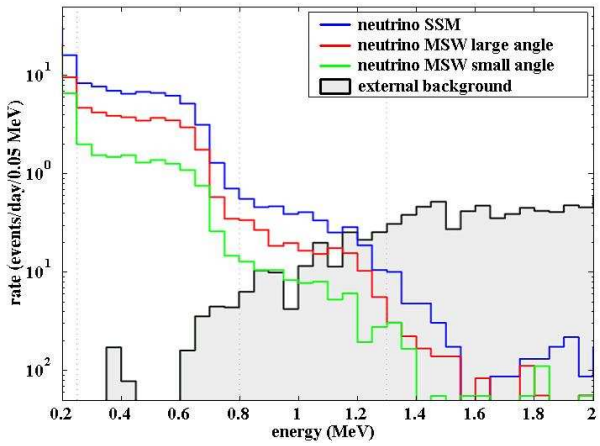

FIGURE 4.7: ENERGY SPECTRUM OF NEUTRINO SIGNAL AND EXTERNAL BACKGROUND IN A 100 TON FIDUCIAL VOLUME, IN A DETECTOR WITH PERFECT SPATIAL RESOLUTION, ACCORDING TO THE RADIOPURITY LEVELS IN TABLE 3.4. THE INTEGRATED COUNT RATES IN DIFFERENT ENERGY WINDOWS AND WITH ALTERNATIVE FIDUCIAL VOLUME CUTS ARE REPORTED IN TABLE

would lead to a higher neutrino event rate. The final value will be defined by the external background rates that will be measured during data-taking.

4.1.2 INTERNAL BACKGROUND

As internal background, we consider all the background events from internal radioactivity, intrinsic to the scintillator. Even if it has a much lower activity (see table 4.6) than external background, internal background is the major concern for the experiment. If the fiducial volume cut used to reject external backgrounds is very powerful and could be made even more restrictive by shrinking the fiducial volume, the internal radioactivity is instead virtually unshieldable and undistinguishable from neutrino events and it can be really reduced only by purification of the scintillator (distillation, water extraction, solid column purification, and nitrogen stripping).

4.1.2.1 SOURCES

The most significant sources of internal activity are the β decays of ^{14}C , an integrant part of the scintillator molecules, and the α , β and γ decays of the radioactive impurities present as trace elements, in particular ^{238}U , ^{232}Th and ^{40}K .

Since our organic liquid scintillator is predominantly composed of carbon, the main internal background at low energies is the intrinsic concentration of the radioisotope ^{14}C . This isotope decays producing a continuous β spectrum with an endpoint at 167 KeV. Since these β events are indistinguishable from the low energy neutrino scattering events, the only way to reject this background is through an energy threshold cut. Since the ^{14}C event rate is several orders of magnitude higher than the neutrino rate, the energy threshold is

established at 5 σ above the β spectrum endpoint. Here σ is the energy resolution of the detector and it is given by:

$$\frac{\sigma(E)}{E} = \frac{\sqrt{n(E)}}{n(E)} = \frac{1}{\sqrt{NE}} \tag{4.1}$$

where $n(E)$ is the number of photoelectrons detected at energy E and N is the number of photoelectrons per MeV. From Monte Carlo simulations and comparisons with CTF data, we know that N is about 400, so:

$$\sigma(E)/E = 13\% \qquad \text{at 150 KeV} \tag{4.2}$$

The energy threshold is then fixed at 250 KeV. Assuming a ^{14}C /^{12}C contamination of 10^{-18} (design value) the residual number of event mimicking the neutrino signal is 0.3 events/day, including the effect of DAQ pile-up[3]of two successive ^{14}C events.

Tables 4.4 and 4.5 show the expected internal background rates in BOREXINO due to the isotopes in the ^{238}U and ^{232}Th chains. The energies of the β particles are distributed from 0 to 2.2 MeV and the energies of the γ -rays go from 0 to 3.1 MeV. The α particles have, instead, higher energies, from 4.0 MeV to 8.8 MeV, but, due to scintillation quenching[4], they produce light pulses with β -equivalent energies from 260 KeV to 990 KeV. As a result, an α with energy around 5 MeV resembles a 500 KeV electron energy deposit, thus appearing in the neutrino window.
The background rates reported in these tables are quoted assuming a contamination of 10^{-16} g/g both for uranium and thorium. This residual background can be further reduced only offline, via some data analysis cuts. These background-rejection methods are described in the next section, and their efficiency is also reported in tables 4.4 and 4.5.

In the uranium chain, it is important to single out ^{222}Rn as a critical item. Radon is a noble gas, chemically inert and with a great capacity of diffusion in air and through matter. Moreover, since it also fairly long-lived ($\tau_{1/2}$= 3.83 days) it can be far out of equilibrium with the rest of the uranium chain. Therefore, if radon diffuses out of the nylon vessel into the scintillator or if it originates from the outside and diffuses through the nylon, there might be an elevated ^{222}Rn concentration - compared to the amount of ^{238}U .
This was the limiting factor in the measurement of the uranium concentration during the CTF 1 campaign: our measurement was only the equilibrium "floor level" for ^{222}Rn in the detector.

A different story is ^{40}K . This isotope has an abundance of 0.0117 % in natural potassium and decays by two modes: via β^- with a probability of 89.3% and an endpoint of 1311 KeV or via electron capture with a probability of 10.7% and the emission of a 1461 keV γ -ray from the first excited state of ^{40}Ar . Neither pulse-shape discrimination or the delayed coincidences method can be used to reject this background. A possible ^{40}K rejection method could be the spectral identification of the 1461 keV γ -ray and the statistical subtraction of the β^- counts in the neutrino window. However, this will ultimately depend on the rates of the other background sources in that energy window (in particular ^{234}Pa of the ^{238}U chain).

Finally accidental exposure to air can introduce also ^{85}Kr in the scintillator, as occured in CTF 1. Krypton is a noble gas; the ^{85}Kr isotope is not present in nature but it is present

[3] *Pile-up* is a coincidence event composed by two ^{14}C decays reconstructed in the fiducial volume and in a coincidence time window less than about 100 *ns* , so that they can not be disentangled offline.

[4] In liquid scintillators, the light output is quenched by a factor of about 10 for α particle scintillation. See also section 3.3.5.

Isotope	***Decay type***	***Energy [KeV]***	***Weight [%]***	***Rates [ev/day]***			
				No Cuts	***DC***	***PSD***	***SS***
^{238}U	α	280	77	10.6	10.6	1.1	1.1
	$\alpha+\gamma$	278	23				
^{234}U	α	338	72	10.6	10.6	1.1	1.1
	$\alpha+\gamma$	386	28				
^{230}Th	α	330	76.3	10.6	10.6	1.1	1.1
	$\alpha+\gamma$	371	23.4				
^{226}Ra	α	339	94.5	10.6	10.6	1.1	1.1
	$\alpha+\gamma$	321	5.4				
^{222}Rn	α	417	99.9	10.6	10.6	1.1	0.05
^{218}Po	α	482	99.9	10.6	10.6	1.1	0.05
^{214}Po	α	746	99.99	3.2	0.2	0.02	0.02
^{210}Po	α	395	100	10.6	10.6	1.1	1.1
^{234}Th	β	-	-	0	0	0	0
	$\beta+\gamma$	-	-				
^{234}Pa	β	0-2290	98.6	3.9	3.9	3.9	3.9
	$\beta+\gamma$	760-2290	0.7				
^{214}Pb	β	0-1023	9.4	9.3	9.3	9.3	0.5
	$\beta+\gamma$	290-1023	40.7				
	$\beta+\gamma$	350-1023	47.3				
	$\beta+\gamma$	430-1023	2.5				
^{214}Bi	β	0-3230	19	0.5	0.02	0.02	0.02
^{210}Pb	β	-	-	0	0	0	0
	$\beta+\gamma$	-	-				
^{210}Bi	β	0-1116	100	6.4	6.4	6.4	6.4

TABLE 4.4: EXPECTED INTERNAL BACKGROUND RATES IN A 100 T FIDUCIAL MASS AND IN THE Neutrino Window (250-800 KEV) DUE TO THE ISOTOPES IN THE ^{238}U CHAIN, ASSUMING A CONTAMINATION OF 10^{-16} G/G. THE BACKGROUND EVENTS WERE SIMULATED WITH THE GENEB AND THE TRACKING CODE. AN EFFICIENCY OF 95% IS ASSUMED FOR THE DELAYED COINCIDENCES (DC) AND STATISTICAL SUBTRACTION (SS) CUTS. FOR THE PULSE-SHAPE DISCRIMINATION (PSD) CUT, AN EFFICIENCY OF 90% IS ASSUMED.

in the atmosphere as a product of nuclear fission in nuclear reactors. Its activity in central Europe is $\sim$1Bq/m^3 . It decays with 99.57% branching ratio to ^{85}Rb emitting a β particle with 687 KeV of endpoint and 10.7 years of meanlife. The krypton could be removed by the nitrogen stripping.

Isotope	Decay type	Energy [KeV]	Weight [%]	Rates [ev/day] No Cuts	DC	PSD	SS
^{232}Th	α	266	77	3.4	3.4	0.3	0.3
	$\alpha+\gamma$	330	23				
^{228}Th	α	409	72.7	3.5	3.5	0.4	0.02
	$\alpha+\gamma$	483	26.7				
^{224}Ra	α	440	94.5	3.5	3.5	0.4	0.02
	$\alpha+\gamma$	542	5.5				
^{220}Rn	α	519	99.9	3.5	3.5	0.4	0.02
	$\alpha+\gamma$	-	-				
^{216}Po	α	590	99.9	3.5	3.5	0.4	0.02
	$\alpha+\gamma$	-	-				
^{212}Po	α	989	63	0	0	0	0
^{212}Bi	α	492	9.7	1.3	1.3	0.1	0.01
	$\alpha+\gamma$	527	25.2				
^{228}Ra	β	-	-	0	0	0	0
	$\beta+\gamma$	-	-				
^{228}Ac	β	0-2180	10	0.3	0.3	0.3	0.3
	$\beta+\gamma$	330-2180	9.6				
	$\beta+\gamma$	480-2180	6.7				
^{212}Pb	β	571	13	3.1	3.1	3.1	0.2
	$\beta+\gamma$	332-571	82				
	$\beta+\gamma$	155-571	5				
^{212}Bi	β	0-2251	40.3	0.8	0.04	0.04	0.04
	$\beta+\gamma$	700-2251	4.4				
^{208}Tl	β	-	-	0	0	0	0
	$\beta+\gamma$	-	-				

Table 4.5: Expected internal background rates in a 100 t fiducial mass and in the Neutrino Window (250-800 KeV) due to the isotopes in the ^{232}Th chain, assuming a contamination of 10^{-16} g/g. The background events were simulated with the GENEB and the tracking code. An efficiency of 95% is assumed for the delayed coincidences (DC) and statistical subtraction (SS) cuts. For the pulse-shape discrimination (PSD) cut, an efficiency of 90% is assumed.

4.1.2.2 Rejection methods

If we assume secular equilibrium for the uranium and thorium chains and consider a level

	Rates [ev/day]			
α sources	***No Cuts***	***DC***	***PSD***	***SS***
^{238}U	77.4	74.4	7.7	5.6
^{232}Th	18.7	18.7	2.0	0.8
Total α	96.1	93.1	9.7	6.4
β source	***No Cuts***	***DC***	***PSD***	***SS***
^{238}U	20.1	19.6	19.6	10.8
^{232}Th	4.2	3.4	3.4	0.5
^{40}K	1.5	1.5	1.5	1.5
Total β	25.8	24.6	24.6	12.9
Total	***122***	***118***	***34***	***19***

TABLE 4.6: SUMMARY TABLE FOR THE INTERNAL BACKGROUND IN 100 T FIDUCIAL MASS AND IN THE Neutrino Window . THE RESULTS QUOTED ASSUME SECULAR EQUILIBRIUM AND A CONTAMINATION OF 10^{-16} G/G FOR ^{238}U AND ^{232}Th AND 10^{-14} G/G FOR K_{nat} .

of 10^{-16} g/g for ^{238}U and ^{232}Th contamination and of 10^{-14} g/g for K_{nat} [5], we still have, in the Neutrino Window and in the 100 t fiducial volume, $\sim$26 β +γ events/day and $\sim$96 α events/day. This residual background can be further reduced only offline, during data analysis. Three standard techniques are used:

- *Delayed coincidences:* both this method and the statistical subtraction method are based on the detailed structures of the radioactive decay chains of uranium and thorium. In a radioactive chain the decay of a father in a daughter has the time constant of the meanlife of the second isotope. If this meanlife is much shorter than the inverse of the random background rate (for the signal given by the decay of the daughter) the sequence can be tagged very effectively by means of the only delay time. Moreover, the use of an energy cut can improve the rejection efficiency.
  In the uranium and thorium chains there are two polonium isotopes with a half-life small enough to be observed as a delayed coincidence: ^{214}Po ($\tau_{1/2}$= 164 μs , father ^{214}Bi) in the ^{238}U chain and ^{212}Po ($\tau_{1/2}$= 300 ns, father ^{212}Bi) in the ^{232}Th chain. An identification efficiency of 95% reduces the background events to $\sim$25 β +γ events/day and $\sim$93 α events/day (see table 4.6).

- *Statistical subtraction:* once the correlated $^{214}Bi(\beta)^{214}Po(\alpha)$ and $^{212}Bi(\beta)^{212}Po(\alpha)$ events have been identified, the activities of these particular isotopes and of the chain segment with which they are in equilibrium[6]are established. This means the ^{226}Ra - ^{214}Po segment for the uranium chain and the entire segment following ^{226}Ac for thorium. The knowledge of the activity of these isotopes allows us to statistically subtract the counts due to these events from the measured energy spectrum. This

[5] For uranium and thorium, these levels are supported by the CTF results, but for natural potassium, they are only assumed, due to the lack of measurements with enough sensitivity. In addition, secular equilibrium of the radioactive chains is assumed.

[6] A valid assumption only for the short-lived and non-mobile parent isotopes that precede the coincidence.

subtraction can be done reliably; however, it does not have the event-by-event rejection feature of the DC and PSD cuts. It must be performed last, after sufficient statistics have been accumulated.

- *Pulse-shape discrimination:* this is main rejection method for the background events from the uranium and thorium radioactive decay chains. In organic liquid scintillators α particles have a higher ionization density than electrons or γ -rays, resulting in a greater light emission in the longer time components of the scintillation pulse. The pulse shape is then different between α and β scintillations and the differences in the time distribution tails can be used to discriminate the two particles.
  In CTF simply using the tail-to-total ratio, an a identification efficiency of 90% was reached, allowing a β -misidentification of 5% . The results reported in Table 4.6 are quoted using this conservative estimate, even if, since in BOREXINO we will be able to take into account the whole time distribution and not only a threshold integral, we expect better efficiencies.

The summary of the final internal background rates after the application of all these offline rejection methods is reported in table 4.6. Clearly, we can single out ^{238}U as the most important contaminant and pulse-shape discrimination as the most effective analysis cut.

4.1.3 Cosmogenic backgrounds

Other potential sources of background, of cosmogenic nature, include backgrounds from muons and muon-induced spallation products, neutrons and cosmogenic radioactivity for materials that have been exposed at the surface.

The main issue are the direct muons: the muon flux in the underground laboratories is 1 m^2/h. This means ~5000 muons/day crossing the stainless steel sphere and about the same quantity crossing only the water tank. Being the SSM prediction ~50 neutrino events/day in the 100 t fiducial volume, the rejection level required for this muon induced background is very stringent. The maximum tolerable level of background in the energy window $0.25 \div 1.5$ MeV (less than 0.5 event/day) fixes the efficiency of the muon veto system (see section 3.3.7) to 99.98% of the muon-caused events.

4.1.3.1 Neutron flux from the rock walls

Neutrons are produced in the outer rock layers due to fission and (α , n) reactions on light elements. The measured neutron flux from the rocks of the laboratory is $\sim 3.78 \times 10^{-6}$ n/cm^2/s, 77% of which are thermal. This means about 3×10^6 neutrons/day impinging on BOREXINO . Yet, Monte Carlo simulations proved that the 2 m of water shielding are enough to reduce this flux by a factor 10^8 .

4.1.3.2 γ -rays from capture of cosmogenic neutrons

Ultrarelativistic muons may collide with atomic nuclei in the detector and produce hadronic showers and energetic neutrons. The frequency of these showers is a few 10^{-2} /m of path in water or scintillator. Neutrons are then thermalized by inelastic and elastic collisions and captured by protons in the reaction:

$$n + p \rightarrow {}^2H + \gamma \text{ (2.216 MeV)} \tag{4.3}$$

Neutrons have a capture mean time of about 300 μs in pseudocumene. In BOREXINO , we expect 100 neutrons/day, one third of them in the fiducial volume. Virtually, all these events fall outside the energy range of interest; moreover, they can be completely suppressed by means of the 3 ms time correlation between the neutron capture and the preceding muon event.

4.1.3.3 RADIONUCLIDES PRODUCED BY MUONS IN THE SCINTILLATOR

The hadronic showers which produce the energetic neutrons may also create radioactive nuclei in reactions involving the carbon atoms of the scintillator. The estimate for the total background rate is 30 events/day in the scintillator and 10 events/day in the fiducial volume.

Owing to the high endpoint energies, none of the very short lived isotopes is expected to give a background of more than 1 event/day, even without further cuts. Moreover most resulting isotopes have half-lives of 0.8 s or less and their contribution can still be reduced simply imposing an off-line cut. If a dead time of 3 seconds is imposed after each Cerenkov event, hits from these isotopes are reduced by a factor 15 with only 10 % data loss.

The remaining, longer-lived isotopes are listed in 4.7. The rates at which these cosmogenic nuclides are produced in the fiducial volume are not well known. The rates quoted in this table are extrapolated from the data of an experiment done at CERN [47].

Isotope	$t_{1/2}$	***E/Mev***	***Decay Path***	***Events/day in Fiducial Volume***
^{11}Be	13.8 s	0 - 11.5	β^-	< 0.034
^{10}C	19.3 s	0 - 1.9	β^+ + 0.72 Mev γ	1.95 ± 0.21
^{11}C	20.4 min	0 - 0.99	β^+	14.55 ± 1.49
^{7}Be	53.3 days	0.478	γ	0.34 ± 0.04

TABLE 4.7: LONG-LIVED COSMOGENIC NUCLIDES IN BOREXINO .

Of these, the least problematic is ^{11}Be , for its decays usually yield energies well outside the ^{7}Be neutrino window.

The two carbon nuclides both emit positrons. Since during their production one or two neutrons are emitted and can be captured by protons, ^{10}C can be tagged very well through the clear 2.16 MeV γ ray signature. Any suspected neutrino event may be checked for the presence of a recent nearby neutron capture event. Given the likelihood of convection in the scintillator, the 20 m meanlife of ^{11}C is instead too long for a time correlation with the preceding muon. Though, since it is a β^+ emitter, it deposits in the scintillator an energy in the range of 1-2[7]MeV, shifting the amount of energy hitting the PMTs beyond the neutrino window.

Ironically, ^{7}Be is most troublesome; its monoenergetic decay interferes directly with the ^{7}Be neutrino window. However, it is relieving to note that this isotope should produce background events at the average rate of only one per three days.

[7] Due to the 1.022 MeV positron-electron annihilation energy,

Yet, overall cosmogenic radionuclides should not produce a background greater than 0.5 events/day within the fiducial volume and in the energy range of most interest.

4.1.3.4 Muons and prompt secondaries

Finally the first CTF campaign (CTF 1) showed that the ultrarelativistic muons that cross the detector produce a prompt background of low energy events in the Neutrino Window . These events arise mostly from muons that intersect the non-active buffer region and produce Cerenkov and scintillation light.

In CTF these muon events were selected by their time coincidence with events observed in two external wire chambers. For 75% of events in this sample the reconstructed energies fell outside the interesting range of less than 1 MeV [56].
To select the remaining events various software cuts were applied. Since Cerenkov radiation is directed in a cone in front of the muon and since all muons arrive from above, the pattern of photomultiplier hits resulting from Cerenkov radiation is asymmetric. In addition the Cerenkov radiation produced along the entire track of the muon reaches the photomultiplier tubes over a broad time period. The mean delay time for arriving photons, measured from the very first PMT hit, is on average greater for muon events than for β point-like events (see Figure 4.8(b)). In CTF 1 ~95% of the muon-induced events in the neutrino energy window were recognized through this tests: this gave an overall recognition efficiency of 99% .

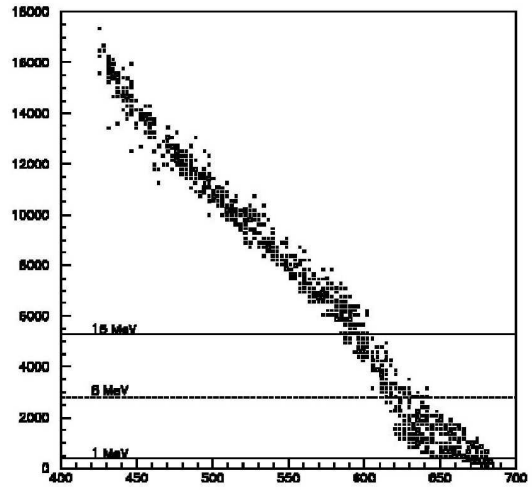

(a) Figure 4.8: monte carlo simulation of the pmts ' total photoelectron yield as a function of muon track impact parameter. The p.e. yield corresponding to 15 MeV, 8 Mev and 1 MeV are shown.

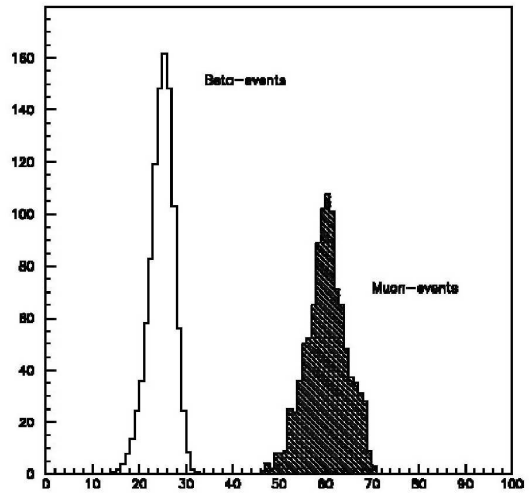

(b) Figure 4.8: mean time distribution (*ns*) of β events and of events due to muon tracks passing through the buffer fluid for a monte carlo simulation.

This result can still be optimized for BOREXINO . The detector is substantially larger than CTF , thus both the light yield of Cerenkov events and the time spread of PMT hits will be greater. If it is conservatively assumed that the time spread can distinguish Cerenkov events

with an efficiency of 95% , a 90% efficiency[8]for the reconstructed energy cut gives, in BOREXINO , an overall efficiency of 99.5% . The remainder ~25 muon events/day still slipping through are then rejected with an hardware veto: the outer muon veto system (see section 3.3.7).

4.2 NEUTRINO SIGNAL IN BOREXINO

Solar neutrino detection in BOREXINO is based on the neutrino elastic scattering reaction $\nu_e + e^- \rightarrow \nu_e + e^-$.

The target electrons are those in the liquid scintillator molecules. The momentum transfer in the elastic scattering of protons or other nuclei is too low to produce charged particles with enough kinetic energy for useful detection.
Since the energy of the incoming neutrinos is much higher than the typical electronic molecular binding energies (a few keV), the electron can then be considered free. The first order Feynman diagrams for $\nu - e$ scattering are shown in figure 4.9(a). The scattering reaction is neutrino flavour insensitive, so charged and neutral currents contribute to the amplitude of the basic reaction. Since only electron neutrinos interact via charged current, the cross section for ν_e -e scattering is larger than that for ν_μ -e , ν_τ -e .

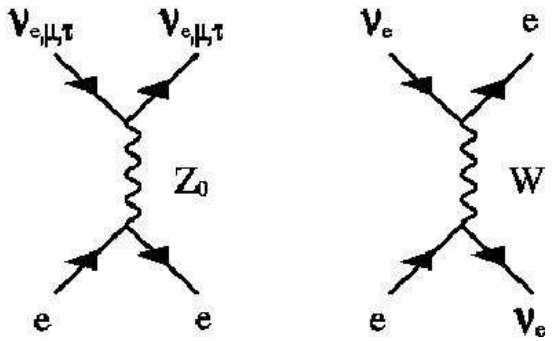

(a) FIGURE 4.9: FIRST ORDER FEYNMAN DIAGRAMS FOR $\nu - e$ ELASTIC SCATTERING. ONLY ELECTRON NEUTRINOS INTERACT VIA CHARGED CURRENT.

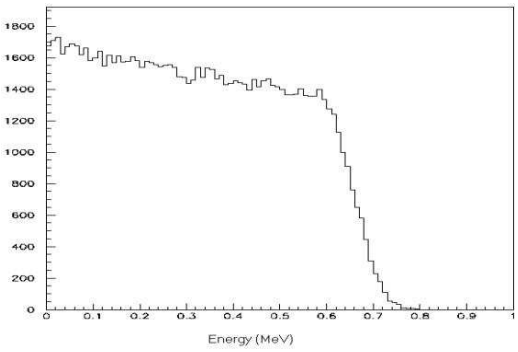

(b) FIGURE 4.9: THE DISTINCTIVE *Compton edge* SIGNATURE FOR THE MONOCHROMATIC ^7Be SOLAR NEUTRINOS IN BOREXINO .

The maximum kinetic energy of the scattered electron is:

$$T_{\max} = \frac{E_\nu}{1 + \frac{m_e}{2E_\nu}} \tag{4.4}$$

where E_ν is the energy of the neutrino. The signal from the monochromatic ^7Be solar neutrinos (862 keV) shows then a distinctive *Compton edge* of the scattered electron at 667 keV, as can be seen in figure 4.9(b).

[8]Only the tracks that barely graze the inside of the SSS are problematic. Monte Carlo simulations show that only tracks with an impact parameter greater than 6.5 m might be confused with neutrino events. Being the SSS diameter 13.7 m, the proportion of such tracks is at worst 10% .

There is also a temporal signature for the solar neutrino flux: the eccentricity of Earth's orbit provokes a seasonal variation of the the total measured rate. This effect is a 7% annual variation of the neutrino rate.

4.3 THE PHYSICS POTENTIAL OF BOREXINO

4.3.1 SOLAR NEUTRINO PHYSICS FROM BOREXINO

The main focus of the physics program for BOREXINO is the measurement of the ^7Be solar neutrino flux and the investigation of neutrino oscillations.

The interaction rate for neutrino electron scattering is given by:

$$R = N_e \int_0^{q_{\max}} \Phi_{\text{Earth}}(q) \left[P_{ee}(q) \cdot \int_0^{t_{\max}} \sigma_e(q,t)dt + \big(1 - P_{ee}(q)\big) \cdot \int_0^{t_{\max}} \sigma_{\mu,\tau}(q,t)dt \right] dq \quad (4.5)$$

where N_e is the electron density in the target material, $\Phi_{\text{Earth}}(q)$ the average solar neutrino flux on Earth, $P_{ee}(q)$ the electron neutrino survival probability, and $\sigma_e(q,t)$ and $\sigma_{\mu,\tau}(q,t)$ are, respectively, the differential cross sections for electron neutrinos and for muon and tau neutrinos[9].

The electron neutrino survival probabilities $P_{ee}(q)$, and therefore the interaction rate 4.5, depend on the allowed Δm^2 and $\tan^2\theta$ parameters. These are inferred from a global analysis of all solar and reactor experimental data and I already anticipated in section 2.6.2, that the LMA solution is now the only allowed solution at 3 σ.
In this scenario, the prediction for the reduced ^7Be ν -e scattering rate,

$$f(^7Be\ ) = \frac{\Phi(^7Be\ )}{\Phi_{\text{BP00}}(^7Be\ )} = 0.64 \pm 0.02\ \ (1\sigma) \quad (4.6)$$

is remarkably precise and remarkably stable. The predicted event rate has a precision of 3% in units of the rate calculated with the BP00 flux and assuming no neutrino oscillations. No more than 40 events/day are expected, approximately 25 of which are from ^7Be neutrinos. Yet, for this solution, the predicted ^7Be day-night asymmetry[10]averaged over a year is too small to be observed. Within the current 3σ allowed oscillation region, the limit on the predicted values of A_{N-D} is:

$$|A_{N-D}(^7Be\ )| < 0.001,\ \ (3\sigma) \quad (4.7)$$

No significant day-night asymmetry nor seasonal variations are then expected for ^7Be neutrino measurements by BOREXINO .

[9] Actually, the lower limit of the rate's integral is a value different from 0 and set by the experiment's trigger threshold.

[10] Due to MSW flavour regeneration in the Earth. This was a strong signature for the LOW solution.

4.3.2 Physics beyond solar neutrinos

BOREXINO can detect electron antineutrinos via their capture on protons in the scintillator:

$$\overline{\nu}_{\mathrm{e}} + p \rightarrow n + \mathrm{e}^{+} \qquad E_{\mathrm{thresh}} = 1.8 MeV \tag{4.8}$$

The positron energy is related to the $\overline{\nu}_{\mathrm{e}}$ energy as: $E(\mathrm{e}^{+}) = E(\overline{\nu}_{\mathrm{e}}) - Q + 1.02$ MeV. The neutron capture induces emission of a 2.2 MeV γ after 0.2 ms. The delayed coincidence between e^{+} and γ provides a definite signature for the detection of $\overline{\nu}_{\mathrm{e}}$.

There are several interesting $\overline{\nu}_{\mathrm{e}}$ sources. Nuclear power reactors are strong sources of antineutrinos, emitted in the β decay of various isotopes produced in the fission of Uranium. These $\overline{\nu}_{\mathrm{e}}$ are produced with a known flux and spectrum, at energies up to 8 MeV. With no active reactor present in Italy, BOREXINO is sensitive to antineutrinos in France, Switzerland and Germany. The predicted eventrate is of about 30 $\overline{\nu}_{\mathrm{e}}$ per year. Evidence for neutrino oscillations would come from the disappearance of these neutrinos and from distortions in their spectral shape.
A measurement of the electron antineutrino flux from natural radioactivity (e.g. ^{238}U and ^{232}Th) in the Earth's crust and mantle [59] would provide important constraints on the heat generation within the Earth and probe the radiochemical composition of Earth. According to the current knowledge of the radiochemical composition of Earth, several tens of $\overline{\nu}_{\mathrm{e}}$ events per year with energies up to 3 MeV are expected in BOREXINO [60].
Finally, no antineutrino emission is expected from the Sun. Possible detection of solar $\overline{\nu}_{\mathrm{e}}$ would be a smoking gun for non-standard neutrino physics.

4.3.3 Supernova neutrino detection in borexino

Intense neutrino and antineutrino fluxes of all flavours are also emitted in supernovae collapses. Type II supernovae result from the gravitational collapse of red giant stars with masses larger than about eight solar masses. Their colossal explosion releases a typical binding energy $\epsilon_B \simeq 3 \times 10^{53}$ ergs. The total light emitted in the supernova outburst is only about 1% of this energy; the remainder 99% comes off in the form of neutrinos, all within a few seconds. These supernovae neutrinos have average energies in the $10 \div 30$ MeV range (see figure 4.10).

The dominant channel for detection of supernova neutrinos in BOREXINO is again the antineutrino capture on protons (equation 4.8). The signature from these events is a delayed coincidence between the prompt positron and the 2.2 MeV γ ray emitted in the neutron capture on a proton (0.2 ms). This signature is essentially free of background within the few second time interval of a supernova explosion. An event rate of about 80 neutrinos are expected in BOREXINO from a typical supernova collapse in the center of our galaxy. More details can be found in [57, 58].

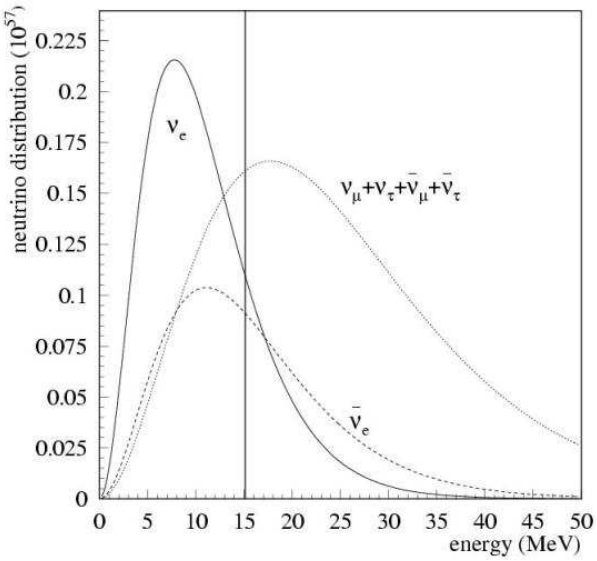

FIGURE 4.10: ENERGY SPECTRA OF THE NEUTRINOS AND ANTINEUTRINOS EMITTED IN A SUPERNOVAE COLLAPSE.

Daq and data handling

5.1 The electronic chain

BOREXINO electronics can be divided into two independent sub-systems: the inner and the outer detector[1] read-outs. A basic block diagram of our electronics system and DAQ structure is shown in figure 5.1.

The inner detector read-out, often called the Laben system, includes 14 identical racks that perform HV distribution, complete analog signal handling, digitalization, data processing and data transfer to the main DAQ cpu. Each rack houses:

- a patch panel with the electrical connections between the water-proof cables of the PMTs and the analog electronics;
- a resistive fan-out (the test and calibration signal distributor), which allows the possibility of injecting a charge into the calibration input of each front-end board;
- a low voltage power supply;
- 14 high energy summers;
- 14 analog front-end boards;
- 20 digital Laben boards;
- a high voltage C.A.E.N. mainframe and 7 HV boards.

The read-out and digitalization electronics of the outer muon PMTs is instead an independent system. The dedicated outer muon rack houses:

- 9 high voltage decoupler units;
- 14 front-end boards;
- 1 standard C.A.E.N. TDC unit.

[1] The former is composed of the 2200 PMTs mounted inside the sphere: 1800 for neutrino detection and 400, without the light concentrator, for the inner muon veto system. The latter is made up of the 208 PMTs mounted outside the sphere, in the water tank.

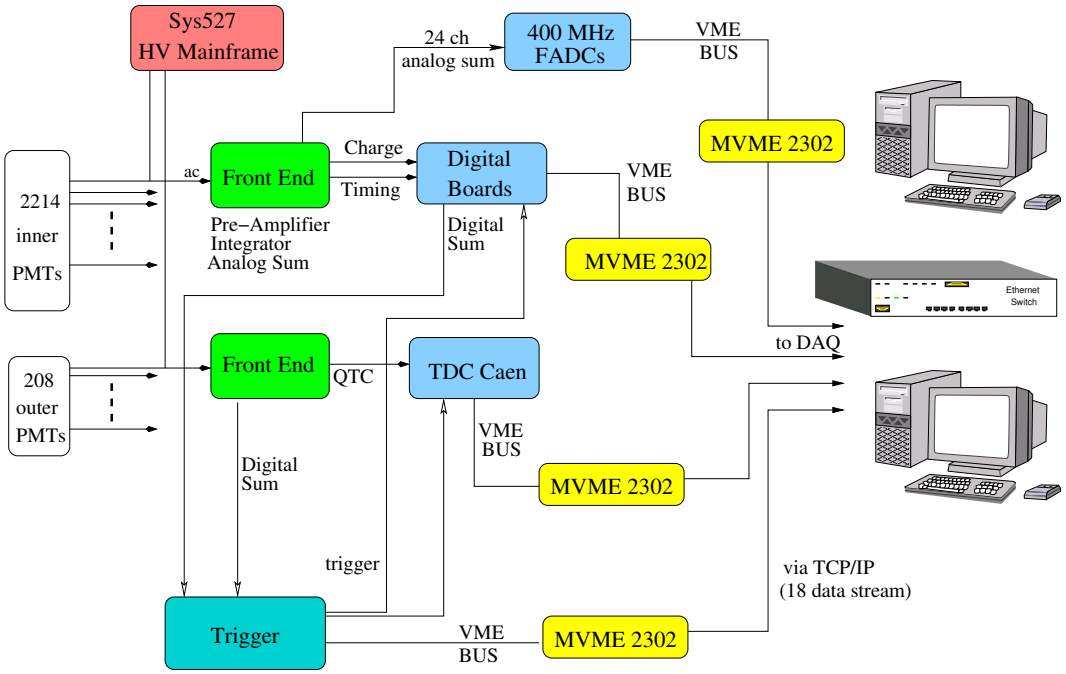

FIGURE 5.1: BLOCK DIAGRAM OF THE ELECTRONICS SYSTEM AND DAQ STRUCTURE FOR THE BOREXINO DETECTOR.

5.1.1 THE EXPECTED PMT 'S SIGNAL

The PMTs used in BOREXINO have been already described in section 3.3.6. The signals corresponding to single photoelectrons released from the PMT photocatode have a mean amplitude of ~12 mV, a width of 15 *ns* and, assuming an effective PMT gain of 10^7 , correspond to a charge of 1.6 pC. A typical single photoelectron signal is shown in figure 5.2.

Our electronics must be able to detect and characterize three different signals:

1. single photoelectrons signals, due to scintillation light or to the few KHz of PMT 's dark noise;

2. signals corresponding to multiple hits, two or more photoelectrons on the same PMT , mostly due to scintillation events. The multiple hit probability in BOREXINO is in the order of 10% for 1 MeV event in the detector center, increasing with the scintillation distance from the detector center and the deposited energy. In case of multiple hits, the delay time between the photoelectrons is related to the spread of the photons pathlength from the production point to the PMT . This spread is due to the different photon interaction mechanisms (elastic scattering and absorption-remission) within the scintillator and buffer liquid. This delay can affect the charge measurement and the effect must be taken into account for a good energy reconstruction.

3. signals, single or multiple hits, corresponding to time correlated events originated by the radioactive decay of a nuclide producing a dautgher with a mean life of hundreds of

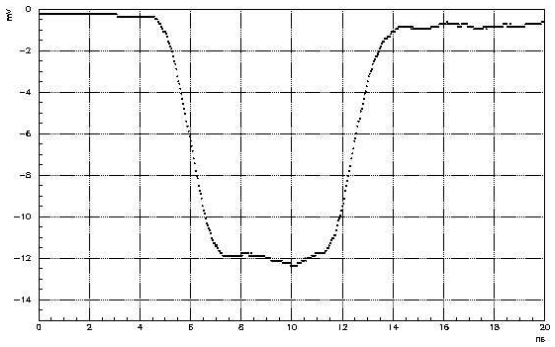

FIGURE 5.2: PULSE GENERATOR SIGNAL EMULATING THE MEAN PHOTOELECTRON SIGNAL AT THE INPUT OF THE FRONT END. THE SIGNAL HAS A WIDTH OF 7 *ns* , A RISE TIME AND A FALL TIME LESS THAN 2 *ns* , AND AN AMPLITUDE OF 12 *mV*.

ns or μs . The identification of these fast correlated events is one of the most powerful methods for our background tagging.

5.1.2 THE FRONT END ELECTRONICS

5.1.2.1 THE INNER DETECTOR FRONT END ELECTRONICS

Each photomultipler is connected to two cascaded electronic networks: the front end circuit, where the handling of analog signals take place, and the digital circuit, that provides to the digitalization of the energy and time informations.

The main functions of the front end circuit are:

- to connect the high voltage, generated by an external power supply, to a proper connector, in order to send it, via a coaxial cable, to the remote PMT voltage divider;
- to decouple the PMT signal from the high voltage that travels on the same coaxial cable, filtering also the noise eventually coming from the HV power supply;
- to provide the best impedance matching to the 50 Ω coaxial cable over a wide frequency range;
- to provide two outputs for each PMT : the timing and the charge signals. The former is an amplified copy of the PMT signal and is used for the time measurement; the latter, an integrated copy of the PMT signal, gives back the charge information;
- to perform the analog sum of the 160 photomultiplier signals of one electronic rack;
- to allow for the possibility of connecting external pulses for tests and calibrations.

The front end electronics is organized in boards. Each board contains 12 electronic chains, a circuit providing the analog sum of the PMTs signals and a circuit distributing a calibration signal in parallel to all the channels. One crate allocates 14 boards, corresponding to 168 channels. Actually only 160 are used.

The input connections of the single coaxial cable carrying both the PMT signal and the operating high voltage are on the rear side of the board, together with the 12 wires high voltage connector (see figure 5.3(b)). The timing and charge outputs, the analog sum of the 12 signals and the calibration distributor input are instead on the front side (see figure 5.3(a)).

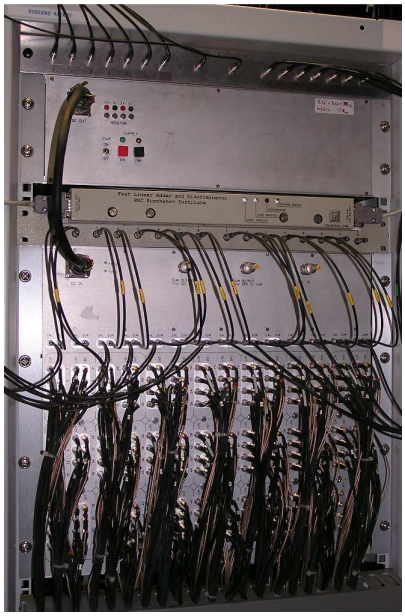

(a) FIGURE 5.3: FRONT VIEW OF ONE ELECTRONIC RACK. FROM THE TOP WE CAN SEE: THE CALIBRATION DISTRIBUTOR PATH PANEL, THE LOW VOLTAGE POWER-SUPPLY, THE FADC MODULE AND THE FRONT-END CRATE. THE OUTPUT SIGNALS OF THE 12 FRONT END BOARDS ARE ALREADY CONNECTED.

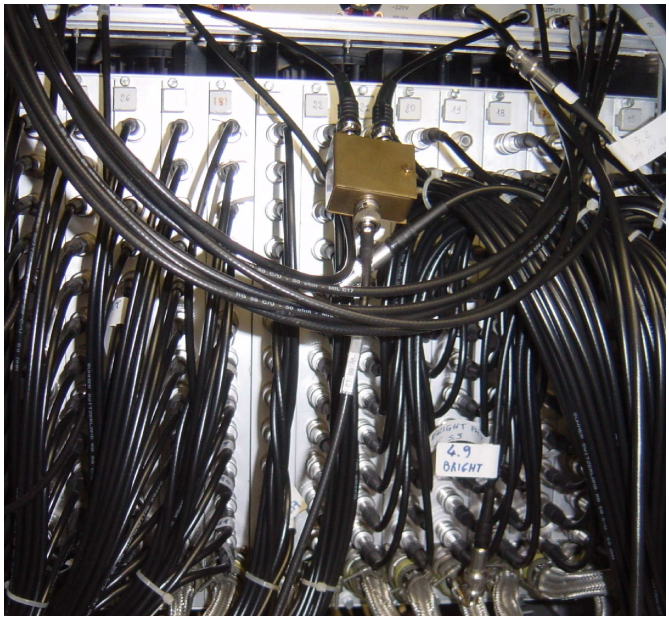

(b) FIGURE 5.3: REAR VIEW OF ONE FRONT-END CRATE. THE BLACK CABLES ARE THE HV CABLES; THE SILVER ONES, ON THE BOTTOM, ARE THE HV SUPPLY CABLES.

The timing output is a fast amplified copy of the input signal. Its gain is ~20 (see figure 5.5(a)): the single photoelectron output is ~230 mV and has an expected signal to noise ratio of about 4×10^{-3} [2].

The charge signal is instead the output of a gateless charge integrator [61]. The principle of operation of this integrator is strongly related to the particular features of the input

[2] The rms noise was measured in absence of input.

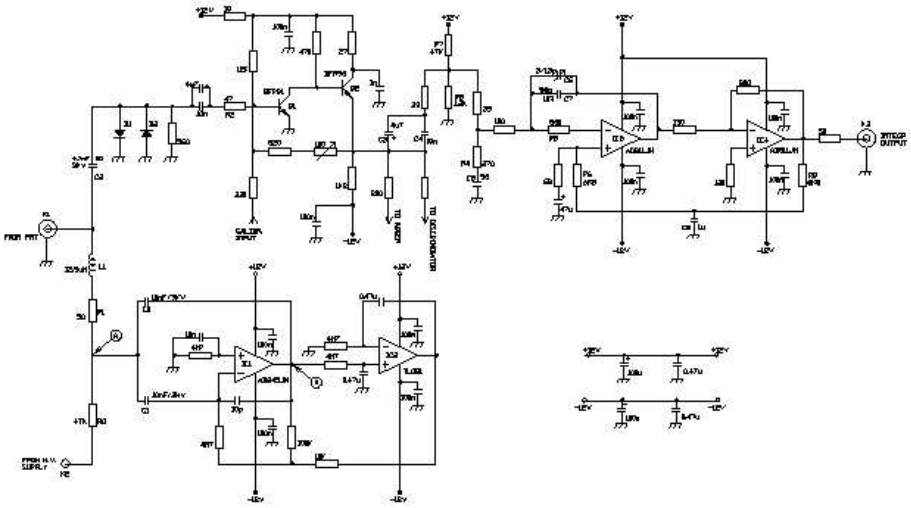

Figure 5.4: borexino front-end circuit schematic. The 12 channels front end board is obtained by repeating 4 times a 3 channels basic scheme and then completing the sum and the calibration networks.

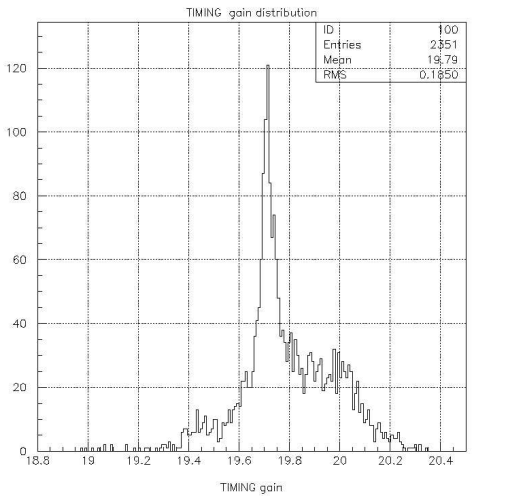

(a) Figure 5.5: distribution of the timing output gain values.

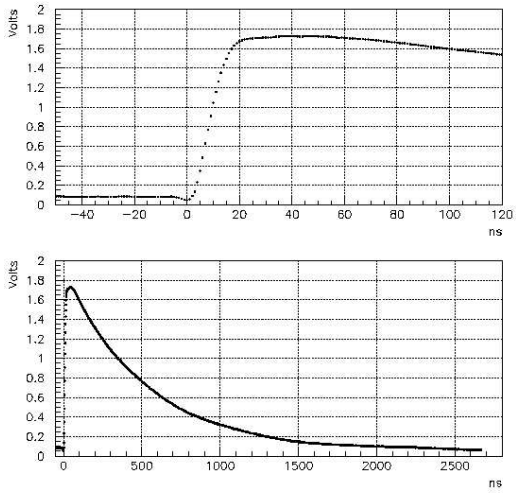

(b) Figure 5.5: integrated charge output for a pmt pulse.

signals.

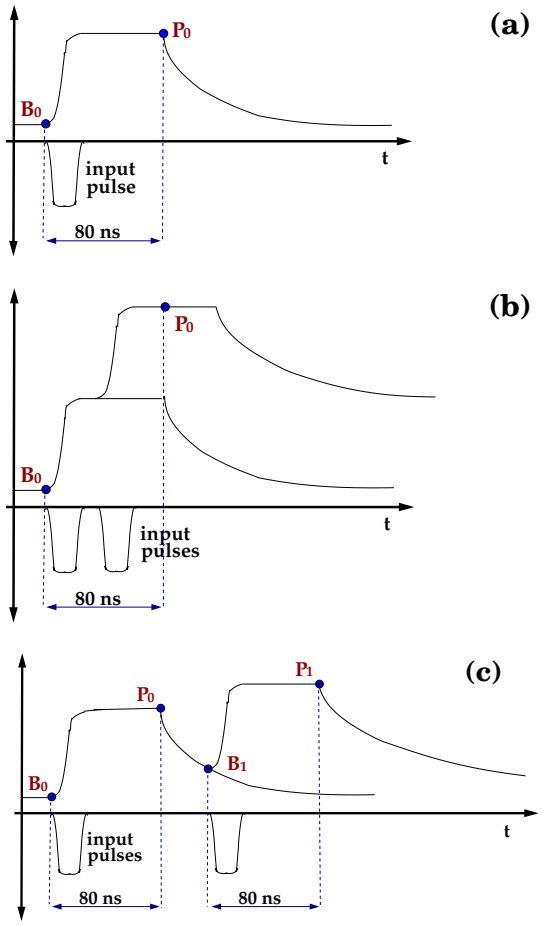

FIGURE 5.6: IDEAL GATELESS CHARGE INTEGRATOR OUTPUTS.

The *ideal* gateless charge integrator behaviour is sketched in figure 5.6, together with the corresponding ideal input pulses. The integrator output starts rising at the time t_0 (signal arrival time) and reaches a level proportional to the pulse charge after a time equal to the pulse duration. Then it mantains this level for $\sim$80 *ns* (T) and finally starts an exponential decay, with a time constant τ $\sim$500 *ns* (see figure 5.6(a)).
Figures 5.6(b) and 5.6(c) show the output in case of a multiple hit, with the second pulse detected respectively within or after 80 *ns* . In both cases we have the so called *pile-up* effect, i.e. the charge of the second hit is affected by the presence of the first hit. The importance of this effect depends on the time delay between the two hits and affects, obviously, our energy reconstruction efficiency.
Yet, we can recorrect *offline* our data. Our digital electronics measures the charge sampling twice the integrated output: see figure 5.7. The first sample (B_0) falls on the signal baseline,

the second (P_0), 80 *ns* later, falls exactly in the region where the signal has its maximum. In case of a single hit (5.6(a)), the charge is then the plain difference of the two samples:

$$Q_0 = P_0 - B_0 \tag{5.1}$$

The baseline subtraction is forced by the presence of an offset value, about 180 mV, on the charge output signal[3]. This subtraction rejects the possible offset drifts of the front-end amplifiers but acts also as a filter for spurious signals at low frequencies (less than few MHz).

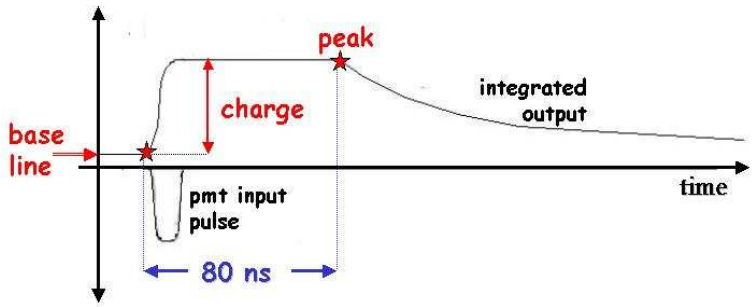

FIGURE 5.7: DIGITAL ACQUISITION OF THE CHARGE INTEGRATED OUTPUT. THE CHARGE TO DIGITAL CONVERSION IS DONE SAMPLING THE SIGNAL'S BASELINE AND PEAK VALUES (INDICATED WITH THE TWO RED STARS).

With multiple hits the situation is more complex: our digital electronics records differently, depending on their time delay, two consecutive hits on the same PMT . If the delay is less than 80 *ns* they are registered as a single hit. The time information is merely the time of the first hit[4], but the charge information is the sum of the two signals (see figure 5.6(b)) and equation 5.1 is still valid. If the time delay is instead between 80 and 140 *ns* , the second hit is completely lost (see section 5.1.4.1 for more details). Finally, with delays above 140 *ns* we record two independent hits. Therefore, we can correct for the *pile-up* effect only in this case. The charge of the second hit is now:

$$Q_1 = (P_1 - B_1) - Q_0 \cdot e^{-\frac{\Delta t}{\tau}}\left[1 - e^{\frac{T}{\tau}}\right] \tag{5.2}$$

where Δt is the time delay between the two hits, T is 80 *ns* and τ is 500 *ns* .

Actually, due to the presence of the high voltage decoupling capacitor, the PMT 's unipolar input pulse (shown in figure 5.2) is transformed into a bipolar signal, having a null area and a positive tail decreasing by an exponential law[5]. This influences the charge output

[3]This offset assures always positive signals in entrance to the ADC.

[4]In this case we lose the time information of the second hit.

[5]The exponential decay constant depends on the parameters of the front end impedance adapting network (RLC network) and of a further impedance adapting network (RC network having R=50 Ω) mounted on the PMT anode.

signal, causing a distortion of the simple exponential decay law. Figure 5.5(b) shows the real charge output for a PMT signal.

5.1.2.2 The outer detector front end electronics

The outer muon veto system is a water Cerenkov detector which provides the ability to suppress the background produced by the residual atmospherical muon flux. The detection of Cerenkov light is performed by the 208 PMTs arranged on the outer side of the SSS and on the floor of the water tank.

As for the inner detector, the signal is carried out from the photomultiplier to the electronic equipment and the high voltage vice versa through 55 m long coaxial cables. The electronic modules supplying the high-voltage and performing the AC decoupling of the fast PMT pulses from the HV are the High Voltage Decoupler (HVD). Each unit has 24 channels and a total of 9 units are then needed for the muon system.

The signal is then feed to the input channel of the Charge to Time Converter (QTC) front end boards, through a 50 Ω terminated cable.

(a) Figure 5.8: the high voltage decoupler units HVD used for the outer muon system read-out.

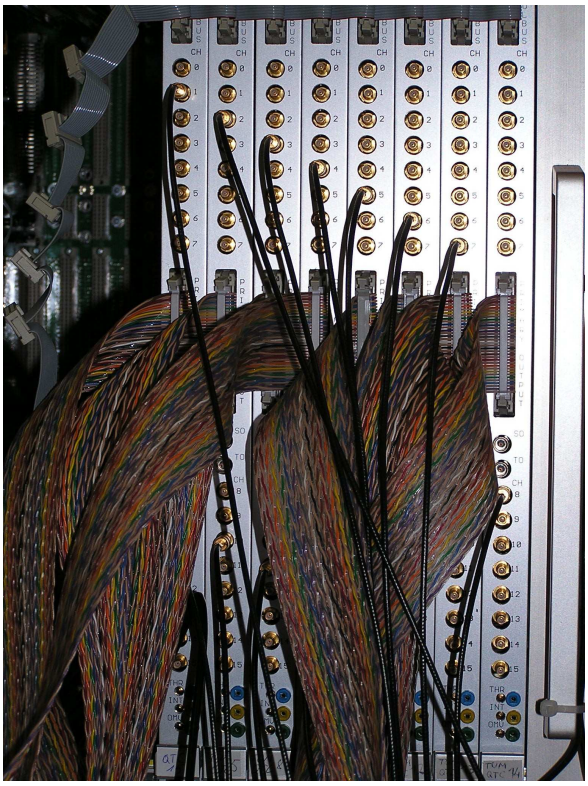

(b) Figure 5.8: the QTC front-end boards mounted in the outer muon rack.

Each QTC board serves 16 input channels, for a total of 14 boards for the whole system.

Each board has three outputs. The primary output (PO) is a logic ECL pulse whose width is proportional to the charge of the input pulse and whose leading edge gives the time of the arrival of the photoelectrons. This output is forwarded to the TDC units (standard C.A.E.N. modules) and digitized. There is one PO for each channel of the board.

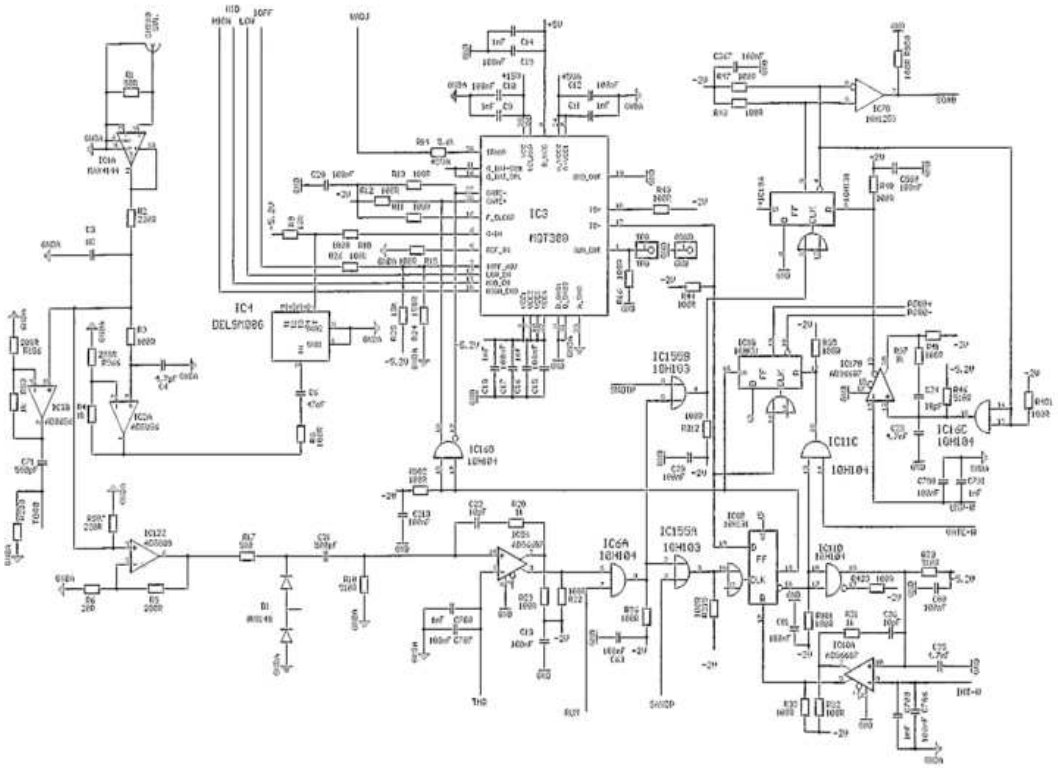

FIGURE 5.9: SCHEMATIC DIAGRAM OF ONE QTC BOARD'S CHANNEL.

The second output (SO) is instead a logic signal. There is a single SO for each board and it creates a step function, such that the number of steps is equivalent to the number of fired photomultipliers on the board in a certain programmable time window ($\sim$150 *ns*). This signal is sent to the muon trigger board (MTB), where the outer muon trigger is produced and sent to the BOREXINO trigger board (BTB).
Finally each QTC board has also a tertiary output (TO), which is the analog sum of the PMTs signals at the input of the board. This output is used to build a second trigger, in case we should need to lower the multiplicity threshold below 6 hit PMTs (see section 5.2).

The complete block diagram of the outer detector front end electronic, including the PMTs and the high-voltage units, is sketched in figure 5.10.

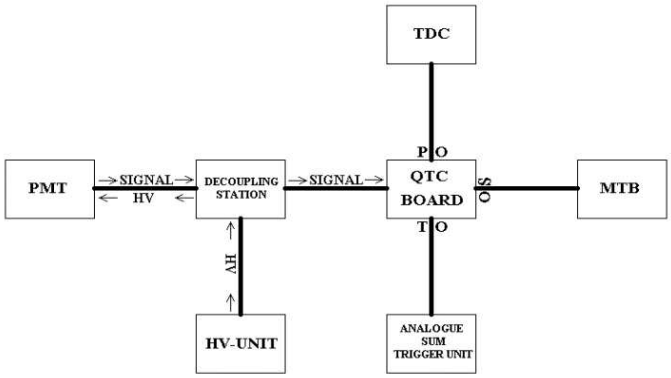

FIGURE 5.10: BLOCK DIAGRAM OF THE OUTER DETECTOR FRONT END ELECTRONIC, INCLUDING THE PMTS AND THE HIGH-VOLTAGE UNITS.

5.1.3 THE HV POWER SUPPLY

Each photomultiplier needs a high voltage supply of ∼1500 V and ∼100 μA . The need of some kind of remote control on the power supply units and a useful modularity pushed the collaboration to choose the model SY527 from C.A.E.N. [62]. The system is organized into crates; each crate serves 160 PMT channels.

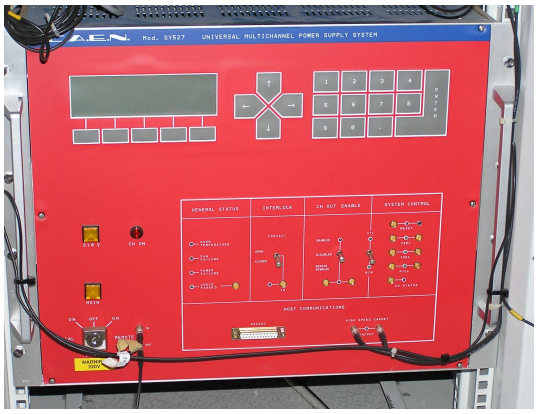

(a) FIGURE 5.11: THE SY527 C.A.E.N. MULTICHANNEL POWER SUPPLY SYSTEM USED FOR BOREXINO .

(b) FIGURE 5.11: REAR VIEW OF THE SY527 HV MAINFRAMES.

Each crate may be controlled locally or remotely. Local control is performed manually through a key-pad and a LCD display located on the front panel. Remote control is performed

by means of a VT100 terminal, plugged into an RS232C connector, or by a link with a proprietary serial bus (CAENET), which allows to plug up to 98 units accessed by a master board installed in a PC. It is exactly this CAENET serial bus that allows our HV power supply to be remotely controlled via a dedicated PC[6].

The modules bearing the output voltages are the A932AP Channel Boards [65]. They home a primary high voltage channel, with 2.5 KV of maximum output, and 24 active distributor output channels, directly supplied by the primary channel.
The internal primary channel has a complete set of parameters that can be programmed: high voltage, current limit (1 μA resolution), ramp-up and ramp-down times, over-current behaviour, ... Also the voltage on each distributed output can be independently programmed, but only inside a maximum drop of 900 V from the primary channel setting.
The output voltages are provided via two multi-conductor block-type connectors. The output connectors have two pins dedicated to realize the safety board interlock. This protection allows to disable the primary HV generation when the distributor outputs are not connected to their loads.

5.1.4 The digital read out electronics

5.1.4.1 The inner detector digital electronics

The inner detector digital electronics provides for amplitude and time to digital conversion for each front-end channel. Each board homes electronics for 8 front-end channels and up to 20 boards can be plugged in a VME crate, for 160 channels in total on one electronic rack.

These boards were designed and built in collaboration with `Laben` S.p.A.. The board architecture is composed of two main functional blocks: the single acquisition channel, replicated 8 times - once per channel, and the main control block.

The single acquisition channel (see figure 5.13), acquires asychronously and continuously the hits coming from the photomultipliers. Each channel has two inputs from the front-end stage: an inverted and amplificated copy of the PMT signal and an integrated output. The fast signal provides for the arrival time of the light pulse, while the associated charge (energy) is obtained from the integrated output.

The timing signal is sent to a programmable dual threshold discriminator. The choice of a dual threshold discriminator was done to find the best compromise[7]between a low *walk effect* and time jitter (at the level of a small fraction of a *ns*) and a good rejection of the non negligible dark rate of photomultiplier's pulses smaller than the single photoelectron.
This discriminator is built with two comparators in AND condition: the channel is fired only if the photomultiplier signal crosses the higher threshold but the timing information is related to the lower crossing. The threshold is programmable between 0 and 500 mV; a single photoelectron signal is $\sim$200 mV and the present threshold is $\sim$50 mV.

If the discriminator fires, it is automatically disabled for about 140 *ns* . This dead time was introduced to prevent data jamming during the sampling and the writing of the data

[6]This PC mounts an ISA/CAENET interface [63] and a dedicated Linux driver for this interface has been written inside our collaboration [64].

[7]The first requirement needs thresholds as low as possible, the second needs instead higher values.

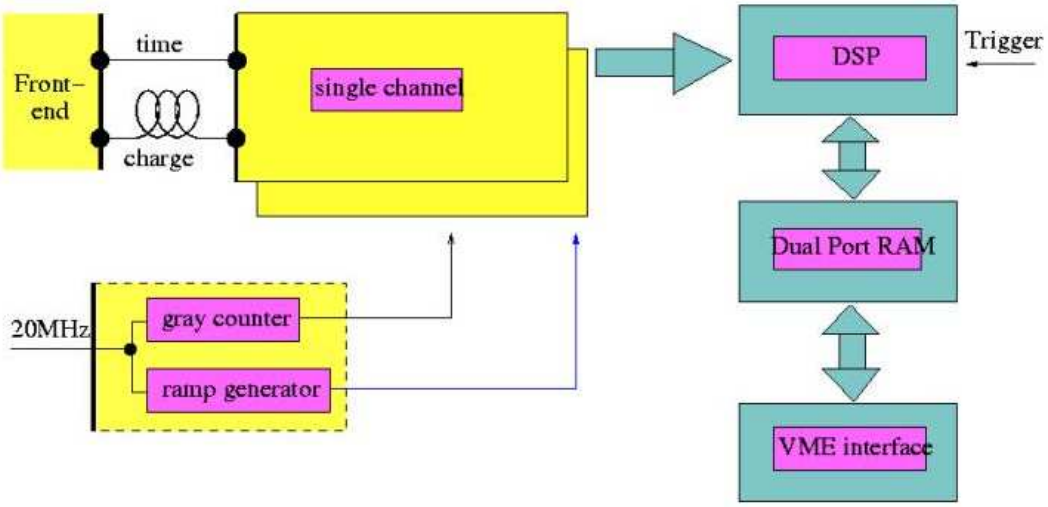

FIGURE 5.12: BLOCK DIAGRAM OF THE DATA ACQUISITION LABEN BOARDS USED IN BOREXINO .

on the internal memory buffers. This is a real DAQ dead time only for multiple hits with time delays between 80 and 140 *ns* . Actually if two hits reach the same PMT in less than 80 *ns* , the timing information of the second one is lost, but the charge sampling is able to keep track of the presence of this second hit. The impact of this dead time on the physics is then of the order of few percent for the typical neutrino events in the fiducial volume and therefore negligible.

The discriminator output is then used to fire a double pulse generator. Two 30 *ns* wide and 80 *ns* delayed pulses are generated and sent as a trigger to a dual input FADC , with 8 bit resolution. In addition, the first of the two pulses fires also an on-board coincidence unit, that computes the number of activated channels in an adjustable time window of about 50 *ns* , acting as the first level trigger.

The first FADC channel samples twice a 10 MHz triangular wave[8]. At the same time the first of the two pulses latches the content of a 20 MHz driven 16 bit counter (Gray counter) in a buffer register. These three informations allow to reconstruct the timing informations of the hit with a maximum span of 3.2 ms and a resolution better than 500 ps (see section 7.3 for more details on the reconstruction method). Special cares have been taken in designing the TDC hardware, in order to obtain a good ramp linearity and a low noise.
The second FADC samples the integrated charge signal. Thanks to a well calibrated delay line, the two samples fall exactly on the baseline and on the peak of the charge pulse (see figure 5.7). The case of multiple hits has already been discussed in section 5.1.2.1: if the delay is less than 80 *ns* only one hit is recorded, but the charge is the sum of the two charges. If the delay is more than 140 *ns* we have two single hits and we must take into account the *pile-up* effect.

[8] Generated on board by a triangular wave generator synchronous with the 20 MHz base clock.

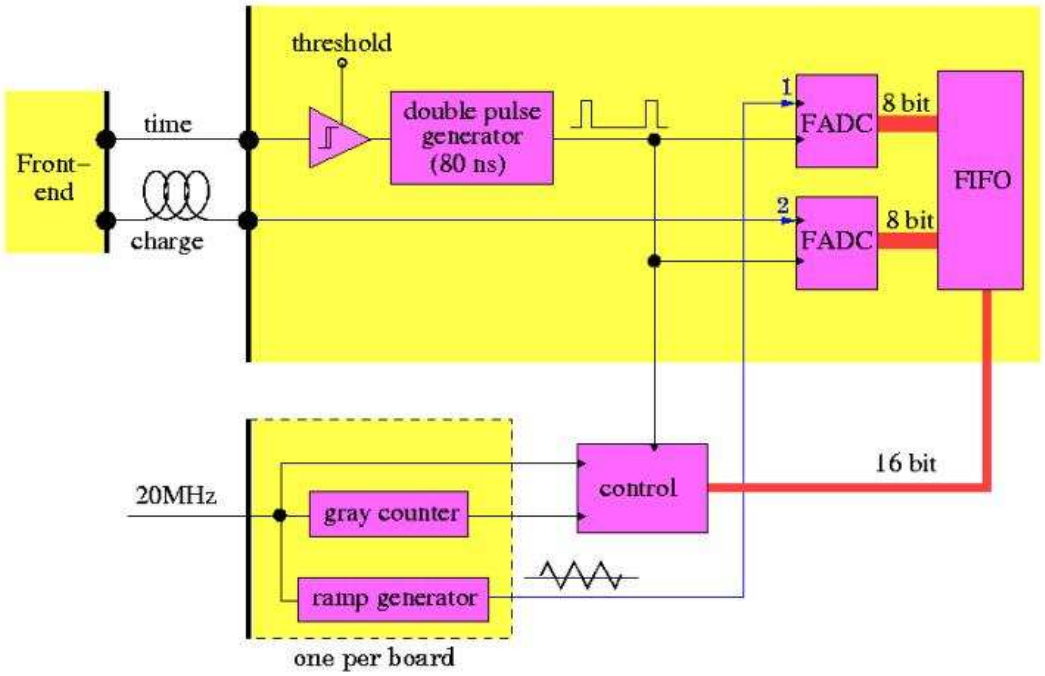

FIGURE 5.13: THE SINGLE CHANNEL ACQUISITION BLOCK.

The ADC and TDC data temporary stored in an internal memory (local FIFO buffer) are then managed by the main control block, common to all channels of a board. Almost all the function of this block are executed by a DSP (Digital Signal Processor).

Ordinarily the DSP controls the status of the eight channel's FIFO and waits for triggers. The oldest data (older than 6 μs) are continuously discarded, except if a special request of monitoring is sent to the system, i.e. when the online analyzer is running. Upon this request the untriggered data can be analyzed by the board itself to produce time and charge histograms. These histograms are then sent, via socket connection, to the online monitor server (section 5.4).

When a trigger condition occurs, the BOREXINO Trigger Board delivers to the Laben DSPs a master trigger interrupt and the 16 bit trigger number identifier. Under this interrupt the DSP starts the procedure to build the data record: all the hits registered in the digital FIFOs are collected and stored in a 2 Kbytes memory, together with a header containing the trigger number. The depth of this memory allows to store hundreds of the typical size BOREXINO event. The DSP processing time under a trigger condition is about 80 μs . Since the fast coincidences, with time delays less than 80 μs , are very important for BOREXINO , the DSP architecture was designed to handle also a second interrupt in queue within this processing time. However, if another interrupt occurs during this DSP BUSY time, this third trigger is lost.

The memory bank used is a dual port memory, accesible both from the DSP and from a VME bus. A dedicated process running on the Laben PPCs waits for an interrupt to read

these data, store them in a single data structure and send them to the DAQ processes.

A more exhaustive description of the digital boards can be found in [66].

5.1.4.2 The outer detector digital electronics

Both the time and charge informations of the outer detector PMTs signals are provided by the QTC primary outputs: their width are proportional to the charge of the pulses, while their leading edge give the arrival time of the photons. The primary outputs of the QTC boards are acquired and digitalized by two standard Time to Digital Converter units (C.A.E.N. TDC module V673).

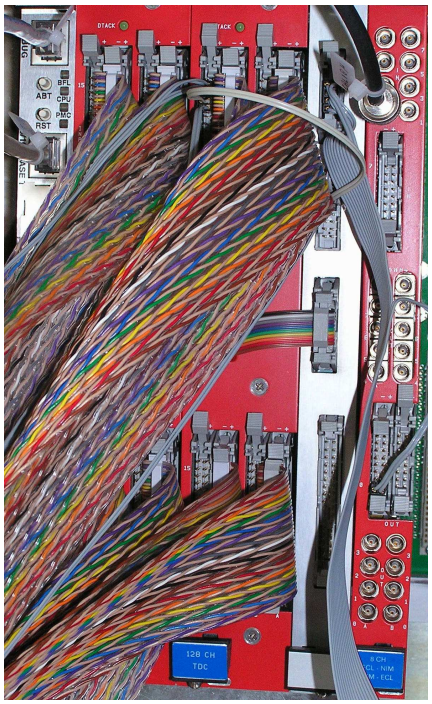

(a) Figure 5.14: the C.A.E.N. TDC units mounted in the outer muon crate.

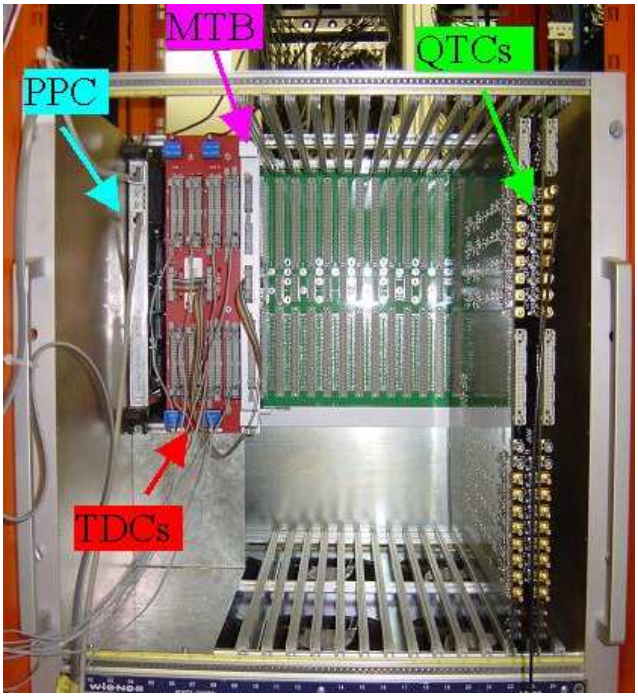

(b) Figure 5.14: general view of the outer muon crate. The PPC and the MTB, QTC and TDC boards are explicitly indicated.

5.2 The trigger system

The BOREXINO trigger system is designed to perform the following functions:

- identify good candidate events, requiring that at least K PMTs have fired within a time window of 48 *ns* . The energy threshold K can be programmed from 1 to 255 and the time window can be adjusted between 30 and 70 *ns* ;
- identify external muon veto events;
- provide test and calibration triggers, that can be generated via software, automatically with an internal timer or with an external signal;
- provide the possibility to fire the laser systems or to receive a signal to flag laser events;
- handle the absolute time clock.

The complete system, sketched in figure 5.15, is composed of the main BOREXINO Trigger Board (BTB), the outer Muon Trigger Board (MTB), an absolute time clock (GPS clock), one Clock Generator (CKG), one trigger fan-out (TFO), 14 Trigger Backplanes (TBP) and 5 Trigger Adder Boards (TAB).

5.2.1 The trigger alghoritm and the borexino Trigger Board

The main trigger system can be basically divided in four step levels. The two highest levels take place in the main trigger crate, the first two are done locally in the digital electronic boards and in the `Laben` crates.

An on board coincidence unit placed on each `Laben` board (see section 5.1.4) computes the number of activated channels in an adjustable time window of about 50 *ns* . Every time a fast timing input fires, a monostable (one for each channel) is activated and kept active for three clock cicles of a dedicated line running at 60 MHZ nominal (16 *ns*). A 4 bit adder gives the sum of the 8 channel of each board.

The output of this unit is sampled at 60 MHz: in practical at the output of each digital board we have the number of hit PMT every 16 *ns* . This number is then sent to a dedicated board, the Trigger Backplane unit (TBP), common to all the boards of one crate. This unit, placed in the rear of each crate, collects trigger data from the 20 `Laben` boards and computes the sum of hit PMT per crate, building an 8 bit data which carry a number in the range 0-160, at 60 MHz frequency. The TBP is also devoted to receive the 16 bit TRIGGER NUMBER that arrives together with the TRIGGER signal and deliver it to the digital boards[9].

The 8 bit total sum is then sent to 5 specialised boards on the main crate: the Trigger Adder Boards (TAB). They are basically adders: they receive the partial sums from the previous level, performs 2 addition steps every 16 *ns* and pass data to the next level. Each board receives data from 4 `Laben` crates. To read all the 14 crates and sum them up, 5 adders are needed. The output of the last adder board is the total sum of hit PMTs in the whole `Laben` system every 16 *ns* .

[9] The DSP of the `Laben` board attaches this number in the header of each recorded hit to allow `DAQ` to associate each stored hit to the right trigger.

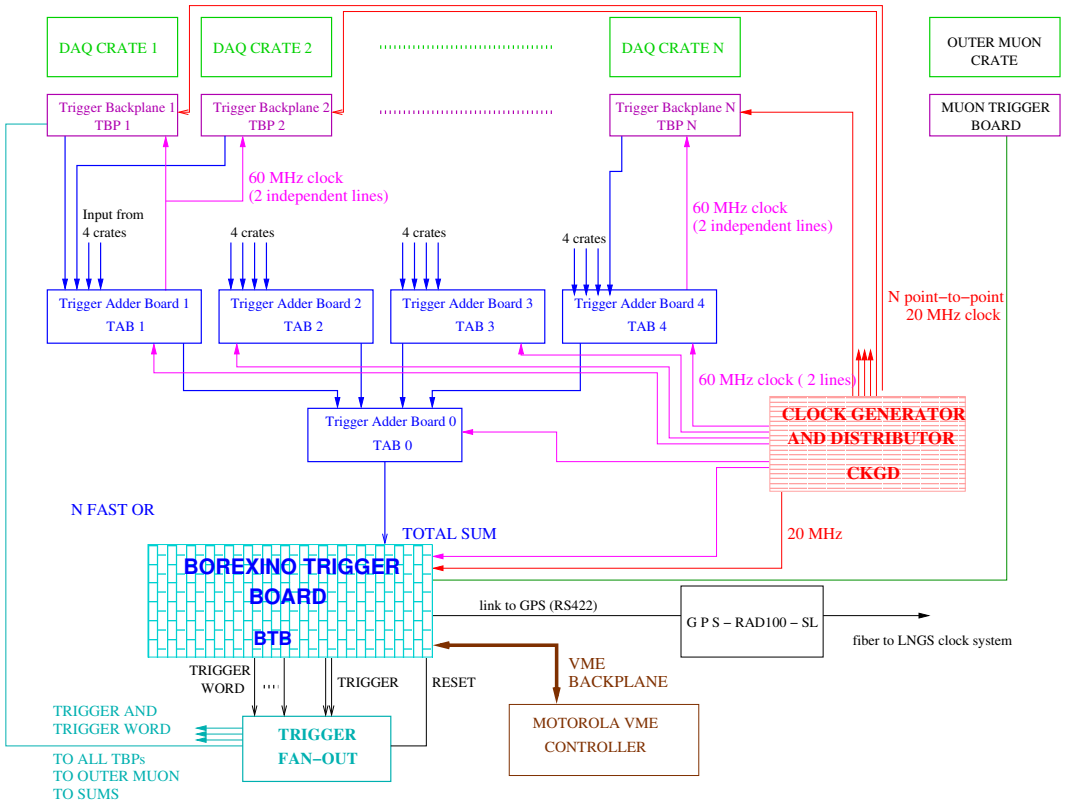

FIGURE 5.15: BLOCK DIAGRAM OF THE BOREXINO TRIGGER SYSTEM.

All the intelligent trigger functions are then controlled and performed by the BOREXINO Trigger Board (BTB), a dedicated VME board controlled by a DSP and placed in the VME trigger crate. The trigger board acts basically as the supervisor of the entire data acquisition system, receiving data from the preceding levels and taking the decision if and when generate the trigger. Its main functions are:

- implement the trigger alghorithm, using the total number of PMT fired or serving the external triggers;
- generate the trigger signals;
- read out the absolute time of the event;
- generate the trigger record and store it in memory;

Sixteen independent external input and output lines (Lemo connectors) are provided on the front panel. Since the output signals generated by this card must be distributed to all the DAQ system components, an additional external fan out stage, on the rear of the crate, is also foreseen. On the front panel there are also 8 additional Lemo output connectors with a

(a) FIGURE 5.16: CLOSE PICTURE OF THE TRIGGER RACK. FROM THE TOP: ONE OF THE TWO NIM CRATES, THE GPS CLOCK AND THE LABEN TRIGGER CRATE.

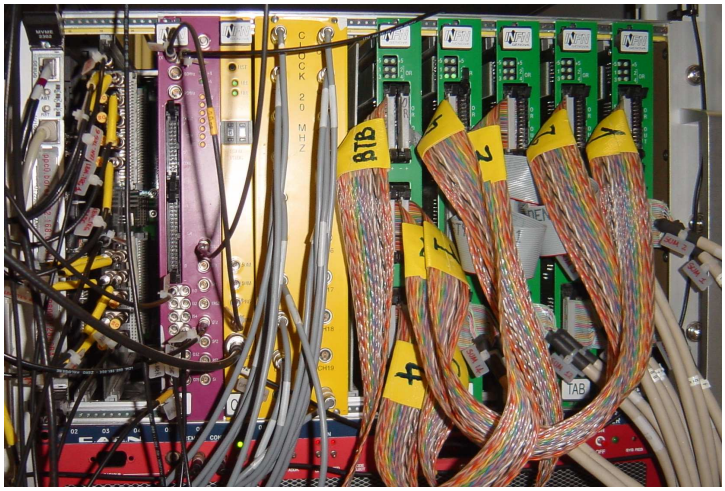

(b) FIGURE 5.16: CLOSE PICTURE OF THE LABEN TRIGGER CRATE. FROM THE LEFT: THE TRIGGER POWER PC (*gray*), A SIGNAL FAN-OUT UNIT, THE BTB (*red*), THE CLOCK GENERATOR BOARDS (*yellow*) AND THE 5 TAB BOARDS (*green*).

copy of all generated signals, a 26 pin connector for the fired PMT number input signal and one flat connector for the communication with the Absolute Time Clock (see section 5.2.5).

The trigger signals generated every time a trigger condition occurs are three TTL signals:

- TRIGGER : the real trigger signal, a $\sim$2 μs TTL pulse;
- GATE : the TRIGGER and GATE signals are generated with a programmable delay. This delay is necessary to tune the acquisition time before the trigger: the rising and falling edge of this signal fix the start and end time of the data readout inside the `Laben` boards. The total data acquisition window is 7 μs : from $\sim$400 *ns* before the TRIGGER to $\sim$6.6 μs after.
- TRIGGER NUMBER : the TRIGGER signal increments also the trigger number 16 bit counter. This number is sent in parallel to all data acquistion crates and is written in the acquired `Laben` data for each event.

Also the RESET signal is handled by the BTB . This signal is distributed to the acquisition boards at the start of each `DAQ` run and is used to synchronize the entry data acquisition system, resetting the time counters. An additional external signals of VETO is provided.

Our trigger board allows also the possibility to generate a trigger using an external signal: this is useful for all the service-triggers needed for laser, calibration, test or debugging runs (see section 5.2.3 and table 5.1). In addition a trigger can be generated also via software, writing an appropriate command in the VME accessible register.

A 4K $\times$ 32 bit FIFO is also provided. It is used to store the record of information generated for each trigger signal. The format of the record is shown in table 5.2.

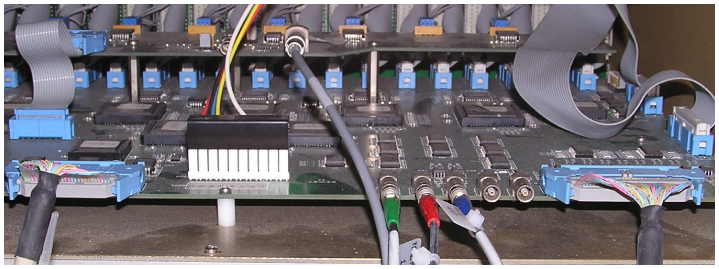

(a) FIGURE 5.17: THE TRIGGER BACKPLANE UNIT, ON THE REAR OF EACH LABEN CRATE. THE 8 BIT FLAT CABLE, ON THE LEFS, IS THE TOTAL SUM OUTPUT; THE THREE LEMO CONNECTORS AND THE 16 BIT FLAT CABLE, ON THE RIGHT, ARE THE FOUR TRIGGER INPUT SIGNALS.

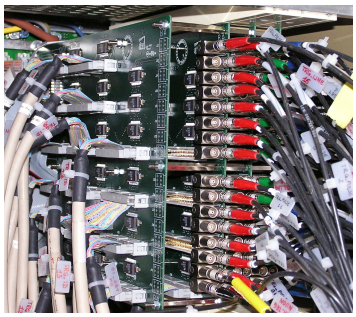

(b) FIGURE 5.17: THE EXTERNAL FAN OUT STAGE FOR THE DISTRIBUTION OF THE TRIGGER SIGNALS. ON THE REAR OF THE LABEN TRIGGER CRATE.

The first values are general informations related to the status and configuration of the trigger board. Then the informations on the trigger condition that has generated the trigger signal follows. *"Trigger Number"* is the trigger identification number; the less significant byte of the *"Trigger Word"* holds the Trigger Type field, used to identify the kind of trigger; the remaining byte (MSB) is a bit-field used to identify which BTB input was active when the trigger occured[10](see table 5.1). Every time a trigger is generated, the BTB reads the absolute time clock and store the information in the *"Trigger Time"* timing tag. Flag to

[10]The values given in table 5.1 are the typical values. It is not forbidden, and it might happen, that a trigger has more than one active bit in MSB, for example when two triggers occur almost at the same time. In this case the trigger is flagged according to the priority that is given in the table but MSB keeps track of this rare double triggering condition.

Trigger	***Trigger Type (dec)***	***Trigger Word (hex)***	***BTB In***	***BTB Out***	***MSB***	***Priority***
Neutrino	1	0x0001	Comp	1	0	1
MuonMTB	2	0x0402	3	4	32	2
MuonTotC	128	0x0880	4	3	8	3
Laser355	4	0x1004	5	7	16	4
Laser266	16	0x2010	6	8	32	5
Laser394	8	0x4008	7	2	64	7
Calibration	32	0x4020	7	5	64	6
Random	64	0x4040	7	6	64	8

TABLE 5.1: LIST OF THE DIFFERENT TRIGGER TYPES FORESEEN FOR BOREXINO DATA TAKING.

indicate FIFO conditions (empty, half, full) are also accessible reading the VME register.

5.2.2 THE BTB 'S DSP FIRMWARE

The behaviour of the BTB is almost entirely determined by the DSP software[11].
The total sum signal from the TABs is sent to a programmable comparator. When this comparator fires the highest priority interrupt to the DSP is generated. If the run is enabled and no veto is active the DSP starts the procedure to serve this interrupt: it disables the other interrupts, turns off the comparator, writes in the dedicated register the trigger number, generates the three trigger signals, reads the comparator value, sets the NEUTRINO trigger flag, raises the relative output line (OUT#1), increases the number of unserved triggers, waits for $\sim$1 μs and finally restarts the comparator.
This 1 μs dead time is due to a bad behaviour of the Trigger Backplane units. When these units receive the trigger interrupt from the BTB they modify the content of their sum registers. This would cause a prompt and fake retriggering, which is instead avoided disabling the comparator. It is important to notice that, from the physical point of view, this 1 μs dead time is completely negligible.
In the same way, if one of the 8 independent external input lines is high a lower priority interrupt signal is generated. Again, if the run is enabled and no veto is active, the DSP sets the trigger flag and raises the relative output line accordingly to the trigger type - input/output channel mapping reported in table 5.1, writes the trigger number register, generates the trigger signals and increases the number of unserved triggers.

Then, the procedure to build the trigger record header and the trigger record data (table 5.2) starts. The whole procedure requires $\sim$10 μs . If a second trigger occurs in this time

[11]The DSP boots its software from an external flash EPROM.

Trigger Record Header	***Lenght in bytes***
Event Size (bytes)	4
Run Number	4
Event Number	4
Laben Data Offset	4
Laben Data Offset	4
Sum Data Offset	4
Muon Data Offset	4
MCTruth Data Offset	4
Event Time (PC clock)	8

Trigger Record Data	***Lenght in bytes***
Lenght of Trigger Record	2
Error Flag	2
Number of sub-records	2
Daq Version	2
BTB DSP Register 1	2
BTB DSP Register 2	2
Trigger Threshold	2
BTB Firmware Revision	2
Trigger Time	2
Trigger Number	2
TAB Sum Value	2
Trigger Word	2
GPS Word 0,..,4	1

TABLE 5.2: STRUCTURE OF THE TRIGGER RECORD (HEADER AND DATA) GENERATED FOR EACH TRIGGER SIGNAL AND WRITTEN IN THE RAW DATA FILE.

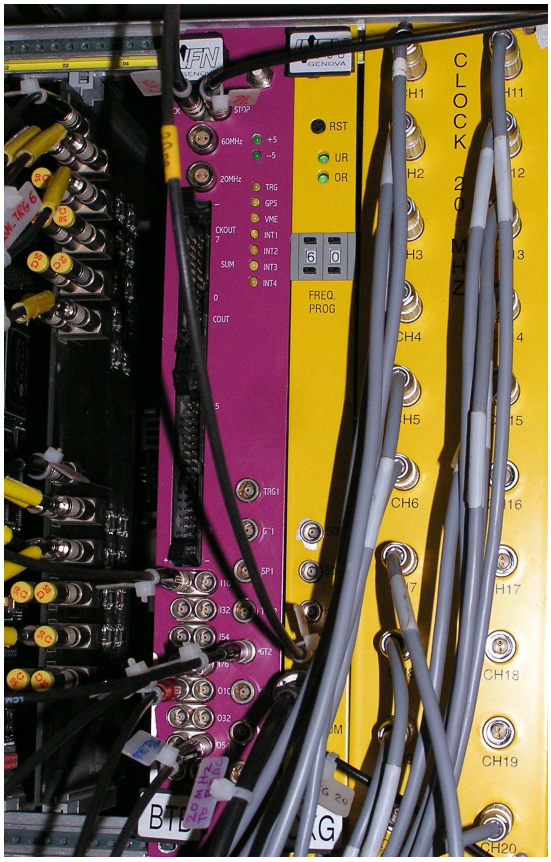

(a) FIGURE 5.18: CLOSE PICTURE OF THE BOREXINO TRIGGER BOARD (*red*) AND OF THE CLOCK GENERATOR BOARDS (*yellow*).

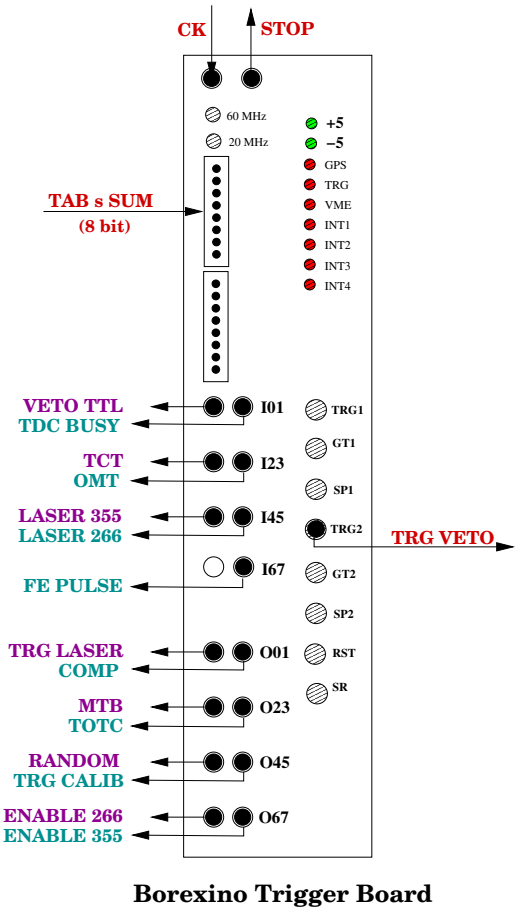

(b) FIGURE 5.18: SCHEMATIC DRAWING OF THE INPUT AND OUTPUT SIGNALS CONNECTED TO THE BTB MODULE.

window it is ignored[12]. This is a real dead time of our system, but, luckily, all the relevant delayed coincidences fall outside this time window and there is no real efficiency loss. Actually, the lower decay time is the one of the isotope ^{212}Po in the thorium chain, with a halflife $\tau_{1/2}$= 300 *ns* but then there is a jump towards definitely higher values: the second lower time is ^{214}Po , in the uranium chain, with $\tau_{1/2}$= 164 μs .

In addition also another dead time must be evaluated. Since the procedure to read and format the data inside the `Laben` board is quite slow (it takes about 80 μs) and since the DSP of these boards can handle only one interrupt in queue within the processing time

[12] The *"unserved trigger"* counter is decreased only at the very end of the DSP cycle, after the whole trigger record has been written in the FIFO . The functions that manage the trigger interrupts execute a simple check on this counter, and procede only if it is null.

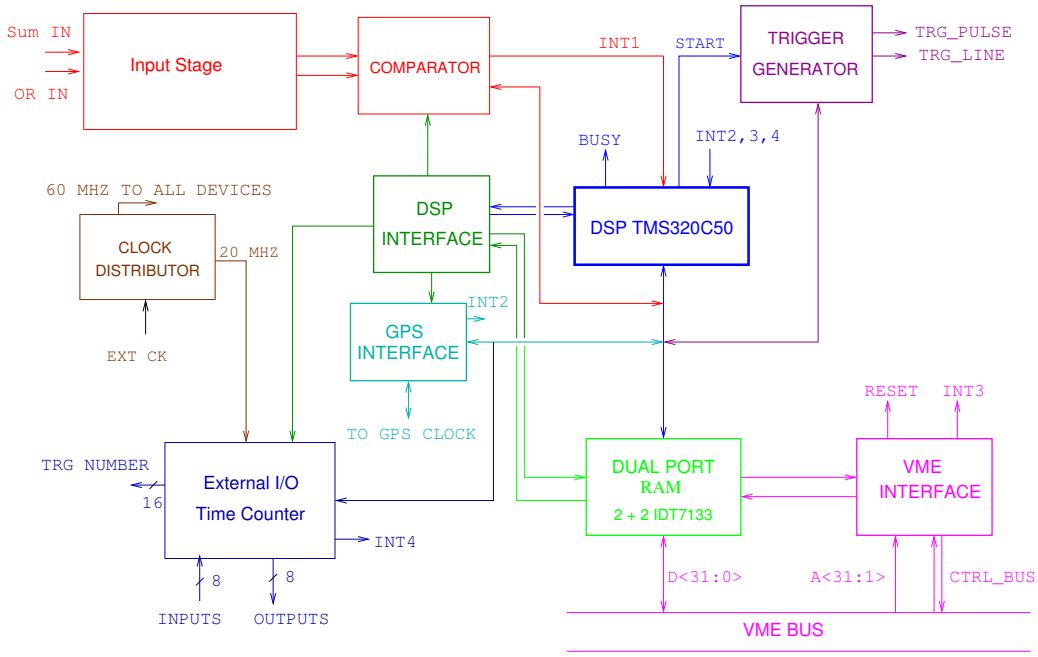

FIGURE 5.19: BLOCK DIAGRAM OF THE BOREXINO TRIGGER SUPERVISOR BOARD (BTB).

(when it is in the BUSY state) we added an hardware veto (see section 5.2.3.1) to the trigger system. If more than two triggers occur in less than 100 μs only the first two are served, while the following ones are ignored. Again, also this efficiency loss has no real impact on physics.

Finally also a software burst suppressor mechanism has been added, in order to avoid noise bursts of more than 10 events in ~50 ms. The check is done using the 200 Hz input triggers on the BTB input line IN#7 (see section 5.2.3.2) as time reference.

5.2.3 THE SERVICE-TRIGGERS

The so called NEUTRINO TRIGGER condition, requiring a programmable number of hit photomultipliers within a 50 *ns* time window, is the standard trigger conditions that will be used in BOREXINO during normal data taking. Nevertheless, in addition to that we need also a lot of service-triggers, for calibration, test and debugging purposes. The following description refers to the DSP firmware and to the related hardware set-up that has been implemented for these service triggers handling.
This system is now in its final configuration and has been extensively tested.

5.2.3.1 VETO SIGNALS

When a trigger condition occurs an interrupt signal from the BTB forces the DSP of each `Laben` board to read and format the data stored in its FIFO and to write them on the dual port RAM on the VME interface. The DSP processing time required for these operations is about 80 μs [66].
Since the fast sequences of events, with time constants below 80 μs , play an important role in BOREXINO , the boards has been designed in order to be able to handle also a second interrupt within the processing time of the first one.

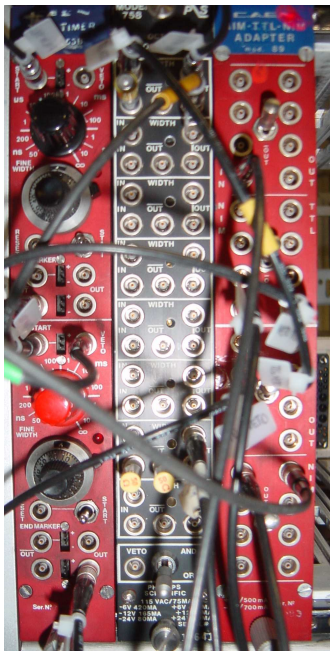

(a) FIGURE 5.20: CLOSE PICTURE OF THE NIM CRATE WITH THE VETO SIGNAL HARDWARE.

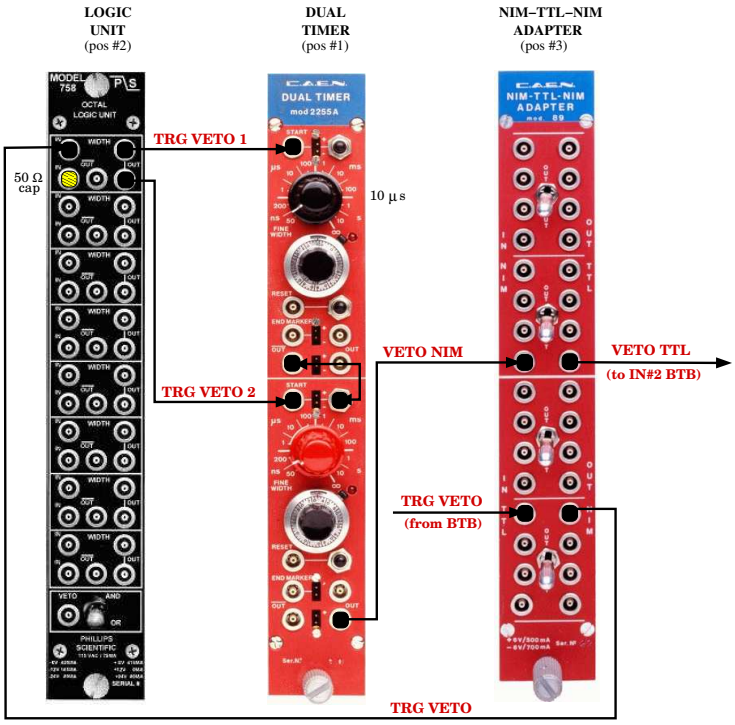

(b) FIGURE 5.20: HARDWARE SET-UP OF THE VETO SIGNAL LOGIC.

Nevertheless, if a third trigger condition occurs before also the second interrupt routine is over, the DSP is no longer able to handle it and the trigger is lost. To avoid possible crashes of the `DAQ` due to this loss, we have added an hardware veto. If two triggers occur in a time window lower than 100 μs a veto signal (VETO TTL), 100 μs long, is generated and sent to the BTB input line IN#2 (see figure 5.20(b)). This line is a real hardware veto: as long as the input signal is high no trigger interrupt can be served by the BTB DSP .

A second veto signal is also foreseen: it is be provided by the outer muon detector (TDC BUSY) and sent to the BTB input line IN#1 .

5.2.3.2 Calibration pulses

The time reconstruction algorithm [67] used in the offline code is quite complex. Some non linearities and non ideal behaviours of the `Laben` boards forced us to develope a pre-decoding routine: a first pre-analysis of the raw data is needed to align *a posteriori* the detector (see section 7.3 for more details). This procedure can obviously be done only if the data contains some synchronous events. Since the test and calibration signal distributor can deliver the same signal to all the front end boards[13] we decided to use this system to generate the needed number of these events at the start of each run.

A dedicated timing unit generates a pulse with an adjustable rate set, by default, about 200 Hz. This NIM pulse is converted TTL and sent to the BTB input line IN#7 (see figure 5.22).

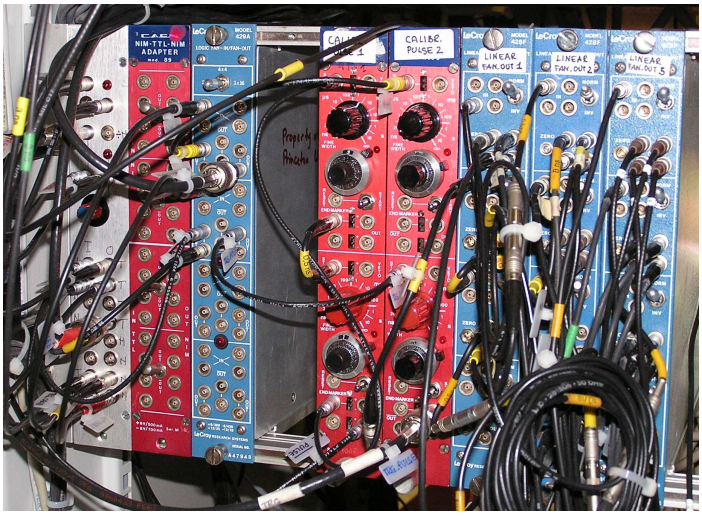

(a) Figure 5.21: close picture of the trigger NIM crate that handles the service triggers. The standard timing unit of the nearby picture is housed here.

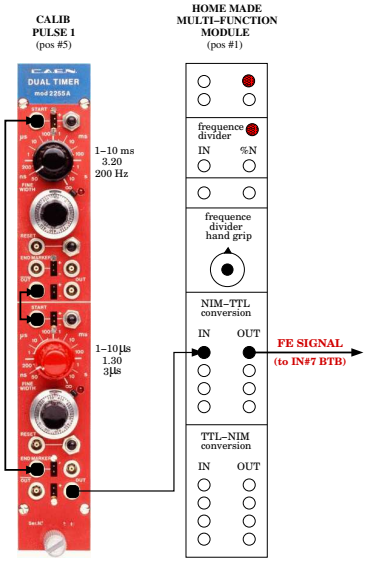

(b) Figure 5.21: standard timing unit that automatically generates an adjustable rate (200 Hz) of pulses. These are converted TTL and sent to the BTB LEMO inputs.

At the start of the run, the BTB firmware accepts all these external pulses, up to a programmable number (*calib_max*), as real triggers, starts the procedure to generate the trigger signals, writes the trigger record flagging these events as Calibration (table 5.1) and generates a signal on its output OU7.
This TTL pulse, about 2 μs long, is converted in a signal similar to the typical photomultiplier's signal[14] and sent as input to the fan-out of the calibration signal distributor (figure

[13] This is what we call a CALIBRATION trigger: all the 2240 electronic channels are pulsed at the same time.

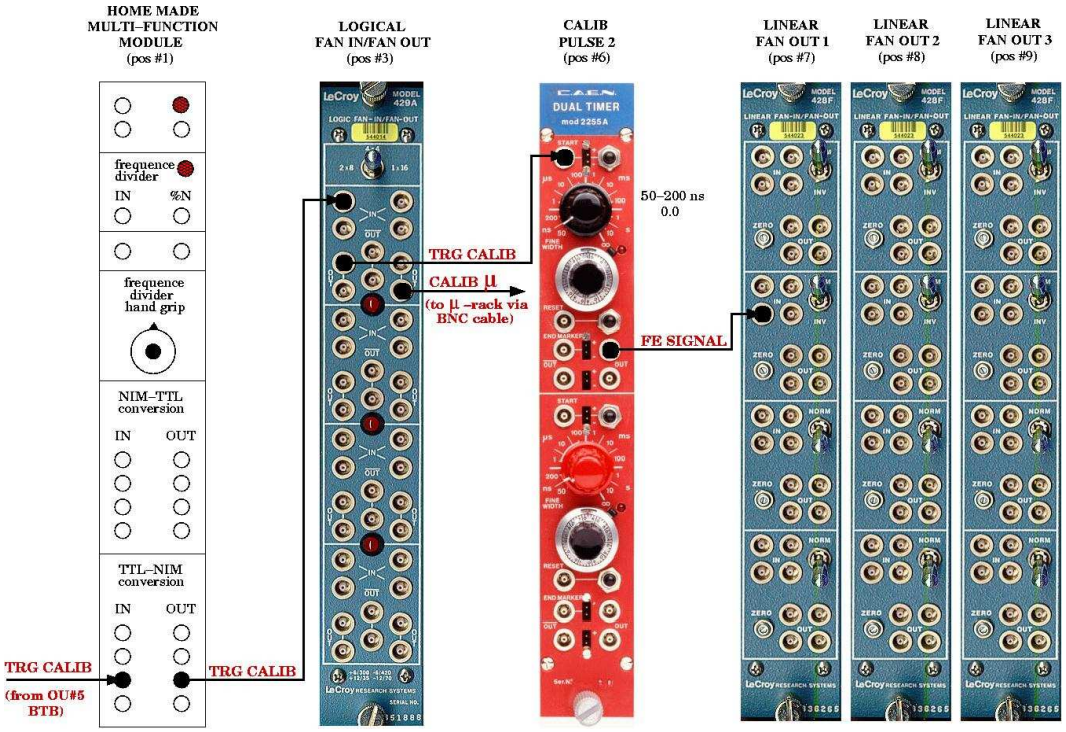

FIGURE 5.22: THE TTL SIGNAL GENERATED ON THE BTB OUTPUT LINE OUT#5 IS CONVERTED IN A CALIBRATION SIGNAL AND SENT TO THE FAN OUT OF THE CALIBRATION SIGNAL DISTRIBUTOR.

5.21).
After serving *calib_max triggers*, the BTB starts pre-scaling them by another programmable factor (*calib_prescale*): the output line OUT#7 is then active only if the condition:
calib_triggers % *calib_prescale* = 0 is verified.

The two programmable parameters *calib_max triggers* and *calib_prescale* have the default values 1000 and 100, but they can be modified from the *"Trigger Set-Up"* page of our data acquisition program: *BorexinoDAQ* . More details on this program can be found in section 5.3.

5.2.3.3 RANDOM TRIGGERS

The same 200 Hz pulse rate, generated with the NIM logic described above handles also the timing laser and the random gates logic. We define RANDOM GATE a trigger interrupt generated from an external pulse at any arbitrary time and not associated with any light event in the detector; this allows us, for example, to study the dark noise of the photomultipliers.

We refer again to the *"Trigger Set-Up"* page of *BorexinoDAQ* : on this page, where the operators defines the trigger conditions of the new data run, there are several variables that

[14] It is a signal with a width of about 15/20 ns and an amplitude of about five photoelectrons.

can be enabled or disabled; one of them is the variable *"Random"*. When *"Random"* is enabled, the DSP of the BTB serves the first *calib_max* triggers as CALIBRATION TRIGGERS; then it ignores the prescale factor and serves all the interrupts received on its input IN#7 as RANDOM TRIGGERS. Actually, the reduced rate of calibration events is still present.

5.2.3.4 CALIBRATION LASER TRIGGERS

The timing laser logic is exactly the same of the RANDOM triggers logic. If the variable *"Laser 394"* (calibration laser) is enabled from the *"Trigger Set-Up"* page, after the first *calib_max* CALIBRATION triggers, the un-prescaled rate of calibration pulses is served as laser triggers. The triggers are flagged as LASER394 triggers (table 5.1) and a TTL pulse is sent on the BTB output line OUT#2 .

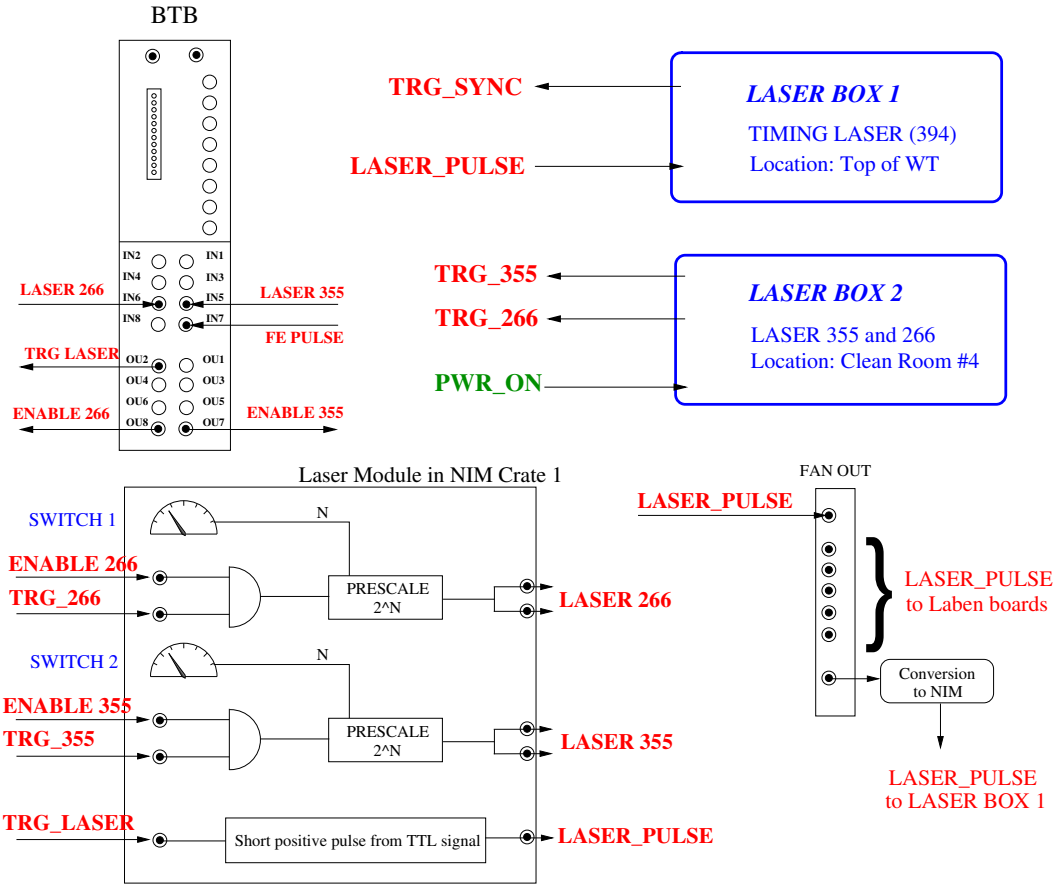

FIGURE 5.23: THE COMPLETE TRIGGER LOGIC OF THE THREE DIFFERENT LASER SYSTEMS: TIMING LASER (394), LASER 355 AND LASER 266.

This signal, convert TTL , is used as an external trigger for the laser calibration systems

(3.3.9.1, 3.3.9.2).

5.2.3.5 Laser 355 and laser 266 triggers

Both these two lasers can not be driven by an external pulse, but oscillate at a fixed frequency, around 11 KHz. The synchronization between the laser and the trigger systems is then done using their external SYNC signals. These signals, moreover, need a proper prescaling, since the maximum rate our acquisition system can stand is some hundred Hz.
In addition, since the two systems are housed both in quite unconfortable places[15] we have foreseen an hardware set-up that permits to turn them on and off remotely and to enable them from the web, from the standard *"Trigger Set-Up"* page.

On this page two dedicated fields, *"Laser355"* and *"Laser266"*, are foreseen. By default the two values are *disabled* and the BTB ouput lines OUT#7 and OUT#8 are low. Since these levels are ORed with the laser SYNC signals, as shown in figure 5.23, when this laser fields are *disabled* no signal can arrive to the BTB , even with the lasers turned on.
When the shifter enables one of the two lasers, the BTB ouput line OUT#7 (for Laser355) or OUT#8 (for Laser266) goes high and a prescaled signal is sent in the BTB input line IN#5 or IN#6 . Every time the BTB 's DSP finds one of these two lines high, it starts the generation of the trigger signals and flags them as Laser355 or Laser266 triggers.

5.2.3.6 Outer muon triggers

BOREXINO may trigger on an event in three ways. The first possibility is that an event is detected by both the internal PMTs and by the outer detector. This situation is almost certainly a muon track, and the hits on the internal PMTs no longer need be considered as a potential neutrino event. On the other hand, an outer muon trigger may occur with no corresponding internal PMTs hits. This is likely a muon track that does not penetrate inside the Stainless Steel Sphere. Nevertheless, a hadronic cascade produced by such an event may travel through the SSS into the outer buffer and generate delayed light in the internal system. And in the same way, an event observed by the inner detector but with no hits on outer muon PMTs is probably not muon-related, but it could be the result of a hadronic shower, which must be correlated with the muon that caused it. For these reasons, and also to ensure synchronization between the readouts of the inner and outer detectors, both detectors are read out every time either of them triggers.

Two different triggers can be generated by the outer detector: one based on the hit multiplicity and provided by the Muon Trigger Board (MTB [68]) and the second based on the total charge detected [69].
This additional trigger logic is realized using the *tertiary outputs* of the outer detector front end boards [70], which provide the analog sum of the input signals coming from 16 photomultipliers.

The two triggers, OMT (outer muon trigger) and TCT (total charge trigger) in figure 5.18(b), are sent into two different BTB input lines, IN#3 and IN#4 respectively. These two lines can be individually enabled or disabled from the usual *"Trigger Set-Up"* page of *BorexinoDAQ* ; if they are enabled the BTB flags properly the two triggering conditions, as MUONMTB or MUONTOTC triggers (table 5.1) and raises the output lines OUT#4 or OUT#3 . In case both triggers fire, the trigger word will show this information.

[15] Laser 355 is on the top of the Water Tank while Laser 266 is mounted inside Clean Room 4.

5.2.4 The clock generator

Three different clocks are needed in our trigger system. The first, a 20 MHz clock for the time and charge measurement (see section 5.1.4) has to be one for each crate[16]. Moreover, to count the hits that occured in a given time window, all BOREXINO TBPs and TABs must be properly synchronized with the main trigger board. This is done distributing a single clock generator for the whole system: an internal 60 MHz clock. Finally a third programmable clock, with a frequency range of 30-70 MHz, is used to set the trigger time window.

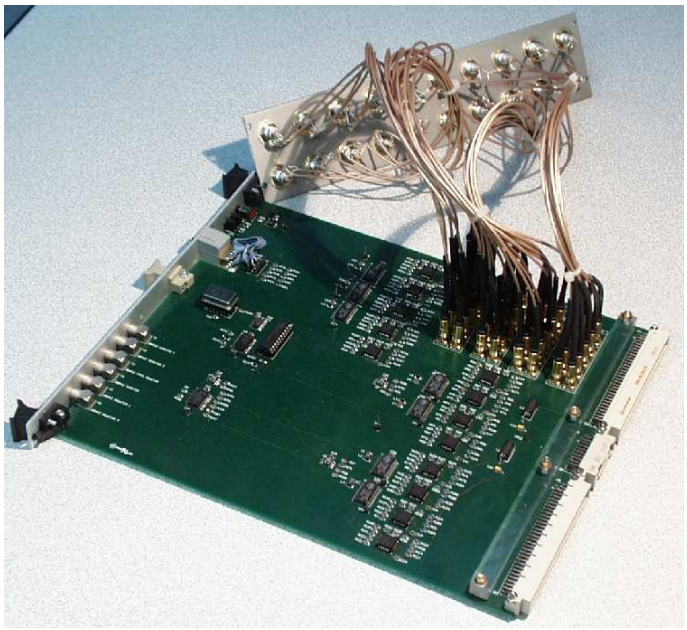

FIGURE 5.24: THE BOREXINO CLOCK GENERATOR BOARD.

A single clock generator unit (CKG) has been built for this purpose. It is a VME board with a single 20 MHz oscillator. All other clocks are generated from this signal through a dedicated microprocessor. All signals are distributed with cables of equal lenght to all racks via a Trigger Fan-Out mounted the rear of the main trigger crate, via a 20 connectors yellow panel in the front of the crate and via a flat cable installed in the rear of the VME trigger crate.

5.2.5 The absolute time clock

The record of information generated for each trigger signal (see table 5.2) contains two timing flags, one in the trigger header and the second in the trigger data structure.

[16]This signal is then splitted and delivered to the DSPs of the 20 **Laben** boards of each crate.

FIGURE 5.25: THE BOREXINO GPS RECEIVER MOUNTED IN THE TRIGGER CRATE.

The 8 bytes *"Event Time"* word holds the crate controller CPU time, on which runs NTP [17]. Its precision is a few seconds, depending on the trigger rate, and cannot therefore be used for an absolute time synchronization of the system, but only as a consistency check.

The real absolute time informations (*"Trigger Time"*)are read from a GPS device. We use the LNGS clock system, whose precision is $\pm$ 100 *ns* . We have a local receiver housed in our trigger crate and updated every ms through a point to point fiber-optic link.
At each trigger a STOP signal, synchronous with the trigger signal, latches the time information and writes it in some dedicated registers. This operation takes about 2 μs . When

[17] Network Time Protocol.

this process ends an acknowledge allows the BTB DSP to readout, at full speed, the 5 timing words (16 bit each).
If the GPS interface does not respond to the readout request (if it is down, disconnected or broken) the temporary registers is filled with 0, so it will be possible to identify the untagged events and associate them with the less precise timing informations coming from the crate controller CPU.

5.3 The data acquisition system

The BOREXINO data acquisition system (`DAQ`) is a complex software system, composed of many software elements written in different languages and technologies, that run on our online computing system. This is made up of 22 CPUs: 17 Power PCs and 5 PCs (*bxbuild*, *bxdb*, *bxweb*, *bxmon*, *bxslow*) running Linux.

The lowest level runs on the Power PCs . Inside our LAN we have 17 PPCs : one per crate on all the sub-systems, except the Sums system, where a single processor reads data from three VME crates.
They are basically the front end part of the `DAQ` system: event by event data are readout from each hardware element (i.e. the `Laben` boards) through the VME bus and written in a dual-port RAM.
Once every 30 triggers a dedicated driver running on a Linux PC, the Crate Receiver[18], opens a TCP-IP socket connection with the PPC , reads its memory, stores the data in a single data structure and copies them in a local FIFO , that can also be accessed by the Event Builder process. This process, running on the same Linux PC (*bxbuild*) of the Crate Receivers, continuosly checks this internal FIFO for new data.
When there is some data it builds the event following a fixed data structure (see section 7.2) and stores it in a raw data file on two local disks (`/rawdata1` and `/rawdata2` of *bxbuild*). If required it can send the events also to the online analyzer process (see section 5.4).

The whole set of processes running on the main `DAQ` computers receive commands from a dedicated process named Run Controller, or *BorexinoDAQ* . It accepts commands from the user interface programs, dispatches them to all processes on PCs or on Power PCs , receives possible errors and takes proper actions when these exceptions occur. Each process in the system communicates with *BorexinoDAQ* through socket connections, so the processes can be arranged on different CPUs.

A set of Perl scripts (CGI-BIN) that use the CORBA technology are the glue between *BorexinoDAQ* and the user interface. A strong interaction with the database is also maintained.

5.3.1 The graphical user interface

The graphical user interface is web based. A set of dynamic HTML pages guides the user thought four possible `DAQ` management sections:

- *Run Controller:* the real web-interface of *BorexinoDAQ* . From these pages the shifter can start a new run, define the trigger conditions, check the data acquisition rate and pause or stop the run.

[18] Actually there is one process for each PPC and each sub-system has its own, dedicated, Crate Receiver: the Trigger Receiver for PPC 0, the Laben Receiver for PPC 1-14, the Muon Receiver for PPC 15 and the Sum Receiver for PPC 16.

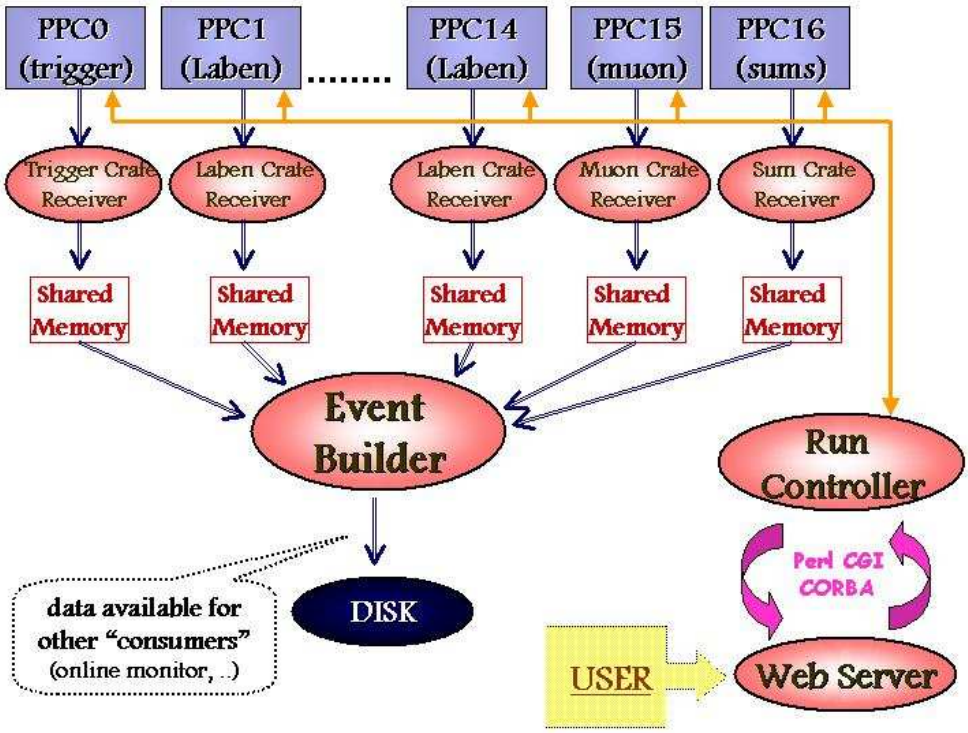

FIGURE 5.26: MAIN DAQ STRUCTURE. EACH PPC IS CONNECTED TO A RECEIVER PROCESS. THESE PROCESSES, RUNNING ON A DEDICATED LINUX PC, EXCHANGE COMMANDS WITH THE REMOTE PPCS VIA SOCKET CONNECTION AND RECEIVE AND STORE THEIR DATA IN A UNIX SHARED MEMORY. RECEIVER 0 GETS THE TRIGGER RECORD DATA, RECEIVERS 1,..14 GET THE LABEN DATA, RECEIVER 15 THE OUTER MUON DATA AND RECEIVER 16 THE FADC DATA. THE EVENT BUILDER PROCESS READS EACH OF THESE MEMORY CHUNKS, BUILDS THE EVENT RECORD AND WRITES DATA ON DISK. THE CRATE RECEIVERS AND THE EVENT BUILDER PROCESSES COMMUNICATE WITH THE RUN CONTROLLER VIA SOCKET. SYNCHRONIZATION IS GUARANTEED BY UNIX SEMAPHORES.

- *Profile Manager:* these web-pages allows the user to create a new *Online Profile* or to select the *profile* to be associated with a new run.
  A *"milestone"* of both the online and offline BOREXINO softwares is the use of the *profile* concept (see also section 7.4). Actually we distinguish between two different profiles: the *OnlineProfile* and the *CalibProfile*. These two variables were created besides the *Run Number* to simplify both the online initialization of the detector before a new run and the offline processing of the acquired data.
  Our detector can be considered a quite stable detector, with not so many degrees of freedom. However, mostly for debugging reasons, the DAQ was designed to allow a lot of freedom in the low level settings: the logical channel mapping, the bitmap of active channels, the value of the Laben thresholds, ... All these informations must be saved in the database; nevertheless almost all these parameters are always set to their default values and are changed only for debugging runs or when the hardware changes. The decision was then to write in the *OnlineProfile* every information needed

FIGURE 5.27: SCREENSHOT OF THE *BorexinoDAQ* GUI HOME PAGE.

to start a new run. A profile can be created by scratch or by inheritance from some other profile and more than one run can be associated to the same profile.

- *Online Monitor:* this web-interface provides the shifter a set of standard histograms to be used as a diagnostic and monitoring tool of the detector status during data taking. The most useful runtime informations are certainly the time charge and countrate histograms. See section 5.4 for more details.

- *System Monitor:* a simple web-page that allows to monitor and switch on/off the standard DAQ processes that runs on the whole online BOREXINO cluster (from the VME processes running on the PPC to the *BorexinoDAQ* , Builder, Crate Receivers, ... programs running on the Linux PCs).

5.3.2 The slow control

The slow control chain handles the control and feedback system to maintain the stability of the apparatus. It allows to remotely turn on/off electronics, to monitor and control both HV and LV power supplies, to retrieve data from the fluid handling system and to store them into the Data Base.

The control of the high-voltages, the low voltages and the VME crates is done by a single server, running on a dedicated Linux machine (*bxslow*). This software is completely independent from the remaining `DAQ` processes and has also his own web interface (`http://bxweb.lngs.infn.it/slowcontrol/login.html`). From this page the user can remotely power on/off single crates/boards/channels, change the current/default high-voltage values, monitor the status of the HV/VME system,...

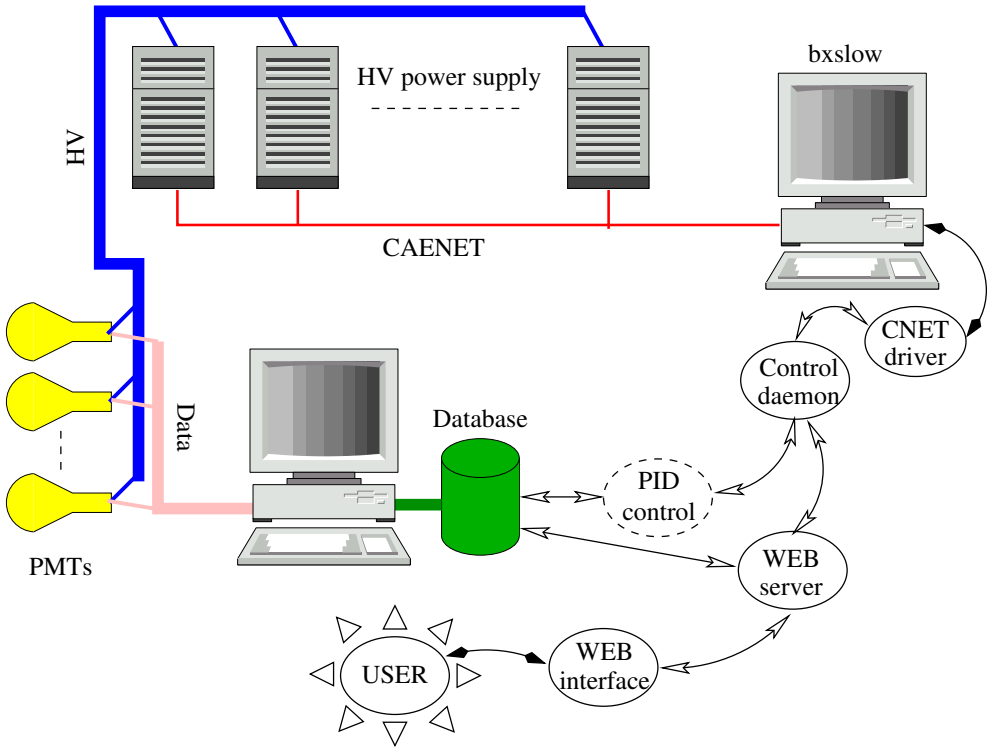

Figure 5.28: Logic scheme of the high-voltages control of our Slow Control system.

This system is already ready and debugged. One part is still missing: the software to automatically adjust the PMTs gain within a predefined precision (up to 2%), so to guarantee the same gain on all phototubes. The gain of each PMT is determined by several factors, like the applied voltage or the enviroment temperature, and can drift during the time. The feedback algorithm should check the single photo-electron peak position, calculate the correction to maintain the gain stable and send this information to the HV mainframes.

5.4 Online Analyzer

Its purpose is to have a real time monitor of the detector during data taking, determining in an easy and efficient way if it is deviating from the standard state and, if yes, the failure points. Eventually it could also broadcast some kind of alarm.

Two different types of information can be visualized with this online monitor. First of all a predefined set of histograms is always kept update and available, even if the main `DAQ` was not started. The data displayed in this case are the data continuosly acquired by the `Laben` boards DSPs when they are not busy with a master trigger interrupt. The major diagnostic that can be done with these random noise data is to monitor the countrates (for all reasonable subsets of the system, like individual PMTs , individual electronic sections, individual rings, ...) and the raw[19]time and charge distributions.

In addition we have also foreseen the possibility to process on the fly, during the data acquisition, the current run. Being intended to be an online monitor, the reconstruction level used in the offline code in this mode is the lowest possible: the time raw data are converted in *ns* times and the charge samplings are corrected for pile-ups, but no more complex analysis is attempted.
At the start of a new run the Builder starts automatically the histogram analyzer[20]on *bxweb* , sets up a socket connection with this process and starts processing the events.
The `HistogramServer.f` routine[21]creates and keep up to date a set of standard root histograms with the informations needed by the analyzer. These histograms, saved as ascii files in a common area on *bxweb* and overwritten every fixed number of events, are the histograms available on the analyzer web-page
(`http://bxweb.lngs.infn.it/script/s_omon_main.pl`).

[19]Still in TDC and ADC units.

[20]The reconstruction code enabled to work in this on-line mode.

Event simulation code

6.1 The Monte Carlo simulation chain

The Monte Carlo code for event simulation in BOREXINO is divided in three independent programs (see figure 6.1):

- GENEB : a Monte Carlo simulation of the physical process. The particle interaction inside the scintillator is converted into energy deposits.
- *Tracking:* a Monte Carlo simulation of the light production, propagation and detection. The energy deposit is transformed into emitted photons and the event becomes a list of charge and time signals on the phototubes.
- *Electronic Simulation:* a complete simulation of the electronic chain, from the digital acquisition boards up to the main trigger behaviour. All the known and relevant effects of our `DAQ` , including also the non idealities of the system, are implemented. The *ns* times and the photoelectron charges of the hits are converted into TDC and ADC samples and a trigger interrupt is eventually generated.

The output of this chain is a file with the same data format of the real `DAQ` files, that can be processed with the same reconstruction code (described in section 7.1). This code has been developed by a wide *offline* working group, including Genova, Milano, College de France, Munich, Dubna, Kurchatov, Princeton and Queen's institutions. The development of this code has been part of my PhD activity.

6.2 GEneration of NEutrinos and Background

GENEB (Generation of Neutrinos and Background) is a Monte Carlo code to simulate the energy depositions due to neutrino and background induced interactions inside our detector.

Solar neutrinos interact in BOREXINO via the elastic scattering reaction $\nu_x + e^- \rightarrow \nu_x + e^-$, which produces electrons with kinetic energy ranging from 0 to ~18 MeV (end-point of the *hep* neutrino spectrum). In addition, the natural radioactivity of the scintillator and of the materials of construction of the detector induce background events of type $\beta + \gamma$, with an energy range from 0 to 5 MeV, and α , with an energy range from 3 to 9 MeV. It should be underlined that GENEB takes into account only the effects due to the natural radioactivity of the materials which form or surround the detector, neglecting, instead, the contribution due to cosmic muons-induced reactions and radioactivity. These effects are handled by a different code [71].

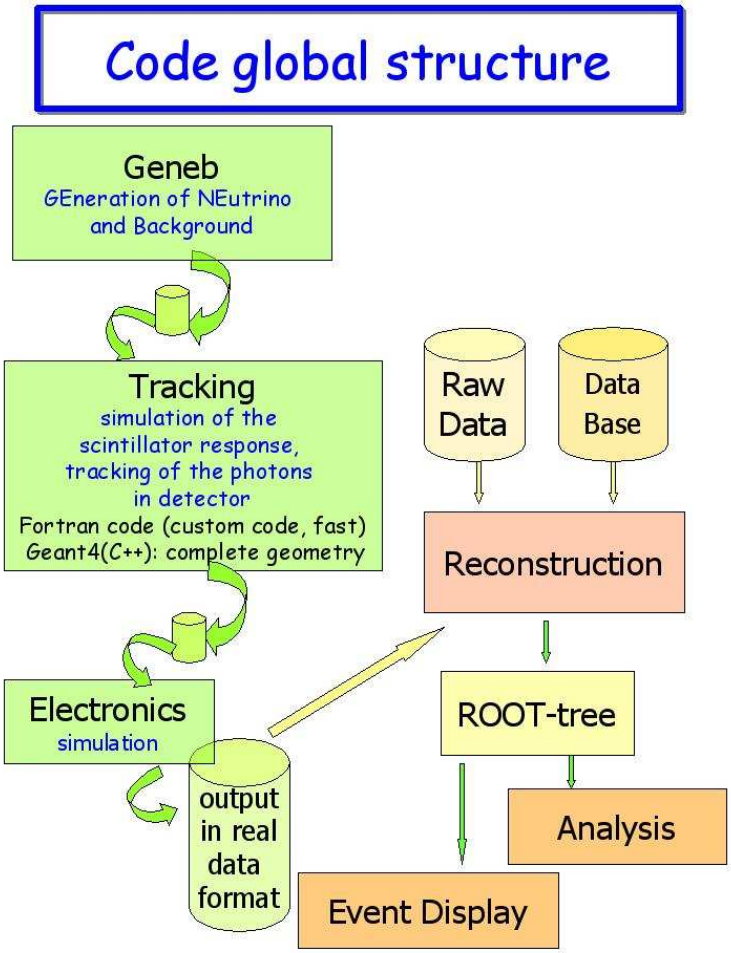

FIGURE 6.1: A SKETCH OF THE BOREXINO SIMULATION CODE STRUCTURE, INCLUDING ALSO THE RECONSTRUCTION CODE AND THE FINAL ROOT FILE.

6.2.1 BACKGROUND EVENTS

The background from the ^{238}U and ^{232}Th radioactive chains is generated from a random choice of the decay modes, based on their branching ratio.
Given the high ionization density and stopping power of α particles we consider their energy to be completely deposited in their generation point and no propagation is thus necessary. β particles and γ -rays cause instead electromagnetic showers and their energy deposits cannot be considered pointlike. Their propagation is handled by means of EGS4 routines [72]. The processes that affect the propagation of the γ -rays are:

- *Photoelectric effect:* $\gamma\ A \rightarrow e^-\ A^*$

- *Compton scattering* $\gamma\ e^- \rightarrow \gamma\ e^-$
- *Pair production:* $\gamma\ (N) \rightarrow e^-\ e^+\ (N)$

The cutoff energy for photon propagation is 5 KeV. In the detector, gamma rays generate large, extended showers: in pseudocumene the average dimension of a shower produced by a 1 MeV γ -ray is 40 cm.
The processes considered for the propagation of electrons and positrons are instead:

- *Möller scattering:* $e^-\ e^- \rightarrow e^-\ e^-$
- *Bhabha scattering:* $e^+\ e^- \rightarrow e^+\ e^-$
- *Elastic scattering from atoms:* $e^\pm\ N \rightarrow e^\pm\ N$
- *Ionization:* $e^\pm\ N \rightarrow e^\pm\ N^* e^-$
- *Positron annihilation:* $e^+\ e^- \rightarrow \gamma\ \gamma$
- *Bremsstrahlung:* $e^\pm\ (N) \rightarrow e^\pm\ \gamma\ (N)$

In the energy range of interest for BOREXINO , the dominant processes are Möller scattering and elastic scattering from atoms. Since the average electron path length of 1 cm (at 1 MeV) can be considered negligible, if the electron does not produce a Bremsstrahlung photon until it reaches the cutoff energy of 10 KeV, the energy deposit is considered pointlike. In addition to the energy and position of the energy deposits, GENEB can also store the information about direction and speed of the relativistic electrons, in order to allow the simulation of Cerenkov light production.

6.2.2 NEUTRINO EVENTS

The incident neutrino source is selected randomly among all sources, with a probability proportional to each source flux. The code chooses then the neutrino energy, accordingly to the SSM predicted distributions. The flavor of the neutrino can be changed from electron to other flavors (ν_μ and ν_τ are not distinguished) according to the survival probability predicted in several neutrino oscillation scenarios.
At this point GENEB decides wheteher the scattering interaction $\nu_x + e^- \rightarrow \nu_x + e^-$ has taken place or not according to the integrated cross section:

$$\sigma_{tot} = \int_0^{T_{max}} \frac{d\sigma(q,T)}{dT} dT \tag{6.1}$$

where T_{max} is the maximum kinetic energy of the recoil electron. The differential cross section for neutrino-electron scattering is given by:

$$\frac{d\sigma}{dT} = \sigma_0 \left[g_L^2 + g_R^2 \left(1 - \frac{T}{q}\right)^2 - g_L g_R \frac{T}{q^2} \right] \tag{6.2}$$

where:

$$\begin{array}{lll} g_r = sin^2\theta_W & & \\ g_L = \frac{1}{2} + sin^2\theta_W & \text{for } \nu_e \text{ -}e^- \text{ interactions} & \\ g_L = -\frac{1}{2} + sin^2\theta_W & \text{for } \nu_\mu \text{ -}e^- \text{ interactions} & \end{array} \tag{6.3}$$

T is the kinetic energy for the scattered electron, q is the neutrino energy, $sin^2\theta_W = 0.23$ and:

$$\sigma_0 = \frac{2G_F^2 m_e^2}{\pi\hbar^4} = 88 \times 10^{-46} cm^2 \tag{6.4}$$

If the interaction occurs, the energy of the recoil electron is generated from the differential cross section 6.2, considering the contributions from charged and neutral current interactions. Obviously, for non-electron flavor neutrinos only neutral currents are considered. Once the kinetic energy of the scattered electron has been choosen, the event is then treated exactly as a standard β event, and is propagated through the medium via EGS4 code.

6.2.3 The code

The different steps of the GENEB simulation are:

1. Read out of the user input file at the beginning of the job. The user can select the number and kind of materials to be put in the detector, the position where the events are generated, the total number of events and the kind of generation to be made (neutrino or background).

2. Read out of the input data files to gather the relevant information about the neutrino and background physics (standard solar model fluxes; branching ratio, particle type and energy of the several background decay modes; ...).

3. Decay selection, accordingly to the user input indications. If a neutrino generation has been requested the code chooses an appropriate solar neutrino-source and determines the energy of the neutrino and of the scattered electron. In case of a background generation the code selects the isotope decay and determines the energy and type of the daughter particles coming from it.

4. Position selection. The starting position of each generated event is selected along the z axis following a z^2 distribution and it is up to the tracking code to take these events and uniformly "*scatter*" them in the detector. The direction of the particle starting the event is always generated randomly.

5. Particle propagation through the medium, accordingly to the kind of particle generated.

6. Output writing, in a binary file, of all the relevant informations: position and relative time of each energy deposit of the shower, some details on the type of decay which originated the event, ... This is the input file of the tracking code.

6.3 TRACKING

6.3.1 THE FORTRAN TRACKING CODE

The tracking code simulates the conversion of the excitation and ionization energy deposited by charged particles in the scintillator into optical photons. The path of the optical photons inside the detector is tracked up until their absorbtion in the detector materials and surfaces or their detection on the PMTs .

The tracking procedure takes into account the following processes:

- scintillation light production, according to the known light yield, decay times, and emission spectrum of PC +PPO ;
- Cerenkov light production, based upon the data on position and direction of the relativistic electrons, stored by GENEB ;
- absorption and reemission processes in the scintillator;
- elastic scattering in the scintillator and in the buffer liquid;
- diffusion on the nylon vessels;
- reflection on the detector surfaces (SSS and light concentrators);
- detection on the PMTs , according to their quantum efficiency;

The light collected on the photocathodes is then converted into a time and charge signal, thus simulating the real data collection.

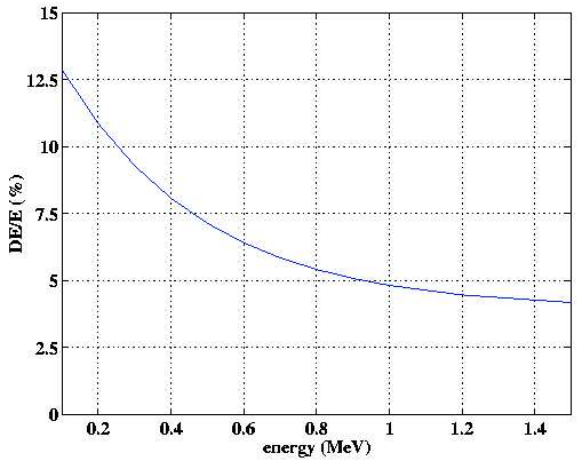

FIGURE 6.2: FRACTIONAL ENERGY RESOLUTION IN BOREXINO , SIMULATED FOR ELECTRON POINT-LIKE EVENTS.

Liquid Scintillator	
radius of spherical volume	4.25 m
fluorescence yield	1.2×10^4 photons/MeV
α quenching factor	Q(E) = 20.3 - 1.3 E [MeV]
emission spectrum	340-450 nm (peak at 370 nm)
decay time (main component)	3.5 ns
absortion length (380 nm)	5.1 m
re-emission probability (PPO quench. effect)	82%
elastic scattering interaction length (380 nm)	4.1 m
refractive index	1.505
Photomultipliers	
total number	2214
distance from center	6.52 m
cathode diameter	19 cm
quantum efficiency (average)	20%
practical coefficient	60%
Light concentrators	
total number	1844
diameter	31.4 cm
length	23 cm
reflection coefficient (inside)	90%
reflection coefficient (outside)	75%
Stainless Steel Sphere	
Radius	6.85 m
reflection coefficient - specular	4%
reflection coefficient - diffuse	36%

TABLE 6.1: MOST RELEVANT PARAMETERS OF THE BOREXINO DETECTOR, USED IN THE TRACKING SIMULATION.

Table 6.1 summarizes some of the main parameters included in the simulation.

From the tracking simulations, we obtain the detector energy resolution: figure 6.2 shows the resulting resolution of electron events as a function of their energy. Electron interactions in the scintillator produce light pulses with, on average, 386 detected photoelectrons per MeV of deposited energy. The energy resolution is 5% at 1 MeV and is found to be inversely proportional to $\sqrt{E}$.

6.3.2 THE GEANT4 BASED TRACKING CODE

GEANT4 is an object oriented simulation toolkit developed at CERN for the next generation of HEP experiments. It has been chosen for the simulation of BOREXINO detector, in order to meet the requirements of high flexibility, extensibility for the user and transparency of physics processes. GEANT4 provides standard instruments for detector geometries definition, for tracking and transportation of particles, for different physics processes and for visualization of the generated events.

Presently a fairly complete simulation of BOREXINO has been written. Comparison with the `Fortran` code results are underway. The tests performed up to now show that GEANT4 is well suited as a tracking software. Some physical processes still missing in the traditional `Fortran` code, like the light reflection on the PMTs photocatodes, can instead be easily added inside this framework, encouraging in using this tool to develop a complete BOREXINO tracking code. An outer detector μ tracks simulation is actually already on going.
Needless to say that the output of this simulation is a binary file with exactly the same data format of the fortran output.

6.4 Simulation of the electronics

This software, based on an Object Oriented design and written in `C++` , reads the tracking ouput file and simulates the whole electronic chain of our data acquisition system.
Basically, the output of the tracking code is a list of times and charges on our internal phototubes. The main job this simulation is then is to provide a main trigger sytem. Yet, the code not only provides the very basic requirements, i.e. a method to decide if a trigger condition has occured, to write the event's record, to transform a *ns* time into a TDC sample,... but implements also all the known behaviours of our system. These include, for istance, the jitter of the trigger signal, the generation of the trigger and laser reference signals, the non-ideal behaviour of the `Laben` boards, the presence of dark noise hits,... The ouput file has then the same format of the real `DAQ` files.
Presently a complete and deeply tested simulation of the internal detector has been written. The simulation of the flash ADC and and of the outer muon veto systems is instead still missing. However the extreme versatility of this code makes it easy to extend the work to other `DAQ` units and some job in this direction has already started.

Structure of the data analysis

7.1 General description of the code structure

Both the DAQ raw data files and the output files generated with the Monte Carlo simulation chain need a complex reconstruction software to convert the list of TDC and ADC samples in a resulting ^7Be flux.

The most important steps of this *offline* software are:

1. data pre-processing and Data Base read-out;
2. conversion of the raw TDC and ADC samples in real times and charges (i.e. expressed in *ns* and in photoelectrons);
3. identification of the multiple events and selection of the hits belonging to the real physical events, discarding the dark noise background;
4. position and energy reconstruction;
5. background rejection and neutrino signal identification.

This software has been already and intensively tested, both on real data and on Monte Carlo data and in the last years has experienced a fast developing phase. So far, only the very last point is still missing[1].

The general structure of the code is sketched in figure 7.1. As for the simulation code, also the offline code is the result of the collaboration of a wide group of physicists. The development of this reconstruction code has been the major part of my PhD activity. More details can be found in the following sections.

[1] The working plan for this very last and high level analysis is to develope an independent code. This will be, basically, a dedicated object oriented tool-kit of flexible analysis cuts and filters.

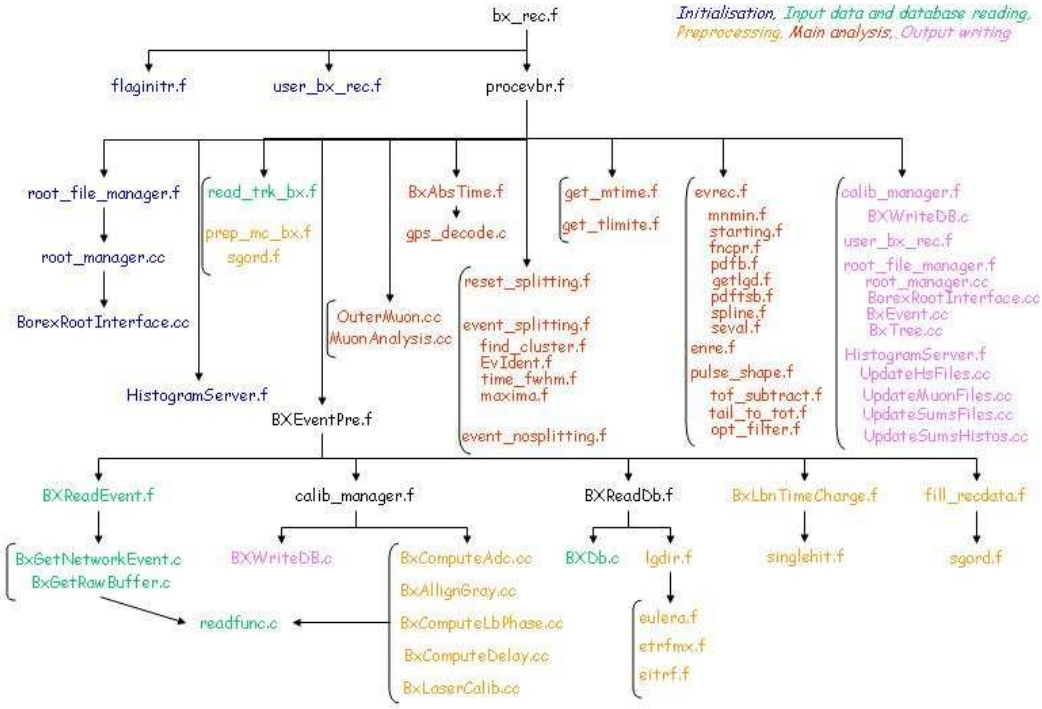

FIGURE 7.1: SKETCH OF THE ARCHITECTURE OF OUR EVENT RECONSTRUCTION CODE.

7.2 EVENT READOUT AND DECODING

Data are gathered from each individual data stream, built together in a single event record and written by the *BorexinoDAQ* process on two dedicated disks of a dedicated PC . These rawdata files are then saved on tape with a back-up procedure.

The offline code reads directly these files. A `C` function (`BxGetRawBuffer.c`) extracts in succession the single event's buffers from the entire file and a simple `Fortran` routine (`BXReadEvent.f`) decodes the single fields of the event format and fills the dedicated common blocks (`event_read.inc`). The structure of the event format is composed of six independent sections:

- *Event header:* contains some general information on the current run and event. The detailed structure is reported in table 7.1.
- *Trigger Record:* two dedicated programs that run on the trigger power PC build the trigger event record with all the relevant informations regarding the status of the trigger and send it to the main `DAQ` process. These informations are: the trigger number, the threshold, the GPS time, the trigger type (see the list in table 5.1), ... The detailed structure is reported in table 7.2.
- *Laben Data:* in the same way, all the informations received by the fourteen `Laben` Crate Receivers are built together in a common data structure and sent to the main

Event Header	*Lenght*	*Offline*
Event size in bytes	4	bxSize
Run Number	4	bxRun
Event Number	4	bxEvent
Bit Field for enabled crates	4	bxCrateFlag
Laben Data Offset	4	iLaben
Sum Data Offset	4	iSums
Muon Data Offset	4	iMuon
MC Truth Data Offset	4	iMCTruth
Event Time as C-like time_t	4	bxTime
Fractional ns event time	4	bxTimens

TABLE 7.1: HEADER DATA STRUCTURE. THE LENGHT IN BYTES AND THE CORRESPONDING OFFLINE NAMES, AS DEFINED IN THE EVENT_READ.INC COMMON BLOCK, ARE ALSO LISTED.

Trigger Record	*Lenght*	*Offline*
Lenght of trigger record	2	TrRecLen
Error flag	2	TrRecErrors
Number of sub-records (1)	2	TrRecords
Daq version	2	TrRecVersion
BTB DSP register 1	2	TrReg1
BTB DSP register 2	2	TrReg2
Trigger threshold	2	TrThresh
BTB firmware revision	2	TrRevision
Trigger time	2	TrTime
Trigger number	2	TrgNum
TAB Sum value	2	TrSum
Trigger Type	1	TriggerType
BTB input channel	1	TriggerChan
GPS word 0,... 4	1	TrGps0,... 4

TABLE 7.2: TRIGGER RECORD DATA STRUCTURE.

`DAQ` process.
The `Laben` boards acquire continuosly the hits coming from each PMT ; when a trigger condition occurs an interrupt signal forces the boards to read and save all their data from 6 μs before the interrupt up to 1 μs later. The saved informations are the TDC and ADC samples of each hit, the 20MHz counter's sample, the logical channel of the hit photomultiplier and some bytes for the DSP 's messages. The detailed structure is reported in table 7.3.

- *Muon Data:* as the inner detector hits' informations are saved in a common `Laben` data structure, also the outer detector informations have their own data record, with

Laben Data	***Lenght***	***Offline***
Number of laben Hits	4	LbNumHits
Number of errors	4	LbNumErrors
Logical channel hit pmt	2	LbHits(i,1)
10 MHz first sampling	1	LbHits(i,2)
10 MHz second sampling	1	LbHits(i,3)
20 MHz counter sampling	2	LbHits(i,4)
Charge baseline sampling	1	LbHits(i,5)
Charge peak sampling	1	LbHits(i,6)
Laben DSP hit flag	2	LbHits(i,7)
Laben DSP error flag	2	LbHits(i,8)

TABLE 7.3: LABEN DATA STRUCTURE.

all the relevant informations concerning the outer PMTs hits.

- *Sums Data:* this structure merges all the informations collected by the FADC data stream.
- *McTruth Data:* contains all the informations coming from the Monte Carlo simulation chain. Both GENEB , the tracking and the electronic simulations *truth* is saved in this structure.

7.3 THE PREPROCESSING ALGORITHM

A precise time reconstruction algorithm that, starting from the TDC data written on the raw file, computes the absolute time of the single event is one of the crucial requirements of our reconstruction software. Theoretically the algorithm to convert these TDC data in *ns* times is quite simple; unluckily, the non ideal behaviour of the `Laben` electronics forced us to develope a specialized pre-analysis code [67] to reach the expected precision on the time measurement.

The software works on a run basis and makes use of the one thousand dedicated CALIBRATION triggers delivered automatically by the BTB at the start of each run (section 5.2.3.2). It is an independent module called at the very beginning of the data processing, before the main loop on the single events starts.
This algorithm is made up of four independent routines: `BxComputeAdc.cc`, `BxAllignGray.cc`, `BxComputeLbPhase.cc` and `BxComputeDelay.cc`. Each routine opens the raw data file, reads only the first one thousand CALIBRATION triggers, decodes the needed variables and computes its pre-calibration parameters. Since these four consecutive readings of the raw data file are time consuming and since some of the computed parameters are strictly connected only to the hardware profile, we decided to store some of these parameters in the `bx_calib` Data Base[2], in a dedicated online profile (*ProfileID*) dependent table (`Laben_PredInfos`).

[2] See section 7.4 for more details on the Data Base structure and logic.

BXReadEvent.f: First event readout and filling of "event_read.inc"

BXDb.c: DataBase read out for present run.
DbCalibFlag value setting.

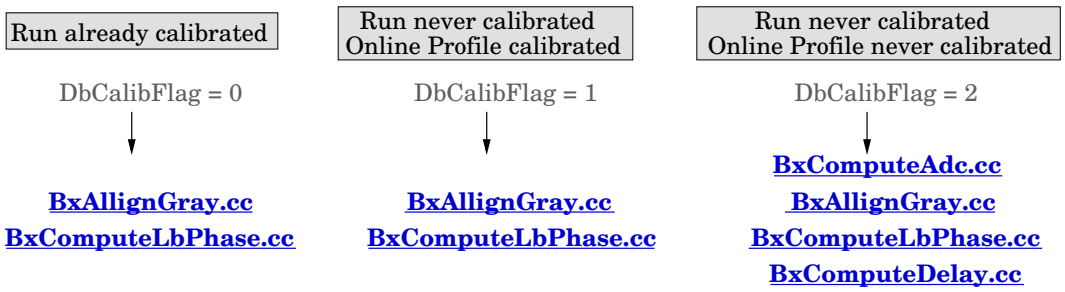

FIGURE 7.2: LOGICAL SCHEME FOR THE CALLING OF THE FOUR PRE-CALIBRATION ROUTINES.

The routine that reads the Data Base (`BxDb.c`), called at the very beginning of the reconstruction - before the predecoding routines, checks if the online profile of the current run was already calibrated and sets the *CalibFlag* parameter. On the basis of this flag, the `calib_manager.f` routine calls the four pre-calibration routines for the non calibrated profiles, but only two of them for the already calibrated ones (see the predecoding logic in figure 7.2).

A brief description of the four routines is reported below.

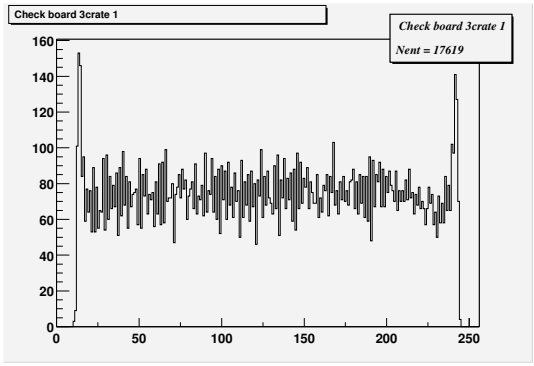

(a) FIGURE 7.3: DISTRIBUTION OF THE LABEN TDC SAMPLES. THE x-AXIS IS TDC COUNTS.

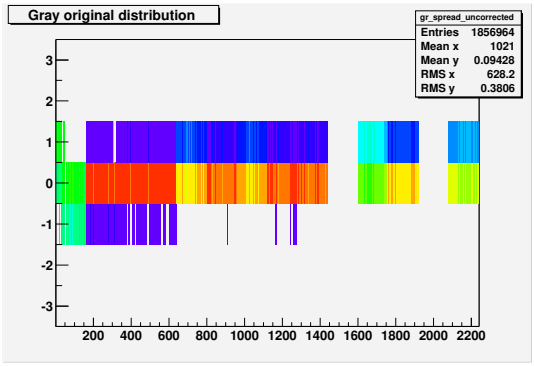

(b) FIGURE 7.3: SPREAD OF THE DIFFERENCE OF THE GRAY COUNTERS' SAMPLES ON CALIBRATION EVENTS. THE x-AXIS IS THE LABEN CHANNEL.

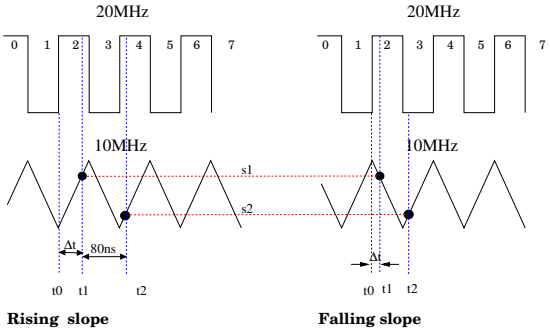

(a) FIGURE 7.4: RELATIONSHIP BETWEEN THE SLOPE OF THE 10 MHz TRIANGULAR WAVE AND THE PARITY OF THE 16-BIT GRAY COUNTER. THE RECONSTRUCTED TIME IS DIFFERENT IN THE CASE OF RISING OR FALLING EDGE.

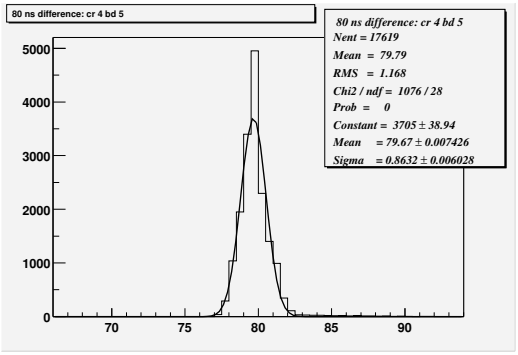

(b) FIGURE 7.4: DISTRIBUTION OF THE NOMINAL 80 *ns* DELAY TIME. THE MEAN VALUE IS USED IN THE OFFLINE CODE FOR THE SINGLE HIT TIME RECONSTRUCTION. THE x-AXIS IS *ns* .

- *BxComputeAdc.cc:* called only at the first reconstruction of an uncalibrated online profile. It opens the raw data file, reads the first one thousand CALIBRATION triggers decoding only the `Laben` time informations, and fills 2240 histograms with the 10 MHz triangular wave samples of each channel. The typical histogram (see figure 7.3(a)) is a flat distribution between the minimum and the maximum excursion values of the wave samplings and two accumulation areas close to these edges [67]. The routine computes, for each channel, the exact position of these edges and writes these informations in the Data Base.

- *BxAllignGray.cc:* called always. This routine was developed to correct the small fraction of sistematic shifts of one counter's clock (50 *ns*) that can arise if the RESET signal crosses the clock (see section 8.2.1). The routine opens the raw data file, reads the first one thousand CALIBRATION triggers and plots the distribution of the differences between the gray counter of each channel with the one of a single reference channel. Since these events are synchronous we should find a flat distribution; the typical distribution, reported in figure 7.3(b), is instead different. The shifts plotted in this figure are exactly the time corrections that must be applied to each gray counter to realign it with all the others.

- *BxComputeLbPhase.cc:* called always. This routine is executed to retrieve *"a posteriori"*, through an heuristic method, the relationship between the 10 MHz triangular wave of each `Laben` channel and the 20 MHz counter[3]. This relationship is run dependent, but its knowledge is fundamental for a good resolution of the hits' reconstructed times (see figure 7.4(a)).
  The raw data file is read for the third time and, for each hit of the first CALIBRATION triggers, the time relative to the 50 *ns* window is evaluated in the two hypothesis of

[3] This is what is called the parity of the 10 MHz triangular ramp in [67].

having the first TDC sample on the positive and on the negative slope. Then in both cases the hypothetical position of the second TDC sample, 80 *ns* later, is calculated and compared to the real value. If one of the two projections is close enough to the real value and the other one far enough, the parity of that hit is determined; otherwise we simply ignore the hit. Applying this routine to a great number of events (one thousands events) we can reach enough statistic to determine with a low error the relationship between the parity of the gray counter and the ramp.

- *BxComputeDelay.cc:* like `BxComputeAdc` also this routine is called only at the first reconstruction of a new online profile. It opens the raw data file, reads the first one thousand events, computes the time of the first and of the second samples and fills a 2D histogram with the time differences of each channel. The typical histogram (see figure 7.4(b)) should be a narrow, few *ns* wide, gaussian distribution, peaked around the nominal delay time (80 *ns*). The mean values of these gaussian distributions are then written in the Data Base and used by the main code to compute the time of those hits whose first time sampling is not reliable (for example because it is near the edge of the triangular wave).

7.4 Data Base interface

PostgresSQL is a free client-server data base package, SQL compatible. Many different software products can access the Data Base, to read or write data, from any remote host machine. The acces can be realized both using interactive interfaces or any software program, through an Application Program Interface. An API library is basically a set of functions that allow the programs to open connections to the DB , submit queries and recover data. The API library used for our reconstruction code is written in `C` .

Our main Postgres server is installed on one of the local PCs and a dedicated `C` interface allows the reconstruction program to connect to the DB from every machine[4].
The data stored in the our Data Base can be divided in 5 main groups (see figure 7.5), that allow different Postgres Data Bases.

The first group, composed of three DBs , is the `DAQ` group: it is filled by *BorexinoDAQ* during data taking and stores all the informations needed to describe the status of the detector during the run. A few examples are the mapping and settings of the `Laben` boards, the map of the crate enabled and the trigger configuration.
The second group is the offline group. Its three Data Bases are divided on the basis of the time-scale varibility of their parameters. The first (`bx_geometry`) stores the electronics mapping and all the hard-wired parameters needed to build the detector's geometry. The second (`bx_physics`) contains instead all the time independent parameters with a physical meaning, like the photon yield, the quenching factor, the time decay constants,... Finally the last one (`bx_calib`) handles the time dependent parameters of the detector. The nylon transparency, the scintillator decay constants and properties are some examples, but also some of the parameters computed during the reconstruction, e.g. the predecoding constants or the PMTs timing equalization constants, are written here.
The third main group is the *online monitor* Data Base. When, during data taking, we run the offline as an *online monitor* (see section 5.4) we produce a set of well defined and run dependent histograms, that are stored in this dedicated DB .
Finally, also all the relevant informations needed to describe the status of our electronics (High Voltages, Low Voltages and VME) and fluid handling plants have their own Data Bases.

[4] Actually, for security reasons, the external machines used to run the offline should be authenticated by the main Postgres server.

The organization of the single Data Base is hierarchical: each DB is a list of tables and each table, composed of different fields, is a list of records. Figure 7.6 shows, as an example, the schematic structure of the `daq_config` data base and of its `LabenChannelMapping` table.

Data Base	Process involved
daq_config	DAQ
daq_users	DAQ
daq_histograms	DAQ
bx_geometry	Offline
bx_calib	Offline
bx_physics	Offline
bx_slow	Slow_Control
bx_fluid	Fluid Handling
channelhistory	Analyzer

FIGURE 7.5: BOREXINO DATA BASES LIST. THEY CAN BE DIVIDES IN 5 MAIN GROUPS, ACCORDINGLY TO THE DATA STORED AND TO THE MAIN PROCESS INVOLVED IN READING AND WRITING THE RELATIVE INFORMATIONS.

To handle this large number of tables and Data Bases, we have introduced two extra keys besides the run number: the online profile (ProfileID) and the calibration profile (CalibProfile) numbers.
The first is linked to the hardware profile of the detector: different runs can share the same online profile and a new online profile is generated only when some work is done on the apparatus (changing some boards, cabling new PMTs , ...). Actually most of the parameters stored in our Data Bases, e.g. the electronic mapping, depend only on the hardware profile of the detector. If we write then the relative DB tables as a function of the ProfileID key instead of the run number, we avoid to duplicate a lot of informations. Then, a single run-dependent table maps each run number to its online profile key. As an example, the complete list of tables of the `daq_config` Data Base, together with their contents and key-access, is reported in table 7.4.
The same logic holds for the CalibProfile number and the slow time-dependent calibration parameters, like the nylon trasparency, the scintillator properties, ...

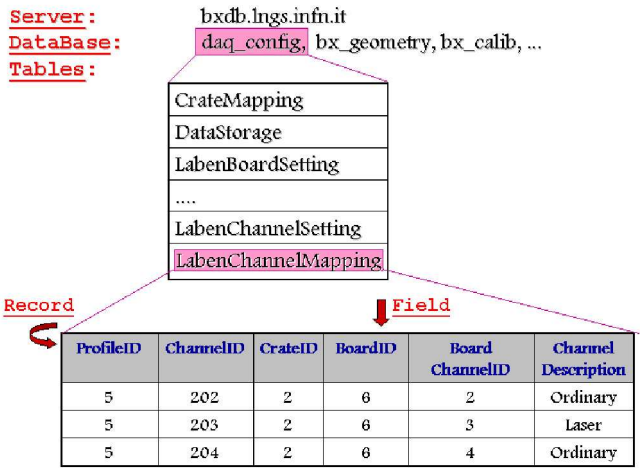

FIGURE 7.6: BOREXINO DATA BASE STRUCTURE.

Table	*Key Access*	*Contents*
CrateMapping	ProfileID	Crate addresses and Daq enables
DataStorage	RunNumber	Raw data back-up infos and records
LabenBoardSetting	ProfileID	Laben boards trigger enables
LabenChannelMapping	ProfileID	Channel description
LabenChannelSetting	ProfileID	Laben channels thresholds and enables
Logging		
MuonChannelMapping	ProfileID	Some TDC and QTC parameters and channel description
MuonGeneralSetting	ProfileID	TDC general parameters
Profiles	ProfileID	List of existing online profiles
Run	RunNumber	Run number/online profile association
SumsBoardSetting	ProfileID	FADC channel enables and parameters
SumsChannelMapping	ProfileID	FADC mapping
SumsGeneralSetting	ProfileID	FADC general settings
Trigger	ProfileID	BTB/MTB thresholds and settings

TABLE 7.4: DAQ_CONFIG DATA BASE: LIST OF TABLES.

The real interface between the offline code and the Data Base is the `C` routine `BXDb.c`. At the first call it reads from a file the configuration parameters to open the connection with the Postgres Data Base (the name server, the port numbers, the Postgres user, ...) and opens, sequentially, a connection with each one of the above mentioned Data Bases. An SQL query reads then the different tables and copies the field values in some dedicated `Fortran` common blocks.
Since the offline code can process sequentially different runs in the same job and since different runs can share the same online and/or calibration profiles a check on these profile numbers is also done. Every time the run number changes the routine compares the online and calibration profiles of the new run with the old ones. If one of them or both are unchanged the connection with the online and calibration profile dependent tables is skipped and the code makes use of the values already stored in its common blocks.

The Data Base writing logic is handled in the same way by the `BXWriteDB.c` routine. The parameters computed and written in the Data Base by the offline code are the precalibration constants and the dark noise and laser calibration constants. The former are automatically written every time a new online profile is reconstructed. Both the dark noise and laser calibration constants are instead computed and written only if a dedicated flag is enabled. This can be done only by a special user and on special runs (dedicated timing laser runs for the PMTs equalization constants or dark noise runs for the detector's status and dark noise).

7.5 EVENT SPLITTING

The identification of two separate events recorded in a single trigger record (7 μs time window) is one of the crucial points of our reconstruction. Both delayed coincidences or random events may produce these double or multiple events and a dedicated 'splitting'

package should be able to identify them. Moreover, both in the case of single or multiple events, the code must be able to select only the hits belonging to the real events, discarding the dark noise hits.

The main *splitting* routine (`BxCluster.cc`) is merely a list of calls to some methods of the BxEventFragment class (see section 7.8). This has the advantage to let the user free to work even interactively inside ROOT , without any need to reprocess data.

The main steps of the routine are:

1. Identification of the number of physical events in the current trigger record.
   The mean dark noise rate of the detector for the current run is read from the Data Base and the number of dark noise hits expected in 16 *ns* is computed. The photons' times are then binned in 16 *ns* bins and the routines looks for the first bin over this dark-noise threshold: this is a cluster candidate.

2. Re-application of a sofware trigger threshold.
   When a cluster candidate is found, the number of hits collected in the first three consecutive bins (48 *ns*) is compared with the trigger threshold[5]. If this number is below 90% of the setted threshold the candidate is discarded.

3. Check with the trigger time for the first cluster.
   For each event a copy of the trigger signal is also acquired (see section 8.2.3). Besides the jitter time of the trigger signal (100 *ns*), this gives a precise internal timing between the hits and the trigger. Particularly, the delay between the triggering light and the trigger signal is ~ 2 μs . The time of the first candidate cluster must fullfill this requirement.

4. Identification of the first photon of the cluster.
   We use again the mean dark noise rate of the detector, read from the DB , to compute the mean time separation between two consecutive dark noise hits. Then, starting from 30 *ns* before the start time of the candidate cluster, we look for five consecutive photons with a time delay below one third of the dark noise expected value. Actually, when the dark noise rate is low (a few KHz), this delay time is some tenths of *ns* : this means that also only one wrongly selected dark hit can heavily affect the cluster's start time. A second loop is then done to look for a more stringent condition: three consecutive photons with a delay below 3 *ns* . If this condition is found the first of these three photon is taken as the first photon of the cluster; otherwise the first of the five is taken.

5. Identification of the last photon of the cluster.
   We decide the cluster ends when three consecutive 16 *ns* bins are found to be less than the same dark noise threshold computed in point 1. The end time is taken as 50 *ns* more than the time of the last bin.

This routine has been already tested both with Monte Carlo and real data; the results are presented in section 8.9. However, a secondary and more sofisticared analysis to study the shortest delayed coincidences, with the two events almost overlapped, is still missing.

[5] A threshold of K PMTs requires exactly K PMTs in trigger in a 48 *ns* time window.

7.6 Event reconstruction

7.6.1 Spatial Reconstruction

In order to perform fiducial volume cuts and external background reductions, it is important to have a good position fitter code that, given the charge and time signal at the phototubes for each event, calculates the event position. The existing fitter is essentially a vertex reconstruction, based on the principle that the shape of the time signal distribution depends on the distance between the event and the detector's center.
Actually the time which passes from the excitation of the scintillator until the time when the photomultipliers detect the photons has the following components:

- *Event time:* the time when the energy is deposited and the scintillator excited (astronomical time);
- *Scintillator decay:* the emission of a photon is delayed due to the scintillator decay time;
- *Time of flight:* the propagation of a photon from the excitation point to its photomultiplier takes a time t_f that depends on the event's position;
- PMT *time jitter:* this time is due to the different transit times in the photomultipliers.

The idea is then to use the phototube hit time signal corrected for the time of flight to maximize, with the resources of the MINUIT code [75], the likelihood function:

$$L(t_{ev}, \vec{\mathbf{r}}_{ev}) = \prod_{i=1}^{N} f(t_i; t_{ev}, \vec{\mathbf{r}}_{ev}) \tag{7.1}$$

The probability density function $f(t_i; t_{ev}, \vec{\mathbf{r}}_{ev})$ (p.d.f.) describes the probability that a photon detected at time t_i by the i-th phototube has originated in the space-time coordinates $(t_{ev}, \vec{\mathbf{r}}_{ev})$. It takes into account the properties of scintillator and phototubes. At this stage, the p.d.f. is calculated with the Monte Carlo method; a more realistic distribution will be provided by a calibration source in the detector.
To make the reconstruction procedure faster and more efficient a rough event position is determined by calculating the center of gravity of the hit PMTs . The maximum likelihood method finds then more precise values starting from these initial position.

The resolution of the spatial reconstruction is directly proportional to the error of the single time signal and inversely proportional to the square root of the number of hits of the fragment.

7.6.2 Energy Reconstruction

The simplest way to define the energy of an event is to assume a linear dependence of the collected charge (N_{pe}) on the event energy (E), through the scintillator light yield factor ($Y\ [p.e./MeV]$):

$$E = \frac{N_{pe}}{Y} \tag{7.2}$$

The relative energy resolution is then inversely proportional to the number of detected photons:

$$\frac{\Delta E}{E} = \frac{1}{\sqrt{E \cdot Y}} \tag{7.3}$$

Actually the energy resolution of this method is limited by the finite resolution of the PMTs and the real energy resolution is not following the precise $1/\sqrt{N_{pe}}$ law. A possible strategy to achieve this theoretical limit improving the reconstruction algorithm has been already studied. More details can be found in reference [74].

7.7 Particle identification

This is one of the last steps of our analysis. So far only some work on α/β discrimination, based on pulse shape analysis, has been implemented. Pulse shape discrimination is a key property in many applications involving liquid scintillators. It is very often used to discriminate the desired signal against the unwanted background which is affecting the measurement. Here the PSD is exploited to identify the alpha induced signals produced by the natural radioactivity, essentially ^{238}U and ^{232}Th , allowing to disentangle the true neutrino signal from these alpha background events.

Even if the real work done so far was dealing only with an α/β discrimination, we have developed a more general particle ID framework. This framework is basically a set of C++ *BxClassifier* and *BxSample* objects and its structure is depicted in figure 7.7.

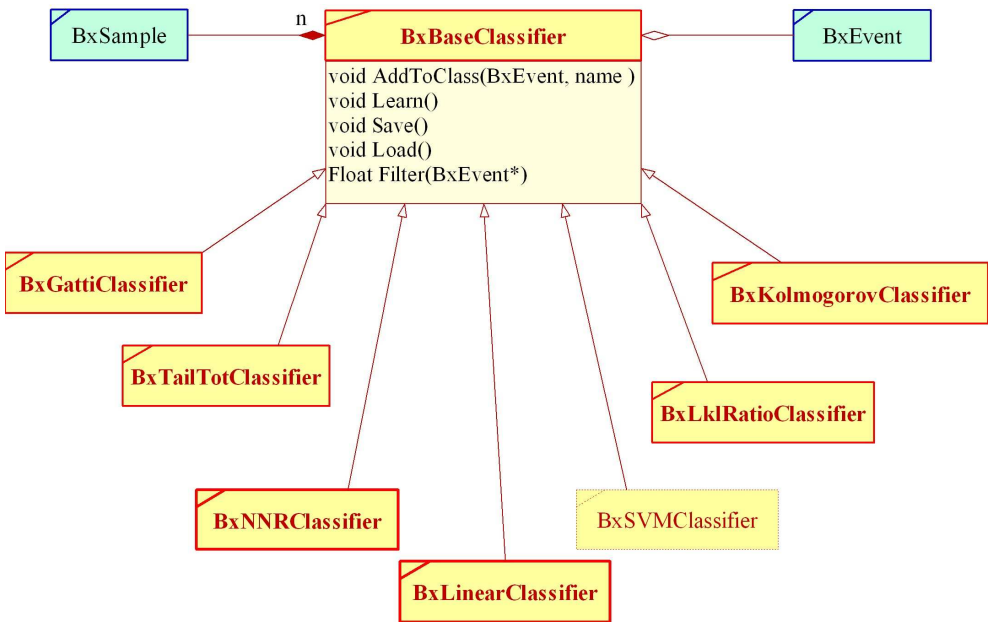

Figure 7.7: structure of the root based particle ID package.

Each classifier handles a list of events (each of them internally described as a *BxSample*

object, i.e. a vector of real numbers) and a list of learning and filtering function. Events of the different types (e.g. α and β) are grouped in classes[6]and each classifier returns a discriminating variable that tells how well a given event can be associated to a defined class. Some classifier can easily perform classification among more than two classes, while some of them are designed for two classes only. The classifiers are designed to be used in the offline program as a filter or interactively using ROOT .

The discrimination methods already implemented, and briefly described in section 9.1, are the tail to total ratio (*BxTailClassifier*), the Gatti Filter (*BxGattiClassifier*), the likelihood function (*BxLklClassifier*), the Kolmogorov distance (*BxKolmogorovClassifier*), the nearest-neighbor technique (*BxNNRClassifier*) and the Support Vector Machines.
The only exception are Support Vector Machines, that are not yet implemented as a standard *BxClassifier*. We have used a `WEB` available code, named $\mathcal{SVM}$ *Light* [76], as a stand-alone module, and a set of ROOT macros to interface the two programs. Yet, a real integration of this code in the general *BxClassifier*s framework is already foreseen.
This `WEB` code is made of two independent programs, one for the learning phase and one for data classification. The main degrees of freedom we have in selecting the Support Vector Machine are the choice of the kernel function and of the relative parameters and some learning options, like the factor by which training errors on the examples of one class outweight the errors of the other class or the possibility to remove inconsistent training examples and retrain the learning.
Some preliminary results obtained with this PID framework on real data and on α/β discrimination are reported in chapter 9.

7.8 Interface to ROOT

ROOT is an object-oriented `C++` analysis package written by the creators of PAW. The main justification for us to move from PAW to ROOT was the possibility to use the *TTree* object. Basically a *TTree* is the equivalent of a PAW Ntuple, though far more powerful. An Ntuple is limited to only hold floating-point numbers, while a *TTree* can hold all kind of data, such as objects or arrays, in addition to all the simple types.
Moreover the *TTree* class is optimized to reduce disk space and enhance access speed. Each *TTree* object is not written individually, but rather collected and written a bunch at a time: this is where the *TTree* takes advantage of compression and will produce a much smaller file than if the objects were written individually.

7.8.1 Output data structure: the BxTree class

The output data structure foreseen for BOREXINO analysis is a `BxTree`, that is a collection of `BxEvent` objects. The `BxEvent` class, created to easily store and manipulate all the informations of an event, is made of several subclasses (see table 7.5).

More precisely:

- *Class BxEventHeader:* stores some general informations of the current event. Its structure is reported in table 7.6.

[6] A class is described by a vector of *BxSample* objects and each class is given a name.

BxEventHeader header ...	event header infos
BxMuonVeto muon	outer muon veto infos
BxSums fadc	flash adc infos
TClonesArray *frags	list of *BxEventFragment*s
TClonesArray *hits	list of the inner detector's *BxHit*s
TClonesArray *muon_hits	list of the outer detector's *BxMuonHit*s
TClonesArray *mc_frames	list of the MonteCarlo's *BxMcTruthFrame*s

TABLE 7.5: BXEVENT CLASS DETAILED STRUCTURE.

***BxEventHeader* class**	
run	run number of the current event
evnum	event number (trigger ID)
sec	seconds since 01-01-2000
nsec	nsec since 01-01-2000
trgtype	trigger type for the current event
btbin	input channel number on BTB board
nfrags	number of fragments the current event was split
dtprev_event .	time after previous trigger
dtnext_event .	time to next trigger
nprev	event number of previous event
nnext	event number of next event
hits_event ...	number of hits for the current event
pmts_event ..	number of hit pmts for the current event
trgtime	mean `Laben` time for trigger reference signals
lasertime	mean `Laben` time for laser reference signals
lbtrgtimes[14]	`Laben` time of the 14 `Laben` reference times
lbtrggray[14] .	Gray time of the 14 `Laben` reference times

TABLE 7.6: BXEVENTHEADER CLASS DETAILED STRUCTURE.

- *Class BxMuonVeto:* stores the data coming from the muon veto reconstruction software.
- *Class BxSums:* stores the data coming from the FADC reconstruction software.
- *Class BxEventFragment:* stores the data coming from the "*event splitting*" routine. At each trigger all the hits acquired by the `Laben` boards in a 7 μs window are collected and merged together in a single data structure. The "*splitting*" routine discards the dark noise hits, finds the double events patterns, identifies the single *fragments* and fill this structure with all the relevant informations. The detailed structure is reported in table 7.7.
  A maximum of three fragments are expected for each event and all the fragments found

for the current event are stored in a `BxEventFragments` array (the *"frags"* array in table 7.5).

***BxEventFragment* class**	
energy[3]	nominal beta energy for the different reco methods
x[3], y[3], z[3]	position in cartesian coord for the different reco
r[3], theta[3], phi[3]	position in polar coord for the different reco
cov[3][4][4]	covariance matrix for the different reco (cart coord)
tfrag[3]	time relative to the absolute time for the different reco
photon_time	*ns* time of each photon after *tof* correction
npe	number of detected photoelectrons
nhits	number of hits
npmt	number of hit pmts
npmt_conc	number of hit pmts with concentrators
mean_time	meant time of all detected photons
tail75	tail to total PSD parameters at 75
tail90	tail to total PSD parameters at 90
optpsd	linear Optimum filter PSD parameter
palpha	probability for the particle to be alpha
pbeta	probability for the particle to be beta
pgamma	probability for the particle to be gamma
pmuon	probability for the particle to be a muon
uptot	energy in the upper hemisphere / total energy
conctot	energy in the concentrators / total energy
dtprev	time after previous fragment or trigger
dtnext	time to next fragment or trigger

TABLE 7.7: `BxEventFragment` CLASS DETAILED STRUCTURE.

- *Class BxHit:* stores the relevant informations of the single inner detector's hit. For each `BxEvent` an array of `BxHits` (*"hits"*), with all the current hits, is stored. The detailed structure is reported in table 7.8.
- *Class BxMuonHit:* since the informations and parameters needed for data analysis of the inner and outer detectors are different, two separate hit's structures have been foreseen for the two detectors. Also an independent array (*"muon_hits"*) with the list of the outer detector's hits is then foreseen.
- *Class BxMcTruthFrame:* stores the *simulation truth* data coming from the Monte Carlo chain.

This is the complete list of informations available, for each event, to the ROOT user for data analysis. Actually some informations are more general and depend not on the single event, but on the run number; this is the case, for example, of the PMT mapping or of the time equalization constants. To save disk space these kind of data, still fundamental for data analysis, are stored in a more general class: the `BxTree` class.

***BxHit* class**	
lg	logical channel of the hit pmt
flag	valid hit flag
bs	charge baseline sampling (Adc count)
pk	charge peak sampling (Adc count)
adc1	first sample of the 10MHz ramp (Tdc counts)
adc2	second sample of the 10MHz ramp (Tdc counts)
gray	sample of the 20MHz gray counter
guess	time info: guess_slope (singlehit.f)
slope_error	estimation of the hit error
d80	80 *ns* reconstructed value
rawt	*ns* time in the 3.2 ms window
t	*ns* time related to trigger/laser time
q	p.e. charge corrected for pile-up
wg[i]	probability to belong to i-th fragment

TABLE 7.8: BxHit class detailed structure.

The `BxTree` class is, first of all, the container of the `BxEvents` list, but it also holds the complete hardware mapping[7] and a set of methods to return informations like the PMT 's position, the PMT 's fiber bundle, the PMT 's `Laben` channel, ...
In addition, this class contains also three special sub-classes: `BxPredecoding`, `BxCalib` and `BxDark`. These classes were created mostly for debugging reasons and they will probably be removed from our future `BxTree` structure. The first class was created to store the precalibration parameters computed by the offline during the preprocessing phase. The other two are instead filled only when a dedicated flag is enabled and are devoted to store the PMTs time and charge equalization constants (`BxCalib`, see section 7.10) and the detector status' parameters (`BxDark`, see section 7.9). The detailed structure of `BxPredecoding` and `BxDark` classes is reported in tables 7.9 and 7.10.

7.8.2 The ROOT interface routines

Being ROOT an object-oriented `C++` package, the creation and the filling of the `BxTree` structure is done in `C++` . An interface between the already existing `Fortran` code and this ROOT -based structure is then needed. This job is done with two routines: `BorexRootInterface.cc` and `root_manager.cc`. The first defines the set of `C++` functions necessary to manage the ROOT file (to open and close the file, to fill the BxTree, to save the created histograms, ...) and the second provides the `C` wrapping of these methods. This allows us to call them even inside the `Fortran` code. Then, a list of pointers to structures that are identical to the `Fortran` common blocks permits the transparency between the `Fortran` and the `C++` data.

The `BxTree` is then filled run time, event by event, and the handling of the ROOT file is automatic: a separate file is written for each of the processed runs and saved in a dedicated

[7] From the positions of PMTs ' holes inside the SSS to the front-end and Laben channels.

***BxPredecoding* class**	
phase[2240]	phase of the gray counters
grshift[2240]	shift of the gray counters
grerr[2240]	error on previous shift
gr_phase	2D histo: gray phase bitmap
gr_correction	2D histo: gray counter shift correction
gr_spread_uncorrected ...	2D histo: gray c. spread ordinary channels
trg_gr_spread_uncorrected	2D histo: gray c. spread trigger channels
lsr_gr_spread_uncorrected	2D histo: gray c. spread laser channels

TABLE 7.9: BXPREDECODING CLASS DETAILED STRUCTURE.

***BxDark* class**	
rate[2240] ..	computed dark rate for each Pmt
pmt_gate ...	2D histo: hits' times distribution
pmt_rates ..	2D histo: dark rates
pmt_alive ..	2D histo: alive value
pmt_outgate	2D histo: % of hits outside the gate
alive	2D histo: dark rate vs. alive value
outgate	2D histo: dark rate vs. % of hits out gate

TABLE 7.10: BXDARK CLASS DETAILED STRUCTURE.

directory.

7.9 THE DARK NOISE RUNS ANALYSIS

A RANDOM GATE trigger is generated by the BTB at an arbitrary time: it is completely uncorrelated from any light pattern and acquires only the dark noise hits of the phototubes. During the standard data taking a small fraction of RANDOM triggers is always present, but we may also have dedicated random noise runs.
These events offer an easy handle to monitor the status of the detector. In particular we use these events to compute the single PMT 's dark rates and some statistical information, like the mean dark rate of the detector, the number of dead, disconnected or hot PMTs , the number of PMTs with high rates of `Laben` errors, ... All these parameters are then written in the Data Base, in two dedicated tables, and used for high level analysis. The splitting algorithm, for examples, makes use of the mean dark rate of the detector to set its candidate-cluster threshold.

A dedicated offline module (`DetectorEfficiency.cc`), called only when a proper flag is enabled, processes only these random triggers, filling 2240 histograms with the distributions of the time of the hits inside the 7 μs gate window. These histograms, one for each PMT ,

are then fitted with a flat function and the fit parameters are used to infer the PMT 's dark rate. Also the run's statistics is inferred from these histograms.
Some of the results obtained with this random noise events are reported in section 8.6.

7.10 Time and charge calibration routines

7.10.1 The time calibration

The multiplexed system of optical fibers described in section 3.3.9.1 has been designed for the time and charge calibration of the 2200 PMTs mounted inside the BOREXINO Stainless Steel Sphere. Its time accuracy, under 0.05 *ns* , is much better than the PMT time jitter and the detector's time resolution is therefore dominated by the time spread of the PMTs .

I already explained (section 5.2.3.4) that during the standard data taking only a few Hz rate of LASER394 triggers are acquired, but also some dedicated calibration laser runs, with 200 Hz of laser triggers, will be taken on purpose.
These data allows us to improve, offline, the inter-PMT time equalization of the detector. The time calibration parameters consist of the time differences among the responses of all the PMTs to the common and simultaneous laser light pulse. The time spread of the laser light on the whole detector is ∼4 *ns* (see figure 7.8(a)), but the single PMT spread is instead less than 2 *ns* (see figure 7.8(b)).

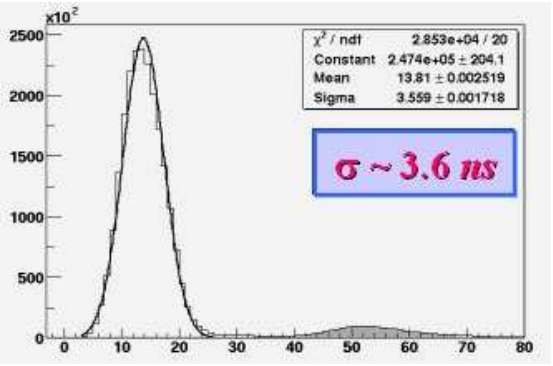

(a) Figure 7.8: direct light peak and first reflection peak obtained with the calibration laser data on the whole detector. The x-axis scale is *ns* .

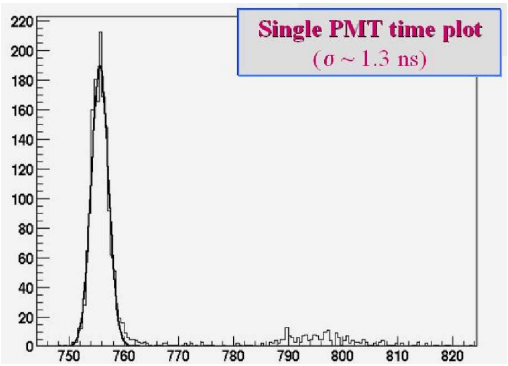

(b) Figure 7.8: direct light peak and first reflection peak obtained with the calibration laser data on a single PMT . The x-axis scale is *ns* .

A dedicated time calibration routine filters the timing laser events, fills a 2D histograms with the time difference between the laser pulse and the hits of each PMT , fits the direct light peak with a gaussian function and takes these mean values as the needed calibration constants.
Actually, all good PMTs have the same plot: a constant and low background in the whole

gate window, a sharp central peak in coincidence with the direct laser pulse and a much smaller peak, the reflected light peak, about 41 *ns* later. In order to exclude the reflected light from the gaussian fit, the fit range is limited to 20 *ns* around the central value. The typical standard deviations are $1.2 \div 1.6$ *ns* , very close to the PMT 's jitter time value.
These values are then written in a dedicated table of our Data Base and treated as constant shifts to be added to the time of each hit during the standard reconstruction.
This calibration procedure has been already implemented and tested and the results are presented in section 8.4. However, some improvements are still on going. For istance, no correlation between the charge and the PMT pulse rise time has been taken into account so far.

7.10.2 The charge calibration

The same timing laser data used for the inter-PMT time equalization of the detector, are used also for the charge calibration.

The charge calibration consists in finding the conversion factor between the measured ADC channel number and the number of photoelectrons detected. The centroid of the single electron response peak is the calibration parameter.
The precise determination of the single response of the phototube requires very low illumination level, between 1%p.e. and 5% p.e., in order to reduce both the contribution of dark noise and multi-electron pulses to less than 1%.

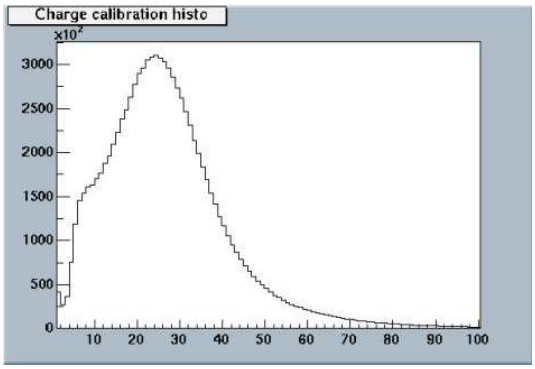

(a) Figure 7.9: typical charge spectrum for a calibration run. The x-axis scale is adc counts.

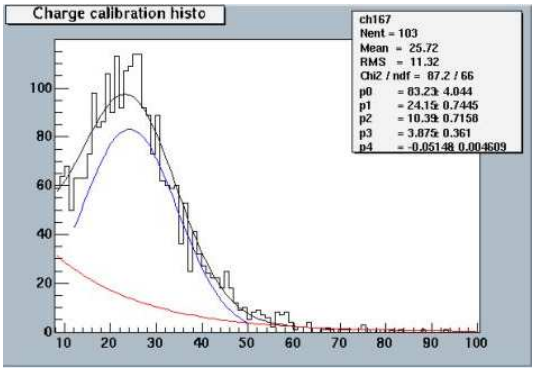

(b) Figure 7.9: exponential contribution to the single photoelectron peak due to the thermoionic noise from dynodes. The x-axis scale is adc counts.

A typical charge spectrum from a calibration run is shown in figure 7.9(a). The single photoelectron peak is basically the sum of a gaussian function with two exponetial decays: the first, in the low energy range, is due to the thermoionic noise from dynodes; the second is instead a tail at higher energies due to the non-gaussianity of the single photoelectron signal. Actually, our `Laben` boards threshold cuts completely the low energy exponential contribution (figure 7.9(b)).
The calibration is then performed with a simple gaussian fit of the charge spectrum, within

3 σ from the central peak. Some deeper studies on the PMTs charge linearity and on the `Laben` threshold effect are still on going.

The Air Runs data

In 2002/2003 we had several periods of data taking with all available PMTs on: the so called *Air Runs*. All data were collected with the detector still empty: up to now none of the two nylon vessels have already been installed and the sphere is filled with air. About 2000 PMTs are already mounted and cabled and only the 200 PMTs on the lower part of the sphere and on the door are still missing.

These data gave us the oppotunity to debug our detector, both from the hardware and the software point of views. Since the first period, a lot of improvements have been done. The main electronics and trigger systems have been fully tested using electronics, laser pulses and radioactive sources hanged inside the sphere. The main trigger is now in its final configuration. A scaler system, devoloped at the Moscow university, has been installed and integrated in the DAQ system. A problem related to the bad quality of the low voltage front end connectors has been identified and solved.
Extensive work has been done also on the electronics and DAQ software of the outer muon system. All hardware has been tested and installed; the PPC software was completed and the outer system has been integrated into the complete DAQ software and into the trigger system. The installation of a dedicated LED calibration system is on going.

Finally also the construction of the FADC boards has been completed and more than 50% of them are already installed in Hall–C . DAQ is up and running in all parts and the system. Fine tuning is in progress.

I have personally partecipated to all Air Runs, working both on hardware debugging and on software development.

8.1 The first low level debugging

The first two periods of data taking were the very first tests of the whole electronics and DAQ chain and the debugging level was actually focused on very basic items.

At first we turned on high voltages and carried out an accurate check of the PMTs status. We identified about 150 bad channels, among bad HV cables, bad front-end or digital electronics channels and bright or flashing PMTs . Figure 8.1 shows the phototubes dark rate distribution during the first days of Air Run I and immediately after a flasher PMT was found and turned off. This accurate and methodical job of channel-by-channel monitoring of the phototubes conditions has been repeated during all following air runs and today we have a very clear map of the individual PMTs status. More than 30 dead or problematic PMTs were removed and replaced with the spare ones.

Later on the trigger system has been operated and tested in different ways: with external triggers from a pulser or from the laser SYNC output and in its internal mode, setting the number of hit PMTs in trigger.
The laser controller was interfaced to the trigger system and both the timing fibers and

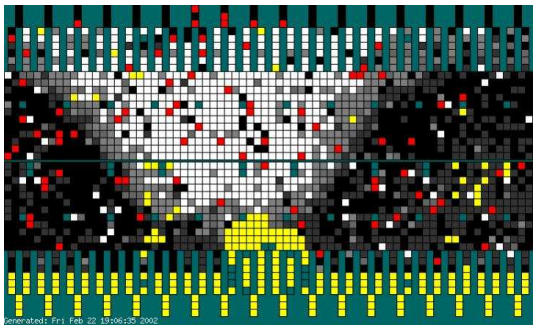

(a) FIGURE 8.1: DARK RATE MAP OF THE DETECTOR WITH A FLASHER PHOTOTUBE LIGHTENING THE FRONT-SIDE PMTS . THE COLOR-CODE IS WHITE FOR THE HIGH RATES (SEVERAL TENS OR EVEN HUNDREDS OF KHZ) AND DARK FOR THE LOWER ONES.

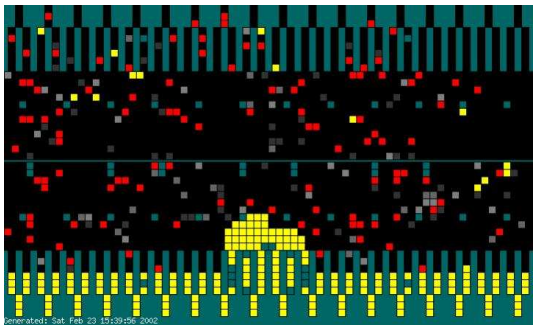

(b) FIGURE 8.1: DARK RATE MAP OF THE DETECTOR AFTER THE REMOVAL OF THE FLASHER PMT . THE MAP IS PROVIDED BY THE ONLINE ANALYZER SOFTWARE.

the trasparency measurement fibers could be tested. The `Laben` data readout through the analyzer interface was also tested successfully and provided the first plot of the charge signal of the PMTs dark noise (see figure 8.2).

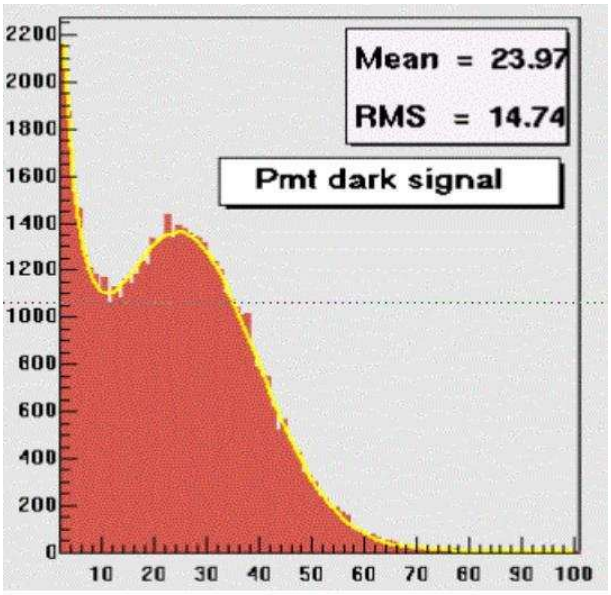

FIGURE 8.2: THE CHARGE PLOT, IN ADC COUNTS, OF THE DARK NOISE HITS ON ONE PHOTOTUBE.

Finally also the DAQ could be carefully debugged. A gradual upgrade of the system was performed, solving some instabilities and improving its efficiency, stability and speed. More than 5×10^6 events (many Gbytes) were written on disk and the system proved to be able to tolerate rates of several hundreds Hz for normal events.

8.2 The time and charge measurement problems

8.2.1 The time measurement problems

The real data analysis of the data collected during these air runs practically started only during Air Run III.

We immediately found some problems with the hits time measurement. These problems were due to the non ideal behaviour of the Laben boards and forced us to develope a quite complex decoding method [67] of the raw timing informations. The different problems met and the steps towards the construction of the final pre-decoding algorithm (section 7.3) are briefly described here.
Actually two independent problems were identified:

- sometimes the time measurement of some hits falls outside the physical 7 μs gate window of data reading. Figure 8.3 shows the clear pattern of the gate window and the small and asimmetric tail of hits with a wrong time measurement, for random noise or timing laser triggers. In the second case the laser light peak is also well visible.

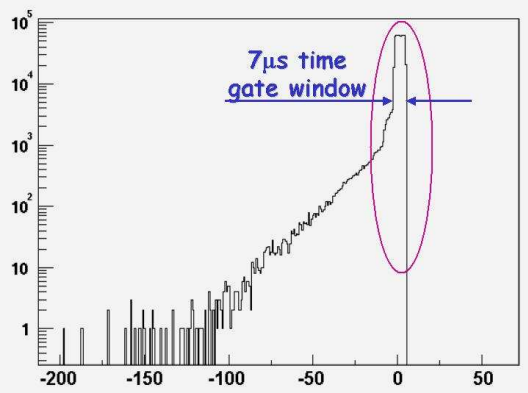

(a) Figure 8.3: time distribution of the acquired hits in a random noise run. The x-axis scale is μs .

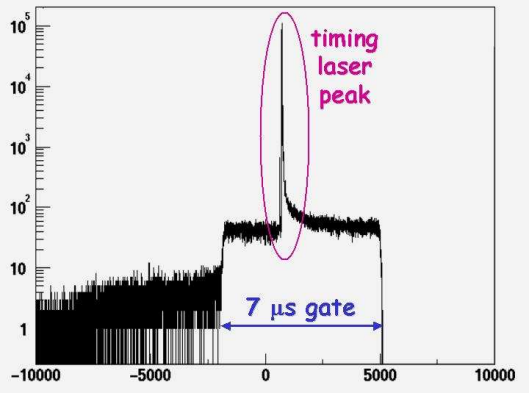

(b) Figure 8.3: time distribution of the acquired hits in a timing laser run. The x-axis scale is ns .

- studying the time allignment of all channels (using only the valid hits, with a time inside the gate window) we met some *"fine tuning"* problems, observing time differences up to 20 ns among different electronics racks and random shifts of 50 or 100 ns among different channels.

The first problem, a ∼2% effect, was found always on the same `Laben` channels. We replaced most of the `Laben` boards with these bad channels with the spare ones and increased also the threshold of the dual threshold discriminator of the `Laben` boards. This decreased the rate of triggers due to the PMT dark noise. As a result the fraction of hits outside the gate window went down to values lower than 0.5% . Figure 8.4 shows the comparison of the hits time distributions with all channels and removing about 20 bad `Laben` channels. A channel-by-channel fine debugging of the `Laben` system is still on going.

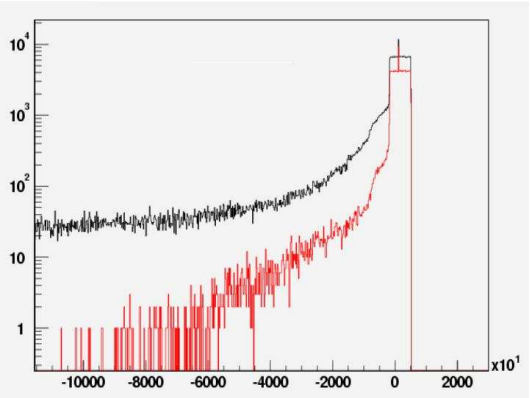

(a) FIGURE 8.4: COMPARISON OF THE HITS TIME DISTRIBUTION IN A RANDOM NOISE RUN, WITH ALL THE ACQUIRED HITS (BLACK) AND REMOVING ABOUT 20 BAD LABEN CHANNELS (RED). THE x-AXIS SCALE IS ns .

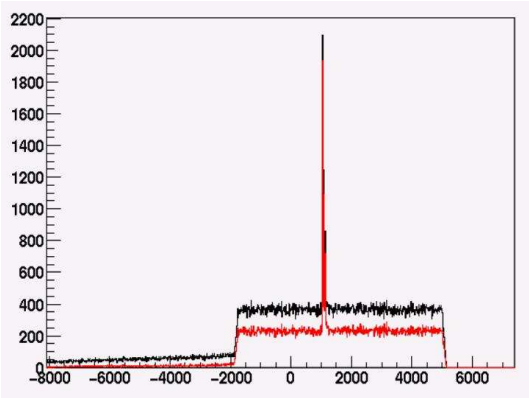

(b) FIGURE 8.4: SAME COMPARISON IN LINEAR SCALE. THE x-AXIS SCALE IS ns .

Once fixed this problem we started studying the time allignment of the whole detector. The first test was done using the synchronous calibration signals of the test and calibration signal distributor and the result is shown in figure 8.5.

A first effect is that about 1% of the channels show systematic shifs of 50 or 100 ns . Actually, when the RESET signal delivered by the main trigger board at the beginning of a new run crosses the clock we can have for some channels the *hazard* situation of figure 8.6. In this case, these channels have the GRAY counter systematically shifted by 1.

If we plot the distribution of the differences of the Gray counters of all channels with that of a reference channel for the only synchronous CALIBRATION triggers, we can easily identify the shifted channels and software-correct their counters (see figure 8.7).
This results, see figures 8.8 and 8.9, in a good internal calibration of the single electronics racks. The whole detector distribution still shows some steps, but they are now rack based and, most important, run-independent. These time constants, mainly due to delays in the 20 MHz clock signal distribution, can be measured and added to the offline code as software systematic shifts.

The final result, see figure 8.10, is a spread in the time equalization distribution of the whole detector (2200 channels) lower than 1.2 ns . This is referred only to CALIBRATION triggers and is therefore the time resolution of our electronics. We still have about 0.1% of the hits with a systematic shift of 100 ns . This is due to a non perfect alignment of the

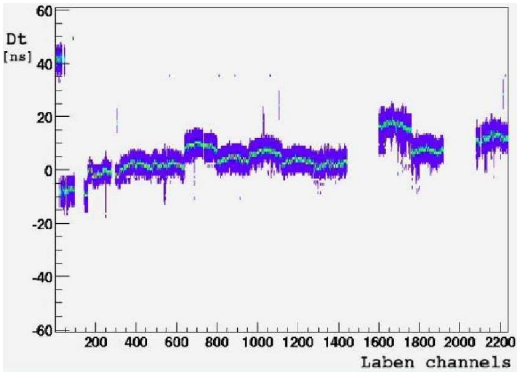

(a) FIGURE 8.5: DIFFERENCE OF THE HITS TIME MEASUREMENTS OF ALL LABEN CHANNELS WITH RESPECT TO A SINGLE REFERENCE CHANNEL.

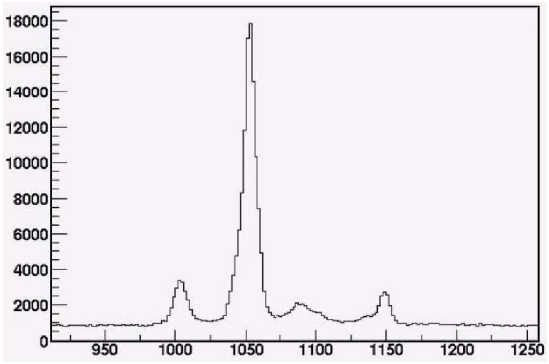

(b) FIGURE 8.5: Y-PROJECTION OF THE PREVIOUS PLOT. THE BROAD CENTRAL PEAK AND THE SEVERAL PEAKS BESIDE SHOW CLEARLY THE DISALLIGNMENT OF THE ELECTRONIC CHANNELS. THE x-AXIS SCALE IS ns .

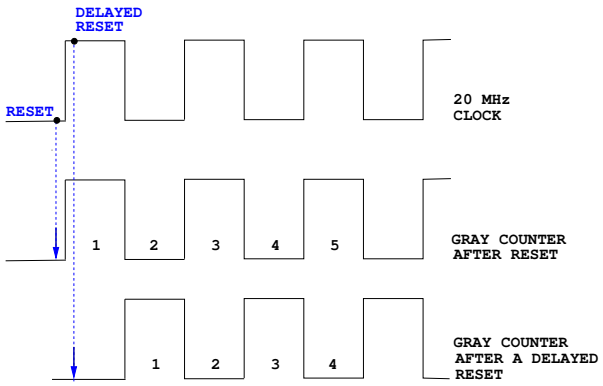

FIGURE 8.6: SISTEMATIC SHIFT OF 50 ns DUE TO SMALL DELAYS BETWEEN THE RESET SIGNAL ON DIFFERENT LABEN CHANNELS.

GRAY counter and of the triangular wave, but is unavoidable with this system. As is shown in chapter 9 no effect alters the physics results because of this problem.

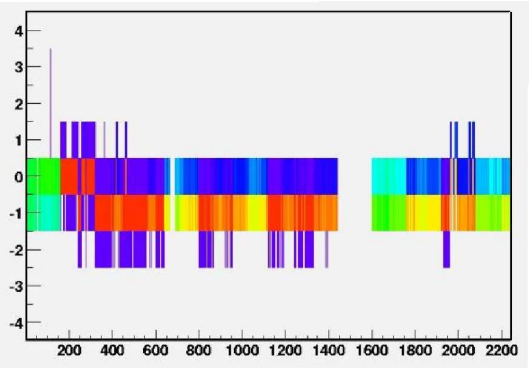

(a) FIGURE 8.7: TYPICAL SPREAD OF THE DISTRIBUTION OF THE LABEN GRAY COUNTERS DIFFERENCES. THE x-AXIS SCALE IS THE LABEN CHANNEL; THE y-AXIS THE GRAY COUNTERS DIFFERENCE.

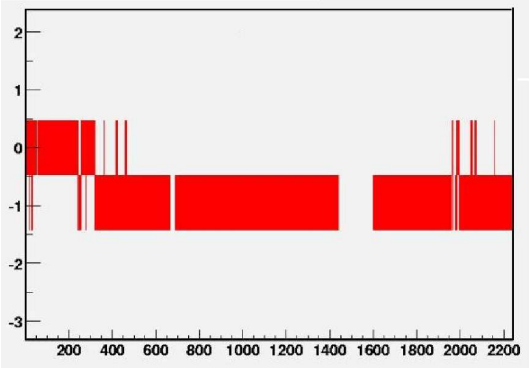

(b) FIGURE 8.7: CHANNEL DEPENDENT CORRECTION TO SOFTWARE ALLIGN THE LABEN GRAY COUNTERS. THE x-AXIS SCALE IS THE LABEN CHANNEL; THE y-AXIS THE GRAY COUNTER CORRECTION.

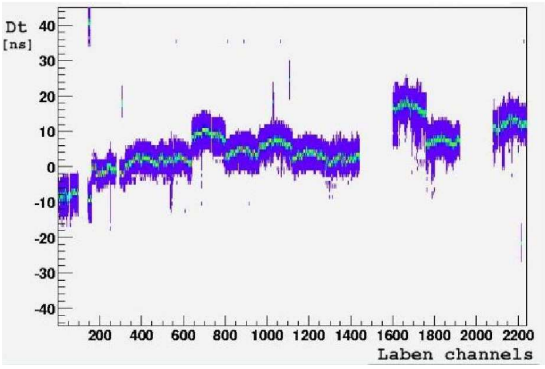

(a) FIGURE 8.8: DIFFERENCE OF THE HITS TIME MEASUREMENTS OF ALL LABEN CHANNELS WITH RESPECT TO A SINGLE REFERENCE CHANNEL AFTER THE SOFTWARE ALLIGMENT OF THE GRAY COUNTERS.

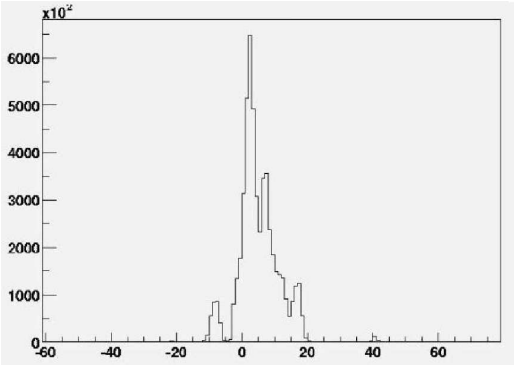

(b) FIGURE 8.8: Y-PROJECTION OF THE PREVIOUS PLOT. THE 50 ns SHIFTS ON THE FIRST CHANNELS OF RACK 1 (CHANNELS 1...24) OF FIGURE 8.5 DISAPPEARED. THE x-AXIS SCALE IS ns .

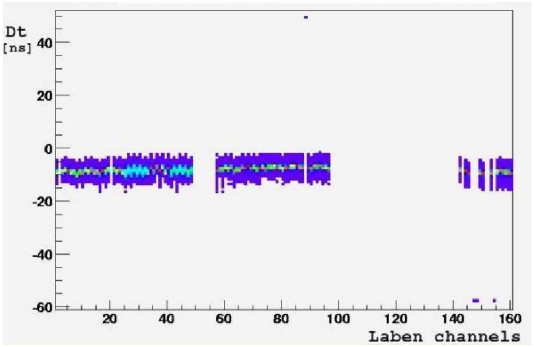

(a) FIGURE 8.9: DIFFERENCE OF THE HITS TIME MEASUREMENTS OF ALL LABEN CHANNELS OF RACK 1 (CHANNELS 1 . . . 160) WITH RESPECT TO A SINGLE REFERENCE CHANNEL AFTER THE SOFTWARE ALLIGMENT OF THE GRAY COUNTERS. THE x-AXIS SCALE IS THE LABEN CHANNEL; THE y-AXIS THE TIME DIFFERENCE IN ns .

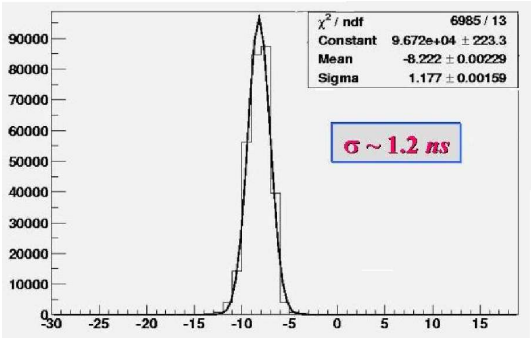

(b) FIGURE 8.9: Y-PROJECTION OF THE PREVIOUS PLOT. THE 50 ns SHIFTS ON THE FIRST CHANNELS OF RACK 1 (CHANNELS 1 . . . 24) OF FIGURE 8.5 DISAPPEARED. THE x-AXIS SCALE IS ns .

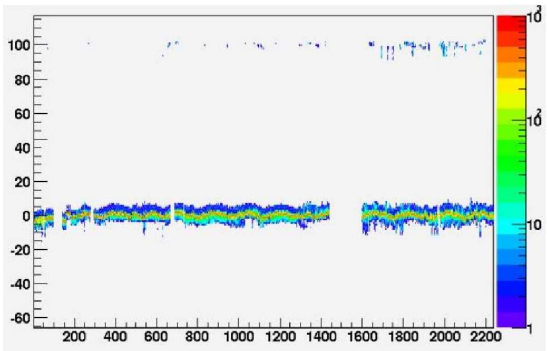

(a) FIGURE 8.10: DIFFERENCE OF THE HITS TIME MEASUREMENTS ALL LABEN CHANNELS WITH RESPECT TO A SINGLE REFERENCE CHANNEL AFTER THE SOFTWARE ALLIGMENT OF THE GRAY COUNTERS AND THE SUBTRACTION OF THE SYSTEMATICS DELAYS. THE PLOT WAS OBTAINED USING THE ONLY CALIBRATION TRIGGERS. THE x-AXIS SCALE IS THE LABEN CHANNEL; THE y-AXIS THE TIME DIFFERENCE IN ns .

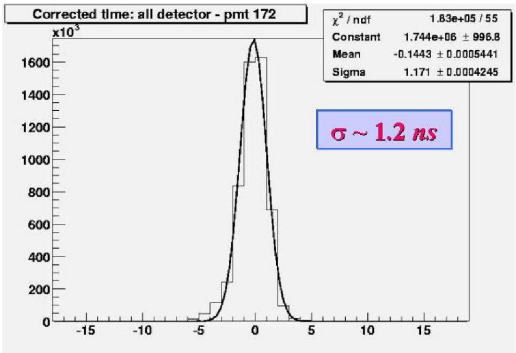

(b) FIGURE 8.10: AFTER SOFTWARE CORRECTIONS, THE CONTRIBUTION OF THE ELECTRONICS CHAIN TO THE TIME SPREAD OF THE WHOLE DETECTOR RESULTS TO BE LESS THAN 1.2 ns . THE x-AXIS SCALE IS ns .

8.2.2 The charge measurement problems

Analysing the data of the first air runs we identified also a problem with the charge measurement: a rather large number of channels, ∼30% , got a zero charge measurement in about 25% of the hits. The effect was found to be independent from high voltages. Moreover, the channels showing this charge problem were spread out on the whole detector and changed from one run to another (figure 8.11(b)). The typical charge plot with the big *"zero charge"* peak is shown in figure 8.11(a).

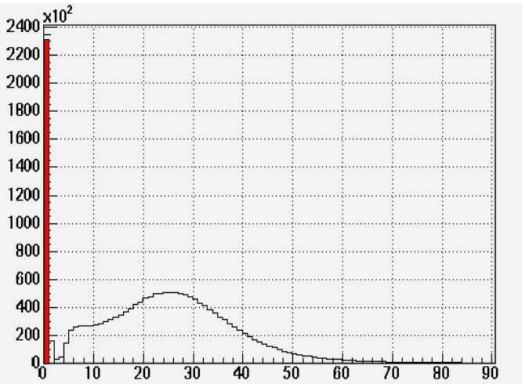

(a) Figure 8.11: charge measurement plot for a timing laser run. The big *"zero charge"* peak is in red. The x-axis scale is ADC counts.

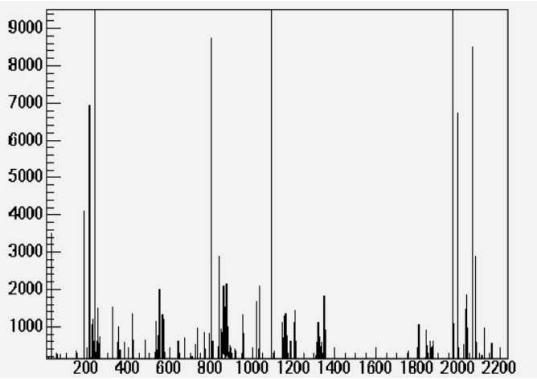

(b) Figure 8.11: map of the *"zero charge"* channels in a timing laser run. The x-axis scale is the Laben channel.

The problem was traced back to the bad quality of the connectors for the low voltage power supplies. The bad connections induced a lot of low frequency noise on the charge signals and their baselines were drifted outside the ADC range and the two charge samples were then always 0 or 255. This noise was not stable, therefore not easy to identify in normal test conditions.
All the cables and connectors between the front end and the low voltage power supplies were then replaced with better quality connectors and shielded cables. The result, for a pulser run taken immediately after the modification, is shown in figure 8.12. Now only about 40 specific electronic channels still show this *"zero charge"* problem, for a total of ∼3% of bad hits to be fixed by replacing the boards.
Excluding these 40 bad electronic channels, the fraction of *"zero charge"* hits quoted for a timing laser runs went down to less than 2% (figure 8.13(b)). The modification of the front end connectors reduced then by a factor greater than 10 the *"zero charge"* problem and now only a fine channel-by-channel debugging of the detector can reduce to zero the remaining 2% . This work is already scheduled and will be done in the near future.

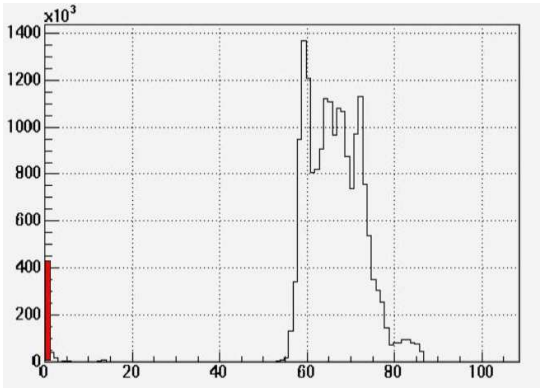

(a) FIGURE 8.12: CHARGE MEASUREMENT PLOT FOR A PULSER RUN AFTER THE FRONT END CABLES MODIFICATION. ABOUT 3% OF THE HITS STILL CONTRIBUTE TO THE *"zero charge"* PEAK. THE x-AXIS SCALE IS ADC COUNTS.

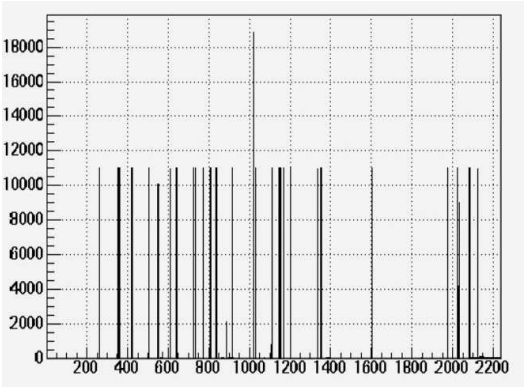

(b) FIGURE 8.12: MAP OF THE *"zero charge"* CHANNELS IN A PULSER RUN AFTER THE FRONT END CABLES MODIFICATION. NOW ONLY ABOUT 40 CHANNELS STILL SHOW THIS PROBLEM. THE x-AXIS SCALE IS THE LABEN CHANNEL.

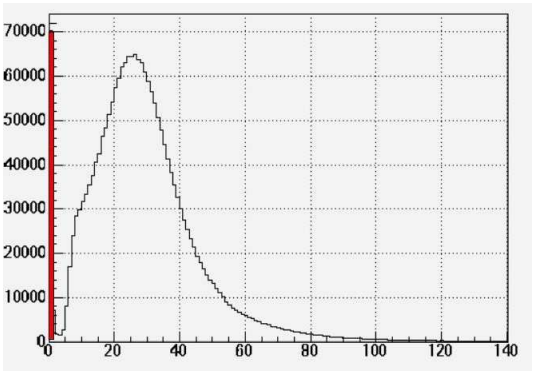

(a) FIGURE 8.13: CHARGE MEASUREMENT PLOT FOR A TIMING LASER RUN AFTER THE FRONT END CABLES MODIFICATION. THE x-AXIS SCALE IS ADC COUNTS.

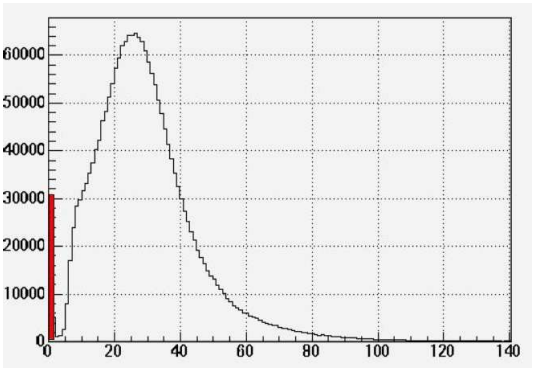

(b) FIGURE 8.13: CHARGE MEASUREMENT PLOT FOR A TIMING LASER RUN AFTER THE FRONT END CABLES MODIFICATION AND EXCLUDING THE 40 PROBLEMATIC CHANNELS IDENTIFIED WITH THE PULSER RUNS. THE *"zero charge"* PEAK WAS REDUCED FROM ABOUT 30% TO LESS THAN 2% . THE x-AXIS SCALE IS ADC COUNTS.

8.2.3 The trigger and laser time reference signals

Every time a trigger occurs, the BTB 's DSP reads the GPS clock and stores this information in the trigger data record. This is the best absolute time information we can have for each event. The precision of the clock is about 1 μs . On the other hand the Laben electronics can give us very precise time measurements, with 1 *ns* resolution, but valid only inside the 3.2 ms time span of the TDC gray-counter clock.
However, the real significant information for us is not the absolute time of the single event, but the time difference between two events. For the fastest coincidences, with delays lower than 3 ms, we can use then the Laben system for the measurement of the time differences, reaching a precision of $\sim$1 *ns* . When the time difference between two consecutive events exceeds 3 ms the 1 μs resolution given by the GPS clock is more than adeguate.

A copy of the TTL trigger signal, available on the fan-out unit on the rear of the trigger rack, is inverted, shaped and sent to five spare Laben channels (see figure 8.14). The map of these dedicated channels is written in the Data Base and for each event the offline computes the Laben trigger time as the average value of the five channels times. This gives us a 1 *ns* precision on the measurement of the trigger time.

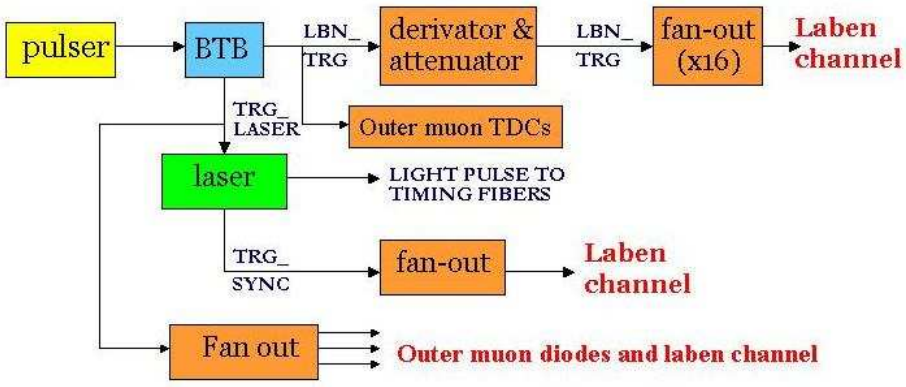

Figure 8.14: Sketch of the hardware set-up to acquire the Laben times of the trigger and laser signals.

In addition, we decided also to devote a few others Laben channels to the time measurement of the calibration laser signal. As already described in another section (5.2.3.4) the timing laser is externally triggered by a pulse generated by the BTB itself. The laser is also equipped with a *sync out* signal, synchronous with the external trigger. This TTL signal is inverted and shortened with the same logic used for the trigger signal and sent to other five spare channels. This allows a precise measurement of the time delay between the laser pulse and the arrival time of the light on the PMTs. Being the sync-out signal synchronous with the external trigger we have no time jitter.
Figure 8.15 shows the difference between the time of the hits and the Laben reference time of the trigger 8.15(a) and of the laser 8.15(b).

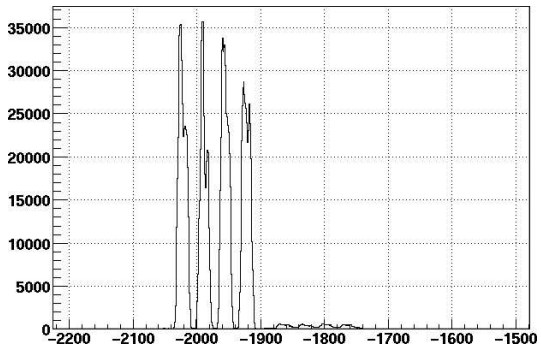

(a) FIGURE 8.15: DISTRIBUTION OF THE TIME DIFFERENCE BETWEEN THE HITS AND THE LABEN TRIGGER TIME FOR A CALIBRATION LASER RUN. THE TRIGGER TIME SIGNAL COMES DIRECTLY FROM THE BTB AND IS THEREFORE SUBJECT TO THE INTRINSIC DSP 'S JITTER (100 *ns*). THIS IS THE REASON OF THE FOUR BROAD PEAKS. THE x-AXIS SCALE IS *ns* .

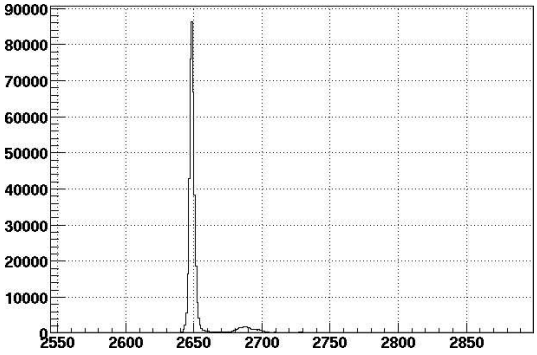

(b) FIGURE 8.15: DISTRIBUTION OF THE TIME DIFFERENCE BETWEEN THE HITS AND THE LABEN LASER TIME FOR A CALIBRATION LASER RUN. THE LASER TIME SIGNAL IS SYNCHRONOUS WITH ITS LIGHT AND THE RESULTING TIME PLOT SHOWS A CLEAR AND SHARP PEAK. THE x-AXIS SCALE IS *ns* .

8.3 THE STATUS OF THE DETECTOR

The data taken during all air runs allowed also a deep check and debugging of the general status of the detector, since the whole electronic chain, from the PMT and optical fiber to the electronics and data acquistion system, can be individually tested. The last channel-by-channel analysis of the detector was done with the data taken in August 2002, but since then no important works were done on the detector and its status should be quite stable.
At that time the status of the detector was the following: 1862 PMTs out of the 1993 installed had high voltages on (64 PMTs from the upper emisphere were discabled in order to allow some works in the water tank, while the remaining 67 PMTs were temporary turned off because they needed further checks). Among these 1862 PMTs , 1686 have been successfully calibrated, while the remaining ones showed different problems:

- 85 channels had electronic problems(both on the front end and on the `Laben` systems).
- 12 PMTs were suspected to be dead, since they gave no signal.
- 79 PMTs had problems with the laser fiber: they clearly did not received any direct laser light (see figure 8.16(b)). Luckily, 40 of them belonged to the same fiber cluster that had to be disconnected from the light source during some works in the water tank. The real fiber problems were, therefore, only on 39 PMTs .

Today a great part of the electronic problems have been already solved. Also the laser fiber has been investigated and we found out that most of the 39 fibers suspected to be broken were actually alive, but their light transmission was deeply reduced. These channels need only a specific laser calibration with a higher laser intensity. Finally, only about one half of the PMTs suspected to be dead turned out to be really dead; the other ones were either disconnected or still discabled. The bad PMTs have been then replaced.

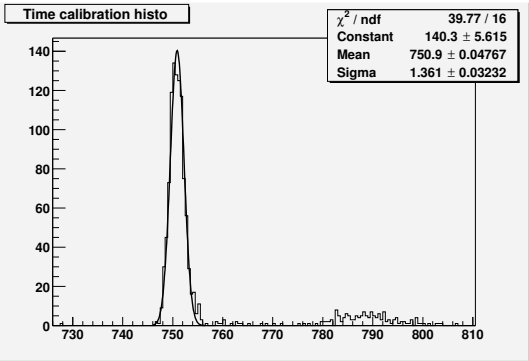

(a) FIGURE 8.16: TIME DISTRIBUTION FOR A SINGLE PMT ILLUMINATED WITH THE TIMING LASER CALIBRATION SYSTEM. THE x-AXIS SCALE IS ns .

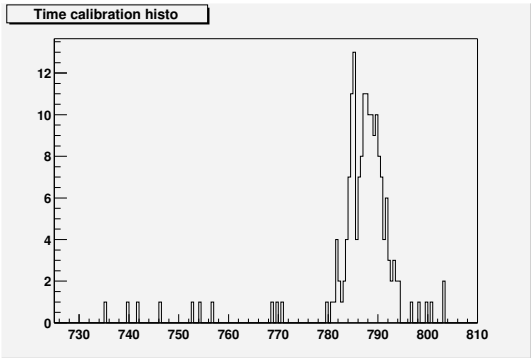

(b) FIGURE 8.16: TIME DISTRIBUTION FOR A PMT WITH NO DIRECT LASER ILLUMINATION. THE PMT CLEARLY DETECTS ONLY THE LIGHT REFLECTED FROM THE PHOTOCATHODE OF THE PMTS LYING ON THE OPPOSITE SIDE OF THE SPHERE. THE x-AXIS SCALE IS ns .

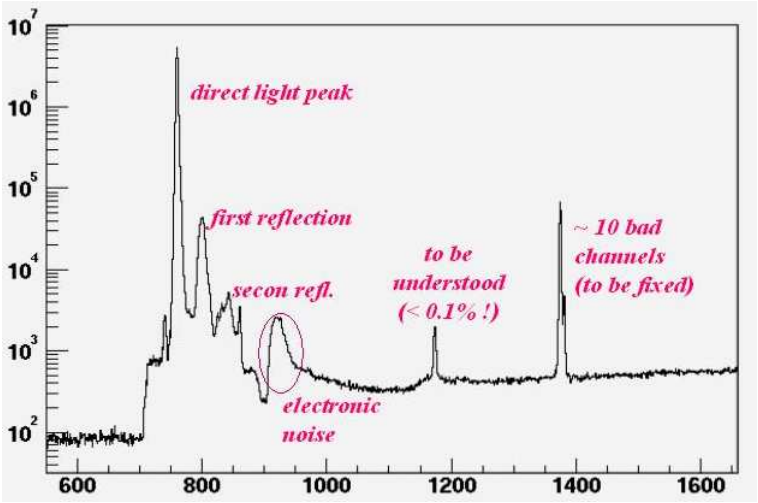

FIGURE 8.17: TIME DIFFERENCE BETWEEN THE LASER PULSE AND THE LIGHT HITS ON THE PMTS . THE DIRECT LIGHT AND THE FIRST AND SECOND REFLECTION PEAKS ARE WELL VISIBLE. THE ADDITIONAL PEAKS AND STRUCTURES ARE DUE TO ELECTRONIC NOISE, BAD CHANNELS OR OTHER PROBLEMS. THE x-AXIS SCALE IS ns .

8.4 The calibration laser data

The synchronous events delivered by the time equalization system to the whole detector are a natural test of the precision of the time reconstruction algorithm used in the offline code.

The typical plot of the time difference between the laser signal and the light hits on the PMTs is shown in figure 8.18. These data pulsing the laser with double pulses with 1 μs delay: figure 8.18(a) shows clearly the 7 μs trigger gate window, populated with the hits due to the constant and uncorrelated random noise of the PMTs , and the two laser pulses. Each laser pulse produces at least three well separable light peaks, about 41 ns delayed (see figure 8.19(a)).

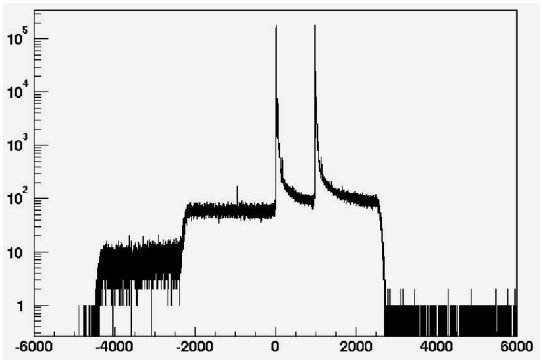

(a) Figure 8.18: time difference between the laser pulse and the light hits on the PMTs in logarithmic scale. The x-axis scale is ns .

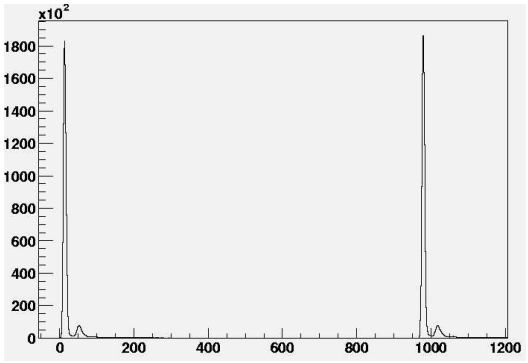

(b) Figure 8.18: time difference between the laser pulse and the light hits on the PMTs in linear scale. The x-axis scale is ns . Note that x-axis range is different in the two figures.

The first peak is obviously the direct light peak; its width, less than 4 ns , gives an estimation of the time spread of the detector with respect to a synchronous light pulse.
The second peak is due to the light reflection on the photocatodes: a small fraction of the photons can be reflected on the PMT 's glass and detected by the PMTs placed on the opposite side of the sphere. This interpretation is confirmed by the time delay between the two peaks, about 41 ns : the distance between the centre of the sphere and the photocatodes is 6.522 meters and, being in air, we obtain:

$$\frac{13.044\ m}{3 \times 10^8\ m/s} \sim 41\ ns \tag{8.1}$$

In the same way, the third peak is simply the second reflection of the reflected photons.

However, this good result can be still improved. An accurate offline time calibration procedure (already described in section 7.10.1) computes the single PMT calibration constants starting from these laser data and greatly improves the *offline* inter-PMT time equalitazion. Figure 8.20 shows the comparison between the direct light peaks without any calibration and after this offline calibration procedure: the time spread of the detector goes from 3.6 ns to an excellent 1.6 ns .
Moreover, it is significant to note that, since the mean PMT jitter time is about 1.1 ns and

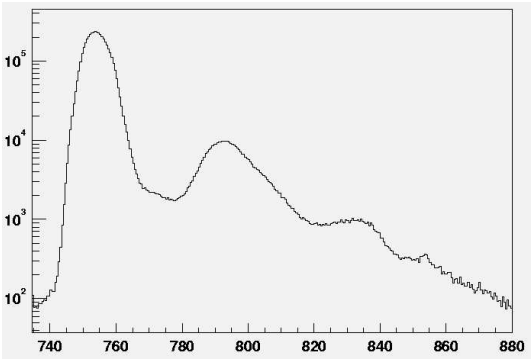

(a) FIGURE 8.19: ZOOM OF A SINGLE LASER PULSE IN LOGARITHMIC SCALE. THE FIRST PEAK IS THE DIRECT LIGHT TO PMTS . THE SECOND AND THIRD PEAKS ARE DUE TO LIGHT REFLECTION ON PMTS AND ON SSS . THE x-AXIS SCALE IS ns .

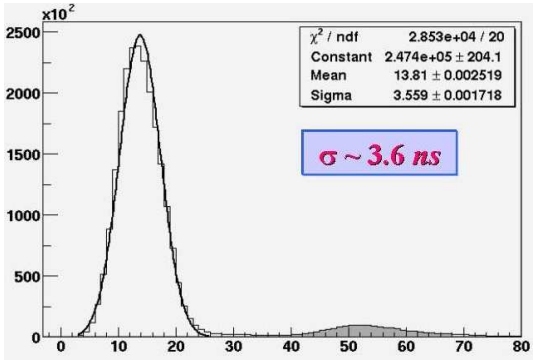

(b) FIGURE 8.19: ZOOM OF THE FIRST AND SECOND LASER LIGHT PEAKS IN LINEAR SCALE. THE GAUSSIAN FIT OF THE DIRECT LIGHT PEAK GIVES ~ 3.6 ns OF TIME SPREAD ON THE WHOLE DETECTOR, ABOUT 2000 PMTS . THE x-AXIS SCALE IS ns .

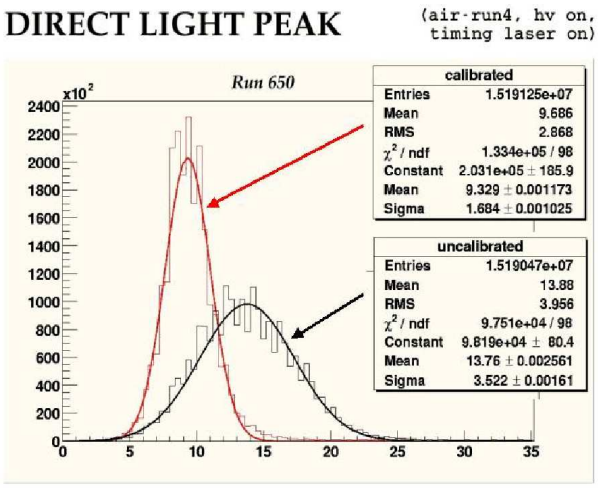

FIGURE 8.20: COMPARISON OF THE TIME CALIBRATED (*black*) AND UNCALIBRATED (*red*) DIRECT LIGHT PEAKS. THE x-AXIS SCALE IS ns .

the intrinsic resolution of the time reconstruction algorithm and of the electronic chain resulted to be about 1.2 ns (section 8.2.1), the value obtained here is exactly the theoretical one expected from the squared sum of the two contributions:

$$\sqrt{(1.1)^2 + (1.2)^2} \sim 1.6 \ ns \tag{8.2}$$

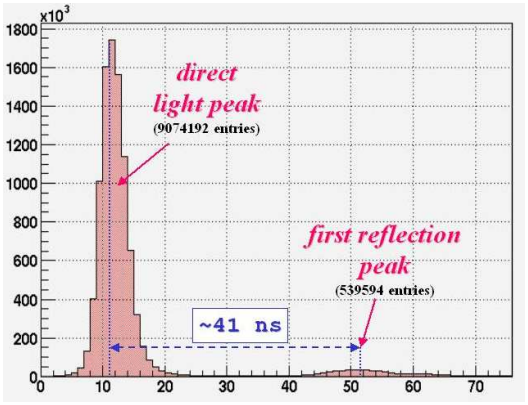

(a) Figure 8.21: direct light peak and first reflection peak obtained with the calibration laser data of Air Run III. The x-axis scale is ns .

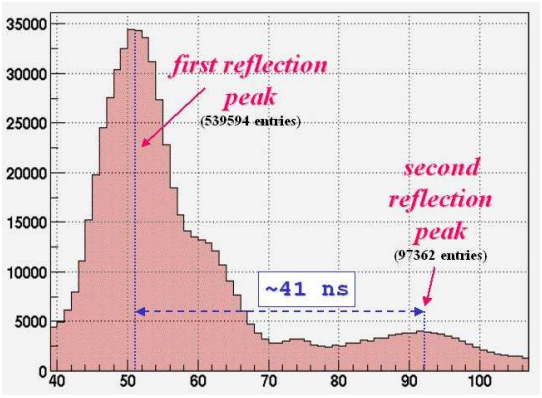

(b) Figure 8.21: first and second reflection peaks obtained with the calibration laser data of Air Run III. The x-axis scale is ns .

We have already mentioned the different reflected-light peaks visible in the time distribution of the detector illuminated by the calibration laser light. With these data we attempted a very preliminary and rough estimation of the stainless steal sphere reflectivity. Actually we could estimate not the direct SSS reflectivity, but only the PMTs glass contribution and the integrated reflectivity, sum of the two contributions.
Since the fiber termination points directly to the photocatode, the first reflected peak is due only to the reflectivity of its glass. This is a known value, but it can be also estimated using the ratio of the areas under the second peak and under the direct light peak (figure 8.21(a)). The trivial ratio of the number of entries under the second and the first peaks is about 10% , and this is consistent with the photocatode's reflectivity value measured in laboratory.
More interesting is the ratio between the second and the third peak. Since the third peak is due to the second reflection of the photons, it gives an estimation of the overall detector's reflectivity, averaging the photocatode's and the sphere's contributions. With the same technique used before, that is evaluating the ratio of the areas under the two peaks, we obtained a reflectivity value of about 20% . This method is obviously too trivial to estimate a precise and reliable reflectivity value, but allows us to exclude with a certain confidence reflectivity values greater than $30 \div 40\%$.

8.5 The optical laser data

Particularly during Air Run III we took a lot of data even with the optical calibration systems. Actually we tested only the two external systems: the radial and oblique beams systems.

These data were essentially a good test of the cable mapping stored in our Data Base. The complete mapping of the system is actually quite complex: a first code links the single

PMT with its dark room specifications; the geometrical position of the PMT on the SSS is identified with the *"hole"* code; an independent code identifies the HV cables connecting the PMTs with the racks patch panels inside the electronic control room; another map correlates the patch-panel codes with the front end channels and a fifth map links finally the front end channels with the `Laben` channels. Any error in the copies of these maps in Data Base would clearly affect the position reconstruction efficiency.

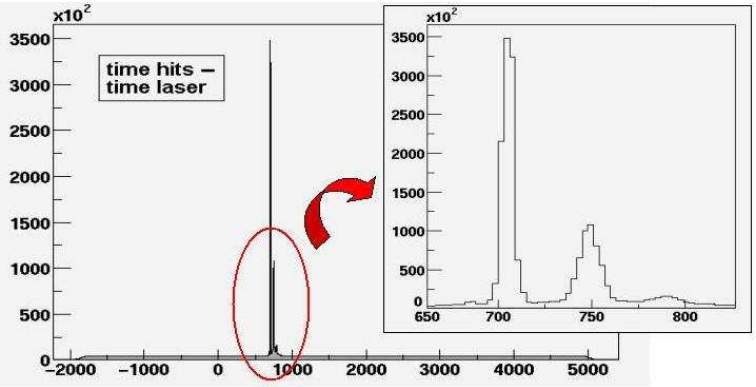

FIGURE 8.22: TIME DIFFERENCE BETWEEN THE LASER PULSE AND THE LIGHT HITS ON THE PMTS , WITH A ZOOM ON THE LASER PULSE REGION. BOTH THE DIRECT LIGHT AND THE FIRST REFLECTION PEAKS (ABOUT 41 *ns* DELAYED) ARE CLEARLY VISIBLE AND SEPARABLE. THE x-AXIS SCALE IS *ns* .

At first we proceeded with a careful debugging of the last part of this map chain, i.e. from the patch panel up to the digital boards. We kept high voltages off and pulsed the system through the test and calibration signal distributor; just turning on and off single racks or single front end and `Laben` boards or manually disconnecting single channels we could reasonably test the DB map. Nevertheless, the check of the very first part of the map needs PMTs turned on and an easy handle to single out the PMTs one by one. The optical lasers data offered a natural way to do this job.

The radial beams system produces light beams sent from the SSS in the direction of the centre of the detector. The fiber carries the laser pulse from outside to the feed-through mounted on the SSS . The PMTs mounted on the opposite side of the sphere, within the aperture angle of the beam, are illuminated primarily with the laser light, while all other PMTs are illuminated only with scattered and reflected light.
We can easily distinguish between the contributions to the direct and to the reflected light peaks through relaxed time cuts (see figure 8.22) and consequently plot the channel map of the involved PMTs . The result, obtained with our Event Display, is shown in figures 8.23 and 8.24. The data refers to a radial laser run with the source placed near the equator line, near the centre of the detector (feed-through codes -2.62 for the source and 2.66 for the target).
Figure 8.26 shows another useful plot: the scattered plot of the time of the hits versus the incident angle. The correlation between the two 41 *ns* delayed time peaks and the direct and first reflection peaks is well visible.
We took data with all 12 radial modules, but no mapping mismatch was found between the

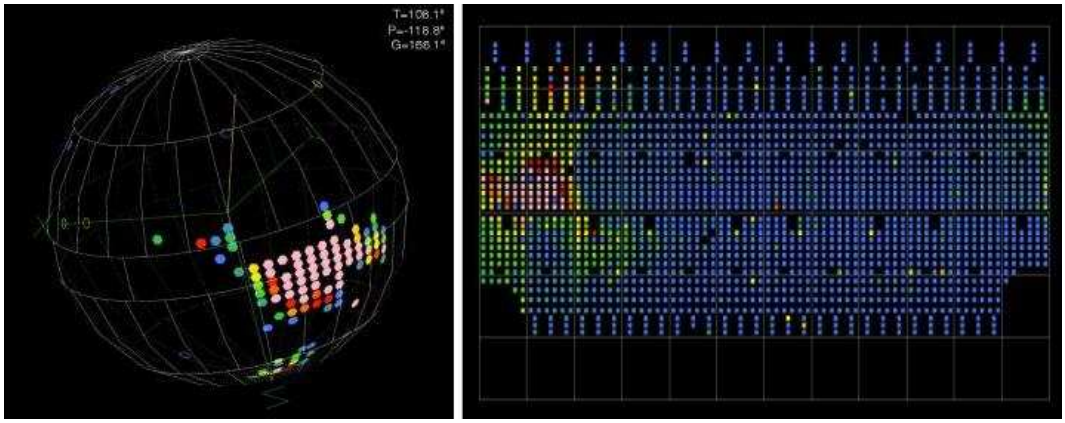

FIGURE 8.23: DETECTOR AND ELECTRONICS MAPS OF THE PMTS CONTRIBUTING TO THE DIRECT LIGHT PEAK. THE WARMER COLORS ARE ASSOCIATED WITH THE HIGHER RATES. THE INVOLVED PMTS , THE RED SPOT IN THE LEFT SIDE OF THE DETECTOR, ARE THE ONES CLOSEST TO THE BEAM TARGET, THAT FALL INSIDE ITS APERTURE ANGLE.

reconstructed data and the source and target real locations.

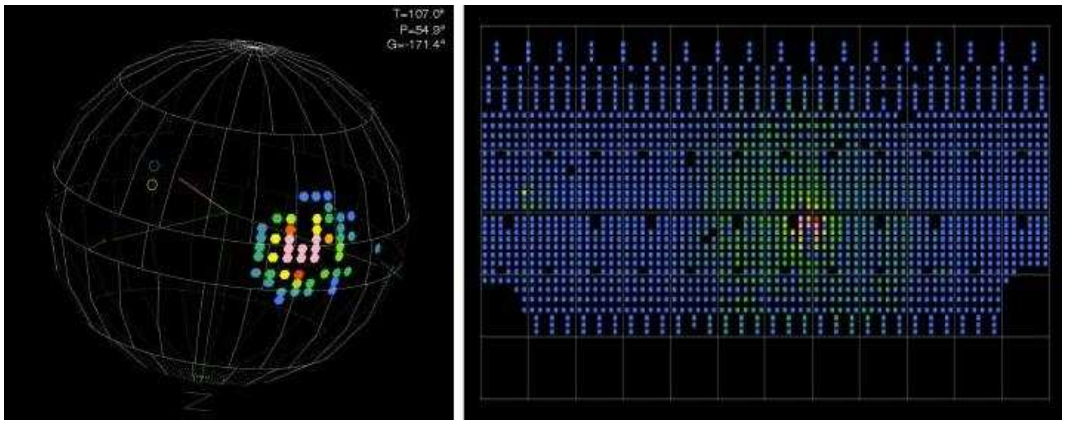

FIGURE 8.24: DETECTOR AND ELECTRONICS MAPS OF THE PMTS CONTRIBUTING TO THE FIRST REFLECTION LIGHT PEAK. THE LIGHT SPOT IS NOW IN THE CENTER OF THE DETECTOR, IN THE SAME POSITION WHERE THE LASER SOURCE IS LOCATED.

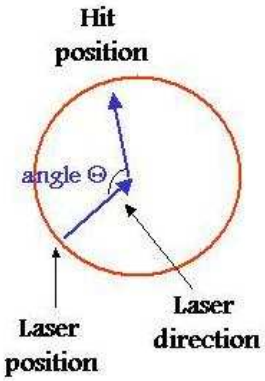

FIGURE 8.25: THE INCIDENT LIGHT ANGLE IS THE ANGLE BETWEEN THE LASER DIRECTION AND THE HIT POSITION.

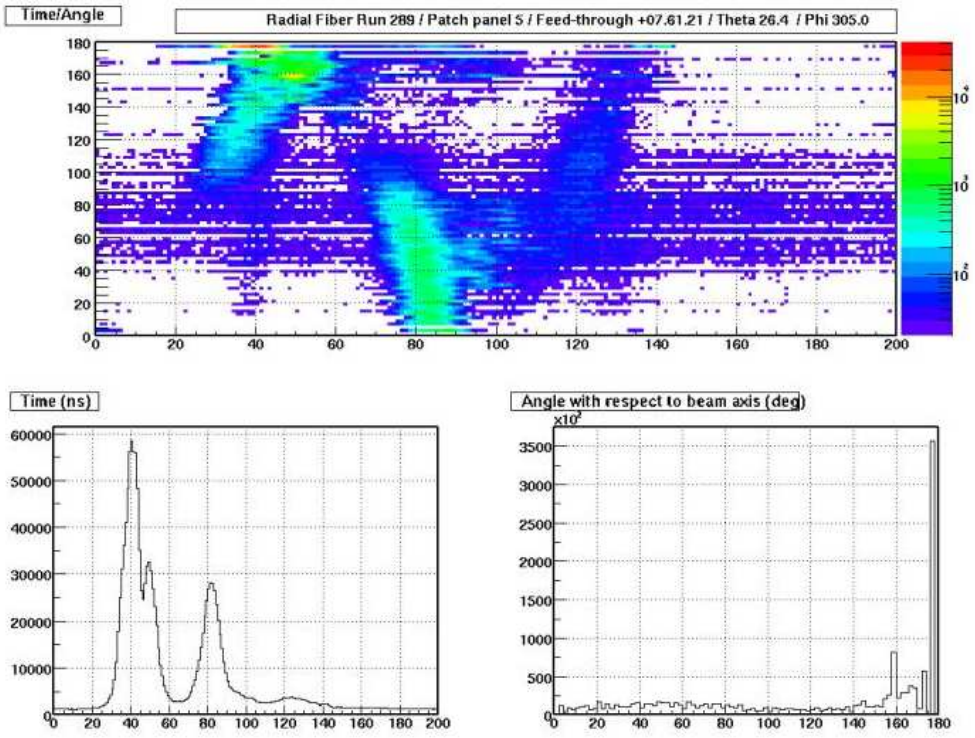

FIGURE 8.26: SCATTERED PLOT OF THE HITS TIMES VERSUS THE INCIDENT LIGHT ANGLE.

The beams of the oblique laser system cross instead only the buffer region, going from a source mounted at some distance from the SSS to a target PMT with no light concentrator[1].
The criterion for the choice of the positions of the 19 oblique beams modules and target PMTs was to allow the widest possible range of distances (ranging from 9.3 m to 2 m). The light beams are extremely focused on the target PMTs , covering no more than the whole photocatode surface.
Several modules have been tested also for these system and in all runs only the target PMT and a few other ones at most contributed to the direct peak (figure 8.28). In addition the target PMT was always found in the exact expected position, confirming no errors in the DB tables.

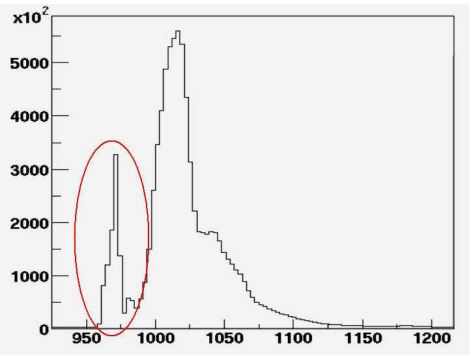

(a) FIGURE 8.27: TIME DIFFERENCE BETWEEN THE LASER PULSE AND THE LIGHT HITS ON THE PMTS . THE DIRECT LIGHT PEAK IS HIGHLIGHTED IN RED.

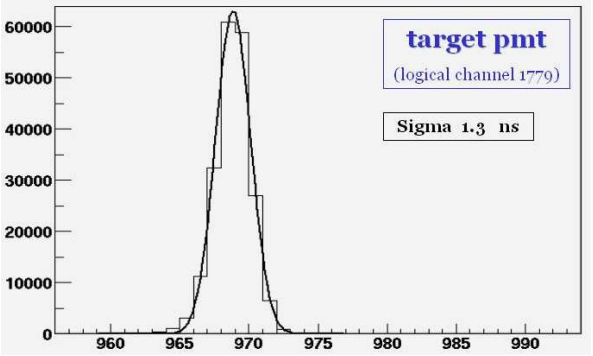

(b) FIGURE 8.27: TIME DIFFERENCE BETWEEN THE LASER PULSE AND THE LIGHT HITS ON THE TARGET PMT . THIS IS GENERALLY THE ONLY CONTRIBUTION TO THE DIRECT LIGHT PEAK.

[1]The geometry of our detector places some constraints to this system: any beam originated in the SSS eitheir crosses the inner vessel or is blocked by the PMTs and light concentrators, and this is why the source must be moved away from the SSS . In addition the shape of the light concentrators is designed to reflect back any photons arriving from the inner vessel: only PMTs without light concentrator can be the targets of these beams.

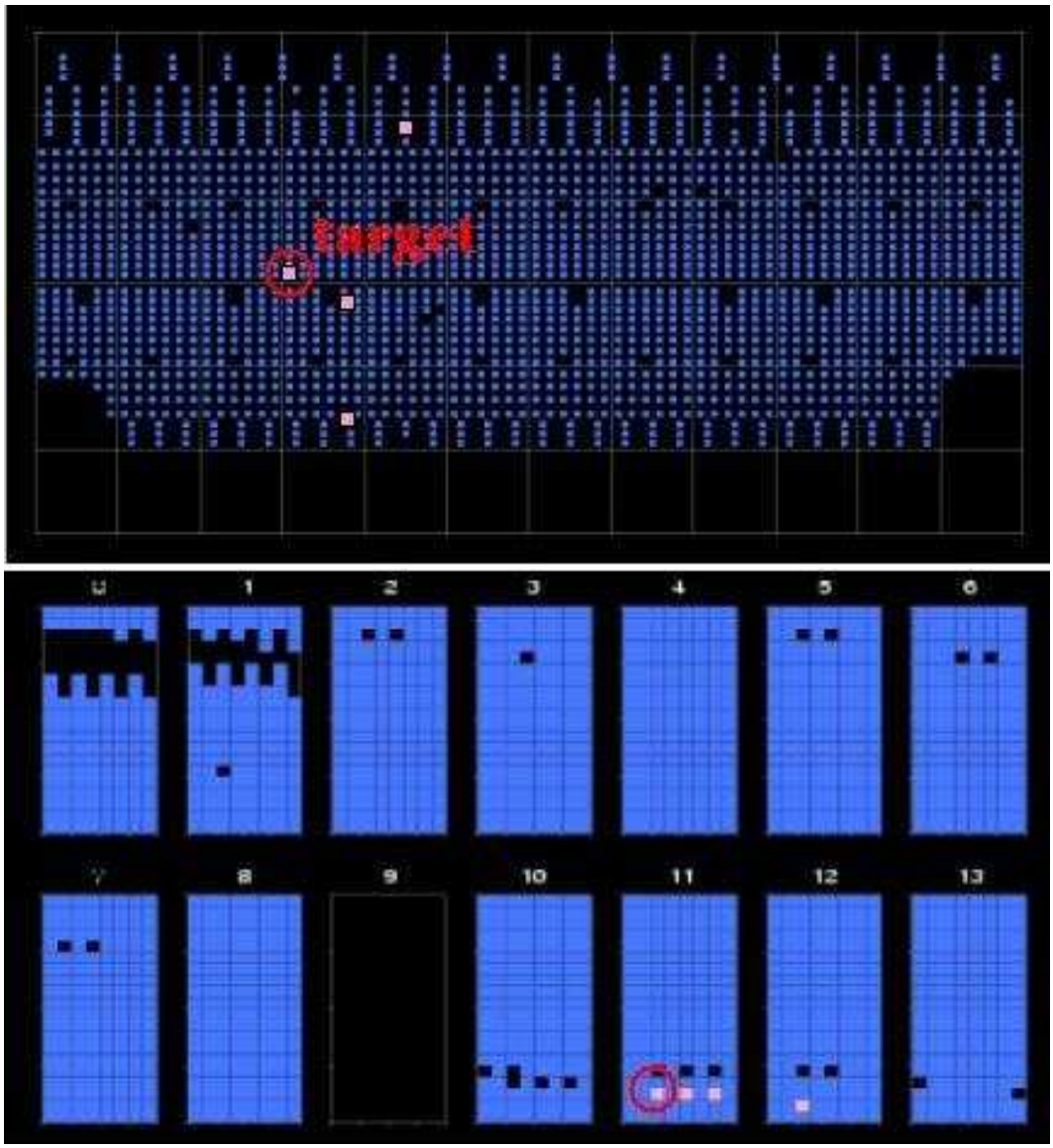

FIGURE 8.28: DETECTOR AND ELECTRONICS MAPS OF THE PMTS CONTRIBUTING TO THE DIRECT LIGHT PEAK. ONLY FOUR PMTS RECEIVED THE DIRECT LASER LIGHT: THE TARGET PMT , TWO CHANNELS ON THE SAME FRONT END BOARD OF THE TARGET PMT (THIS IS ALMOST SURELY AN ELECTRONIC NOISE PILE-UP) AND A FOURTH CHANNEL, PROBABLY A BRIGHT OR HOT PMT .

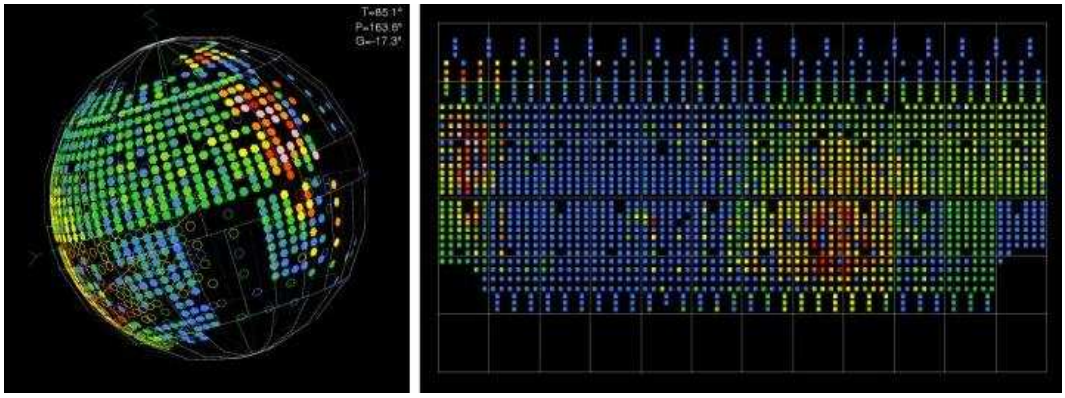

FIGURE 8.29: DETECTOR AND ELECTRONICS MAPS OF THE PMTS CONTRIBUTING TO THE FIRST REFLECTION LIGHT PEAK. THE LIGHT SPOT IS JUST OPPOSITE THE TARGET PMT 'S POSITION.

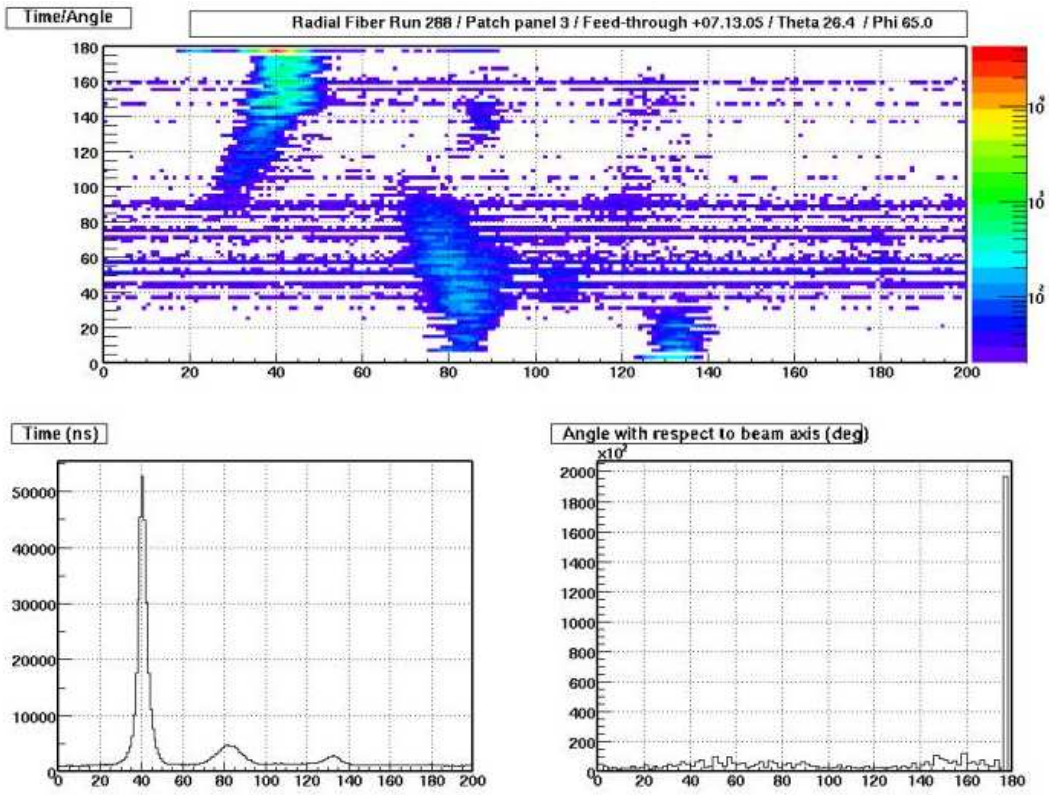

FIGURE 8.30: SCATTERED PLOT OF THE HITS TIMES VERSUS THE INCIDENT LIGHT ANGLE.

8.6 The dark noise data

A RANDOM GATE trigger is generated by the BTB at an arbitrary time: it is completely uncorrelated from any light pattern and acquires only the dark noise hits of the phototubes. During the standard data taking a small fraction of RANDOM triggers is always present, but we may also have dedicated random noise runs.

These events offer an easy handle to monitor the status of the detector. A dedicated offline module (section 7.9) can process these dark noise runs, extract some general parameters characterizing the detector and write them in the data base. These parameters, like the number of dead, disconnected or hot PMTs , the mean dark noise of the detector or the dark rates of each tube, can then be used while processing the others runs near in time.
In addition, the dark rates estimated in this way can also be compared with the dark room measurements. Air Run V data, figure 8.31, provided rates slightly lower than the dark room ones; this is the effect of the different environment's temperature of Hall–C and dark room.

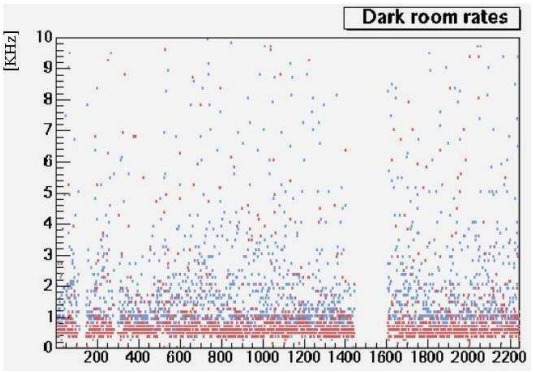

(a) FIGURE 8.31: COMPARISON OF THE DARK RATES COMPUTED BY THE OFFLINE CODE (RED) WITH THE DARK ROOM VALUES (BLUE). THE x-AXIS SCALE IS THE LABEN CHANNEL; THE y-AXIS THE DARK RATE IN KHZ.

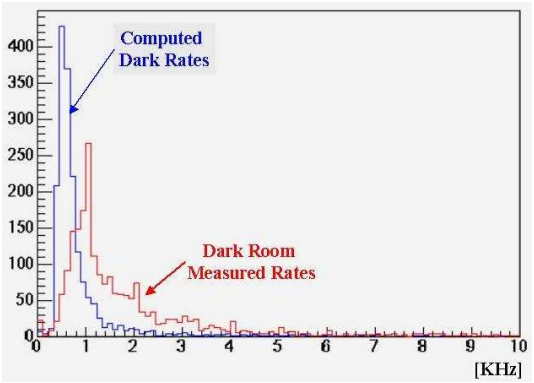

(b) FIGURE 8.31: Y-PROJECTION OF THE PREVIOUS PLOT. THE x-AXIS IS THE DARK RATE IN KHZ.

8.7 Some consistency checks on our electronics

After solving the very basic problems of the time and charge measurements a higher level analysis could be done. Several consistency checks of the good working of our electronics were also possible.

At first we tested the correct setting of the trigger threshold value from our *BorexinoDAQ* software. We took data with the calibration laser turned on (intensity 4.0) and triggered externally (from the BTB) at its full rate (about 200 Hz). During the run the BTB was triggering on the total sum (section 5.2.1), and we made a scan of the trigger rate as a function of the threshold value K. Actually we measured both the rate with the laser

turned on and, immediately after, with the laser off. In this way, we could subtract the dark noise rate and obtain the laser contribution from the difference of the two values.
The number of PMTs hit by the laser light is distributed like a Poisson function with the mean value μ fixed by the laser intensity, or even like a gaussian function in the limit of large number of events. Given the trigger threshold value K, the number of fired PMTs is

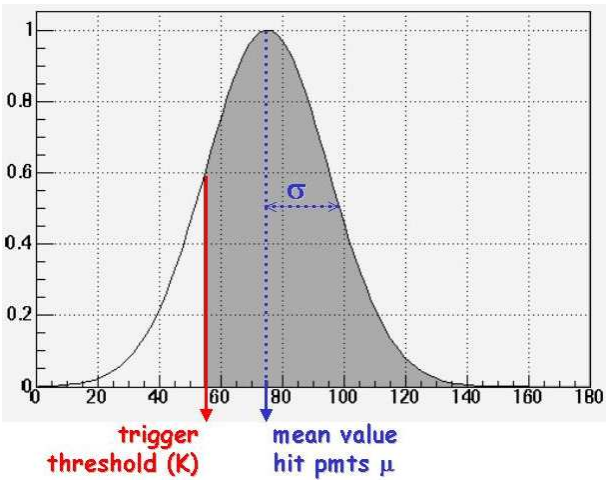

FIGURE 8.32: GAUSSIAN FUNCTION OF THE NUMBER OF PMTS HIT BY THE LASER LIGHT.

then the function's integral from the threshold K to infinity:

$$R_K(\mu,\sigma) \propto \int_K^\infty g(x)dx = \int_K^\infty \frac{1}{\sqrt{2\pi}\sigma} e^{-\frac{(x-\mu)^2}{2\sigma^2}} dx \tag{8.3}$$

The results of this integral is:

$$R_K(\mu,\sigma) \propto \int_K^\infty g(x)dx = \frac{1}{2} Erf\left(\frac{K-\mu}{\sqrt{2}\sigma}\right) \tag{8.4}$$

The list of the trigger rates was then fitted as a function of the threshold values with equation 8.4, with the mean value μ and the standard deviation σ used as free parameters of the fit. The result obtained with the poisson fit is shown in figure 8.33(a), to be compared with the gaussian fit in figure 8.33(b). The gaussian fit, with a slightly larger standard deviation than that of a pure poisson, is the best one and gives a mean number of hit PMTs ~76. I recall here this number refers only to the laser contribution, being the dark noise rate already subtracted.
To check this result, obtained with Air Run VII (August 2003) data, we compared it with an oldest run, taken during Air Run V (December 2002). This run was again a calibration laser run, with the same laser intensity, but this time the BTB was triggered by the laser pulse. As already pointed out in section 5.2.3.4, in this condition the full 200 Hz rate is served as LASER394 triggers, except for a reduced rate of RANDOM triggers still present. The number of hit PMTs for both the triggers, LASER394 and RANDOM, is shown in figure 8.34: the smaller peak is clearly the dark noise contribution, the main one is the total number of hit

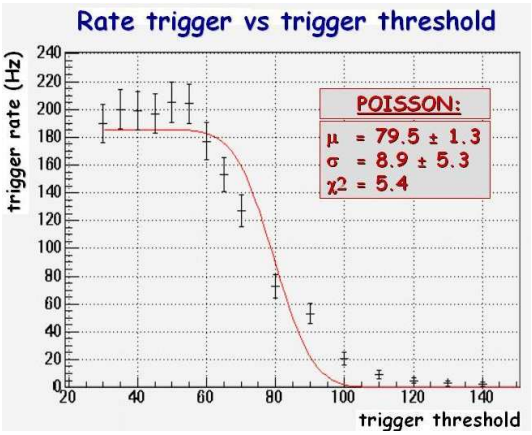

(a) FIGURE 8.33: POISSON FIT OF THE TRIGGER RATE AS A FUNCTION OF THE TRIGGER THRESHOLD. THE MEAN VALUE μ IS THE ONLY PARAMETER OF THE FIT.

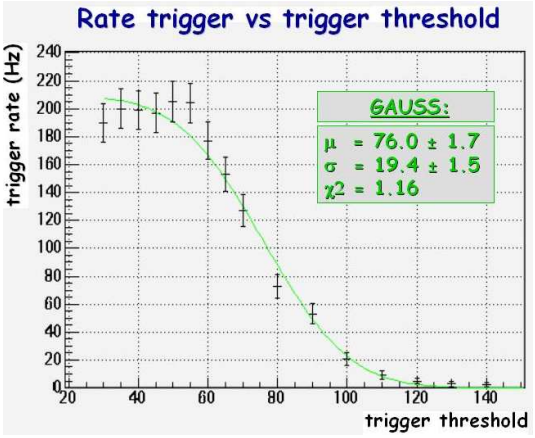

(b) FIGURE 8.33: GAUSSIAN FIT OF THE TRIGGER RATE AS A FUNCTION OF THE TRIGGER THRESHOLD. THE MEAN VALUE μ AND THE STANDARD DEVIATION σ ARE THE TWO PARAMETERS OF THE FIT.

PMTs when the laser is firing. The difference of the two mean values can give us a rough estimate of the laser contribution: about 73 PMTs . This number is well compatible with the (76 ± 1.7) found with the gaussian fit.

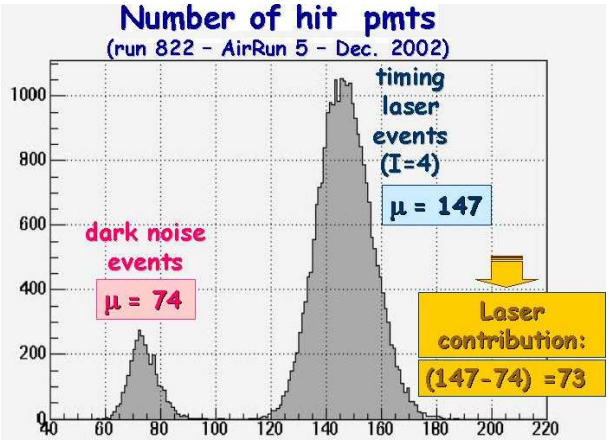

FIGURE 8.34: NUMBER OF HIT PMTS FOR A LASER RUN. THE LASER INTENSITY IS 4.0 AND THE BTB IS TRIGGERED EXTERNALLY, BY THE LASER PULSE. THE x-AXIS IS THE NUMBER OF HIT PMTS .

During the several air runs, we took also some calibration laser runs pulsing the laser with

double pulses. The BTB is triggered by an external pulse, serves the interrupt as a LASER394 trigger and generates an output signal that triggers a pulse generator. The output, a double pulse with a programmable delay, is then sent as external trigger to the laser box.
The data presented here refers to a run taken during Air Run VII, with the double pulses going from 180 *ns* up to 600 *ns* of delay time. This range of variability was choosen on purpose to test the response of the electronics in presence of the already cited *"pile-up"* effect (section 5.1.2.1). Basically, the front end charge output is an integrated signal, with a quite fast rise time (about 10 *ns*), 80 *ns* of constant signal and then a very long, ~500 *ns* , exponential decay time. If a second pulse reaches the same PMT when this long tail is still high, the charge of this second hit is affected by the presence of the first one and the effect depends on the time delay between the two hits.

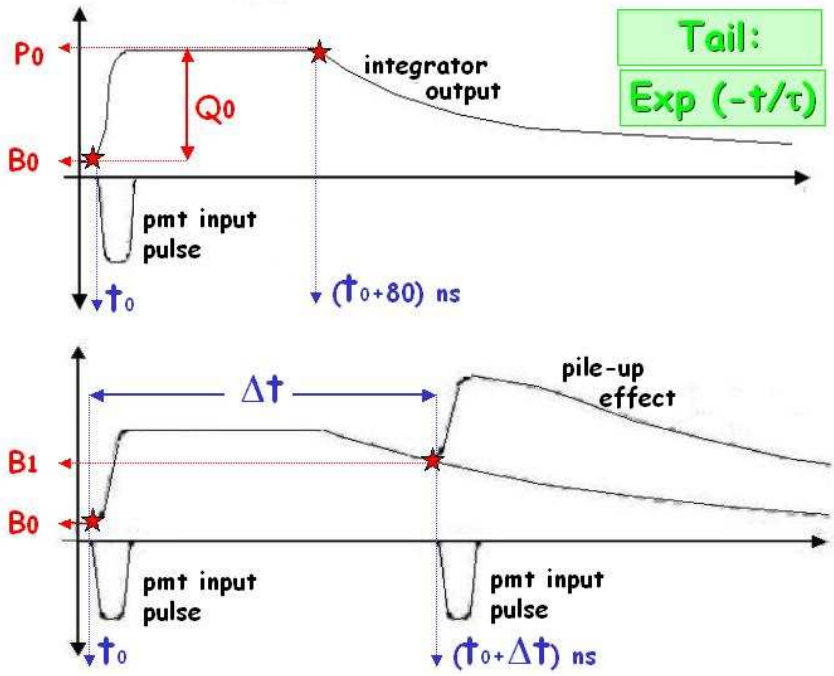

FIGURE 8.35: THE CHARGE MEASUREMENT PRINCIPLE IN OUR ELECTRONICS AND THE *"pile-up"* EFFECT.

More precisely, the baseline sample of the second hit is a function of the charge of the first hit and of the time delay between the two hits:

$$B_1 = B_0 + Q_0 e^{-\left(\frac{\Delta t - 80}{\tau}\right)} \tag{8.5}$$

where 80 is the time interval the signal stays constant and τ is the integrator's exponential decay constant. The distribution of the time constants obtained as results of an exponential fit during the front end boards tests, before their installation in Hall–C , gave a value of (497 ± 0.4) *ns* .
This effect is clearly visible also with these laser data (see figure 8.36). We tried then to

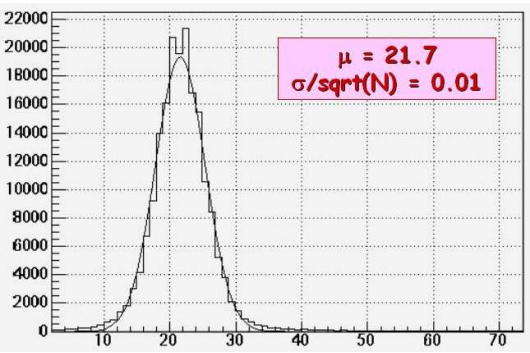

(a) FIGURE 8.36: DISTRIBUTION OF THE CHARGE BASELINE SAMPLE OF THE FIRST HIT FOR ALL PMTS . THE x-AXIS SCALE IS ADC COUNTS; THE ADC RANGE GOES FROM 0 UP TO 255.

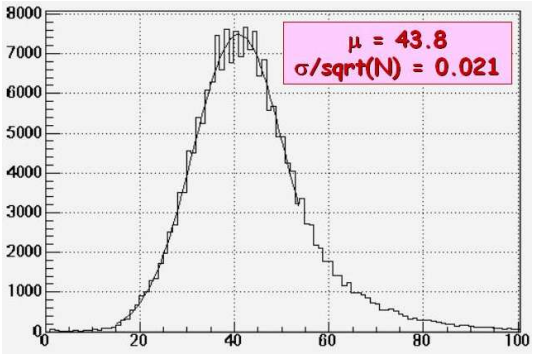

(b) FIGURE 8.36: DISTRIBUTION OF THE CHARGE BASELINE SAMPLE OF THE SECOND HIT FOR ALL PMTS AND ONLY FOR THE 230 ns DELAYED PULSES. THE DARK NOISE HITS WERE EXCLUDED WITH A SHARP CUT ($220 - 240$ ns WINDOW) ON THE TIME DELAY BETWEEN THE TWO HITS. THE x-AXIS SCALE IS ADC COUNTS.

plot the difference of the baselines of the two consecutive hits as a function of their time delay and fit it with the function:

$$B_1 - B_0 = Q_0 e^{-\left(\frac{\Delta t - 80}{\tau}\right)} \tag{8.6}$$

The free parameters of the fit are the charge Q_0 of the first hit and the time constant τ. The fit function (see figure 8.37) follows closely the data and the best values for the two fit parameters are: $Q_0 = (30.0 \pm 0.03)$ ADC counts and $\tau = (490.0 \pm 0.8)$ ns . The time decay constant is therefore in good agreement with the value measured during the front end tests, and also the second parameter, the charge of the first hit, is well compatible with the value obtained from the laser data: (30.6 ± 0.04) ADC counts (figure 8.38(a)).

Finally, another important parameter we can plot as a function of the delay time is the charge ratio:

$$\frac{Q_1}{Q_0} = 1 + e^{-\left(\frac{\Delta}{\tau}\right)} - e^{-\left(\frac{\Delta t - 80}{\tau}\right)} \tag{8.7}$$

We tried to fit this plot with the function:

$$f(cost, \tau) = cost \cdot \left(1 + e^{-\left(\frac{\Delta}{\tau}\right)} - e^{-\left(\frac{\Delta t - 80}{\tau}\right)}\right) \tag{8.8}$$

The result is shown in figure 8.40. The free constant, whose value should be 1, result (0.97 ± 0.02); while the exponential time constant τ is now (539.0 ± 18) ns . The error is bigger compared to the previous fit, but the obtained value is still very near the measured one.

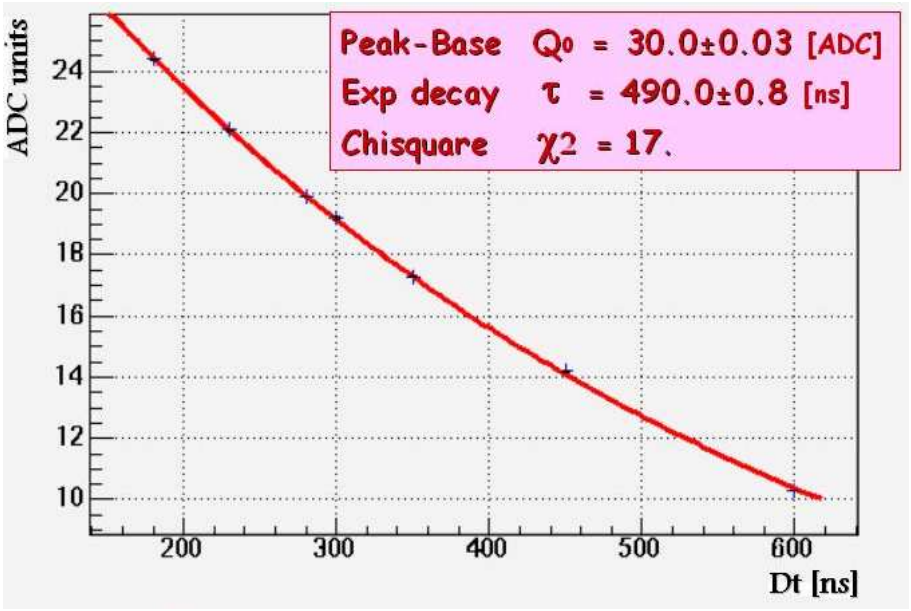

FIGURE 8.37: PLOT OF THE DIFFERENCE OF THE BASELINES OF THE SECOND AND OF THE FIRST HIT $(B_1 - B_0)$ AS A FUNCTION OF THE DELAY TIME BETWEEN THE TWO HITS. THE BEST FIT FUNCTION, SEE EQUATION 8.6, IS ALSO SUPERIMPOSED.

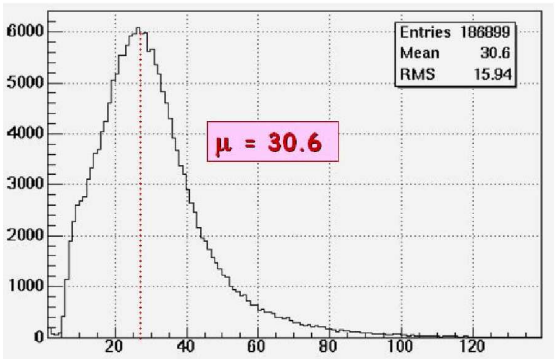

(a) FIGURE 8.38: DISTRIBUTION OF THE CHARGE OF THE FIRST HIT FOR ALL PMTS . THE x-AXIS SCALE IS ADC COUNTS.

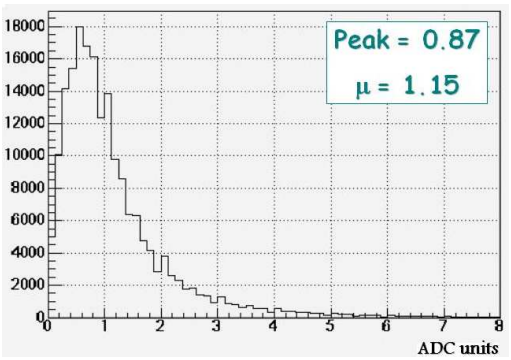

(b) FIGURE 8.38: RATIO OF THE CHARGE OF THE SECOND AND OF THE FIRST HIT FOR ALL PMTS AND ONLY FOR THE 230 ns DELAYED PULSES. THE x-AXIS SCALE IS ADC COUNTS.

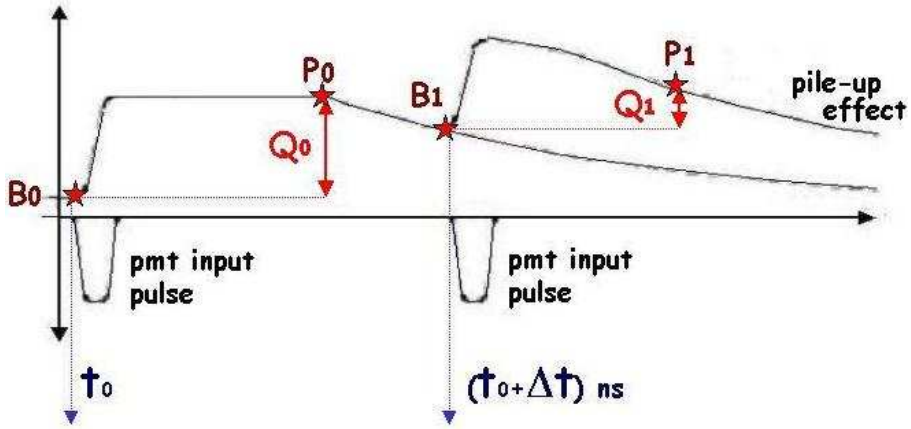

FIGURE 8.39: THE EFFECT OF THE *"pile-up"* ON THE MEASUREMENT OF THE CHARGE OF A MULTIPLE HIT.

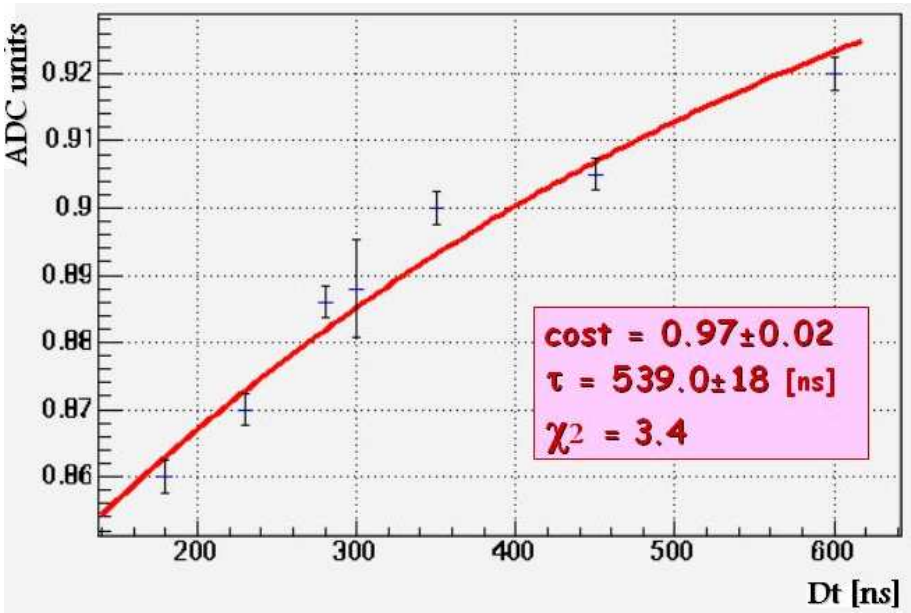

FIGURE 8.40: PLOT OF THE RATIO OF THE CHARGES OF THE SECOND AND OF THE FIRST HIT (Q_1/Q_0) AS A FUNCTION OF THE DELAY TIME BETWEEN THE TWO HITS. THE BEST FIT FUNCTION, SEE EQUATION 8.7, IS ALSO SUPERIMPOSED.

8.8 The first radioactive source data

During the several air runs of 2002/2003 we took also some data with radioactive sources inserted inside our detector. The sources were always quartz vials containing ^{222}Rn -loaded or ^{210}Pb -loaded scintillator.
Basically we used three different sources. All of them were prepared using sources of ^{226}Ra , a long lived isotope that decays α into ^{222}Rn . Actually, the use of a radon source has several advantages:

- the source emits both α and β particles (see the radon decay chain in figure 8.41), allowing for an absolute measurement of the particle discrimination efficiency;
- ^{222}Rn , with a 3.8 days half-life, is sufficiently long lived to permit it to be used over a period of days, yet it decays away quickly enough that it doesn't pose a risk for long term contamination;
- the fast delayed coincidence between the decays of ^{214}Bi and ^{214}Po , short lived radon daughter, allows a good identification of the source signal from the detector background, even with a low activity.

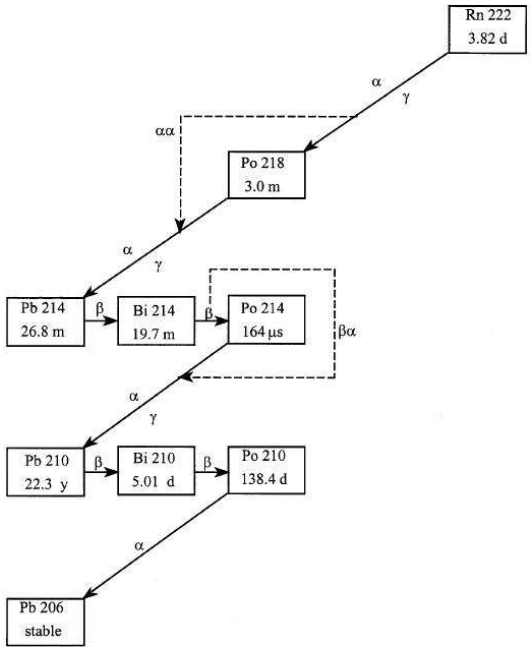

FIGURE 8.41: ^{222}Rn DECAY CHAIN.

Yet, one of them was then sparged with nitrogen, removing in this way the radon content and obtaining instead a ^{210}Pb source.

During the first data taking periods, air runs I-II-III, we used a spherical quartz vial of scintillator, radon-loaded in Munich and then quickly[2]carried inside our detector. The

^{226}Ra source was not a very high intensity source and the exposure time was of same order of the radon meanlife: the resulting radon source had an initial trigger rate of ~100 Hz. The source was then placed inside the sphere, hanging from the top of the SSS . We took several days of data, making a scan on the trigger threshold. Unluckily all data were still affected by the time and charge problems already described in the previous sections. In addition, also the status of the detector was not really stable: a lot of bad PMTs were still connected, flashing the other ones and increasing considerably the dark noise and the `Laben` DSP error rates. This prevented us from an accurate analysis of the splitting algorithm, of the position and energy reconstruction efficiencies and of the α/β discrimination techniques.

Nevertheless, a good result could be equally obtained from the plot of the GPS time differences of two consecutive events.

The radon has among its daughters the fast coincidence $^{214}Bi(\beta)^{214}Po(\alpha)$. ^{214}Bi decays into ^{214}Po emitting β and γ -rays with a meanlife of 28.4 m and a Q value of 3.20 MeV. ^{214}Po decays into ^{210}Pb emitting an α particle with a meanlife of 236 μs . The Q value is 7.69 MeV and the electron equivalent energy is 751 KeV. This is the only fast coincidence of the radon chain: the other lifetimes are at least several minutes.

Figure 8.42(a) shows the distrubution of the GPS time difference of two consecutive events[3]for a run taken during Air Run III, with the source in the center of the sphere.

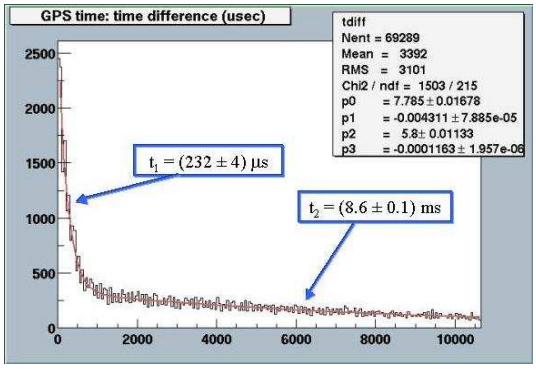

(a) FIGURE 8.42: GPS TIME DIFFERENCES OF TWO CONSECUTIVE EVENTS FOR A SOURCE RUN TAKEN DURING AIR RUN III. THE FIT WITH TWO EXPONENTIAL DECAYS AND THE RELATIVE BEST FIT VALUES ARE ALSO REPORTED. THE x-AXIS SCALE IS μS .

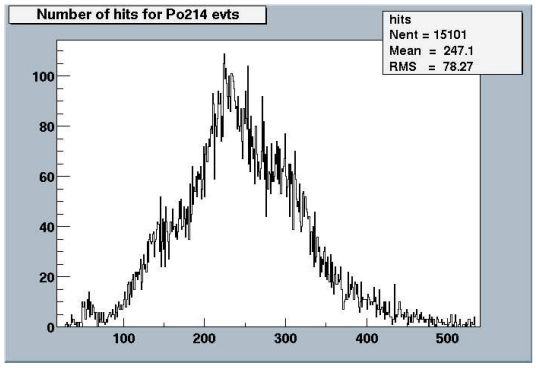

(b) FIGURE 8.42: NUMBER OF HITS FOR THE CANDIDATE ^{214}Po EVENTS. THE x-AXIS SCALE IS THE NUMBER OF HITS.

We tried to fit the plot with two exponential decays. The fastest time constant, (232 ± 4) μs , is well compatible with the 236 μs halflife of ^{214}Po . The second time constant is instead the source trigger rate. The activity of a radioactive sample decays exponentially in time

[2]The radon-loading of the scintillator could not be done on the spot, due to problems in the ^{226}Ra source transport from Munich to Gran Sasso.

[3]The BOREXINO trigger system at each event reads the absolute GPS time from a dedicated clock. Therefore the absolute time of each event is known with ~1 μs precision.

with the law:

$$\frac{1}{\tau}e^{-\frac{t}{\tau}} \tag{8.9}$$

where $\frac{1}{\tau}$ is the transition probability per unit time. The fit value of this time constant results (6.6 ± 0.1) ms; this gives 116 Hz of trigger rate, that is compatible with the measured number.

Finally we selected the $^{214}Bi(\beta)^{214}Po(\alpha)$ fast coincidences[4] and used the ^{214}Po α peak to check the scintillator light yield number. Assuming the CTF light yield, 386 photoelectrons/MeV, we expected the ^{214}Po events to be peaked around 290 hits. Figure 8.42(b) shows a slightly lower mean value. This could be due to some contamination of the scintillator with oxygen: the oxygen acts actually as a quencher, lowering the 751 KeV electron equivalent energy and then the expected 290 hits.

8.9 Monte Carlo studies on the splitting algorithm

The identification of multiple events in a single trigger record and the dark noise background rejection are two crucial points of the reconstruction software. Being the data acquisition window 7 μs , both the dark noise hits and the hits belonging to independent events closer than 7 μs are merged in a single hit list. It is then up to a dedicated offline module, the *"event splitting"* routine (section 7.5), to trace back the hits belonging to the real physical events.

A lot of work was done to prepare and tune the splitting algorithm. This work was mostly based on Monte Carlo: the Monte Carlo Truth (`BxMcTruthFrame`) stores the data coming from GENEB and from the tracking codes and allows then a direct comparison between the *"simulation truth"* and the reconstruction outputs. The data presented here refers to Monte Carlo simulations of α and β particles of different energies.

The first version of the algorithm was structured in two modules. The first module finds the number of *cluster*s in the 7 μs gate window. In our offline language we define a *cluster* a set of hits close in time (some hundreds *ns*) and clearly due to some triggering condition. The real physical event is instead a *fragment*; a single cluster can be made of one, two, or even three fragments. The first module works then with a large time binning (100 *ns*) and with a minimum threshold of hits in one bin (at least 30 hits in 100 *ns*) to identify the longer delayed coincidences.
Yet, the multiple events almost superimposed or closer than 100 *ns* needed a second splitting step. This second module has to deeply study the single cluster's time distribution, searching for more complex structures and for a more precise estimation of the fragment's start and end times.

This two-steps routine had two main weak points: the percentage of fake clusters[5] was large (see figure 8.43(a)) and the identification of the fragment's start time was not precise enough. Figure 8.44 shows a comparison between the Monte Carlo truth's photon times and the fragment's times. Particularly at low energies the fragment's start time is sometimes mistaken for a dark noise hits (see figure 8.45).

[4] The requirement was a delay between the two candidate events included between 20 and 470 μs .

[5] The fake cluster rate was evaluated running the splitting algorithm on a dark noise run, where the expected rate of splitted events is 0.

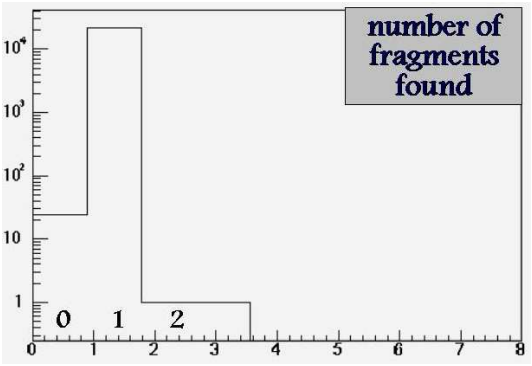

(a) FIGURE 8.43: FAKE CLUSTER RATE OF THE FIRST SPLITTING ROUTINE. THE RATE WAS EVALUATED RUNNING THE SPLITTING ON A DARK NOISE RUN, WHERE THE EXPECTED RATE OF SPLITTED EVENTS IS 0.

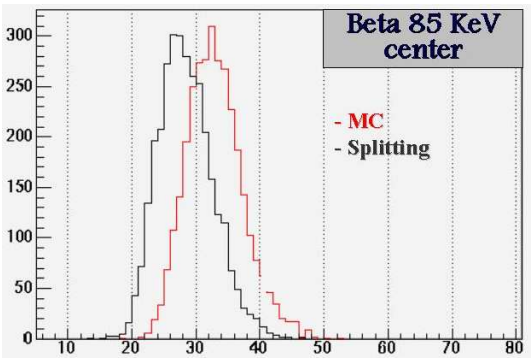

(b) FIGURE 8.43: COMPARISON BETWEEN THE MONTE CARLO TRUTH'S NUMBER OF HITS (RED) AND THE FRAGMENT'S NUMBER OF HITS (BLACK) FOR 85 KEV β EVENTS IN THE CENTER. THE x-AXIS SCALE IS THE NUMBER OF HITS.

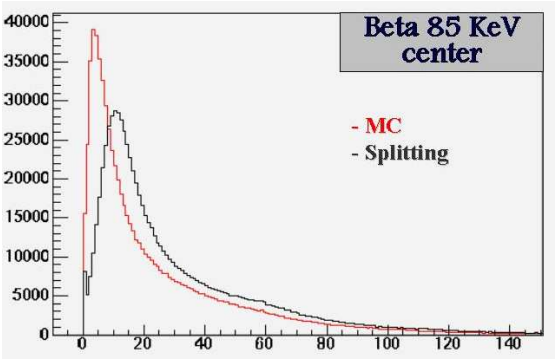

(a) FIGURE 8.44: COMPARISON BETWEEN THE MONTE CARLO TRUTH'S PHOTON TIMES (RED) AND THE FRAGMENT'S TIMES (BLAK)FOR 85 KEV β EVENTS IN THE CENTER. THE x-AXIS SCALE IS ns .

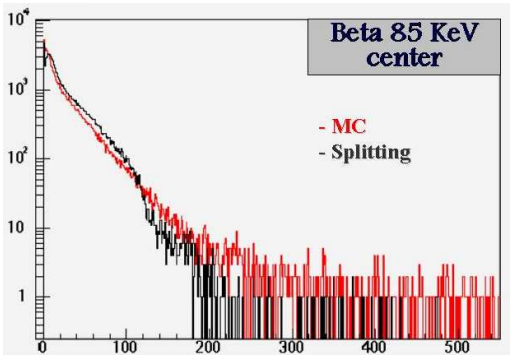

(b) FIGURE 8.44: SAME PLOTS IN LOGARITHMIC SCALE. THE x-AXIS SCALE IS ns .

Several improvements in the splitting algorithm were then made. First of all the informations on the detector channels status (section 8.6) is read from the Data Base and used to exclude the bad hits[6]from the reconstruction. Moreover the new algorithm uses 16 ns bins, instead of 100 ns , and sets its threshold accordingly to the detector's dark noise rate (also this information is read from DB). A more detailed description of the algorithm

[6]The hits flagged with a `Laben` DSP error or belonging to very hot PMTs are discarded.

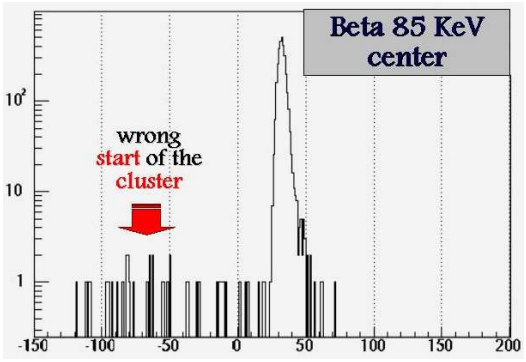

(a) FIGURE 8.45: DIFFERENCE BETWEEN THE MONTE CARLO TIME OF AN EVENT AND THE TIME OF THE FIRST PHOTON OF ITS SPLITTED FRAGMENT. THE PLOT REFERS TO 85 KEV β EVENTS GENERATED IN THE CENTRE OF THE SPHERE. THE SMALL FRACTION OF DARK NOISE HITS MISTAKEN FOR FRAGMENT'S HITS IS CLEARLY VISIBLE. THE x-AXIS SCALE IS ns .

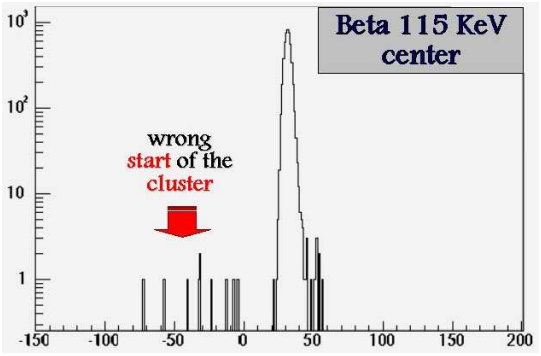

(b) FIGURE 8.45: SAME PLOT FOR 115 KEV β EVENTS IN THE CENTRE OF THE SPHERE. THE IDEAL PLOT SHOULD BE ZERO UP TO A CONSTANT TIME AND THEN SHOW A SHARP PEAK. THE CONSTANT TIME IS THE TIME OF FLIGHT OF THE PHOTONS FROM THE CENTER OF THE DETECTOR UP TO THE PHOTOTUBES, WHILE THE WIDTH OF THE PEAK GIVES THE RESOLUTION OF THE ALGORITHM ON THE FRAGMENT'S START TIME SELECTION. THE x-AXIS SCALE IS ns .

can be found in section 7.5.
The performances of the improved algorithm are a low fake cluster rate (less than 0.5%) and a good identification of the fragment's start time. Table 8.1 and figure 8.46 show the comparison of the time resolution of the original splitting and of the improved version. The time resolution is quoted as the width of the distribution of differences between the Monte Carlo event's time and the fragment's start time.

Energy β events in the centre	***First splitting resolution***	***Current splitting resolution***
85 KeV	3.17 ns	2.51 ns
100 KeV	2.97 ns	-
115 KeV	2.64 ns	1.89 ns
130 KeV	2.47 ns	-
145 KeV	2.30 ns	1.59 ns
160 KeV	2.22 ns	1.49 ns
190 KeV	2.22 ns	1.42 ns

TABLE 8.1: COMPARISON OF THE TIME RESOLUTION OF THE ORIGINAL SPLITTING AND OF THE IMPROVED VERSION.

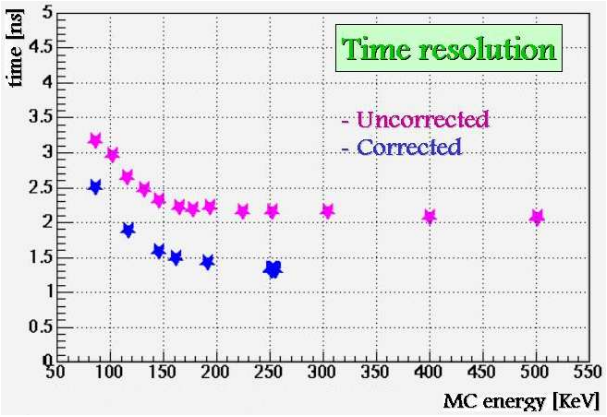

FIGURE 8.46: COMPARISON OF THE TIME RESOLUTION OF THE ORIGINAL SPLITTING AND OF THE IMPROVED VERSION.

Nevertheless, at low energies a non negligible fraction of events is still not correctly splitted (the splitting efficiency for 85 KeV β events is $\sim$75%). The splitting cuts still have to be optimized. A wonderful opportunity to test this code came with the source data taken during the last air run, in particular Air Run V and Air Run VIII. The results of this analysis are presented in the next section 8.10.

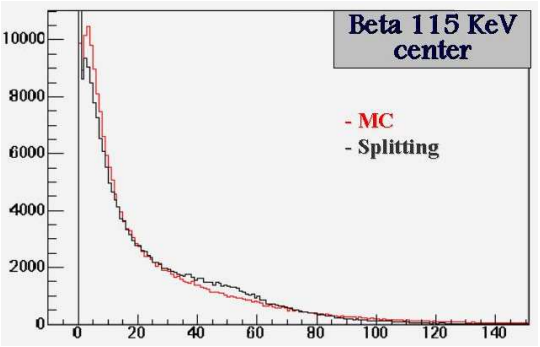

(a) FIGURE 8.47: THE TIMES OF THE MC PHOTONS (RED) ARE COMPARED WITH THE FRAGMENT'S HITS TIMES (BLACK).

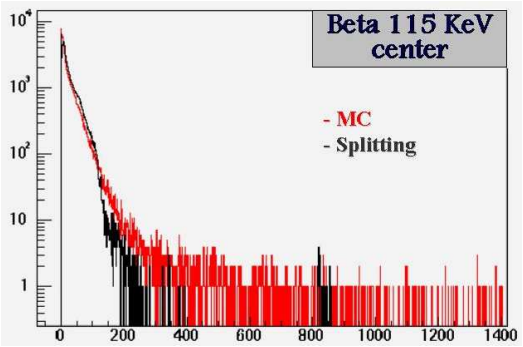

(b) FIGURE 8.47: SAME PLOT ON A LARGER TIME SCALE AND IN LOGARITHMIC SCALE ON THE Y-AXIS. THE DATA REFERS TO 115 KEV β EVENTS GENERATED IN THE CENTRE OF THE SPHERE.

8.10 Air Run V data: the splitting and spatial reconstruction results

During Air Run V we used a radioactive source different from the one used during the first data taking periods. This source, provided by our Princeton University group, was again a quartz cell containing radon-loaded PC , but preparated in such a way to obtain a ^{210}Pb source, instead of a ^{222}Rn source.
First, to remove the contaminants, the PC was distilled; then it was transferred to a glove box where it was sparged with nitrogen, to remove any oxygen that may have entered. After nitrogen sparging radon was added to the PC . The ^{226}Ra source used to fill the PC with radon was a really high intensity source (2 MBq) and the exposure time was definitely longer than some days. Radon was then allowed to diffuse into the PC and decay for 10 days. Finally the PC was sparged for 16 hours to remove the remaining radon, reducing it by six orders of magnitude. Concentrated PPO from a master solution was also added as a wavelenght shifter.

After the scintillator is sparged there are several short lived decay products with half lives on the order of tents of minutes that eventually turn into ^{210}Pb , which has a half life of 22.3 years: this essentially creates a source of ^{210}Pb . In its turn, ^{210}Pb decays into ^{210}Bi and ^{210}Po .
The β decay of ^{210}Pb (Q = 61/17 KeV) has too low energies to be detected; only the ^{210}Bi β decay (Q=1.16 MeV) and the ^{210}Po α decay (5.305 MeV, 395 KeV electron equivalent energy) are visible. Unluckily the ^{210}Bi half life (7.23 days) is too long to allow a fast coincidence correlation. The only signature we can expect from this source is then in its energy spectrum, with the 395 KeV α peak superimposed on a continuous β spectrum, with a 1.16 MeV end point.

The source was inserted inside the sphere and moved in four different positions along the z-axis: in the SSS centre and 1, 2 and 3 meters above the centre. This allowed a real test of the splitting and position reconstruction algorithms.

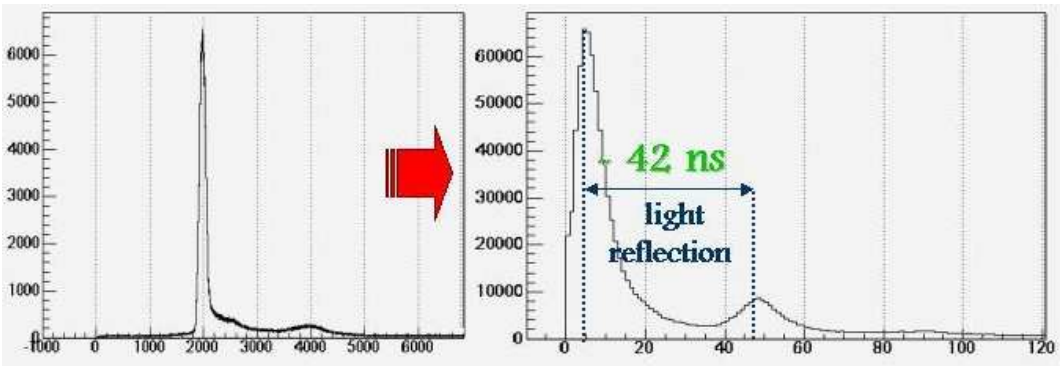

Figure 8.48: time distribution of the hits of correctly splitted events. The data refer to a source run taken during Air Run V. The broad central peak is due to the jitter of the trigger signal (100 ns). Beside we plot instead the time distribution of the fragment's hits. The x-axis scale is ns .

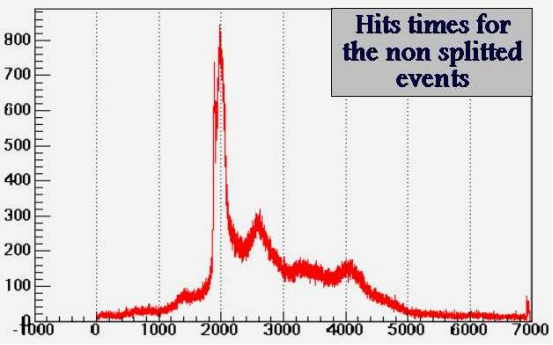

(a) FIGURE 8.49: TIME DISTRIBUTION OF THE HITS OF NON-SPLITTED EVENTS. THE DATA REFER TO A SOURCE RUN TAKEN DURING AIR RUN V. THE x-AXIS SCALE IS ns .

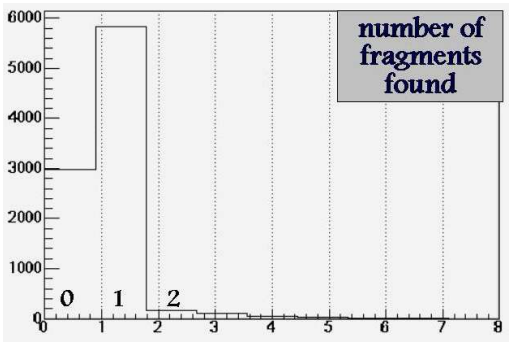

(b) FIGURE 8.49: SPLITTING EFFICIENCY ON REAL DATA. THE ZERO FRAGMENT COLUMN GIVES THE NON-SPLITTED EVENTS RATE.

Figures 8.48 and 8.49 show the result of the splitting algorithm on these data. The splitting efficiency is low (~70%), but the non splitted events are essentially of two types. First of all we have some events with a light pattern lasting several μs (see figure 8.49(a)). Their nature is still to be really understood. Probably they are due to some electronic noise, but for sure are events not correlated with the source. A dedicated routine will discard them before the splitting phase.
Yet, besides these events, we still have some good and non-splitted events. However, the inefficiency of the splitting algorithm on these events is due to the high rate of `Laben` DSP errors we had during this data taking. Actually these bad hits can fall inside the trigger window and contribute to fire the trigger. This results is a lower *real* trigger threshold. When we software re-apply the trigger threshold cut inside the splitting algorithm we can then reject some good but low energy events. Unluckily, these bad have no time or charge measurements (they are set to fake values) and we can not re-correct the cut on the trigger threshold taking into account their effect.

Real position (x,y,z) [cm]	***Reco x [cm]***	***Standard deviation [cm]***	***Reco y [cm]***	***Standard deviation [cm]***	***Reco z [cm]***	***Standard deviation [cm]***
(0,0,0)	-1.7	25	2.6	16	8.4	25
(0,0,100)	4.6	20	5.0	13	93	29
(0,0,200)	-0.4	22	5.0	18	192	25

TABLE 8.2: POSITION RECONSTRUCTION RESULTS ON AIR RUN V DATA, WITH THE SOURCE MOVED IN DIFFERENT POSITIONS ALONG THE Z-AXIS. THE LIGHT PROPAGATION IS IN AIR AND THE REFRACTION INDEX IN THE OFFLINE CODE WAS CHANGED ACCORDINGLY.

The events that are correctly splitted show instead good time distributions (see figure 8.48). In addition, being the light propagation in air and not in PC , the first reflection peak, about 41 *ns* delayed, is also well visible. This could infer the position reconstruction efficiency, since the pulse shape distribution used in the position reconstruction is calibrated for the light propagation in the scintillator. The position reconstruction attempts done so far (see table 8.2) have used this pdf, changing only the refraction index of PC to air. Some work is now on going to simulate the correct pulse shape distribution also for the light propagation in air.

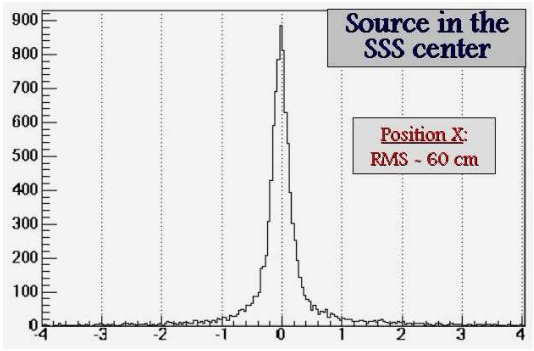

(a) FIGURE 8.50: DISTRIBUTION OF THE RECONSTRUCTED x POSITION FOR THE DATA WITH THE SOURCE PLACED IN THE DETECTOR'S CENTER.

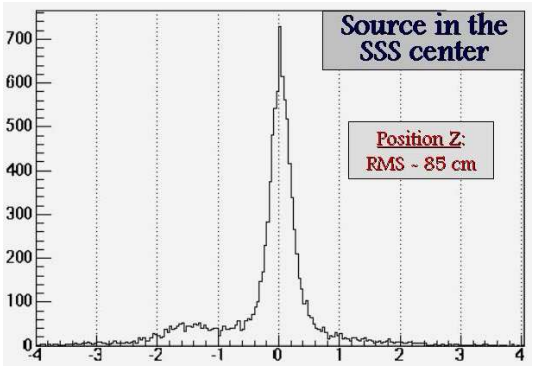

(b) FIGURE 8.50: DISTRIBUTION OF THE RECONSTRUCTED z POSITION FOR THE DATA WITH THE SOURCE PLACED IN THE DETECTOR'S CENTER.

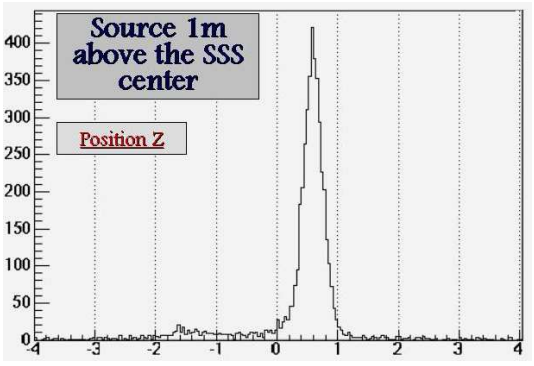

(a) FIGURE 8.51: DISTRIBUTION OF THE RECONSTRUCTED z POSITION FOR THE DATA WITH THE SOURCE PLACED 1 METER ABOVE THE CENTRE OF THE SPHERE, ALONG THE z AXIS.

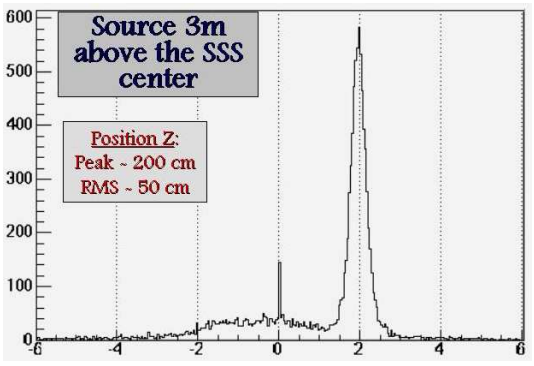

(b) FIGURE 8.51: DISTRIBUTION OF THE RECONSTRUCTED z POSITION FOR THE DATA WITH THE SOURCE PLACED 3 METERS ABOVE THE CENTRE OF THE SPHERE, ALONG THE z AXIS.

The particle identification methods

In BOREXINO signal comes largely from α , β or μ particles. While the last are detected and tagged by a dedicated Outer Muon system, this does not happen for α and β particles produced by the internal radioactivity. Even worse, the quenching effect of the scintillator moves the α emitted spectrum ($4.0 \div 8.8$ MeV) in the ^7Be energy range ($260 \div 990$ KeV). We already quoted in section 4.1.2.1 that, if we assume secular equilibrium for the uranium and thorium chains and consider a level of 10^{-16} g/g for both ^{238}U and ^{232}Th contamination and of 10^{-14} g/g for K_{nat} , we still have $\sim$26 β +γ events/day and $\sim$96 α events/day, in the Neutrino Window and in the 100 t fiducial volume.
To not overestimate the neutrino events because of this internal background, we need then an efficient α/β discrimination technique. This is provided by our scintillator: in organic liquid scintillators α particles have a higher ionization density than electrons or γ -rays, resulting in a greater light emission in the longer time components of the scintillation pulse[1].

In December 2003 we had some days of data taking (*Air Run 8*) with all available PMTs (about 2000) turned on. We took data using both the laser calibration system and a radon loaded PC source hanged to the top of the Stainless Steel Sphere[2]. In this section I focused on some results on α/β discrimination, obtained with the radon source data, and particularly those obtained using a clean sample of $^{214}Bi(\beta)^{214}Po(\alpha)$ coincidences.

9.1 α/β DISCRIMINATION TECHNIQUES IN BOREXINO

A particle identification problem usually involves with the classification of an event among m different classes, when we are given a set of correctly identified events belonging to these m classes.
The set of correctly identified events, called the *training set*, is basically a set $\mathcal{S} = \{\mathbf{x}_i, y_i\}$ of sample-label pairs. Each sample is a vector $\mathbf{x} \in \mathcal{R}^n$ and represents an event belonging to one of the m different classes; $y \in [1, \ldots, m]$ is given to us by a trusted source and labels the class which the event belongs to.
The goal of a classification problem is to produce a model which predicts the class of a previously unseen sample $\mathbf{x} \notin \mathcal{S}$. The fundamental problem is called generalization: how it is possible to infer a law which will be valid for an infinite number of future observations, given only a finite amount of data?

[1] I already briefly outlined in section 3.3.5 the principle of the α quenching and of the α/β discrimination in organic scintillators.

[2] This source was prepared by our Princeton group.

In BOREXINO , α/β discrimination relies on the difference of the time distribution of α and β excitations (see section 3.3.5). Different classification methods that do not require any assumption on the shape of the events can then be applied.
For our purpose, an event is the list[3]of the arrival times $\{(t_i - t_0)\}$ of the hits on the photomultipliers (where t_i is the detected time of the i-th photon and t_0 is the detected time of the first photon). The time distributions of the α and β events of the $^{214}Bi(\beta)^{214}Po(\alpha)$ coincidence as obtained from the source data of December 2003, are shown in figure 9.1(a).

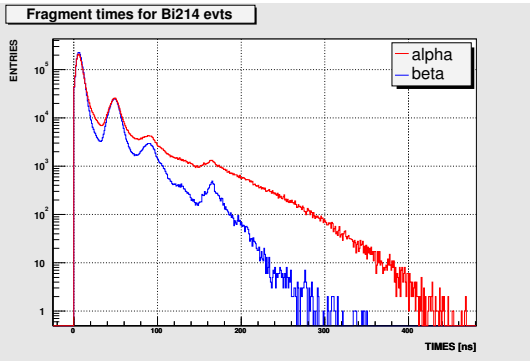

(a) FIGURE 9.1: COMPARISON OF THE TIME DISTRIBUTIONS OF α AND β EVENTS IN AIR. THE DISTRIBUTIONS ARE OBTAINED USING THE SOURCE DATA OF DECEMBER 2003, AND THE EVENTS ARE SELECTED USING THE FAST $^{214}Bi(\beta)^{214}Po(\alpha)$ COINCIDENCE. THE SOURCE WAS IN THE CENTER OF THE SSS . THE CLEARLY VISIBLE SECOND PEAK, ABOUT 40 NS LATER, IS DUE TO THE REFLECTION OF THE LIGHT ON THE PMTS PHOTOCATODES.

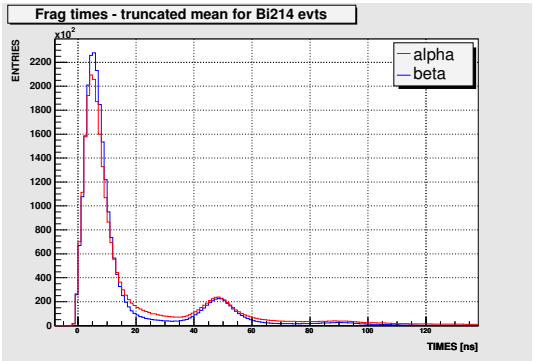

(b) FIGURE 9.1: COMPARISON OF THE TIME DISTRIBUTIONS OF α AND β EVENTS IN AIR. THE PLOT IS NOW IN LINEAR SCALE AND TIMES IS THE DIFFERENCE BETWEEN THE TIME OF EACH HITS AND A TRUNCATED MEAN TIME.

Since these distributions are very sensitive to the time of the first photon we found convenient to subtract to each time a truncated mean time t_m, computed using only the times under the central peak (among 3 *ns* and 30 *ns*). In this way we should limit the effect of a dark noise hit taken for the first hit of an event and shifting therefore the total distribution $\{(t_i - t_0)\}$.

Since particle identification methods are generally solved in a space with fixed-dimension ($\mathcal{R}^n$), while the size of the arrays of the photons times depends on the number of hits of the events (because they have different energies or because of statistical fluctuations), we had to introduce a standard time binning. The i-th component of the sample $\mathbf{x}$ is then the content of the i-th bin.
We have binned the $[0, 500]$ *ns* time window in 63 bins. We used a not uniform binning: the bins goes from 2 *ns* under the central peak to 50 ns in the farther region, to store up enough statistics in the tails of the distributions. The binned time plot of a single event is shown in

[3]This list of times includes obviously only the hits the offline code has identified as belonging to a real physical event, excluding therefore dark noise and spurious hits. In particular this job is done inside the *splitting* routine.

figure 9.2. Some tests on different binnings, including a uniform binning, were also carried out, but all with worse results.

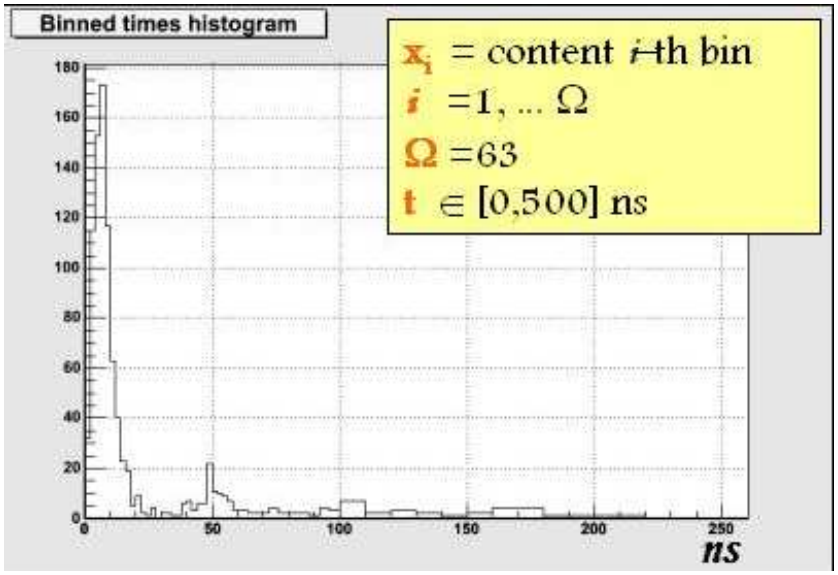

FIGURE 9.2: BINNED TIME PLOT FOR A SINGLE β EVENT (905 HITS). THE TIMES ARE BINNED USING THE REFERENCE HISTOGRAM CHOSEN FOR THE α/β ANALYSIS. THE BINNING IS NOT UNIFORM!

We let:

- Ω the total number of bins used (63);
- i labels the bins and runs from 1 to Ω;
- x_i = the number of entries in the i-th bin;
- $\mathbf{x} = \{x_i\}$ the sample, i.e. the *event* to be classified;
- $N = \sum_i x_i$ the total number of entries. We assume all events to be normalized to the same total number. Events of different energies can therefore be compared.
- $X_i = (\sum_{j=1}^{i} x_j)/(\sum_{j=1}^{\Omega} x_j)$, the number of entries in the i-th bin for the cumulative distribution, normalized to 1;
- $\mathbf{X} = \{X_i\}$ the cumulative sample;
- N_α = size of the α training set, i.e. the number of good α events used as examples;
- N_β = size of the β training set, i.e. the number of good β events used as examples;
- $\mathbf{x}_j^\alpha = \{x_{ij}^\alpha\}$ the j-th sample of the α training set $(i = 1, \ldots, \Omega, j = 1, \ldots, N_\alpha)$;
- $\mathbf{x}_j^\beta = \{x_{ij}^\beta\}$ the j-th sample of the β training set $(i = 1, \ldots, \Omega, j = 1, \ldots, N_\alpha)$;

- $\alpha_i = \left(\frac{1}{N_\alpha}\sum_{j=1}^{N_\alpha} x_{ij}^{\alpha}\right)$ the number of entries in the i-th bin for the average sample of the α training set;
- $\alpha = \{\alpha_i\}$ the average sample of the α training set;
- $\beta_i = \left(\frac{1}{N_\beta}\sum_{j=1}^{N_\beta} x_{ij}^{\beta}\right)$ the number of entries in the i-th bin for the average sample of the β training set;
- $\beta = \{\beta_i\}$ the average sample of the β training set;
- $a_i = (\sum_{j=1}^{i} \alpha_j)/(\sum_{j=1}^{\Omega} \alpha_j)$, the number of entries in the i-th bin for the average cumulative distribution (normalized to 1) of the α training set;
- $\mathcal{A} = \{a_i\}$, the average cumulative sample of the α training set;
- $b_i = (\sum_{j=1}^{i} \beta_j)/(\sum_{j=1}^{\Omega} \beta_j)$, the number of entries in the i-th bin for the average cumulative distribution (normalized to 1) of the β training set;
- $\mathcal{B} = \{b_i\}$, the average cumulative sample of the β training set;

Below I briefly summarize the different discrimination techniques used in this analysis.

9.1.1 The tail to total ratio

Undoubtedly this is the simplest pulse-shape discrimination method we can apply in this context and does not even need any learning on a training set.
Given a normalized sample $\mathbf{x}$, we compute the ratio:

$$t = \frac{\sum_{i=tail}^{\Omega} x_i}{\sum_{i=1}^{\Omega} x_i}$$

where *tail* is a cut on time, generally placed around 20-30 ns for these data.
Due to the fact that α events have a longer tail we expect the distribution of this ratio t to be centered around higher values for α than for β events.

9.1.2 The Gatti linear discriminant

Let $\{\alpha_i\}$ and $\{\beta_i\}$ be the quantities defined before (section 9.1) for normalized events. The more general linear filter is given by a particle identification signal $\mathbf{S}$ that can be written as a weighted sum of the α and β contributions:

$$\mathbf{S}_\alpha = \sum_i P_i\alpha_i \qquad \mathbf{S}_\beta = \sum_i P_i\beta_i$$

The two signals differ by:

$$\Delta = \mathbf{S}_\alpha - \mathbf{S}_\beta = \sum_i P_i(\alpha_i - \beta_i)$$

The Gatti filter is the linear discriminant defined by the weights $\{P_i\}$ that reduce the relative variance $(\epsilon_\Delta^2/\Delta^2)$ of this difference to a minimum.

It can be readily proved[81, 86] that, in the hypothesis of statistical Poisson fluctuations for the $\{\alpha_i\}$ and $\{\beta_i\}$ quantities and assuming the same size for the two training sets ($N_\alpha = N_\beta$), the weights $\{P_i\}$ turn out be be:

$$P_i = \frac{\alpha_i - \beta_i}{\alpha_i + \beta_i}$$

This filter results to be the optimum linear discriminant that can be built and the quantity:

$$g = \sum_{i=1}^{\Omega} \frac{\alpha_i - \beta_i}{\alpha_i + \beta_i} \cdot x_i$$

is the discriminant variable used.

9.1.3 The maximum likelihood functions

In the hypothesis of Poisson fluctuations for the $\{\alpha_i\}$ and $\{\beta_i\}$ quantities and neglecting any correlation between neighbouring bins, we can compute the likelihood of the sample $\mathbf{x}$ to belong to the α or to the β class using Poisson. We have:

$$\begin{cases} P(\alpha_i, x_i) = \dfrac{{\alpha_i}^{x_i} e^{-\alpha_i}}{x_i!} \\ \\ P(\beta_i, x_i) = \dfrac{{\beta_i}^{x_i} e^{-\beta_i}}{x_i!} \end{cases}$$

that means:

$$\begin{cases} L_\alpha(\mathbf{x}) = \displaystyle\prod_{i=1}^{\Omega} \frac{{\alpha_i}^{x_i} e^{-\alpha_i}}{x_i!} \\ \\ L_\beta(\mathbf{x}) = \displaystyle\prod_{i=1}^{\Omega} \frac{{\beta_i}^{x_i} e^{-\beta_i}}{x_i!} \end{cases}$$

In practice, we use the logarithm of the likelihood function, that is:

$$\begin{cases} \mathcal{L}_\alpha(\mathbf{x}) = \displaystyle\sum_{i=1}^{\Omega} x_i ln(\alpha_i) - ln(x_i!) - \alpha_i \\ \\ \mathcal{L}_\beta(\mathbf{x}) = \displaystyle\sum_{i=1}^{\Omega} x_i ln(\beta_i) - ln(x_i!) - \beta_i \end{cases}$$

We can also compute the likelihood ratio:

$$\mathcal{L}_R(\mathbf{x}) = \frac{\mathcal{L}_\alpha(\mathbf{x})}{\mathcal{L}_\beta(\mathbf{x})} = \sum_{i=1}^{\Omega} x_i ln\left(\frac{\alpha_i}{\beta_i}\right) - (\alpha_i - \beta_i)$$

Both $\mathcal{L}_\alpha$,$\mathcal{L}_\beta$ and $\mathcal{L}_R$ can be used as discriminant variables. Please note, however, that the three variables are correlated, and only two of them are useful in a multi-discrimination method approach.

9.1.4 The Kolmogorov distances

This test of hypothesis works only with the cumulative distributions and is based on the maximum distance between the sample curve and the average distributions $\mathcal{A}$ and $\mathcal{B}$. In practice, given the sample $\mathbf{x}$ and built its cumulative distribution $\mathbf{X}$, we look for:

$$\begin{cases} D_\alpha = \max_i \ |a_i - X_i| \\ D_\beta = \max_i \ |b_i - X_i| \end{cases}$$

In this analysis I have used this distance directly as a discriminant variable. Actually a more sophisticated statistical method using the cumulative distributions was already studied in [87, 83]. We plan to introduce this work in this analysis in the near future.

9.1.5 The Support Vector Machines

Started by Vapnik [84] in the Sixties, Support Vector Machines are part of the statistical learning theory, that studies the process of inferring regularities from empirical data.

Basically Support Vector Machines use a linear separating hyperplane to create a classifier, yet some problems cannot be linearly separated in the original input space. Support Vector Machines can non-linearly transform the original input space into a higher, maybe infinite, dimensional feature space. The mapping of the input space in this higher dimensional space is realized through non linear functions choosen a priori, and called the Support Vector Machines's *kernels*. This makes it possible to find a linear optimal separating hyperplane in feature space which correspond to non-linear decision surfaces in input space. This hyperplane is optimal is the sense of maximizing the minimum distance between the hyperplane and any sample of the training data and the distance between this hyperplane and the test samples is then the $\mathcal{SVM}$ discriminant variable.

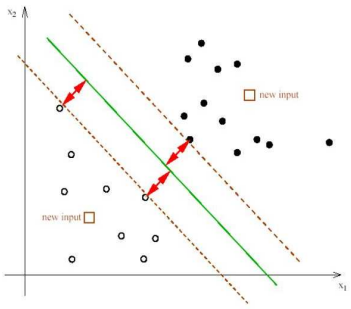

(a) Figure 9.3: support vector machines in a linear separable case.

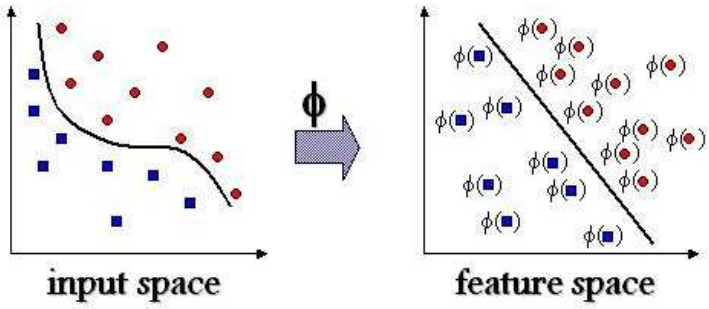

(b) Figure 9.3: linear optimal separating hyperplane in feature space which correspond to non-linear decision surfaces in input space.

Depending on the *kernel* function, different types of $\mathcal{SV}$ machines are constructed. The four kernels used in standard $\mathcal{SVM}$ problems are:

- *linear:* $K(x_i, x_j) = x_i^T x_j$

- *polynomial:* $K(x_i, x_j) = (\gamma x_i^T xj + r)^d \ \ (\gamma > 0)$
- *radial basis function* (RBF)*:*
  $K(x_i, x_j) = e^{(-\gamma ||x_i - x_j||^2)} \ \ (\gamma > 0)$
- *sigmoid:* $K(x_i, x_j) = tanh(\gamma x_i^T x_j + r)$

where γ, r and d are kernel parameters.
The results presented in this chapter were obtained using polynomial kernels. Some attempts with different functions (a linear and a radial basis function) were also made, but all with worse results.

9.2 Results on α/β discrimination efficiency with Air Run 8 data

During Air Run 8 we took several data with a radon source inserted inside the sphere. The source, a small cylindrical quartz vial containing radon loaded scintillator, was hanged in the detector from the top of the SSS and was moved in five different positions along the z-axis (see table 9.1).

Run number	**Total events**	**Radon events**	**z [cm]**
1544	8223	1024	0
1545	9291	1196	0
1546	39854	4920	0
1547	29675	3493	53
1548	23591	2066	53
1550	25599	3044	53
1552	14069	1715	53
1571	19672	1969	153
1572	55739	6658	153
1574	8815	1124	253
1575	6746	853	253
1577	12324	1488	253
1579	29855	3726	253
1582	12636	1636	253
1583	42091	4081	403
1598	17121	2128	0
1600	14551	1862	0
1603	10516	1326	0
1605	66025	8411	0

Table 9.1: List of the source runs taken in December 2003. For each run the source's position (0,0,z) and the statistic of the run are also reported. (0,0,0) is the SSS centre.

These data were very clean and really under control and allowed us useful studies on α/β discrimination. To perform these studies I have also developed a rather general ParticleId package. This is a flexible, ROOT -based software, that can be used both in the offline code and directly inside ROOT . α/β is here just the first application, though of course the most important, but several event classification problems can be implemented inside this framework. A more detailed description of the software can be found in section 7.7.

9.2.1 The selection of the training set

Radon has among its daughters the fast $^{214}Bi(\beta)^{214}Po(\alpha)$ coincidence: ^{214}Bi decays into ^{214}Po emitting β and γ-rays with a meanlife of 28.4 m and a Q value of 3.20 MeV and ^{214}Po decays, in its turn, into ^{210}Pb , emitting an α particle with a meanlife of 236 μs . The Q value is 7.69 MeV and the electron equivalent energy is 751 KeV. This is the only fast coincidence of the radon chain, since the other lifetimes are at least several minutes.

Figure 9.4(a) shows the distribution of the GPS time differences of two consecutive events[4]for a run with the radon source in the center of the sphere. [5]The BOREXINO trigger system at each event reads the absolute GPS time from a dedicated clock. Therefore the absolute time of each events is known with $\sim$1 μs precision.

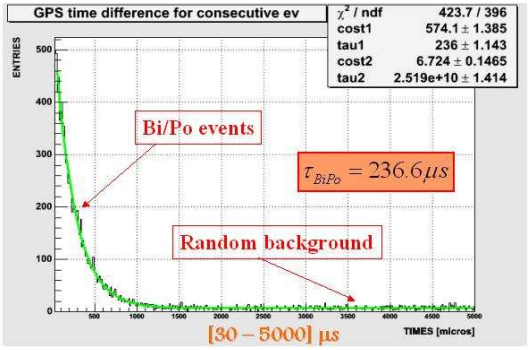

(a) Figure 9.4: Distribution of the GPS time difference of two consecutive events in the time window $[30\mu s\ , 5ms]$. The plot is fitted with an exponential decay plus a constant. The exponential decay time is well compatible with the ^{214}Po halflife.

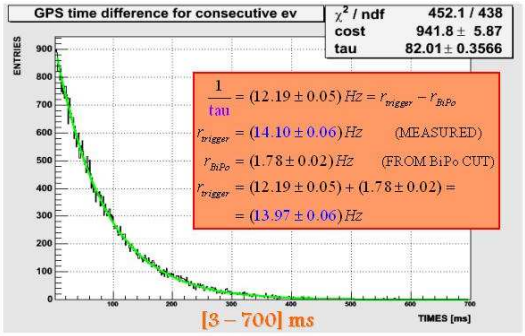

(b) Figure 9.4: Distribution of the GPS time difference of two consecutive events in a farther time window $[3, 700]ms$. The fast $^{214}Bi(\beta)^{214}Po(\alpha)$ coicidence falls outside this window and we can see only the exponential decay due to the activity of the source.

The first plot in figure 9.4 is a fit of the fast coincidence region, between 30μs and $5ms$, with two exponential decays. The fastest time constant, (236.0 ± 1.1) μs , is well compatible with the 236.6 μs halflife of ^{214}Po . The second time constant is linked, instead, with the activity of the source.
The second plot is a fit of the farther region, between 3 ms and 700 ms, with a single exponential decay. In this region we are outside the fast $^{214}Bi(\beta)^{214}Po(\alpha)$ coincidence and the resulting decay constant is basically the trigger rate without the contribution of the $^{214}Bi(\beta)^{214}Po(\alpha)$ events.

For the plot in figure 9.4(b), the $^{214}Bi(\beta)^{214}Po(\alpha)$ rate is 1.78 ± 0.02 Hz (8270 events in 4665 s) and the decay constant gives a rate (1/tau) of 12.19 ± 0.05 Hz. This gives a total rate of 13.97 ± 0.21, that is well compatible with the measured 14.1 ± 0.06 (65954 events in 4665 s).

These plots demonstrate that we can easily select the α and β events of the fast $^{214}Bi(\beta)^{214}Po(\alpha)$ coincidence in the radon chain. This opportunity gives us a wonderful handle to obtain a clear sample of α and β events directly from our data set, without any use of Monte Carlo simulations.
In addition, we can also check the quality of the sample *a posteriori*. We can fit the distribution of the GPS time differences of the consecutive events that have overcome the fast coincidence cut[6] with an exponential decay function (whose decay time is fixed to the exact ^{214}Po meanlife, i.e. 236 μs) plus a constant. The value of this constant baseline is proportional to the number of fake events we have classified as $^{214}Bi(\beta)^{214}Po(\alpha)$ coincidences (figure 9.5). For the plot in figure 9.5 we have less than 80 uncertain events out of 8500 coincidences. No other cuts are therefore needed to select very clean samples.

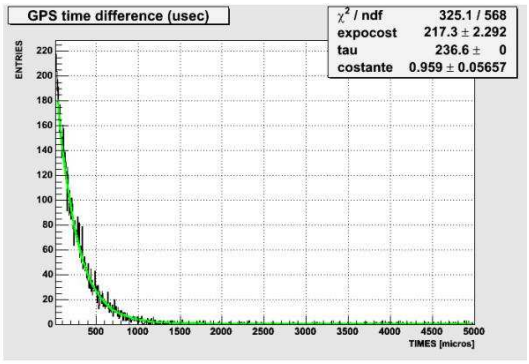

FIGURE 9.5: DISTRIBUTION OF THE GPS TIME DIFFERENCE OF THE CONSECUTIVE EVENTS THAT HAVE OVERCOME THE $^{214}Bi(\beta)^{214}Po(\alpha)$ SELECTION CUT. IF WE FIT THE PLOT WITH AN EXPONENTIAL DECAY PLUS A CONSTANT, FIXING THE DECAY CONSTANT TO THE EXACT VALUE OF THE ^{214}Po MEANLIFE (236 μS), WE CAN ESTIMATE THE CONTAMINATION OF OUR α AND β SAMPLES.

9.2.2 RESULTS WITH THE SOURCE ON THE DETECTOR'S CENTER

The first step of our analysis was obviously the study of the simplest case, with the radon source placed in the center of the sphere. Hereafter I quote the efficiencies of the different discrimination methods obtained with Air Run 8 data.

[6] The requirement is a GPS time difference included between 20 μs and 470 μs and at least 280 hits for the α candidate. The ^{214}Po α peak is centered in $\sim$328 hits, and 280 is further than 3σ from this value.

9.2.2.1 The basic classifiers efficiencies

As α and β events for the training set we have selected the $^{214}Bi(\beta)^{214}Po(\alpha)$ fast coincidence from the run with the highest statistic (1605). As already mentioned, the selection cut required a GPS time difference between 20 μs and 470 μs and a minimum threshold of 280 hits for the α candidate. We ended up with a training set consisting of 8411 α events and 8411 β events with less than 1% of uncertain events.

Given an event consisting of at least one fragment[7], the goal is now to decide whether the event is an α or a β event. We applied all the methods descibed in section 9.1 to the whole set of runs with the source in the sphere's center.
To compare the different discriminants we decided to classify the α and β events of the $^{214}Bi(\beta)^{214}Po(\alpha)$ coincidence and estimate the efficiency of the method quoting the fraction of α (β) identification[8]when the fraction of β (α) identification is 95%, 97%, 98% and 99%. Needless to say, all results are computed on events that were NOT used in the training set.

Run number	Method used	95% of α	97% of α	98% of α	99% of α	95% of β	97% of β	98% of β	99% of β
1544	**Tail to Total**	82.4	72.9	69.1	47.9	75.5	56.3	36.7	22.0
	Lkl Ratio	***95.1***	***93.6***	91.6	***87.9***	***95.9***	***91.5***	84.9	59.2
	Gatti	94.9	93.5	***92.0***	87.5	95.6	90.8	***85.0***	***59.4***
1545	**Tail to Total**	79.9	62.0	58.5	39.9	77.8	61.0	43.8	26.6
	Lkl Ratio	***94.2***	***92.6***	***90.0***	***86.4***	95.4	***92.6***	85.7	***53.4***
	Gatti	***94.2***	92.1	89.5	86.0	***95.4***	92.1	***87.1***	***53.4***
1546	**Tail to Total**	76.2	70.8	64.6	46.5	79.6	64.3	46.3	32.2
	Lkl Ratio	***95.7***	92.7	***91.3***	80.3	95.8	92.8	87.1	66.5
	Gatti	95.5	***93.5***	91.1	***81.1***	***96.0***	***93.4***	***87.2***	64.9
1600	**Tail to Total**	84.2	75.2	72.0	61.0	80.0	61.2	46.0	36.3
	Lkl Ratio	***95.6***	***93.8***	***92.1***	***85.3***	96.5	***93.0***	86.5	***68.5***
	Gatti	***95.6***	93.1	91.9	84.0	***96.6***	92.4	***86.7***	67.1
1603	**Tail to Total**	80.5	73.4	66.6	59.4	83.6	64.3	45.6	30.1
	Lkl Ratio	95.1	93.1	***91.9***	88.5	***96.2***	***91.3***	79.6	64.5
	Gatti	***95.2***	***93.4***	91.8	***89.0***	95.9	89.7	***79.7***	***66.4***

Table 9.2: list of the different discriminants efficiencies for the runs with the source placed in the SSS center. The efficiencies are quoted as the fraction of β /α identification with an α /β identification fixed at 95%, 97%, 98% and 99%.

Tables 9.2 and 9.3 report the efficiencies of the tail to total, the Gatti and the likelihood ratio filters. We omitted the efficiencies of the likelihood α and β because they are almost equivalent to the likelihood ratio, and the efficiencies of the two Kolmogorov distances

[7] In the *offline* language we call *fragment* the real physical event, after the rejection of the dark noise or spurios hits.

[8] That is the number of real α (β) events correctly classified as α (β).

Run number	Method used	95% of α	97% of α	98% of α	99% of α	95% of β	97% of β	98% of β	99% of β
1547	**Tail to Total**	79.4	74.0	64.4	52.8	79.6	63.8	56.6	39.4
	Lkl Ratio	***95.8***	***93.4***	***92.2***	***85.0***	***96.8***	***94.4***	89.1	69.3
	Gatti	95.4	93.3	92.0	84.6	96.9	94.2	***89.3***	***69.5***
1548	**Tail to Total**	74.5	69.9	61.0	52.5	66.2	48.9	38.1	22.0
	Lkl Ratio	***93.2***	***91.3***	88.3	***75.2***	92.5	***86.9***	***80.5***	***62.6***
	Gatti	92.6	***91.3***	***88.5***	74.8	***93.4***	86.4	79.4	***62.6***
1550	**Tail to Total**	77.3	72.1	65.9	51.9	79.7	64.9	50.4	33.5
	Lkl Ratio	***96.1***	***94.0***	***91.6***	85.9	96.6	***94.0***	***87.7***	70.0
	Gatti	96.0	93.9	91.5	***87.2***	***96.7***	93.7	***87.7***	***70.2***
1552	**Tail to Total**	81.0	71.0	67.6	49.1	80.9	62.5	47.9	26.9
	Lkl Ratio	***95.6***	***93.9***	***91.5***	82.4	96.6	89.0	***84.7***	68.3
	Gatti	***95.6***	***93.9***	91.4	***83.1***	***96.9***	***89.4***	82.4	***68.5***

TABLE 9.3: LIST OF THE DIFFERENT DISCRIMINANTS EFFICIENCIES FOR THE RUNS WITH THE SOURCE PLACED AT $z = +53$cm. THE EFFICIENCIES ARE QUOTED AS THE FRACTION OF β /α IDENTIFICATION WITH AN α /β IDENTIFICATION FIXED AT 95%, 97%, 98% AND 99%.

because they are comparable to the tail to total ratio. We also omitted the efficiencies of the $\mathcal{SVM}$ classifiers because they will be quoted in the next sections.
Among these four classifiers (Tail/Total, Gatti, Likelihood, Kolmogorov) the Gatti and the likelihood discriminants are the best ones, with an efficiency almost always comparable, while the tail to total ratio, as expected, is the most rough.

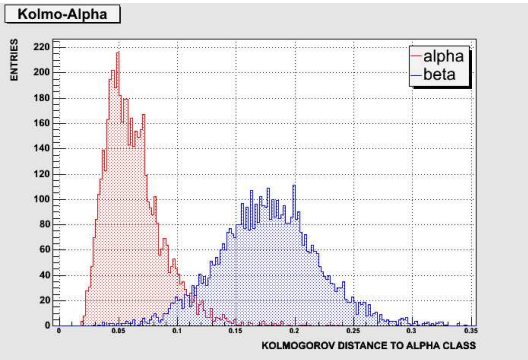

(a) FIGURE 9.6: α/β DISCRIMINATION USING THE KOLMOGOROV DISTANCE TO THE α DISTRIBUTION.

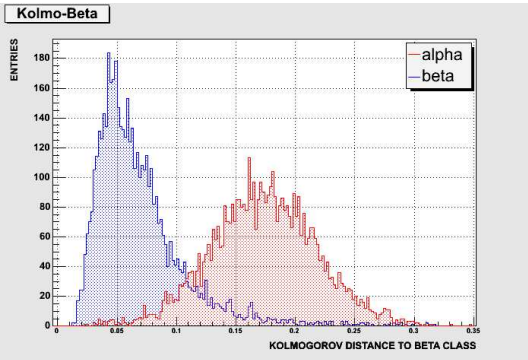

(b) FIGURE 9.6: ALPHABETA DISCRIMINATION USING THE KOLMOGOROV DISTANCE TO THE β DISTRIBUTION.

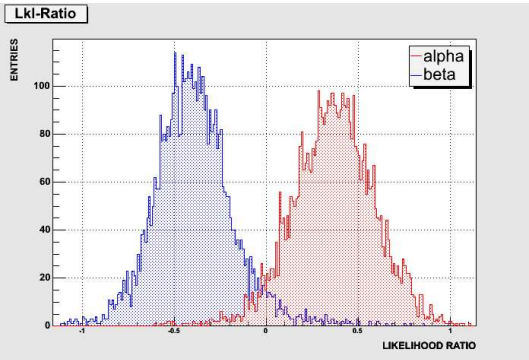

(a) FIGURE 9.7: α/β DISCRIMINATION USING THE LIKELIHOOD RATIO. ON THE x-AXIS WE REPORT THE OUTPUT VALUE OF THE DISCRIMINATION FILTER USED.

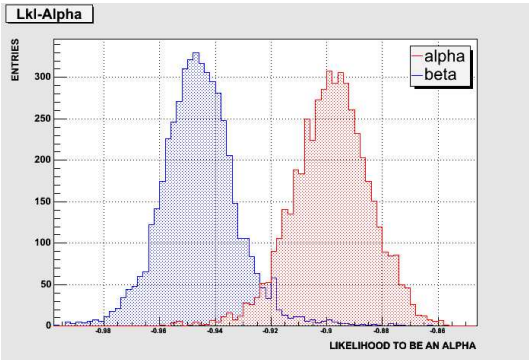

(b) FIGURE 9.7: α/β DISCRIMINATION USING THE LIKELIHOOD TO THE α DISTRIBUTION.

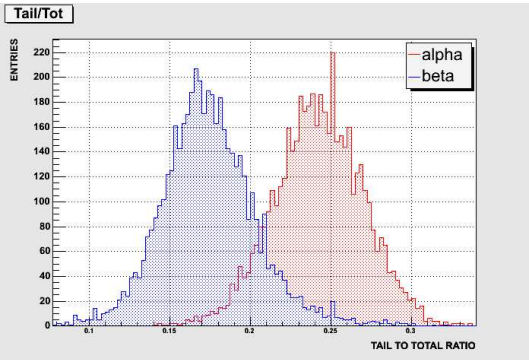

(a) FIGURE 9.8: α/β DISCRIMINATION USING THE TAIL TO TOTAL RATIO.

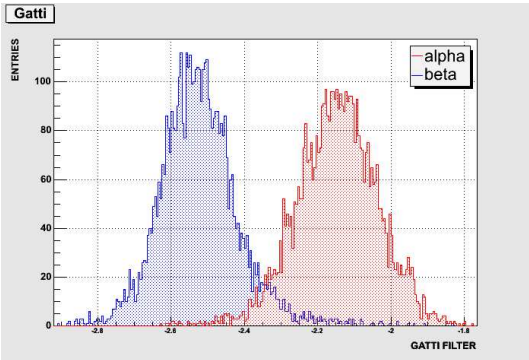

(b) FIGURE 9.8: α/β DISCRIMINATION USING THE GATTI FILTER.

Figures 9.7, 9.6, 9.8 and 9.9 show the discrimination of the different filters for the run with the source in the centre and the highest statistics (1546). Some scattered plots showing the correlation of the filters are also reported (figures 9.11 and 9.12).

9.2.2.2 The *primary* SVM results

The first analysis we made with Support Vector Machines was the study of their discrimination efficiency when making the learning directly on the training sets $\{\mathbf{x}_i^\alpha\}$ and $\{\mathbf{x}_i^\beta\}$, in the $\mathcal{R}^\Omega$ space[9].
We selected the same file choosen for the learning of the basic classifiers (1605), filtered the α and β events of the $^{214}Bi(\beta)^{214}Po(\alpha)$ coincidence, built the samples using the same reference histogram used for the basic classifiers and trained our $\mathcal{SVM}$ with these samples. Then we used the $\mathcal{SVM}$ to classify the α and β events of the $^{214}Bi(\beta)^{214}Po(\alpha)$ coincidence for the other runs.
The efficiency is quoted in table 9.4.

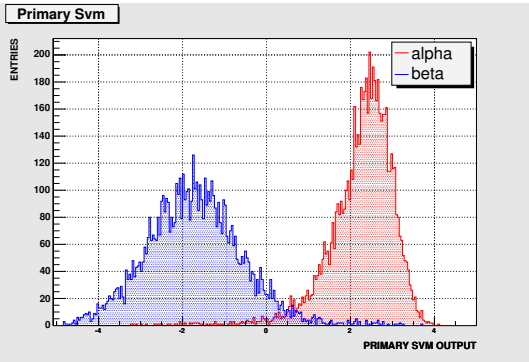

(a) Figure 9.9: α/β discrimination using the primary $\mathcal{SV}$ machine.

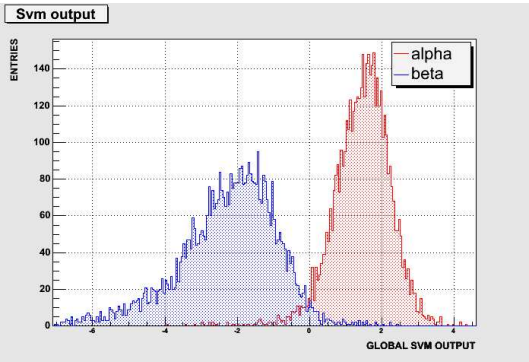

(b) Figure 9.9: α/β discrimination using the global $\mathcal{SV}$ machine.

9.2.2.3 The *global* SVM results

Finally we decided to attempt a global classification using all the discrimination methods cited up to now. Basically we want to train a second $\mathcal{SV}$ machine using as input the results of the basic classifiers and of the primary $\mathcal{SVM}$ classification. The training set of this new $\mathcal{SVM}$ is made of vectors $\mathbf{x} \in \mathcal{R}^6$, where the six variables are respectively: the output of the Gatti filter, the likelihood ratio and the likelihood to be an α , the two Kolmogorov distances and the output of the primary $\mathcal{SVM}$ (see figure 9.10).
We need now two different learning files: one run (1605) is still used for the learning of the basic classifiers and of the primary $\mathcal{SVM}$. The α and β events from the $^{214}Bi(\beta)^{214}Po(\alpha)$ coincidence of the second file (1598) are then classified using the first learning and with the six discriminants outputs we build the training set for the global $\mathcal{SVM}$ learning.
The efficiencies of the two $\mathcal{SV}$ machines, quoted in table 9.5, are almost always equivalent. In some cases we gain something with the global analysis, but the results are still not sufficiently stable. We are planning a deeeper study of the optimization of this global analysis. For

[9] That means directly on the binned times array.

Run number	Method used	95% of α	97% of α	98% of α	99% of α	95% of β	97% of β	98% of β	99% of β
1544	**Lkl Ratio**	95.1	93.6	91.6	87.9	95.9	91.5	84.9	59.2
	Gatti	94.9	93.5	92.0	87.5	95.6	90.8	85.0	59.4
	P. $\mathcal{SVM}$	***98.2***	***97.0***	***95.5***	***89.6***	***98.6***	***97.1***	***95.5***	***89.5***
1545	**Lkl Ratio**	94.2	92.6	90.0	***86.4***	95.4	92.6	85.7	53.4
	Gatti	94.2	92.1	89.5	86.0	95.4	92.1	87.1	53.4
	P. $\mathcal{SVM}$	***97.0***	***95.6***	***92.9***	78.9	***97.7***	***96.0***	***92.7***	***87.5***
1546	**Lkl Ratio**	95.7	92.7	91.3	80.3	95.8	92.8	87.1	66.5
	Gatti	95.5	93.5	91.1	81.1	96.0	93.4	87.2	64.9
	P. $\mathcal{SVM}$	***98.4***	***97.4***	***95.7***	***88.7***	***98.3***	***97.4***	***96.5***	***91.5***
1600	**Lkl Ratio**	95.6	93.8	92.1	85.3	96.5	93.0	86.5	68.5
	Gatti	95.6	93.1	91.9	84.0	96.6	92.4	86.7	67.1
	P. $\mathcal{SVM}$	***98.4***	***97.7***	***97.2***	***92.5***	***98.5***	***98.1***	***96.7***	***91.4***
1603	**Lkl Ratio**	95.1	93.1	91.9	88.5	96.2	91.3	79.6	64.5
	Gatti	95.2	93.4	91.8	89.0	95.9	89.7	79.7	66.4
	P. $\mathcal{SVM}$	***98.2***	***97.4***	***95.5***	***93.1***	***98.5***	***97.4***	***96.2***	***94.4***

TABLE 9.4: LIST OF THE DIFFERENT DISCRIMINANTS EFFICIENCIES FOR THE RUNS WITH THE SOURCE PLACED IN THE SSS CENTER.

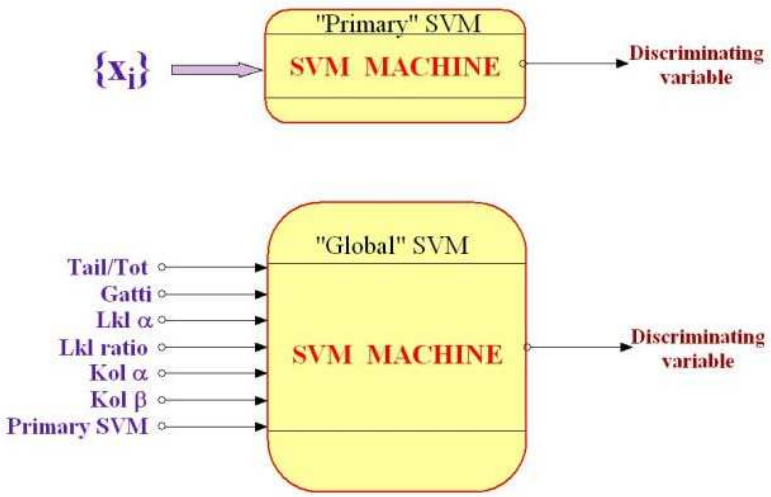

FIGURE 9.10: SIMPLE SKETCH OF THE TWO SUPPORT VECTOR MACHINES USED, IN THIS ANALYSIS, FOR α/β DISCRIMINATION.

Run number	Method used	95% of α	97% of α	98% of α	99% of α	95% of β	97% of β	98% of β	99% of β
1544	**Gatti**	94.9	93.5	92.0	87.5	95.6	90.8	85.0	59.4
	P. $\mathcal{SVM}$	***98.2***	***97.0***	95.5	89.6	***98.6***	97.1	95.5	***89.5***
	G. $\mathcal{SVM}$	***98.2***	96.7	***95.6***	***90.4***	98.4	***97.3***	***95.8***	88.2
1545	**Gatti**	94.2	92.1	89.5	***86.0***	95.4	92.1	87.1	53.4
	P. $\mathcal{SVM}$	97.0	95.6	92.9	78.9	97.7	96.0	92.7	***87.5***
	G. $\mathcal{SVM}$	***97.3***	***95.7***	***93.0***	85.0	***97.9***	***97.0***	***93.6***	86.6
1546	**Gatti**	95.5	93.5	91.1	81.1	96.0	93.4	87.2	64.9
	P. $\mathcal{SVM}$	***98.4***	***97.4***	***95.7***	***88.7***	98.3	97.4	***96.5***	91.5
	G. $\mathcal{SVM}$	***98.4***	96.9	95.4	86.7	***98.4***	***97.6***	96.3	***92.2***
1600	**Gatti**	95.6	93.1	91.9	84.0	96.6	92.4	86.7	67.1
	P. $\mathcal{SVM}$	***98.4***	***97.7***	***97.2***	***92.5***	98.5	***98.1***	96.7	91.4
	G. $\mathcal{SVM}$	98.2	97.5	96.8	91.9	***98.8***	***98.1***	***96.9***	***91.8***
1603	**Gatti**	95.2	93.4	91.8	89.0	95.9	89.7	79.7	66.4
	P. $\mathcal{SVM}$	***98.2***	***97.4***	95.5	***93.1***	***98.5***	***97.4***	96.2	***94.4***
	G. $\mathcal{SVM}$	***98.2***	96.9	***95.9***	91.3	***98.5***	***97.4***	***96.5***	94.3

TABLE 9.5: LIST OF THE DIFFERENT DISCRIMINANTS EFFICIENCIES FOR THE RUNS WITH THE SOURCE PLACED IN THE SSS CENTER.

istance, it is known that if we feed the Support Vector Machine with correlated variables, as it could be the case of the basic classifiers outputs, we can come up against convergence problems of the minimization algorithm.

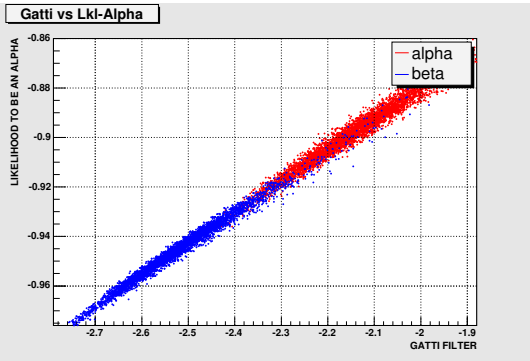

(a) Figure 9.11: scattered plot showing the correlation of the Gatti discriminant variable with the likelihood to be an α .

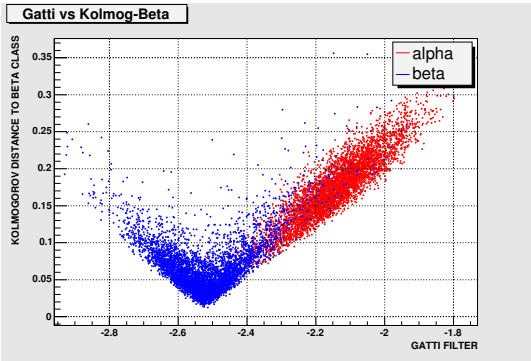

(b) Figure 9.11: scattered plot showing the correlation of the Gatti discriminant variable with the Kolmogorov distance to the β class.

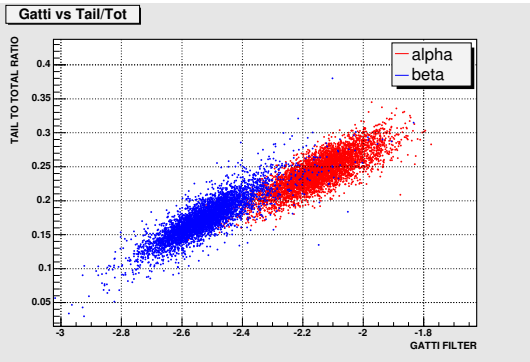

(a) Figure 9.12: scattered plot showing the correlation of the Gatti discriminant variable with the tail to total ratio.

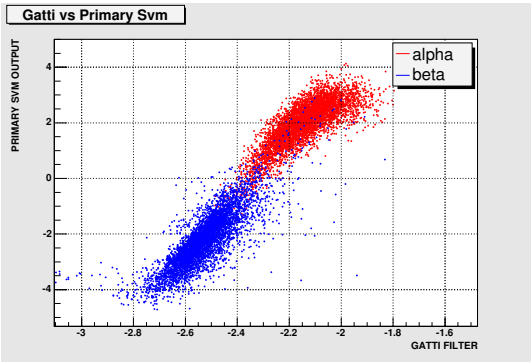

(b) Figure 9.12: scattered plot showing the correlation of the Gatti discriminant variable with the primary $\mathcal{SVM}$ output.

9.2.3 Position dependency studies

The results presented until now were obtained using only the data with the source placed in the centre of the sphere, that is obviuously the best case. The movement of the source upwards, along the z axis, breaks the simmetry and changes drastically the photon times distribution. The comparison of the α and β time distributions with the source in the sphere's center and in its most external position ($z = +400cm$) is shown in figure 9.13.

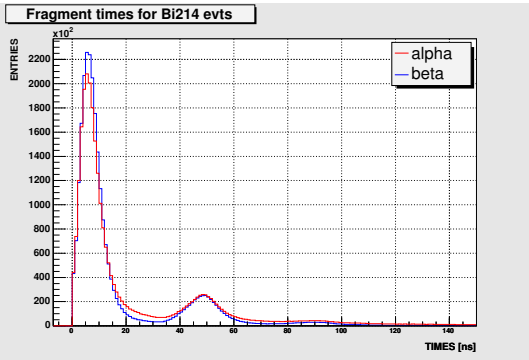

(a) Figure 9.13: Time distributions of the α and β events of the fast $^{214}Bi(\beta)^{214}Po(\alpha)$ coincidence with the source placed in the center of the stainless steel sphere.

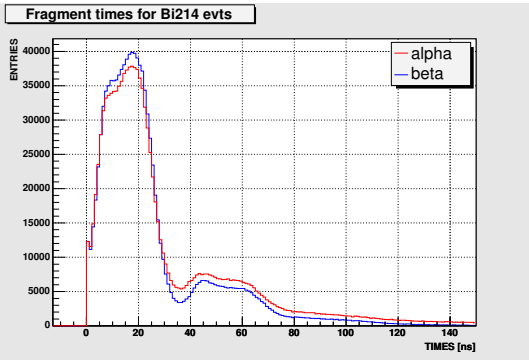

(b) Figure 9.13: Time distributions of the α and β events of the fast $^{214}Bi(\beta)^{214}Po(\alpha)$ coincidence with the source placed in its outermost position: $z = +400cm$.

The strong distortion of the time spectra affects greatly the discrimination efficiencies of all classifiers. In particular, the efficiency of the basic classifiers decreases gradually while increasing the distance to the centre, whereas the Support Vector Machines have a clear step after which become completely useless. Please note that in this paragraph we are quoting the results obtained trying to classify events taken at z=+150 cm or more, without re-training the classifiers. The classifiers, and particularly $\mathcal{SVM}$, are again good after proper actions are taken to fix this problem (see sections 9.2.3.1, 9.2.3.2).
From the numbers quoted in tables 9.6, 9.7, 9.8 and 9.9 we can deduce that up to a distance of ~150 cm from the center all the discrimination efficiencies[10]are still very good and the time distributions distortion can be neglected. The effect starts instead to be significant with the source in $z = +250cm$ and becomes huge in the last position, at $z = +400cm$.

[10]In these tables we have quoted only the efficiencies of the Gatti filter and of the two $\mathcal{SVM}$ methods, because efficiencies of the other classifiers are always comparable or worse than these three.

Run number	Method used	95% of α	97% of α	98% of α	99% of α	95% of β	97% of β	98% of β	99% of β
1547	**Gatti**	95.4	93.3	92.0	84.6	96.9	94.2	89.3	69.5
	P. $\mathcal{SVM}$	98.1	***97.3***	***95.9***	***90.2***	98.6	97.4	***96.3***	***89.8***
	G. $\mathcal{SVM}$	***98.2***	97.2	95.5	89.1	***98.7***	***97.6***	95.8	88.7
1548	**Gatti**	92.6	91.3	88.5	***74.8***	93.4	86.4	79.4	62.6
	P. $\mathcal{SVM}$	***96.8***	94.4	88.0	59.2	***97.4***	95.2	91.9	***79.6***
	G. $\mathcal{SVM}$	96.3	***94.7***	***91.6***	68.1	97.2	***95.9***	***92.8***	79.2
1550	**Gatti**	96.0	93.9	91.5	87.2	96.7	93.7	87.7	70.2
	P. $\mathcal{SVM}$	***98.3***	***97.4***	***96.5***	***94.1***	98.8	97.6	***96.4***	91.3
	G. $\mathcal{SVM}$	***98.3***	97.0	96.2	93.2	***98.9***	***98.1***	96.2	***92.2***
1552	**Gatti**	95.6	93.9	91.4	83.1	96.9	89.4	82.4	68.5
	P. $\mathcal{SVM}$	***98.1***	***97.4***	***96.4***	89.8	***98.5***	97.7	***96.5***	***92.5***
	G. $\mathcal{SVM}$	***98.1***	97.3	96.2	***90.7***	***98.5***	***98.0***	***96.5***	91.7

TABLE 9.6: LIST OF THE DIFFERENT DISCRIMINANTS EFFICIENCIES FOR THE RUNS WITH THE SOURCE PLACED AT $z = +53$cm.

Run number	Method used	95% of α	97% of α	98% of α	99% of α	95% of β	97% of β	98% of β	99% of β
1571	**Gatti**	95.3	93.3	90.6	76.9	96.2	90.7	84.2	60.8
	P. $\mathcal{SVM}$	***98.3***	97.4	96.0	***89.9***	***98.6***	***97.7***	96.6	***91.8***
	G. $\mathcal{SVM}$	***98.3***	***97.5***	***96.1***	89.5	98.5	***97.7***	***97.0***	91.5
1572	**Gatti**	95.0	92.4	89.6	80.0	95.7	91.1	82.3	64.8
	P. $\mathcal{SVM}$	***98.2***	***97.1***	95.3	88.0	***98.3***	***97.4***	96.1	89.6
	G. $\mathcal{SVM}$	***98.2***	97.0	***95.7***	***88.9***	***98.3***	97.3	***96.4***	***89.9***

TABLE 9.7: LIST OF THE DIFFERENT DISCRIMINANTS EFFICIENCIES FOR THE RUNS WITH THE SOURCE PLACED AT $z = +153$cm.

9.2.3.1 THE TIME OF FLIGHT CORRECTION

The straightforward solution to this problem is apparently the correction for the *time of flight*[11]. In table 9.10, first row, we quote the gain in efficiency after the time of flight correction for the outermost position, with the source placed in $z = +400cm$. The corrected time distributions of the α and β events of the $^{214}Bi(\beta)^{214}Po(\alpha)$ coincidence are shown in figure 9.14(a).

[11] The *time of flight* of one photon is calculated from the reconstructed event position to the center of the light guide entry aperture.

Run number	Method used	95% of α	97% of α	98% of α	99% of α	95% of β	97% of β	98% of β	99% of β
1574	**Gatti**	***90.2***	***86.4***	***81.4***	***72.8***	88.6	81.9	62.4	51.3
	P. $\mathcal{SVM}$	86.2	79.4	71.4	65.8	***91.4***	***87.7***	***86.1***	***75.8***
	G. $\mathcal{SVM}$	82.9	74.3	68.5	65.9	88.5	82.7	80.8	66.6
1575	**Gatti**	***90.0***	***85.1***	***83.2***	***76.1***	88.0	74.9	61.0	46.4
	P. $\mathcal{SVM}$	85.3	77.8	71.4	58.3	***91.0***	***86.3***	***81.4***	***78.5***
	G. $\mathcal{SVM}$	83.8	76.1	66.6	56.4	87.0	83.1	77.3	68.1
1577	**Gatti**	***90.5***	***86.8***	***82.0***	***74.3***	***89.1***	75.3	63.2	36.8
	P. $\mathcal{SVM}$	73.9	63.4	55.9	44.0	80.4	***76.1***	***67.9***	***54.9***
	G. $\mathcal{SVM}$	71.1	64.2	54.9	47.0	74.3	67.9	60.3	46.0
1579	**Gatti**	***88.0***	***82.4***	***78.2***	***66.2***	***82.1***	***70.9***	***63.8***	***45.4***
	P. $\mathcal{SVM}$	58.8	52.0	48.0	41.3	60.6	51.9	45.4	32.2
	G. $\mathcal{SVM}$	58.0	51.2	46.6	41.8	52.8	44.5	35.1	24.4
1582	**Gatti**	***87.5***	***82.7***	***78.1***	***68.2***	***84.9***	***72.4***	62.2	31.8
	P. $\mathcal{SVM}$	64.5	57.1	49.2	43.3	73.7	65.0	***62.7***	***38.5***
	G. $\mathcal{SVM}$	61.6	54.1	50.3	45.5	67.9	59.7	53.6	31.0

TABLE 9.8: LIST OF THE DIFFERENT DISCRIMINANTS EFFICIENCIES FOR THE RUNS WITH THE SOURCE PLACED AT $z = +253$cm.

Run number	Method used	95% of α	97% of α	98% of α	99% of α	95% of β	97% of β	98% of β	99% of β
1583	**Gatti**	***78.0***	***72.6***	***68.4***	***59.1***	***58.8***	***45.7***	***36.4***	***24.8***
	P. $\mathcal{SVM}$	1.5	1.2	0.9	0.7	0.8	0.6	0.4	0.1
	G. $\mathcal{SVM}$	1.6	1.5	1.3	1.1	0.6	0.3	0.2	0.1

TABLE 9.9: LIST OF THE DIFFERENT DISCRIMINANTS EFFICIENCIES FOR THE RUN WITH THE SOURCE PLACED AT $z = +403$cm.

While the $\mathcal{SVM}$ classifiers gain something, still remaining useless, the Gatti efficiency becomes even worse. This effect is due to the long non-gaussian tails of the position reconstruction (see figure 9.14(b)). Actually, as a test, we have also tried to use the nominal position of the source, instead of the output value of the reconstruction algorithm. This should mimic the case of an ideal position reconstruction algorithm and gives us only the guesstimate of the best efficiency limits we could obtain with the time of flight correction. The number are quoted in table 9.10, second row.

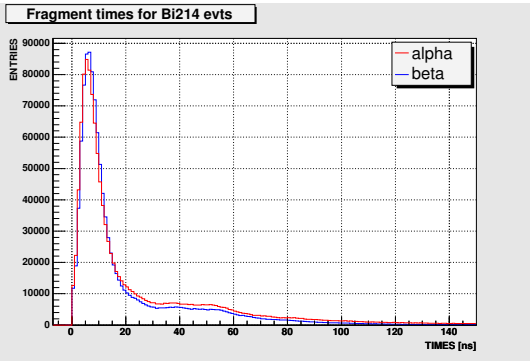

(a) FIGURE 9.14: TIME DISTRIBUTIONS OF THE α AND β EVENTS OF THE FAST $^{214}Bi(\beta)^{214}Po(\alpha)$ COINCIDENCE WITH THE SOURCE PLACED IN ITS OUTERMOST POSITION ($z = +400cm$) AND AFTER THE TIME OF FLIGHT CORRECTION.

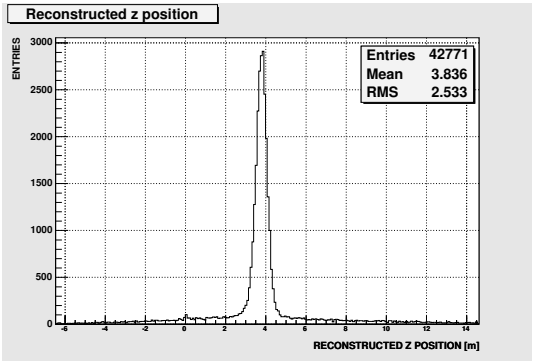

(b) FIGURE 9.14: DISTRIBUTION OF THE RECONSTRUCTED z POSITION FOR THE DATA WITH THE SOURCE PLACED IN ITS OUTERMOST POSITION ($z = +403$cm).

Run number	Method used	95% of α	97% of α	98% of α	99% of α	95% of β	97% of β	98% of β	99% of β
1583	**Gatti**	***69.8***	***64.8***	***61.7***	***57.5***	***33.2***	***22.3***	***17.2***	***10.2***
	P. $\mathcal{SVM}$	20.3	19.4	18.1	16.1	17.4	7.1	2.9	0.7
	G. $\mathcal{SVM}$	39.8	34.5	34.5	31.6	11.5	4.1	1.6	0.2
1583	**Gatti**	***92.6***	***89.9***	***87.6***	***77.0***	***91.1***	81.4	67.6	49.4
	P. $\mathcal{SVM}$	72.7	54.0	40.7	29.4	87.4	***81.5***	***75.9***	***65.6***
	G. $\mathcal{SVM}$	76.1	63.7	58.1	48.6	87.2	***81.5***	75.1	65.4

TABLE 9.10: LIST OF THE DIFFERENT DISCRIMINANTS EFFICIENCIES FOR THE RUN WITH THE SOURCE PLACED AT $z = +403$cm AND AFTER THE TIME OF FLIGHT CORRECTION. IN THE FIRST ROW THE TIME OF FLIGHT IS CALCULATED USING THE RECONSTRUCTED EVENT POSITION; IN THE SECOND ONE USING THE NOMINAL SOURCE POSITION ($z = +403cm$).

9.2.3.2 THE NON-CORRECTION APPROACH

As already pointed out in the past [77], the effect of the first reflection of the light on the photocatode in air is non-negligible. For the reflected photons the above cited time of flight correction is obviously fake and introduces on its turn another distortion of the time distributions and this effect is very big for this source data. However, since both diffused light and absorption and reflection contributions can not be corrected even in principle, we propose here a *non-correction* approach analysis.
Since the data presented in tables 9.6 and 9.7 prove that up to a distance of about 150 cm far from the center the time distribution distortion does not significantly affect the α/β discrimination capacity of our filters, we decided to ideally divide our detector in 3

concentric shells: from the center to 200 cm, from 200 cm to 300 cm and above 300 cm. The source data are then naturally divided into 3 data sets, accordingly to the position of the source in one of the 3 shells. For each of the data sets we made a separate learning for both the basic classifiers and the two $\mathcal{SV}$ machines, using directly the time distributions without any position recorrection.
The results for the first shell were already quoted in table 9.6. Concerning the second shell, we have chosen runs 1579 and 1577 for the learning phase, and table 9.11 reports the efficiencies obtained with the remaining data. Finally for the outer shell we divided run 1583 in three data sets, ~15000 events each. Two of them were used for the learning, while the numbers quoted in table 9.12 refer the the third set. We wish to point out how these efficiencies resemble the best ones quoted in table 9.10 for the ideal position reconstruction algorithm.

Run number	**Method used**	**95% of α**	**97% of α**	**98% of α**	**99% of α**	**95% of β**	**97% of β**	**98% of β**	**99% of β**
1574	**Gatti**	89.5	86.7	82.4	72.3	89.4	81.1	65.1	55.5
	P. $\mathcal{SVM}$	98.2	***97.7***	***95.7***	86.1	98.2	97.6	96.8	***90.6***
	G. $\mathcal{SVM}$	***98.5***	97.2	95.6	***87.3***	***98.3***	***97.8***	***96.9***	90.5
1575	**Gatti**	90.4	85.1	84.8	74.3	88.6	77.5	66.9	51.0
	P. $\mathcal{SVM}$	98.1	95.9	***90.7***	83.6	***97.4***	96.6	***96.0***	87.7
	G. $\mathcal{SVM}$	***98.5***	***96.5***	89.9	***83.8***	97.3	***96.8***	***96.0***	***88.2***
1582	**Gatti**	87.7	82.9	78.5	69.5	86.4	71.7	59.7	34.7
	P. $\mathcal{SVM}$	***96.3***	93.8	***90.6***	***81.9***	96.7	94.7	***92.5***	77.7
	G. $\mathcal{SVM}$	95.7	***94.2***	***90.6***	80.7	***96.9***	***94.9***	***92.5***	***82.0***

TABLE 9.11: LIST OF THE DIFFERENT DISCRIMINANTS EFFICIENCIES FOR THE RUNS WITH THE SOURCE PLACED AT $z = +253$cm AND AFTER A RE-TRAINING OF THE CLASSIFIERS. BOTH THE BASIC CLASSIFIERS AND THE $\mathcal{SV}$ MACHINES WERE TRAINED USING RUNS 1579 AND 1577. THE EFFICIENCIES ARE QUOTED AS THE FRACTION OF β /α IDENTIFICATION WITH AN α /β IDENTIFICATION FIXED AT 95%, 97%, 98% AND 99%.

Run number	**Method used**	**95% of α**	**97% of α**	**98% of α**	**99% of α**	**95% of β**	**97% of β**	**98% of β**	**99% of β**
1583	**Gatti**	78.3	72.5	66.7	55.9	62.8	48.9	38.7	27.5
	P. $\mathcal{SVM}$	***92.2***	***86.2***	***82.5***	***68.9***	93.3	***90.9***	85.7	74.3
	G. $\mathcal{SVM}$	91.7	85.5	78.4	67.1	***94.5***	90.8	***86.0***	***74.5***

TABLE 9.12: LIST OF THE DIFFERENT DISCRIMINANTS EFFICIENCIES FOR THE RUN WITH THE SOURCE PLACED AT $z = +403$cm AND AFTER A RE-TRAINING OF THE CLASSIFIERS. BOTH THE BASIC CLASSIFIERS AND THE $\mathcal{SV}$ MACHINES WERE TRAINED ON A SMALLER STATISTIC EXTRACTED FROM THE SAME RUN. THE EFFICIENCIES ARE QUOTED AS THE FRACTION OF β /α IDENTIFICATION WITH AN α /β IDENTIFICATION FIXED AT 95%, 97%, 98% AND 99%.

9.3 The source spectrum analysis

Having tuned the α/β discrimination techniques to the above mentioned efficiencies, we studied then the overall α and β spectra of our radon source.

Figure 9.15(a) shows the α and β spectra[12]obtained using the simplest discrimination method: the tail to total ratio. Figure 9.15(b) compares this method with the best one found in the previous analysis: the global Support Vector Machine. We can easily notice the clear reduction of the α contamination in the low energy region, and also a significan gain in the β spectrum.

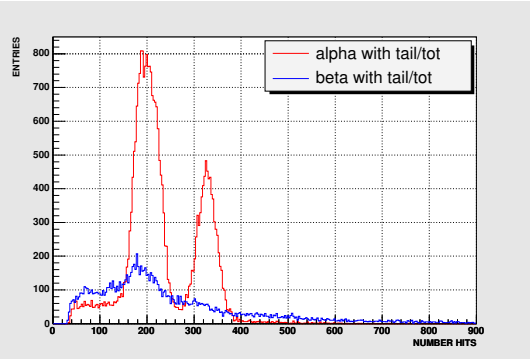

(a) Figure 9.15: overall α and β spectra of the radon source used during Air Run 8. The spectra were obtained using the tail to total ratio. All spectra were obatined using 97% of β /α rejection.

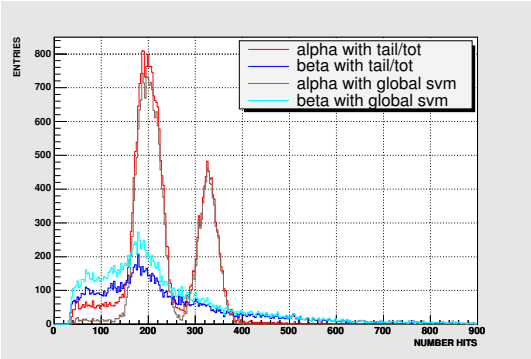

(b) Figure 9.15: comparison of the overall α and β spectra of the radon source. The spectra were obtained using the tail to total ratio and the global $\mathcal{SVM}$ classifier.

Since the results quoted in the previous section indicate the $\mathcal{SV}$ machines and the linear Gatti discriminant as the classifiers with the best α/β separating power, we have compared also these two methods. Figure 9.16(b) shows a zoom of the low energy region. Here, below 140 hits, we are 3 σ far from the first α peak ($\sim$186 hits), and, in theory, we expect no α events: all the events with less than 140 hits and labelled as α events are clearly β misclassified events. To better compare the efficiencies of the two classifiers I have normalized the α and β spectra obtained with the two methods to the same number of events and I have plotted the ratio (bin to bin) of the α and β histograms. The resulting plot is shown in figure 9.17, where I have also reported the absolute energy scale[13]. Since no α events should contribute, we expect the α/β ratio to be, in theory, 0; the closeness of the histogram curves to zero is then a good parameter to judge the efficiency of the filters. The global $\mathcal{SV}$ machine results then the best candidate to obtain the highest α/β separating power.

[12]The spectra are presented here as number of hits. The conversion to an energy is done below.

[13]The number of hits to energy conversion factor (yield) is inferred from our data. The obtained value is quoted below.

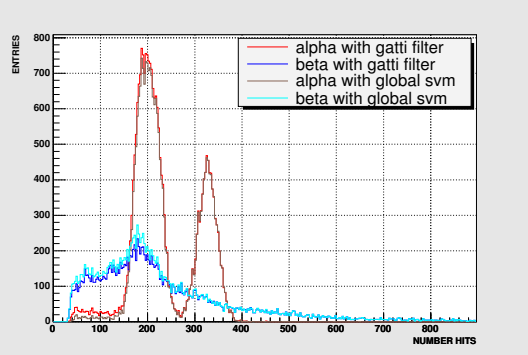

(a) Figure 9.16: comparison of the overall α and β spectra of the radon source. The spectra were obtained using the Gatti discriminant and the global $\mathcal{SVM}$ classifier.

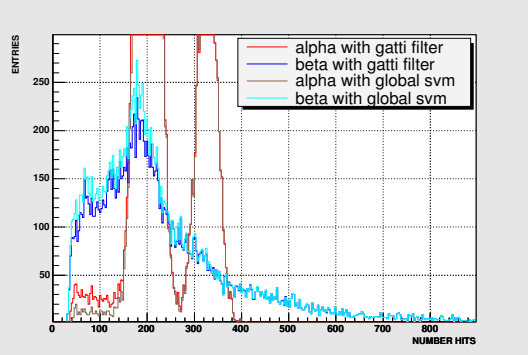

(b) Figure 9.16: zoom of the low energy region.

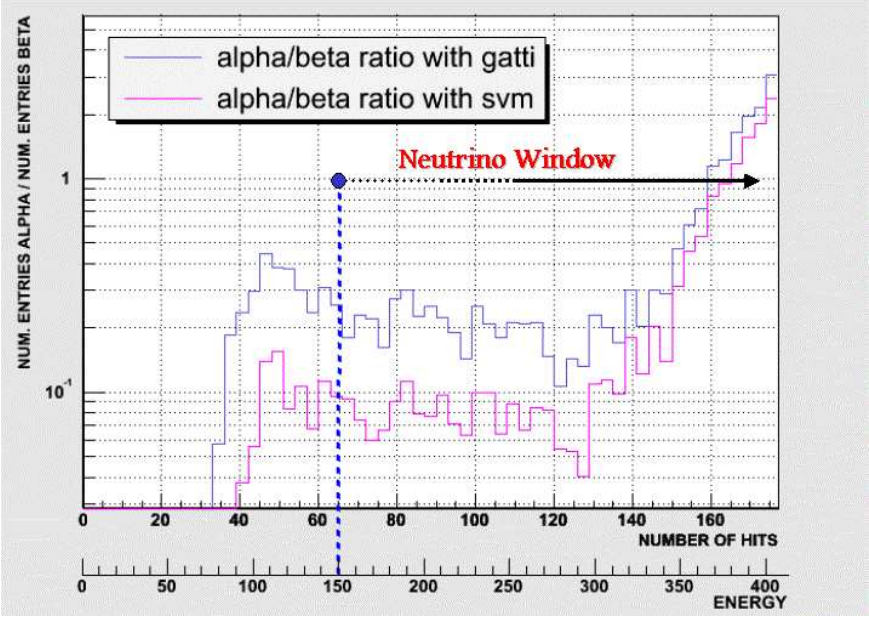

Figure 9.17: α over β spectra ratio. The ratio is done bin to bin and the spectra, obtained through the Gatti and the global $\mathcal{SVM}$ classifiers, are normalized to the same number of events. The energy line corresponding to the edge of the neutrino window (150 KeV) is also highlighted.

We decided then to use the global $\mathcal{SVM}$ classifier to test the compatibility of the two spectra with what we expect from theory. The spectra were now produced with a more stringent cut, i.e. 99% α rejection for the β spectrum and 99% β rejection for the α spectrum, so to have cleaner data.

From the radon decay chain, we expect three α to contribute to the overall spectrum: the 5.49 MeV (410 KeV quenched) α of ^{222}Rn decay, the 6.02 MeV (483 KeV quenched) α of ^{218}Po and the 7.688 Mev (751 KeV quenched) α of ^{214}Po . The fourth 5.305 (398 KeV quenched) α from ^{210}Po comes after ^{210}Pb , and this isotope has a too long lifetime (2.17 y) to give a significant contribute, with its daughters, to our spectrum.
The expected α spectrum is then made of three α peaks, two of them almost superimposed, all underlying the same area and with a width equal to the square root[14] of their peak values. Moreover the position of the α peaks fixes the absolute yield of the scintillator.

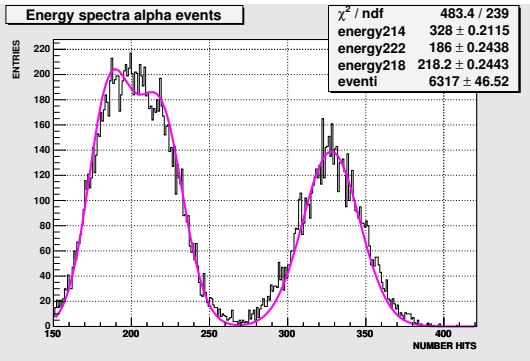

(a) FIGURE 9.18: FIT OT THE OVERALL α SPECTRUM WITH THE SUM OF THREE GAUSSIANS WITH FIXED STANDARD DEVIATIONS.

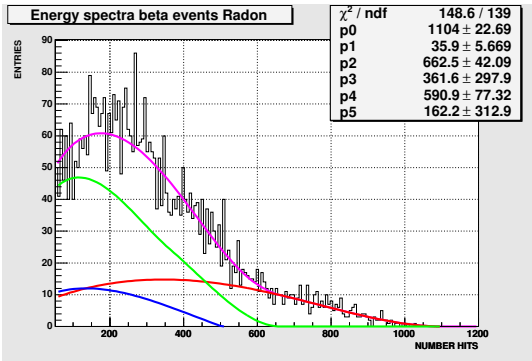

(b) FIGURE 9.18: FIT OT THE OVERALL β SPECTRUM OF THE $^{f}Bi(\beta)^{f}Po(\alpha)$ AST COINCIDENCE WITH THE SUM OF THREE PURE β SPECTRA.

We used the highest peak of the 751 KeV α (from ^{214}Po) to fix the absolute yield, fitting the peak with a gaussian. We found: $(436.8 \pm 0.4) p.e./MeV$. The overall spectrum was then fit keeping the position of the three peaks and the total number of α events as fit parameters. The fit function was the sum of three gaussian, whose width was fixed to the square root values of their peaks. The result is shown in figure 9.18(a).
The position of the three peaks found in the fit (186.0 ± 0.2, 218.2 ± 0.2, 328.0 ± 0.2) does not completely agree with the position we expect from fixing the yield (179,211,328): the low energy α are shifted toward higher energies. The corresponding light yield values are $(453.7 \pm 0.5) p.e./MeV$ for the ^{222}Rn peak and $(451.7 \pm 0.4) p.e./MeV$ for the ^{218}Po peak.

Finally the last thing we attempted was a fit of the β spectrum of the $^{f}Bi(\beta)^{f}Po(\alpha)$ ast coincidence. ^{214}Bi decays β into ^{214}Po with five branches. The most important branching ratios are:

- *19%* : β , Q=3.23 MeV
- *40%* : β +γ, Q=1.51 MeV

[14] That is the energy resolution of our detector.

- *23%* : $\beta + \gamma$, Q=1.02 MeV

The fit of the $^{\beta}\ Bi(\beta)^{\beta}\ Po(\alpha)$ spectrum as a sum of three pure β spectra, keeping both the end-points and the amplitudes as fit parameters, is shown in figure 9.18(b).

Acknowledgements

First of all, I would like to express my great appreciation to prof. Gianpaolo Bellini, spoksperson of the Borexino Collaboration, and to all Borexino collaborators.

I would like to especially thank the whole *software* working group: Barbara, Davide D. and Davide F., Igor, Emanuela, Maria Elena, Alessandro, Andrew and Sergey for their help, expertise and support during the long days in Hall C.
I am also in debt to PMT working group, and especially Paolo, Augusto and Gioacchino. A special thank to Massimo and his invaluable help.

I am grateful to the LNGS staff: Aldo and Andrea, Stefano, Augusto, Roberto and all the others (too many to be listed here!) and to the Genoa group, who kindly helped me in these years: Carlo, Corrado, Gemma, Vittorio, Paolo and Marco A..

There are still many people I would like to acknowledge for their help, teaching and friendship during these years.
Gyorgy, I can't find the right words to say *"nagyon szépen köszönöm"*!
Thanks to all people who shared with me the beautiful moments I spent in Gran Sasso: Laszlo, Burkhard, Ludwig, Christian, Oleg, Didier, Richard and Andrea, Paolo, Alba and Maria. You transformed these years in a wonderful experience.
I have to gratefully ackowledge also my friends in Genova, in particular Marta, Lara, Chiara and Annalisa. Thanks for being always there!

Great appreciation goes to my parents, who constantly supported me with enormous patience.

Finally, the last thanks to my love!

Bibliography

[1] J.N. Bahcall, C. Pena-Garay, "Global analyses as a road map to solar neutrino fluxes and oscillation parameters", JHEP, **11**, 004 (2003).

[2] J.N. Bahcall, M.C. Gonzalez-Garcia, C. Pena-Garay, "Before and After: How has the SNO NC measurement changed things?", JHEP, **07**, 054 (2002).

[3] J.N. Bahcall, M.C. Gonzalez-Garcia, C. Pena-Garay, "Solar Neutrinos Before and After KamLAND ", JHEP, **2**, 09 (2003).

[4] W. Pauli, "Letter to the Physical Society of Tübingen", *unpublished*, (December 4, 1930).

[5] F. Reines, "The neutrino: from poltergeist to particle", *Rev. Mod. Phys.*, **68**, 317 (1996).

[6] F. Reines and C.L. Cowan Jr., "A proposed experiment to detect free neutrino", *Phys. Rev.* , **90**, 492 (1953).

[7] M.C. Gonzalez-Garcia, Y. Nir, "Neutrino Masses and Mixing: Evidence and Implication", *Rev. Mod. Phys.*, **75**, 345 (2003).

[8] K. Hagiwara *et al.*, "Summary tables in the 2002 Review of Particle Physics", *Phys. Rev. D*, **66**, 010001 (2002).

[9] H.A. Bethe, "Energy production in stars", *Phys. Rev.* , **55**, 434 (1939).

[10] J.N. Bahcall, M.H. Pinsonneault and S. Basu, "Solar model: current epochs and time dependencies, neutrinos and helioseismological properties", *Astrop. Phys.* , **555**, 990 (2001).

[11] R. Davis, Jr., D.S. Harmer, and K.C. Hoffman, "Search for Neutrinos from the Sun", *Phys. Rev. Lett.* , **20**, 1205 (1968).

[12] The SAGE collaboration: J. N. Abdurashitov *et al.*, "Measurement of the Solar Neutrino capture rate by SAGE and implications for neutrino oscillations in vacuum", *Phys. Rev. Lett.* , **83**, 4686 (1999).

[13] The GALLEX collaboration: W. Hampel *et al.*, "GALLEX Solar Neutrino observations: results for GALLEX IV", *Phys. Lett. B*, **447**, 127 (1999).

[14] The GNO collaboration: M. Altmann *et al.*, "GNO Solar Neutrino observations: results for GNO I", *Phys. Lett. B*, **490**, 16 (2000).

[15] The Kamiokande collaboration: Y. Fukuda *et al.*, "Solar Neutrino Data Covering Solar Cycle 22", *Phys. Rev. Lett.* , **77**, 1683 (1996).

[16] The Super-Kamiokande collaboration: Y. Fukuda *et al.*, "Solar ^8B and *hep* Neutrino Measurements from 1258 Days of Super-Kamiokande Data", *Phys. Rev. Lett.* , **86**, 5651 (2001).

[17] A. Bandyopadhyay, S. Choubey, S. Goswami, "Neutrino decay confronts the SNO data", *Phys. Lett. B*, **555**, 33 (2003).

[18] J.N. Bahcall, S.Basu and M.H. Pinsonneault, "Solar Models: current epoch and time dependences, neutrinos, and helioseismological properties", *Astrophys.J.*, **555**, 990 (2001).

[19] S. Bludman, N. Hata and P.Langacker, "Astrophysical solutions are incompatible with the Solar Neutrino data", *Phys. Rev. D*, **49**, 3622 (1994).

[20] V. Berezinsky, G. Fiorentini and M. Lissia, "The last hope for an astrophysical solution to the solar neutrino problem", *Phys. Lett. B*, **365**, 185 (1996).

[21] J.N. Bahcall, "An introduction to solar neutrino research", *SLAC Summer Institute on Particle Physics: Physics of Leptons*, **Stanford, CA**, (August 4-15, 1997). hep-ph/9711358

[22] J.N. Bahcall, P. Kravstev, Y. Smirnov, "Where do we stand with solar neutrino oscillations?", *Phys. Rev. D*, **58**, 096016 (1998).

[23] V.N. Gribov, B.M. Pontecorvo, "Neutrino Astronomy and lepton charge", *Phys. Lett. B*, **28**, 493 (1969).

[24] L. Wolfenstein, "Neutrino Oscillations in matter", *Phys. Rev. D*, **17**, 2369 (1978).

[25] S.P. Mikheyev, A.Y. Smirnov, "Resonance enhancement of oscillations in matter and Solar Neutrino spectroscopy", *Sov. Jour. Nucl. Phys.*, **42**, 913 (1985).

[26] L.B. Okun, "Leptons and quarks", *North Holland*, (1982).

[27] T. Kajita, Y. Totsuka, "Observation of atmospheric neutrinos", *Rev. Mod. Phys.*, **73**, 85 (2001).

[28] The Fréjus collaboration: K. Daum *et al.*, "Determination of the atmospheric neutrino spectra with the Fréjus detector", *Z. Phys. C*, **66**, 417 (1995).

[29] The NUSEX collaboration: M. Aglietta *et al.*, "Experimental study of atmospheric neutrino flux in the NUSEX experiment", *Europhys. Lett.*, **8**, 611 (1989).

[30] The Soudan2 collaboration: W.W.M. Allison *et al.*, "The atmospheric neutrino flavor ratio from a 3.9 fiducial kiloton-year exposure of Soudan 2", *Phys. Lett. B*, **449**, 137 (1999).

[31] The MACRO collaboration: M. Ambrosio *et al.*, "Matter effects in upward-going muons and sterile neutrino oscillations", *Phys. Lett. B*, **517**, 59 (2001).

[32] The IMB collaboration: Becker-Szendy *et al.*, "The electron-neutrino and muon-neutrino content of the atmospheric flux", *Phys. Rev. D*, **46**, 3720 (1992).

[33] The Kamiokande collaboration: S.H. Hirata *et al.*, "Observation of a small atmospheric ν_μ /ν_e ratio in Kamiokande", *Phys. Lett. B*, **280**, 146 (1992).

[34] The Kamiokande collaboration: Y. Fukuda *et al.*, "Atmospheric ν_μ /ν_e ratio in the multi-GeV energy range", *Phys. Lett. B*, **335**, 237 (1994).

[35] The Super-Kamiokande collaboration: Y. Fukuda *et al.*, "Evidence for oscillation of atmospheric neutrinos", *Phys. Rev. Lett. B*, **81**, 1562 (1998).

[36] The CHOOZ collaboration: M. Apollonio *et al.*, "Initial results from the CHOOZ long baseline reactor neutrino oscillation experiments", *Phys. Lett. B*, **420**, 397 (1998).

[37] The Super-Kamiokande collaboration: Y. Fukuda *et al.*, "Tau Neutrinos Favoured Over Sterile Neutrinos in Atmospheric Muon-Neutrino Oscillations", *Phys. Rev. Lett. B*, **85**, 3999 (2000).

[38] The LUNA collaboration: M. Junker *et al.*, "Cross section of ^3He (^3He -2p)^4He measured at solar energies", *Phys. Rev. C*, , 5 (1998).

[39] The LUNA collaboration: R. Bonetti *et al.*, "First measurement of the ^3He (^3He -2p)^4He cross section down the lower edge of the solar Gamov peak", *Phys. Rev. Lett.* , **82**, 5205 (1999).

[40] J.N. Bahcall, P.I. Krastev, A.Yu. Smirnov, "Where do we stand with solar neutrino oscillations?", *Phys. Rev. D*, **58**, 1 (2003).

[41] G.L. Fogli, E. Lisi, D. Montanino and A. Palazzo, "Three-flavor MSW solutions of the solar neutrino problem", *Phys. Rev. D*, **62**, (2000).

[42] The SNO collaboration: A.B. McDonald *et al.*, "First neutrino observations from the Sudbury Neutrino Observatory", *Nucl. Phys. Proc. Suppl.*, **91**, 21 (2000).

[43] G.L. Fogli *et al.*, "Getting the most from the statistical analysis of solar neutrino oscillations", *Phys. Rev. D*, **66**, 053010 (2002).

[44] M.E. Moorhead, "Reflectors in Cherenkov detectors", *Ph. D. Thesis Oxford University*, (1992).

[45] A. Ianni, G. Korga, G. Ranucci, O. Ju. Smirnov, A. Sotnikov, "PMT orientation versus Mu-metal shielding", *Internal Report of the Borexino Project*,

[46] A. Ianni, G. Korga, G. Ranucci, O. Ju. Smirnov, A. Sotnikov, "Compensating the influence of the Earth s Magnetic Field on the scintillator detector resolutions by PMTs orientation", *INFN/TC-00/*, **18**, (15/9/2000).

[47] T. Hagner *et al.*, *Astrop. Phys. 14*, 13 (2000).

[48] J. Maneira, "Calibration and Monitoring for the Borexino Solar Neutrino Experiment", *Ph. D. Thesis Milano University*, (2003).

[49] J. B. Benziger *et al.*, "A scintillator puri cation system for a large scale solar neutrino experiment", *Nucl. Instr. Meth. A*, **417**, 278 (1998).

[50] M. Balata *et al.*, "The water purification system for the low background Counting Test Facility of the Borexino experiment at Gran Sasso", *Nucl. Instr. Meth. A*, **370**, 605 (1996).

[51] L. Cadonati, "Il controllo dei livelli di Radon in aria ed in acqua nell'ambito del progetto Borexino: techniche di abbattimento e misure ad alta sensitivita"', *Laurea thesis Universitá degli Studi di Milano*, (1995).

[52] G. Heusser *et al.*, "^{222}Rn detection at the μBq $/m^3$ range in nitrogen gas and a new Rn purification technique for liquid nitrogen", *Appl. Rad. Isot.*, **52**, 691 (2000).

[53] A. Pocar, "Low background techniques and experimental challenges for Borexino and its nylon vessels", *Ph. D. Thesis Princeton University*, (2003).

[54] G.F. Knoll, "Radiation detection and measurement", *John Willey and Sons*, (1989).

[55] J.B. Birks, "The theory and practice of scintillator quenching", *Pergaman Press*, (1964).

[56] Borexino Collaboration, G. Alimonti et al., "A large scale low background liquid scintillation detector: the Counting Test Facility at Gran Sasso", *Nucl. Instr. Meth. A*, **406**, 411 (1998).

[57] L. Cadonati, F. Calaprice, and M. Chen, "Supernova neutrino detection in Borexino", *Astropart.Phys.*, **16**, 361 (2002).

[58] L. Cadonati, "Neutrino Detection in Borexino", *Internal Report of the Borexino Project*, (1999).

[59] Gianni Fiorentini and Alessandro Pascolini, "Journey to the centre of the Earth", CERN *courier 43*, **8**, (2003).

[60] R.S. Raghavan, S. Schoenert, S. Enomoto, J. Shirai, F. Suekane and A. Suzuki, "Measuring the Global Radioactivity in the Earth bu Multidetector Antineutrino Spectroscopy", *Phys. Rev. Lett. 80*, **3**, 635 (1998).

[61] V. Lagomarsino, G. Testera, "A gateless charge integrator for Borexino energy measurement", *Nucl. Instr. Meth. A*, **430**, 435 (1999).

[62] C.A.E.N. SpA, "Technical Information Manual Model SYS527", *Technical information manual*, (2000). (www.caen.it/nuclear/)

[63] C.A.E.N. SpA, "Technical Information Manual Mod A303", *Technical information manual*, (2000). (www.caen.it/nuclear/)

[64] A. Razeto, "Driver per l'interfaccia Caenet", *Internal Report*, (1999).

[65] C.A.E.N. SpA, "Technical Information Manual Model A932A", *Technical information manual*, (1999). (www.caen.it/nuclear/)

[66] F. Gatti, P.Musico, A. Nostro, M. Pallavicini, A. Razeto, M. Ruscitti, S. Vitale, "A multi-hit and multi-event acquisition board for the Borexino experiment", *To be published on Nucl. Instr. Meth. A*, (2001).

[67] D. Manuzio, A. Razeto, "Offline Time Reconstruction Algorithm", *Internal Report of the Borexino Project*, (2003).

[68] "Muon Trigger Board (MTB) Specification Document", (bxweb.lngs.infn.it/docs/Trigger/MuonTriggerBoard.pdf)

[69] D. D'angelo, C. Lendvai, D. Manuzio, L. Oberauer, "Outer Detector Total Charge", *Internal Report of the Borexino Project*, (2003).

[70] "Charge to Time Converters (QTC) Specification Document", (bxweb.lngs.infn.it/docs/Trigger/OuterMuon/Muon_QTC.pdf)

[71] L. Cadonati, "Simulation of gamma rays from the rock in Borexino", *Internal Report of the Borexino Project*, (1996).

[72] W.R. Nelson, H. Hirayama, D.W.O. Rogers, "The EGS4 code system", *SLAC-265 UC-32*, (1996).

[73] D. Manuzio, "Borexino Trigger Layout and Logic", *Internal Report of the Borexino Project*, (2003).

[74] O. Smirnov, "Energy reconstruction strategies", *Internal Report of the Borexino Project*, (2001).

[75] F. James, "MINUIT", *Technical report, CERN Program Library*, (1994).

[76] T. Joachims, "Making large-scale SVM Learning Practical", *Advances in Kernel Methods - Support Vector Learning, B. Schölkopf, C. Burges and A. Smola (ed.), MIT-Press*, (1999). (http://www-ai.cs.uni-dortmund.de/DOKUMENTE/joachims_99a.pdf)

[77] D. Manuzio, M.E. Monzani, "Results from AirRun IV", (2003). Internal Report of the Borexino Project

[78] J.B. Birks, *Proc Phys. Soc*, **A64**, 874 (1951).

[79] S. Bonetti *et al.*, "Ionization quenching: effects on e^- and γ detection in Borexino and in CTF", *Internal Report of the Borexino Project*, (1998).

[80] I. Manno, "Pulse shape discrimination in Borexino", *Internal Report of the Borexino Project*, (1997).

[81] E. Gatti and F. De Martini, "A new linear method of discrimination between elementary particles in scintillation counters", *IAEA Wien*, 265 (1962).

[82] Chakravart, Laha, and Roy, "Handbook of Methods of Applied Statistics, Volume I", *John Wiley*, 392 (1967).

[83] I. Manno, "Probability density function fit", *Il Nuovo Cimento Vol. 108B*, **6**, 699 (1993).

[84] V. Vapnik, "The Nature of Statistical Learning Theory", *Berlin: Springer-Verlag*, (1995).

[85] C. J. C. Burges, "A Tutorial on Support Vector Machines for Pattern Recognition", *Knowledge Discovery and Data Mining*, **2**, 121 (1998).

[86] M.E. Monzani, "Metodi di identificazione delle particelle α/β in grandi volumi di scintillatore liquido, per la reiezione del fondo radioattivo nell'esperimento Borexino", *Laurea thesis Universitá degli Studi di Milano*, (2000).

[87] R. Dossi, "Studio dei fototubi e dello scintillatore per l'esperimento Borexino", *Laurea thesis Universitá degli Studi di Milano*, (1997).